

Springer Theses

Recognizing Outstanding Ph.D. Research

Martin Thomas

Theoretical Modeling of Vibrational Spectra in the Liquid Phase



Springer

Springer Theses

Recognizing Outstanding Ph.D. Research

Aims and Scope

The series “Springer Theses” brings together a selection of the very best Ph.D. theses from around the world and across the physical sciences. Nominated and endorsed by two recognized specialists, each published volume has been selected for its scientific excellence and the high impact of its contents for the pertinent field of research. For greater accessibility to non-specialists, the published versions include an extended introduction, as well as a foreword by the student’s supervisor explaining the special relevance of the work for the field. As a whole, the series will provide a valuable resource both for newcomers to the research fields described, and for other scientists seeking detailed background information on special questions. Finally, it provides an accredited documentation of the valuable contributions made by today’s younger generation of scientists.

Theses are accepted into the series by invited nomination only and must fulfill all of the following criteria

- They must be written in good English.
- The topic should fall within the confines of Chemistry, Physics, Earth Sciences, Engineering and related interdisciplinary fields such as Materials, Nanoscience, Chemical Engineering, Complex Systems and Biophysics.
- The work reported in the thesis must represent a significant scientific advance.
- If the thesis includes previously published material, permission to reproduce this must be gained from the respective copyright holder.
- They must have been examined and passed during the 12 months prior to nomination.
- Each thesis should include a foreword by the supervisor outlining the significance of its content.
- The theses should have a clearly defined structure including an introduction accessible to scientists not expert in that particular field.

More information about this series at <http://www.springer.com/series/8790>

Martin Thomas

Theoretical Modeling of Vibrational Spectra in the Liquid Phase

Doctoral Thesis accepted by
the University of Bonn, Germany

 Springer

Author

Dr. Martin Thomas
Mulliken Center for Theoretical Chemistry
University of Bonn
Bonn
Germany

Supervisor

Prof. Barbara Kirchner
Mulliken Center for Theoretical Chemistry
University of Bonn
Bonn
Germany

ISSN 2190-5053

Springer Theses

ISBN 978-3-319-49627-6

DOI 10.1007/978-3-319-49628-3

ISSN 2190-5061 (electronic)

ISBN 978-3-319-49628-3 (eBook)

Library of Congress Control Number: 2016957490

© Springer International Publishing Switzerland 2017

This work is subject to copyright. All rights are reserved by the Publisher, whether the whole or part of the material is concerned, specifically the rights of translation, reprinting, reuse of illustrations, recitation, broadcasting, reproduction on microfilms or in any other physical way, and transmission or information storage and retrieval, electronic adaptation, computer software, or by similar or dissimilar methodology now known or hereafter developed.

The use of general descriptive names, registered names, trademarks, service marks, etc. in this publication does not imply, even in the absence of a specific statement, that such names are exempt from the relevant protective laws and regulations and therefore free for general use.

The publisher, the authors and the editors are safe to assume that the advice and information in this book are believed to be true and accurate at the date of publication. Neither the publisher nor the authors or the editors give a warranty, express or implied, with respect to the material contained herein or for any errors or omissions that may have been made.

Printed on acid-free paper

This Springer imprint is published by Springer Nature

The registered company is Springer International Publishing AG

The registered company address is: Gewerbestrasse 11, 6330 Cham, Switzerland

Supervisor's Foreword

Over the last decades, theoretical chemistry has become an integral part of scientific research. Computer simulations provide major support in understanding experimental results in greater detail and allow to predict properties of molecules which have not been synthesized yet. The simulation of vibrational circular dichroism spectra in the liquid phase posed a strong challenge for a long time. Previous publications on this topic are scarce. Due to the difficulties to define the magnetic moment, none of them has described completely general *ab initio* spectra on the basis of molecular dynamics. In this thesis, several novel ideas for this field are presented which provide important new contributions to the simulation techniques of liquids and their vibrational spectra.

Dr. Martin Thomas has developed a new method of Voronoi spectra. To achieve this, the electron density had to be divided with the help of a Voronoi tessellation. As a result, the electron density can be allocated to certain molecules. It is of utmost importance not to use the normal Voronoi tessellation but the radical Voronoi tessellation. With this new method it is now possible to calculate the charge as well as the dipole moment. Moreover, the infrared spectra and Raman spectra can be calculated. As the density is written on a grid and is not treated continuously, more developments had to be made. To solve this problem, Dr. Martin Thomas has developed a new algorithm.

The Voronoi tessellation of the electron density in *ab initio* molecular dynamics is shown to be an excellent method to calculate molecular dipole moments. While existing approaches to calculate this quantity often rely on a Wannier localization, which can be very costly regarding computational resources, the Voronoi tessellation allows a significant speedup in simulations of infrared and Raman spectra of liquids. Furthermore, a novel approach is developed to calculate the magnetic moment directly from the electron density. Thus, the first fully *ab initio* simulation of the vibrational circular dichroism spectrum of a liquid could be conducted.

Besides these new developments, all algorithms discussed in this thesis were implemented in TRAVIS (<http://www.thch.uni-bonn.de/tc/travis>), our in-house open-source software tool for the analysis of molecular dynamics simulations.

In this way, the novel ideas are directly available to the scientific community. With the new method Dr. Martin Thomas has implemented in TRAVIS, it is now possible for other groups to use it, as it was already done (e.g., on ionic liquids under high pressure). Therefore, the outstanding results of Dr. Martin Thomas' thesis have already inspired further studies.

Bonn
August 2016

Prof. Barbara Kirchner

Abstract

In this thesis, the theoretical modeling of vibrational spectra in the liquid phase by *ab initio* molecular dynamics simulations is discussed. All presented algorithms are implemented in the open-source trajectory analysis software package TRAVIS to make them publicly available to the scientific community for immediate utilization. The basic equations that define the spectra in terms of Fourier transforms of correlation functions are derived in an alternative manner to highlight the close relation of *ab initio* molecular dynamics and static calculations regarding vibrational properties. To assess the influence of approximating the nuclei by classical particles, molecular dynamics simulations are compared to the exact solution of the nuclear Schrödinger equation for several one-dimensional and two-dimensional example potentials. This reveals that anharmonicity effects are included in molecular dynamics, but the extent depends on the simulation temperature and certain restrictions are imposed such that, e.g., overtones appear at integer multiples of the corresponding fundamental frequency and combination bands show up at exact sums and differences of the corresponding fundamental frequencies. For the evaluation of molecular dipole moments, the scheme of maximally localized Wannier functions is adopted. Molecular polarizabilities are obtained by recalculating the Wannier functions under the influence of an external electric field and taking the differences of the dipole moments. Knowing these quantities allows to compute infrared and Raman spectra of bulk systems with a separation of the components in mixtures and the contributions of solute and solvent in a solution. To avoid the large computational requirements of the Wannier localization, a new method to obtain molecular dipole moments and polarizabilities is developed. It is based on a radical Voronoi tessellation of the electron density that is inherently available in *ab initio* molecular dynamics. The influence of the radii that have to be assigned to the Voronoi sites is investigated, and it is concluded that van der Waals radii are a very reasonable choice to separate the molecules in a bulk phase simulation and to obtain spectra of similar quality as the Wannier approach. Besides the improved computational efficiency, the new method avoids certain artifacts of the Wannier functions that prevent, e.g., the calculation of Raman spectra for aromatic compounds such as benzene. To simulate also vibrational circular dichroism spectra,

a novel method to obtain molecular magnetic moments in the bulk phase is developed. In this approach, a partial differential equation is solved to compute the electric current density on the basis of changes in the electron density during the simulation. The resulting magnetic moments prove to be stable with respect to the simulation parameters and yield vibrational circular dichroism spectra in very good agreement with experimental data. In order to test the implementations, the algorithms are applied to simple organic molecules that are easy to simulate and for which experimental spectra are readily available to compare the results. In particular, the infrared and Raman spectra of methanol, carbon tetrachloride, benzene, and phenol in the bulk phase are discussed. Moreover, the chiral molecules 2-butanol, propylene oxide, and α -pinene are investigated regarding their vibrational circular dichroism spectra in the liquid state. The molecular dynamics approach is shown to be suited very well for a modeling of bulk phase effects that occur due to intermolecular interactions such as hydrogen bonding, e.g., in the alcohols methanol and 2-butanol. This turns it into the primary method to study ionic liquids with their strong and dynamic interaction network. In the example of 1-ethyl-3-methylimidazolium acetate with its potential to form a carbene, it is demonstrated that static calculations of a single ion pair introduce certain deficiencies while *ab initio* molecular dynamics can reproduce the experimental data very well. This is also used to study a mixture with water and to investigate the absorption of carbon dioxide in this ionic liquid.

Parts of this thesis have been published in the following journal articles:

1. M. Thomas, M. Brehm, R. Fligg, P. Vöhringer, B. Kirchner, “Computing vibrational spectra from *ab initio* molecular dynamics”, *Phys. Chem. Chem. Phys.* **2013**, *15*, 6608–6622.
2. M. Thomas, M. Brehm, O. Hollóczki, Z. Kelemen, L. Nyulászi, T. Pasinszki, B. Kirchner, “Simulating the vibrational spectra of ionic liquid systems: 1-Ethyl-3-methylimidazolium acetate and its mixtures”, *J. Chem. Phys.* **2014**, *141*, 024510.
3. M. Thomas, M. Brehm, B. Kirchner, “Voronoi dipole moments for the simulation of bulk phase vibrational spectra”, *Phys. Chem. Chem. Phys.* **2015**, *17*, 3207–3213.
4. M. Thomas, B. Kirchner, “Classical Magnetic Dipole Moments for the Simulation of Vibrational Circular Dichroism by *ab Initio* Molecular Dynamics”, *J. Phys. Chem. Lett.* **2016**, *7*, 509–513.

List of Publications

1. B. Schulze, D. Escudero, C. Friebe, R. Siebert, H. Görls, S. Sinn, M. Thomas, S. Mai, J. Popp, B. Dietzek, L. González, U.S. Schubert, “Ruthenium(II) Photosensitizers of Tridentate Click-Derived Cyclometalating Ligands: A Joint Experimental and Computational Study”, *Chem. Eur. J.* **2012**, *18*, 4010–4025.
2. M. Thomas, F. Latorre, P. Marquetand, “Resonance Raman spectra of *ortho*-nitrophenol calculated by real-time time-dependent density functional theory”, *J. Chem. Phys.* **2013**, *138*, 044101.
3. M. Thomas, M. Brehm, R. Fligg, P. Vöhringer, B. Kirchner, “Computing vibrational spectra from *ab initio* molecular dynamics”, *Phys. Chem. Chem. Phys.* **2013**, *15*, 6608–6622.
4. M. Thomas, S. Mühlig, T. Deckert-Gaudig, C. Rockstuhl, V. Deckert, P. Marquetand, “Distinguishing chemical and electromagnetic enhancement in surface-enhanced Raman spectra: The case of *para*-nitrothiophenol”, *J. Raman Spectrosc.* **2013**, *44*, 1497–1505.
5. M. Thomas, M. Brehm, O. Hollóczki, B. Kirchner, “How Can a Carbene be Active in an Ionic Liquid?”, *Chem. Eur. J.* **2014**, *20*, 1622–1629.
6. M. Thomas, M. Brehm, O. Hollóczki, Z. Kelemen, L. Nyulászi, T. Pasinszki, B. Kirchner, “Simulating the vibrational spectra of ionic liquid systems: 1-Ethyl-3-methylimidazolium acetate and its mixtures”, *J. Chem. Phys.* **2014**, *141*, 024510.
7. M. Thomas, M. Brehm, B. Kirchner, “Voronoi dipole moments for the simulation of bulk phase vibrational spectra”, *Phys. Chem. Chem. Phys.* **2015**, *17*, 3207–3213.
8. M. Brehm, H. Weber, M. Thomas, O. Hollóczki, B. Kirchner, “Domain Analysis in Nanostructured Liquids: A Post-Molecular Dynamics Study at the Example of Ionic Liquids”, *ChemPhysChem* **2015**, *16*, 3271–3277.

9. O. Hollóczki, M. Macchiagodena, H. Weber, M. Thomas, M. Brehm, A. Stark, O. Russina, A. Triolo, B. Kirchner, “Triphilic Ionic-Liquid Mixtures: Fluorinated and Non-fluorinated Aprotic Ionic-Liquid Mixtures”, *ChemPhysChem* **2015**, *16*, 3325–3333.
10. F. Malberg, O. Hollóczki, M. Thomas, B. Kirchner, “En route formation of ion pairs at the ionic liquid–vacuum interface”, *Struct. Chem.* **2015**, *26*, 1343–1349.
11. D. Czurlok, M. von Domaros, M. Thomas, J. Gleim, J. Lindner, B. Kirchner, P. Vöhringer, “Femtosecond 2DIR spectroscopy of the nitrile stretching vibration of thiocyanate anions in liquid-to-supercritical heavy water. Spectral diffusion and libration-induced hydrogen-bond dynamics”, *Phys. Chem. Chem. Phys.* **2015**, *17*, 29776–29785.
12. M. Thomas, B. Kirchner, “Classical Magnetic Dipole Moments for the Simulation of Vibrational Circular Dichroism by *ab Initio* Molecular Dynamics”, *J. Phys. Chem. Lett.* **2016**, *7*, 509–513.

Conference Contributions

- 09/2012 48th Symposium on Theoretical Chemistry in Karlsruhe, Germany
Poster: “Towards a Proper Description of Condensed Phases”
- 05/2013 112th Bunsentagung in Karlsruhe, Germany
Talk: “Computing vibrational spectra from *ab initio* molecular dynamics”
- 09/2013 20th International Conference on “Horizons in Hydrogen Bond Research” in Antwerp, Belgium
Talk: “Vibrational spectra in *ab initio* molecular dynamics”
- 09/2014 50th Symposium on Theoretical Chemistry in Vienna, Austria
Poster: “Simulating the vibrational spectra of ionic liquid systems”
- 09/2015 51st Symposium on Theoretical Chemistry in Potsdam, Germany
Poster: “Simulation of bulk phase vibrational spectra using Voronoi dipole moments”

Acknowledgements

The content of this thesis has been developed in the research group of Prof. Dr. Barbara Kirchner at the University of Leipzig and at the University of Bonn from September 2012 to October 2015. It has only been possible due to the support by many people, whom I would like to acknowledge here.

First, I would like to express my gratitude to Prof. Dr. Barbara Kirchner for giving me the opportunity to join her research group, offering me the scientific freedom to investigate the topics that made this thesis possible, and providing the computational resources to perform all the simulations. Furthermore, I am very grateful to Dr. Martin Brehm for introducing me to the TRAVIS project, and for numerous helpful discussions about scientific topics and programming issues during my work. Moreover, I am very thankful to Roman Elfgem for carrying out calculations to compare the Voronoi approach and the Wannier method regarding molecular dipole moments. In addition, I would like to thank all other current and former group members for supporting me with scientific comments and the nice working atmosphere.

The quality of the simulated vibrational spectra is primarily assessed by comparison to experimental data throughout this thesis. Therefore, I am very thankful to Prof. Dr. Peter Vöhringer from Bonn and to Prof. Dr. Tibor Pasinszki from Budapest for providing experimental spectra as mentioned in the relevant figures.

Concerning technical issues, I would like to thank Dr. Matthias Kudra from Leipzig, as well as Jens Meckelburger and Dr. Werner Reckien from Bonn for maintaining the computers of the research group.

I am very grateful to Dr. Martin Brehm and Henry Weber for proofreading this thesis.

Finally, I would like to thank my parents, my sister, and my friends for making life easier, in particular during this thesis.

Contents

1 Introduction	1
References.	8
2 Theoretical Background	13
2.1 The Schrödinger Equation	13
2.2 Density Functional Theory	15
2.2.1 Hohenberg–Kohn Theorems and Kohn–Sham Method	15
2.2.2 Approximate Exchange–Correlation Functionals	17
2.2.3 Basis Set Expansion	19
2.2.4 The Gaussian and Plane Waves Method	21
2.3 Molecular Dynamics.	22
2.4 Vibrational Spectroscopy	25
2.4.1 The Harmonic Oscillator.	25
2.4.2 Infrared Absorption.	27
2.4.3 Raman Scattering	28
References.	31
3 Methodological Developments.	33
3.1 The TRAVIS Program Package	33
3.2 Vibrational Frequencies	34
3.2.1 Power Spectra of Harmonic Oscillators.	34
3.2.2 Power Spectra of Molecular Dynamics Simulations	39
3.2.3 Comparison of Classical Oscillators and Quantum Oscillators	41
3.2.4 Influence of a Thermostat	54
3.2.5 Normal Coordinates	56
3.3 Infrared and Raman Intensities	61
3.4 Dipole Moments and Polarizabilities	66
3.4.1 Maximally Localized Wannier Functions	66
3.4.2 Voronoi Tessellation of the Electron Density	68
3.5 Magnetic Moments and Vibrational Circular Dichroism.	73
References.	81

4 Applications	85
4.1 Spectra of Single Molecules	85
4.1.1 Comparison of Molecular Dynamics and Static Calculations	85
4.1.2 Temperature Dependence of Molecular Dynamics Spectra	92
4.1.3 Anharmonicity Effects in Molecular Dynamics Spectra.	95
4.2 Spectra of Molecular Liquids	98
4.2.1 Methanol.	98
4.2.2 Carbon Tetrachloride.	101
4.3 Spectra of Solute Molecules	104
4.3.1 Methanol in Carbon Tetrachloride.	104
4.3.2 Pinacol in Carbon Tetrachloride	106
4.4 Spectra of Ionic Liquid Systems	107
4.4.1 Neat 1-Ethyl-3-Methylimidazolium Acetate.	107
4.4.2 1-Ethyl-3-Methylimidazolium Acetate–Water Mixture	115
4.4.3 Carbon Dioxide Absorption in 1-Ethyl-3-Methylimidazolium Acetate.	118
4.5 Voronoi Tessellation of the Electron Density	122
4.5.1 Selection of the Radii	122
4.5.2 Dipole Moments	128
4.5.3 Vibrational Spectra	132
4.6 Vibrational Circular Dichroism	140
4.6.1 Assessment of the Magnetic Moments	140
4.6.2 Analysis of the Spectra	143
References.	148
5 Conclusion and Outlook	151
References.	155
Appendix A: Computational Details	157
Appendix B: Mathematical Derivations.	165
Appendix C: The Method of Imaginary Time Propagation.	183

Acronyms

[C ₂ C ₁ Im] ⁺	1-ethyl-3-methylimidazolium
[OAc] ⁻	Acetate
[C ₂ C ₁ Im][OAc]	1-ethyl-3-methylimidazolium acetate
[C ₂ C ₁ ImCO ₂]	1-ethyl-3-methylimidazolium-2-carboxylate
AIMD	<i>Ab initio</i> molecular dynamics
B3LYP	Hybrid functional combining Becke's exchange functional and exact exchange with the Lee–Yang–Parr correlation functional
BLYP	Combination of Becke's exchange functional with the Lee–Yang–Parr correlation functional
BOMD	Born–Oppenheimer molecular dynamics
DFT	Density functional theory
FWHM	Full width at half maximum
GGA	Generalized gradient approximation
GTH	Goedecker–Teter–Hutter pseudopotentials
GTO	Gaussian-type orbital
IR	Infrared
LDA	Local density approximation
LSDA	Local spin density approximation
MD	Molecular dynamics
OT	Orbital transformation
PBE	Perdew–Burke–Ernzerhof exchange-correlation functional
PBE0	Hybrid functional based on PBE
ROA	Raman optical activity
SCF	Self-consistent field
TPSS	Tao–Perdew–Staroverov–Scuseria exchange-correlation functional
TPSSh	Hybrid functional based on TPSS
VCD	Vibrational circular dichroism

Mathematical Symbols

$A, A(\omega), A(\tilde{\nu})$	Infrared absorption
$\Delta A, \Delta A(\omega), \Delta A(\tilde{\nu})$	Vibrational circular dichroism intensity
a	Width parameter in Morse potential
$a(\omega), a(\tilde{\nu})$	Isotropic polarizability autocorrelation
a_k	Isotropic polarizability derivative along mode k
$B(\mathbf{R}, t)$	Amplitude of the nuclear wave function
C	Coefficient in basis set expansion
C, C^r	(radical) Voronoi cell
\mathbf{C}	Matrix of coefficients in basis set expansion
\mathbf{C}	Transformation matrix in normal coordinate analysis
\mathcal{C}	Coupling operator
C_n^{AB}	Dispersion coefficient in DFT-D
c	Speed of light in vacuum
D	Dissociation energy in Morse potential
D	Finite difference derivative
d	Distance
d	Contraction coefficient in Gaussian-type orbital
E	Energy
$E(\mathbf{R})$	Electronic energy
\mathbf{E}	Electric field
$E[\rho(\mathbf{r})]$	Electronic energy functional
$E_c[\rho(\mathbf{r})]$	Correlation energy functional
$E_x[\rho(\mathbf{r})]$	Exchange energy functional
$E_{xc}[\rho(\mathbf{r})]$	Exchange-correlation energy functional
E_{kin}	Kinetic energy
e	Elementary charge
\mathbf{F}_A	Force acting on nucleus A
\mathcal{F}	Fourier transform
f_{damp}	Damping function in DFT-D
\mathbf{G}	Wave vector

G	Givens rotation matrix
g	Number of degrees of freedom
H	Hamilton function
H	Hermite polynomial
\mathcal{H}	Hamiltonian
h	Planck constant
\hbar	Reduced Planck constant
h	Cell vector
$I, I(\omega), I(\tilde{\nu})$	Raman scattering intensity
I	Identity matrix
i	Imaginary unit
$J[\rho(\mathbf{r})]$	Coulomb energy functional
J	Total electric current density
j	Electric current density
K	Length of thermostat chain
K	Kohn–Sham matrix
k	Force constant
k	Force matrix
k_B	Boltzmann constant
L	Finite difference Laplacian
M	Number of nuclei
M_A	Mass of nucleus A
m	Mass
m, m	Magnetic moment
m_e	Electron mass
N	Number of electrons
N	Normalization factor
N	Number of simulation steps
N_A	Avogadro constant
n	Number of basis functions
n	Number of Voronoi sites
\mathcal{O}	Landau symbol
$P(\omega), P(\tilde{\nu})$	Power spectrum
P_A	Momentum of nucleus A
p	Probability
Q	Mass-weighted normal coordinate
Q	Thermostat mass-like parameter
q	Mass-weighted position
q	Charge
R	Correlation function
R	Rotation matrix
R_A	Position vector of nucleus A
$R_{i \rightarrow f}$	Rotational strength
r	Distance
r	Voronoi radius

\mathbf{r}	Position vector
$S(\omega)$, $S(\tilde{\nu})$	Normalized power spectrum
$S(\mathbf{R}, t)$	Phase of the nuclear wave function
\mathbf{S}	Overlap matrix
s_n	Scaling factor in DFT-D
\mathbf{s}	Voronoi site
\mathbf{s}	Centroid
T	Temperature
T	Kinetic energy
$T[\rho(\mathbf{r})]$	Kinetic energy functional
\mathbf{T}	Translation vector
\mathcal{T}	Kinetic energy operator
t	Time
Δt	Timestep
V	Potential energy
$V[\rho(\mathbf{r})]$	Potential energy functional
\mathbf{V}_A	Velocity of nucleus A
\mathcal{V}	Potential energy operator
$ v\rangle$	Vibrational state
v_{ext}	External potential
W	Window function
$W_{i \rightarrow f}$	Transition rate
\mathbf{X}	Linearly constrained variables in the orbital transformation method
x	Position
\mathbf{x}	Position vector
x_0	Amplitude
Z_A	Atomic number of nucleus A
$\alpha(\mathbf{r})$	Scalar field providing the electric current density
$\boldsymbol{\alpha}$, α	Polarizability
γ	Anisotropic polarizability autocorrelation
γ_k	Anisotropy of polarizability derivative along mode k
δ	Dirac delta distribution
δ	Dihedral angle
ε	Energy
ε_0	Electric constant
ϵ	Orbital energy
ϵ	Matrix of orbital energies
ζ	Orbital exponent
θ	Givens rotation angle
$\theta(\mathbf{r})$	Kohn–Sham orbital
$\boldsymbol{\mu}$, μ	Dipole moment
μ_B	Bohr magneton
$\tilde{\nu}$	Wavenumber
$\tilde{\nu}_{\text{in}}$	Wavenumber of incident laser

$\zeta(\mathbf{r})$	Angular momentum of Gaussian-type orbital
$\zeta(t)$	Thermostat coordinate
ρ	Depolarization ratio
ρ_N	Density of photon states
$\rho(\mathbf{r})$	Electron density
σ	Width parameter in normal coordinate analysis
τ	Time
τ	Thermostat coupling constant
$ \Phi(t)\rangle$	Time-dependent state vector
$\phi(\mathbf{r})$	Basis function
φ	Phase
$\chi(\mathbf{R})$	Nuclear wave function
$\psi(\mathbf{r}, \mathbf{R})$	Total molecular wave function
$ \Psi\rangle$	Time-independent state vector
$\psi(\mathbf{r}; \mathbf{R})$	Electronic wave function
Ω	Cell volume
ω	Angular frequency
ω_0	Eigenfrequency

List of Figures

Figure 2.1	Measurement setup for Raman spectra. The incident light beam propagates along the y axis and is polarized along the x axis. The light scattered along the z axis is detected with a polarization filter for either x polarized or y polarized light	30
Figure 3.1	Five lowest energy eigenvalues and eigenfunctions of a harmonic oscillator with a target wavenumber of $\tilde{\nu}_t = 1000 \text{ cm}^{-1}$. For convenience, the eigenfunctions are shifted to match the energy levels.	43
Figure 3.2	Power spectra of harmonic oscillators with two different target wavenumbers $\tilde{\nu}_t$, applying four different timesteps Δt ; comparison to the spectra of the corresponding quantum oscillators	43
Figure 3.3	Five lowest energy eigenvalues and eigenfunctions in a Morse potential with a harmonic target wavenumber of $\tilde{\nu}_t = 1000 \text{ cm}^{-1}$. For convenience, the eigenfunctions are shifted to match the energy levels.	45
Figure 3.4	Power spectra of an oscillator in a Morse potential with a harmonic target wavenumber of $\tilde{\nu}_t = 1000 \text{ cm}^{-1}$ at four different total energies E ; comparison to the spectrum of the corresponding quantum oscillator	46
Figure 3.5	Wave functions and energy eigenvalues of the six lowest eigenstates in the two-dimensional potential (3.27) with parameter set 1 from Table 3.1.	48
Figure 3.6	Power spectra of a classical oscillator in the two-dimensional potential (3.27) with parameter set 1 from Table 3.1 at four different total energies E ; comparison to the spectrum of the corresponding quantum oscillator.	49

Figure 3.7	Wave functions and energy eigenvalues of the six lowest eigenstates in the two-dimensional potential (3.27) with parameter set 2 from Table 3.1.	50
Figure 3.8	Power spectra of a classical oscillator in the two-dimensional potential (3.27) with parameter set 2 from Table 3.1 at three different total energies E ; comparison to the spectrum of the corresponding quantum oscillator. The insets magnify the region of overtone and combination bands between 1500 and 2500 cm^{-1}	51
Figure 3.9	Wave functions and energy eigenvalues of the six lowest eigenstates in the two-dimensional potential (3.27) with parameter set 3 from Table 3.1.	53
Figure 3.10	Power spectra of a classical oscillator in the two-dimensional potential (3.27) with parameter set 3 from Table 3.1 at three different total energies E ; comparison to the spectrum of the corresponding quantum oscillator.	54
Figure 3.11	Power spectra of a classical oscillator in the two-dimensional potential (3.27) with parameter set 2 from Table 3.1, employing an <i>NVT</i> simulation ($\tau = 100$ fs) at 400 K and different numbers of <i>NVE</i> trajectories with initial conditions randomly drawn from the <i>NVT</i> simulation; comparison to the spectrum of the corresponding quantum oscillator at 400 K, assuming state populations according to a Boltzmann distribution. The insets magnify the region of overtone and combination bands	55
Figure 3.12	Schematic illustration of the radical Voronoi tessellation at the example of phenol. The electron density is indicated by <i>black isolines</i> , the Voronoi radii are denoted by <i>dotted circles</i> , and the radical Voronoi cells are shown by <i>gray lines</i> . Combining the cells of atoms in the same molecule yields the molecular cells drawn in <i>black</i>	70
Figure 3.13	<i>Left</i> Illustration of the discrete integration over Voronoi cells in two dimensions. The <i>dashed lines</i> mark the maximum extent of the cell along \mathbf{h}_2 , the <i>thin solid lines</i> connect the point sets sharing the same coordinate along \mathbf{h}_2 , and the <i>large circles</i> indicate the grid points between the intersections that are added to the integral. <i>Right</i> Local coordinate system of a Voronoi cell face used to calculate the intersection \mathbf{t} with a <i>line</i> . The normal vector \mathbf{n} is perpendicular to the paper plane.	71

Figure 4.1	Spectra of methanol in the gas phase: power spectrum, IR spectrum, and Raman spectrum from an AIMD simulation, IR spectrum and Raman spectrum from a static calculation. The <i>gray dashed lines</i> denote the vibrational frequencies from the static calculation, and the <i>dotted lines</i> show the integrals with the scales on the <i>right</i> side. The Raman depolarization ratios from the static calculation are shown as <i>circles</i>	86
Figure 4.2	Fitness of the reference structures employed in the normal coordinate analysis of methanol in the gas phase. The three probabilities are shown in different <i>colors</i> over the whole trajectory (<i>above</i>) and 1 ps of the trajectory (<i>below</i>)	87
Figure 4.3	Normal coordinate spectra of methanol in the gas phase: total power spectrum and dissection into mode spectra. The <i>colored dashed lines</i> indicate the corresponding vibrational frequencies in the static calculation. Graphical representations of the normal coordinate vectors obtained from the AIMD simulation are given below	88
Figure 4.4	Spectra of acetone in the gas phase: power spectrum, IR spectrum, and Raman spectrum from an AIMD simulation, IR spectrum and Raman spectrum from a static calculation. The <i>gray dashed lines</i> denote the vibrational frequencies from the static calculation, and the <i>dotted lines</i> show the integrals with the scales on the <i>right</i> side. The Raman depolarization ratios from the static calculation are shown as <i>circles</i>	91
Figure 4.5	Spectra of nitromethane in the gas phase: power spectrum, IR spectrum, and Raman spectrum from an AIMD simulation, IR spectrum and Raman spectrum from a static calculation. The <i>gray dashed lines</i> denote the vibrational frequencies from the static calculation, and the <i>dotted lines</i> show the integrals with the scales on the <i>right</i> side. The Raman depolarization ratios from the static calculation are shown as <i>circles</i>	93
Figure 4.6	Power spectra of methanol in the gas phase at four different temperatures. The <i>gray dashed lines</i> denote the vibrational frequencies from a static calculation, and the <i>dotted lines</i> show the integrals with the scale on the <i>right</i> side	94
Figure 4.7	IR spectra and normal coordinate analysis of cyanofornyl chloride. The <i>arrows mark</i> overtones and combination bands. The experimental spectrum and the mode numbering are taken from Ref. [6].	96

Figure 4.8	IR spectra of cyanofomyl bromide. The <i>arrows mark</i> overtones and combination bands. The experimental spectrum is taken from Ref. [6]. The <i>asterisks mark</i> Br ₂ CO impurity bands	97
Figure 4.9	Spectra of methanol in the liquid phase: power spectrum, IR spectrum, and Raman spectrum from an AIMD simulation of 16 methanol molecules, experimental IR and Raman spectra. The power spectrum of the gas phase is shown in <i>gray</i> for comparison. IR experiment 1 has been provided by the research group of Prof. Dr. Peter Vöhringer. IR experiment 2 and the Raman experiment are taken from Ref. [7].	99
Figure 4.10	Normal coordinate spectra of methanol in the liquid phase: total power spectrum and dissection into mode spectra. The power spectrum of the gas phase is shown in <i>gray</i> for comparison. See Fig. 4.3 for graphical representations of the normal coordinate vectors	100
Figure 4.11	Spectra of carbon tetrachloride in the liquid phase: IR spectrum, Raman spectrum, and normal coordinate analysis from an AIMD simulation of 32 carbon tetrachloride molecules. The experimental IR and Raman spectra are taken from Ref. [10]. The mode numbering is adopted from Ref. [11], and degenerate modes are denoted by primes. The inset magnifies the simulated Raman spectrum between 1200 and 1600 cm ⁻¹	102
Figure 4.12	Overtones and combination bands in the IR spectrum of carbon tetrachloride. The experimental spectrum has been provided by the research group of Prof. Dr. Peter Vöhringer. The assignment in the experimental spectrum is taken from Ref. [11].	103
Figure 4.13	Spectra of methanol in carbon tetrachloride: IR spectrum and normal coordinate analysis from an AIMD simulation of one methanol molecule in 32 carbon tetrachloride molecules. The experimental IR spectrum has been provided by the research group of Prof. Dr. Peter Vöhringer. Due to the strong absorption bands of carbon tetrachloride, it is shown only above 2000 cm ⁻¹ . See Fig. 4.1 for graphical representations of the normal coordinate vectors	104
Figure 4.14	Spectra of pinacol in carbon tetrachloride: IR spectrum from an AIMD simulation of one pinacol molecule in 32 carbon tetrachloride molecules. The experimental IR spectrum has been provided by the research group of Prof. Dr. Peter Vöhringer. Due to the strong absorption bands of carbon tetrachloride, certain regions of the experimental spectrum are cut out.	106

Figure 4.15	Carbene formation by a proton transfer in $[\text{C}_2\text{C}_1\text{Im}][\text{OAc}]$	107
Figure 4.16	IR spectra of $[\text{C}_2\text{C}_1\text{Im}][\text{OAc}]$ from static calculations of a single ion pair and a cluster of five ion pairs. The <i>lines</i> are broadened by Lorentzian functions with a FWHM of 20 cm^{-1} . The experimental IR spectrum of the liquid has been provided by Prof. Dr. Tibor Pasinszki	108
Figure 4.17	IR spectra of neat $[\text{C}_2\text{C}_1\text{Im}][\text{OAc}]$: disentanglement of cation and anion contributions in an AIMD simulation of 36 $[\text{C}_2\text{C}_1\text{Im}][\text{OAc}]$ ion pairs. The experimental IR spectrum has been provided by Prof. Dr. Tibor Pasinszki. The <i>dashed lines</i> indicate the peak assignment to cation and anion	109
Figure 4.18	Raman spectra of neat $[\text{C}_2\text{C}_1\text{Im}][\text{OAc}]$: disentanglement of cation and anion contributions in an AIMD simulation of 36 $[\text{C}_2\text{C}_1\text{Im}][\text{OAc}]$ ion pairs. The experimental Raman spectrum has been provided by Prof. Dr. Tibor Pasinszki. The <i>dashed lines</i> indicate the peak assignment to cation and anion	110
Figure 4.19	Reference structures for the normal coordinate analysis in $[\text{C}_2\text{C}_1\text{Im}][\text{OAc}]$. The $[\text{C}_2\text{C}_1\text{Im}]^+$ cation is divided into three parts for the mode descriptions in Table 4.8	111
Figure 4.20	Normal coordinate spectra of $[\text{OAc}]^-$ in $[\text{C}_2\text{C}_1\text{Im}][\text{OAc}]$: total power spectrum and dissection into mode spectra from the AIMD simulation. Graphical representations of the normal coordinate vectors assigned in the experiment	112
Figure 4.21	Normal coordinate spectra of $[\text{C}_2\text{C}_1\text{Im}]^+$ in $[\text{C}_2\text{C}_1\text{Im}][\text{OAc}]$: total power spectrum and dissection into mode spectra from the AIMD simulation. Graphical representations of the normal coordinate vectors assigned in the experiment.	113
Figure 4.22	IR spectra of a $[\text{C}_2\text{C}_1\text{Im}][\text{OAc}]$ -water mixture: disentanglement of cation, anion, and water contributions in an AIMD simulation of 27 $[\text{C}_2\text{C}_1\text{Im}][\text{OAc}]$ ion pairs and 81 water molecules. The experimental IR spectrum has been provided by Prof. Dr. Tibor Pasinszki. The <i>dashed lines</i> indicate the peak assignment to cation, anion, and water. The spectra of the neat ionic liquid (see Fig. 4.17) are drawn in <i>gray</i> for comparison.	116
Figure 4.23	CH stretching normal coordinate spectra of $[\text{C}_2\text{C}_1\text{Im}]^+$ in neat $[\text{C}_2\text{C}_1\text{Im}][\text{OAc}]$ and in the $[\text{C}_2\text{C}_1\text{Im}][\text{OAc}]$ -water mixture. Graphical representations of the normal coordinate vectors corresponding to the ring hydrogen atoms	117

Figure 4.24	Carbon dioxide absorption in $[\text{C}_2\text{C}_1\text{Im}][\text{OAc}]$ by the formation of $[\text{C}_2\text{C}_1\text{ImCO}_2]$	118
Figure 4.25	IR spectra of $[\text{C}_2\text{C}_1\text{ImCO}_2]$ in $[\text{C}_2\text{C}_1\text{Im}][\text{OAc}]$: disentanglement of cation, anion, carboxylate, and $[\text{H}(\text{OAc})_2]^-$ contributions in an AIMD simulation of 35 $[\text{C}_2\text{C}_1\text{Im}][\text{OAc}]$ ion pairs with one $[\text{C}_2\text{C}_1\text{ImCO}_2]$ molecule and one acetic acid molecule. The experimental IR spectrum has been provided by Prof. Dr. Tibor Pasinszki. The <i>dashed lines</i> indicate the peak assignment to cation, anion, and carboxylate. The experimental spectrum of the neat ionic liquid (see Fig. 4.17) is drawn in <i>gray</i> for comparison	119
Figure 4.26	Reference structures for the normal coordinate analysis of $[\text{C}_2\text{C}_1\text{ImCO}_2]$ in $[\text{C}_2\text{C}_1\text{Im}][\text{OAc}]$	119
Figure 4.27	IR spectra of carbon dioxide in $[\text{C}_2\text{C}_1\text{Im}][\text{OAc}]$: disentanglement of cation, anion, and carbon dioxide contributions in an AIMD simulation of 36 $[\text{C}_2\text{C}_1\text{Im}][\text{OAc}]$ ion pairs with one carbon dioxide molecule. The experimental IR spectrum has been provided by Prof. Dr. Tibor Pasinszki. The <i>dashed lines</i> indicate the peak assignment to cation, anion, and carbon dioxide. The experimental spectrum of the ionic liquid after two hours of treatment with carbon dioxide (see Fig. 4.25) is drawn in <i>gray</i> for comparison. The <i>inset</i> magnifies the spectrum of the carbon dioxide molecule around 600 cm^{-1}	121
Figure 4.28	Standard deviation of the molecular charge distribution in a calculation of 16 benzene molecules as a function of the Voronoi radii. The values are given as multiples of the elementary charge. The <i>black</i> cross marks the van der Waals radii, and the <i>dashed line</i> connects all combinations leading to the same tessellation as the van der Waals radii.	123
Figure 4.29	Standard deviation of the molecular charge distribution in a calculation of 16 methanol molecules as a function of the Voronoi radii. The values are given as multiples of the elementary charge. The <i>black</i> cross marks the van der Waals radii	124
Figure 4.30	Mean values and standard deviations of the atomic partial charges in a calculation of 16 methanol molecules as a function of the Voronoi radii. The values are given as multiples of the elementary charge. The <i>cross signs</i> and the <i>plus signs</i> mark van der Waals radii and covalent radii, respectively.	126

Figure 4.31	Standard deviation of the anion's and the cation's charge distribution in a calculation of 36 $[\text{C}_2\text{C}_1\text{Im}][\text{OAc}]$ ion pairs as a function of the corresponding mean charge. The axes are scaled in multiples of the elementary charge. The <i>black</i> crosses mark the result with van der Waals radii	127
Figure 4.32	Dipole moments of a single methanol molecule and a single methane molecule by integration of the electron density and maximally localized Wannier function centers as a function of the cell size	128
Figure 4.33	Magnitude μ and z component μ_z of the dipole moment of a single benzene molecule by integration of the electron density and maximally localized Wannier function centers as a function of the cell size	129
Figure 4.34	Dipole moment μ of methanol and benzene by integration of the electron density and maximally localized Wannier function centers for different molecular orientations in the simulation cell, and x component d_x of the normalized difference vector between these two methods for different molecular orientations in the simulation cell	131
Figure 4.35	Dipole moment of one selected molecule and average dipole moment of all molecules in a bulk phase simulation of 16 methanol molecules over 20 steps. The <i>dotted lines</i> indicate the standard deviation.	132
Figure 4.36	Spectra of methanol in the liquid phase: comparison of IR and Raman spectra by Wannier approach and Voronoi approach from an AIMD simulation of 16 methanol molecules. The <i>dotted lines</i> show the integrals with the scales on the <i>right</i> side. The experimental spectra are taken from Ref. [7].	133
Figure 4.37	Spectra of benzene in the liquid phase: comparison of IR and Raman spectra by Wannier approach and Voronoi approach from an AIMD simulation of 16 benzene molecules. The <i>dotted lines</i> show the integrals with the scales on the <i>right</i> side. The experimental spectra are taken from Ref. [7]. The <i>arrow</i> marks the artificial band introduced by the Wannier localization.	134
Figure 4.38	<i>Left</i> Wannier function centers in benzene. <i>Right</i> Normal mode deforming benzene toward cyclohexatriene.	135
Figure 4.39	Spectra of phenol in the liquid phase: comparison of IR and Raman spectra by Wannier approach and Voronoi approach from an AIMD simulation of 32 phenol molecules. The <i>dotted lines</i> show the integrals with the scales on the <i>right</i> side. The experimental spectra are taken from Ref. [7].	136

Figure 4.40	Raman spectra of phenol in the gas phase by static calculations employing three different exchange-correlation functionals. The <i>lines</i> are broadened by Lorentzian functions with a FWHM of 15 cm^{-1}	137
Figure 4.41	Spectra of neat $[\text{C}_2\text{C}_1\text{Im}][\text{OAc}]$: comparison of IR and Raman spectra by Wannier approach and Voronoi approach from an AIMD simulation of 36 $[\text{C}_2\text{C}_1\text{Im}][\text{OAc}]$ ion pairs. The experimental spectra have been provided by Prof. Dr. Tibor Pasinszki	138
Figure 4.42	IR spectra of a $[\text{C}_2\text{C}_1\text{Im}][\text{OAc}]$ -water mixture: comparison of IR spectra by Wannier approach and Voronoi approach from an AIMD simulation of 27 $[\text{C}_2\text{C}_1\text{Im}][\text{OAc}]$ ion pairs with 81 water molecules. The experimental spectrum has been provided by Prof. Dr. Tibor Pasinszki.	139
Figure 4.43	Vector components of the magnetic moment of a single 2-butanol molecule for three different timesteps	141
Figure 4.44	Vector components of the magnetic moment of a single 2-butanol molecule for three different convergence criteria in the BiCGstab(<i>l</i>) algorithm	142
Figure 4.45	Isosurfaces of the electron density in 2-butanol. <i>Left</i> $\rho = 1.3 \cdot 10^{-2} e/\text{nm}^3$, <i>right</i> $\rho = 50 e/\text{nm}^3$	142
Figure 4.46	Vector components of the magnetic moment of a single 2-butanol molecule for three different values of the background electron density	143
Figure 4.47	IR spectrum and VCD spectrum from an AIMD simulation of (<i>R</i>)-2-butanol in the gas phase. The experimental spectra of a (<i>R</i>)-2-butanol solution in carbon disulfide (0.029 mol/L) are taken from Ref. [76]	144
Figure 4.48	IR spectra and VCD spectra of 2-butanol in the (<i>R</i>)-configuration and the (<i>S</i>)-configuration from AIMD simulations of 16 2-butanol molecules. The <i>dotted lines</i> facilitate the comparison of the VCD spectra of the enantiomers and show the assignment between simulation and experiment. The experimental IR spectrum is taken from Ref. [78]. The experimental VCD spectrum of the (<i>R</i>)-configuration is taken from Ref. [76]	145
Figure 4.49	IR spectrum and VCD spectrum from an AIMD simulation of 16 (<i>R</i>)-propylene oxide molecules. The experimental IR spectrum is taken from Ref. [79]. The experimental VCD spectrum is the inverted spectrum of the (<i>S</i>)-enantiomer from Ref. [80].	147

Figure 4.50	IR spectrum and VCD spectrum from an AIMD simulation of 16 (1 <i>R</i> , 5 <i>R</i>)-(+) - α -pinene molecules. The experimental IR spectrum is taken from Ref. [78]. The experimental VCD spectrum is taken from Ref. [82]. The <i>dotted lines</i> indicate the assignment of simulation and experiment.	148
Figure A.1	Dipole distribution functions of methanol from simulation G1a, acetone from simulation G2, and nitromethane from simulation G3 obtained by the method of maximally localized Wannier functions	161

List of Tables

Table 3.1	Three parameter sets applied within the two-dimensional potential in Eq. (3.27)	47
Table 4.1	Normal coordinates of methanol in the gas phase: Wavenumbers $\tilde{\nu}_{\text{static}}$ from the static calculation, peak maxima $\tilde{\nu}_{\text{AIMD}}$ and average mode temperatures $\langle T \rangle$ from the AIMD simulation.	89
Table 4.2	Vibrational wavenumbers of cyanofornyl chloride from experiment ($\tilde{\nu}_{\text{exp}}$) and AIMD (peak maxima $\tilde{\nu}_{\text{AIMD}}$). The experimental values and the mode numbering are taken from Ref. [6]	97
Table 4.3	Normal coordinates of methanol in the liquid phase: peak maxima $\tilde{\nu}$ and average mode temperatures $\langle T \rangle$	100
Table 4.4	Normal coordinates of carbon tetrachloride in the liquid phase: experimental wavenumbers $\tilde{\nu}_{\text{exp}}$ in the IR spectrum [11], AIMD peak maxima $\tilde{\nu}_{\text{AIMD}}$ and average mode temperatures $\langle T \rangle$. The mode descriptions are adopted from Ref. [11]. In the symmetric modes, the carbon atom remains fixed, while it is displaced in the antisymmetric modes	102
Table 4.5	Comparison of several exchange-correlation functionals regarding the vibrational wavenumbers of carbon tetrachloride predicted by static calculations in the gas phase	103
Table 4.6	Normal coordinates of methanol in carbon tetrachloride: peak maxima $\tilde{\nu}$ and average mode temperatures $\langle T \rangle$	105
Table 4.7	Normal coordinate assignment for $[\text{OAc}]^-$ in the spectra of neat $[\text{C}_2\text{C}_1\text{Im}][\text{OAc}]$. Simulated wavenumbers $\tilde{\nu}_{\text{AIMD}}$ from the AIMD and experimental wavenumbers $\tilde{\nu}_{\text{exp}}$ from the measured IR and Raman spectra	114

Table 4.8	Normal coordinate assignment for $[\text{C}_2\text{C}_1\text{Im}]^+$ in the spectra of neat $[\text{C}_2\text{C}_1\text{Im}][\text{OAc}]$. Simulated wavenumbers $\tilde{\nu}_{\text{AIMD}}$ from the AIMD and experimental wavenumbers $\tilde{\nu}_{\text{exp}}$ from the measured IR and Raman spectra.	114
Table 4.9	Vibrational wavenumbers in neat $[\text{C}_2\text{C}_1\text{Im}][\text{OAc}]$ and in the $[\text{C}_2\text{C}_1\text{Im}][\text{OAc}]$ -water mixture: comparison of simulated wavenumbers $\tilde{\nu}_{\text{AIMD}}$ and experimental wavenumbers $\tilde{\nu}_{\text{exp}}$ in the IR spectra.	116
Table 4.10	Normal coordinate assignment for $[\text{C}_2\text{C}_1\text{ImCO}_2]$ in $[\text{C}_2\text{C}_1\text{Im}][\text{OAc}]$	120
Table 4.11	Vibrational wavenumbers of carbon dioxide in $[\text{C}_2\text{C}_1\text{Im}][\text{OAc}]$ and in the gas phase obtained from AIMD simulations of one carbon dioxide molecule in 36 $[\text{C}_2\text{C}_1\text{Im}][\text{OAc}]$ ion pairs and of a single carbon dioxide molecule. The experimental wavenumbers are taken from Ref. [45]	121
Table A.1	AIMD simulation parameters: exchange-correlation functional with dispersion correction, cubic cell size a , density ρ , thermostat target temperature T , equilibration time t_{eq} , productiontime t_{sim} , and thermostat coupling time constant t_{sim} during production run	158
Table A.2	Methods used to obtain dipole moments and polarizabilities for the AIMD simulations. The start time t_{start} and the end time t_{end} are given relative to the beginning of the production run of the whole simulation (see Table A.1). Their difference t is the time over which the spectra are sampled. The Wannier localization was performed or the electron density was saved, respectively, with a stride of t_{dip} . The dipole moments were evaluated with an external field to obtain polarizabilities with a stride of t_{pol} . The internal grid representation of the electron density in CP2K was written to Gaussian cube files with the stride given in the last column	160

Chapter 1

Introduction

The term vibrational spectroscopy collects a wide variety of analytical techniques that generally deal with the analysis of molecular vibrations or phonons in solids. The frequencies of the vibrations in a molecular system or in a solid are directly determined by the mutual interplay between its atoms, so vibrational spectroscopy allows to study the interactions within a molecule or a solid, as well as between a molecule and its surrounding in great detail. This leads to numerous applications in all fields of natural sciences, medicine, and also in the industry (see, e.g., the recent review articles [1–18] for some examples). There exist many different manifestations of vibrational spectroscopy, and each of them probes the molecular vibrations with specific selection rules, so they often yield complementary information about the system. Two very popular forms already undergraduate students come in contact with are IR and Raman spectroscopy. The former is based on the absorption of electromagnetic radiation due to the excitation of the system to a higher vibrational state with an energy that is typically in the IR region of the electromagnetic spectrum. The corresponding IR spectrum shows vibrations that change the dipole moment of the system. Raman spectroscopy relies on the inelastic scattering of usually visible light, meaning that the energy of an incident photon is changed by the energy difference of two vibrational states in the system. In this case, the spectrum contains vibrations that modify the polarizability of the system. Closely related to these two principles are vibrational circular dichroism (VCD) and Raman optical activity (ROA), which measure the difference in the absorption or the scattering, respectively, of left and right circularly polarized light. These methods provide signals only for chiral molecules.

For a detailed interpretation of vibrational spectra, accurate theoretical models on a molecular level are essential. Today, *ab initio* calculations with the help of computer systems allow to predict vibrational properties just on the basis of fundamental physical laws such as the Schrödinger equation. Although the algorithms to solve this equation sometimes contain a few general empirical constants (see Sect. 2.2), specific parameters fitted to particular experimental vibrational spectra are not needed. This

makes it possible to study any arbitrary system even if it has not been synthesized yet or if it is so reactive that it cannot be isolated in the experiment.

Basic *ab initio* calculations of single molecules can be regarded as a routine task nowadays. Many different software packages provide the possibility to estimate IR and Raman spectra within the harmonic approximation in a black box manner, and the application of such static calculations is usually taught in introductory courses to computational chemistry [19, 20]. The general procedure of this approach is as follows: Starting from a reasonable guess of the molecular structure, a minimum on the potential energy surface is searched for (geometry optimization). In the vicinity of this minimum, the potential energy surface is approximated by a quadratic function, implicating that the molecule behaves like a harmonic oscillator (harmonic approximation). Under this assumption, the vibrational frequencies are readily given by the diagonalized Hessian of the potential energy at the minimum, and the intensities can be obtained as derivatives of the dipole moment and the polarizability for IR and Raman spectra, respectively (see Sect. 2.4).

In usual cases, the harmonic approximation performs very well to reproduce the peak positions and the intensity ratios of the fundamental transitions in a vibrational spectrum [21]. This is often sufficient to interpret experimental data in terms of specific molecular vibrations. For more accurate results, however, the anharmonicity effects that lead, e.g., to a shift of peaks and the occurrence of overtones and combination bands have to be included. To some extent, the shift of the peaks can be taken into account by empirical scaling factors [22–24], which are very common due to their simple applicability. More sophisticated techniques to overcome the harmonic approximation are, e.g., vibrational perturbation theory [25–28], the vibrational self-consistent field method [29–31], vibrational configuration interaction [32, 33], vibrational coupled-cluster theory [34, 35], the multiconfigurational vibrational self-consistent field method [36, 37], and multi-reference vibration correlation methods [38] (see also the review articles [39–41] for an overview and further references). Although these techniques can yield very accurate results, they are computationally demanding, so they can hardly be used for molecular systems in the order of 100 atoms or more [42], and the harmonic approximation remains as the primary approach to study large biomolecules [43].

The static calculations either within the harmonic approximation or including anharmonicity effects are perfectly suited to study single molecules as a model for the gas phase. However, many experimental spectra are measured in the liquid phase, simply because this is the natural aggregate state of the investigated substance under ambient conditions, or just a solution of the substance is available. Depending on the polarity of a molecule and its specific interaction sites, significant differences between the spectra of the gas phase and the liquid phase can occur due to intermolecular interactions or the interplay with the solvent (some examples are shown in Chap. 4). To properly describe these situations, theoretical models are required that include bulk phase effects. The simplest extensions directly available for static calculations are continuum solvation approaches such as, e.g., the polarizable continuum model [44] or the conductor-like screening model [45] (see the review article [46] for an overview and further references). These implicit techniques place the molecule in

a cavity surrounded by a continuum with certain electrostatic properties, so they primarily account for the electrostatic interaction between solute and solvent. For specific direct intermolecular contacts such as, e.g., hydrogen bonds, however, it is necessary to include the neighboring molecules explicitly in the calculation, leading to microsolvation approaches where clusters of molecules are studied (see, e.g., Refs. [47–49]). Such techniques can largely improve the description of the local environment of a molecule, but with increasing cluster size, the necessary geometry optimization becomes a major obstacle. In the cluster, the potential energy surface is often quite flat for the relative orientation of the molecules, making it hard to converge the optimization and to reach a true minimum. Furthermore, there are usually many minima with similar energies, so preferably all of them should be considered to properly average the spectra. A comprehensive search for all minima is, however, not feasible for larger clusters.

In general, computational approaches to the description of liquids resort to molecular dynamics (MD) simulations [50]. This means that the atomic positions are propagated numerically according to Newton's equations of motion for a certain time with a finite timestep. The resulting trajectory can be analyzed to obtain structural properties in terms of, e.g., radial distribution functions or dynamical quantities such as, e.g., the lifetime of a hydrogen bond. From the beginning on, classical force fields with empirical potential functions were applied to model the interatomic forces in MD simulations. Later, the advances in computer technology paved the way to employ also *ab initio* calculations, leading to *ab initio* molecular dynamics (AIMD) [51] with a quantum chemical description of the interatomic interactions. In contrast to a single static calculation of a molecular cluster, an AIMD simulation is not confined to a particular minimum on the potential energy surface, but it samples all molecular configurations accessible in the phase space at a certain temperature (though the sampling is restricted by the simulation times and the system sizes that can be afforded, and special algorithms might be necessary to overcome large barriers and to study chemical reactions). Furthermore, AIMD simulations are easily combined with periodic boundary conditions, avoiding the surface effects present in a molecular cluster and improving the description of the molecular surrounding toward the real liquid.

The particular application of AIMD simulations to calculate vibrational spectra treating the whole system on the same level of theory started with the pioneering investigation of liquid water by Parrinello and coworkers in 1997 [52]. In this approach, the IR spectrum was computed as the Fourier transform of the dipole–dipole correlation function, where the dipole moment under periodic boundary conditions became available by the Berry phase scheme of polarization [53–55]. Shortly after, the method was applied to amorphous silicon [56], amorphous silica [57], and ice under high pressure [58], later also to aqueous solutions of potassium hydroxide [59], liquid methanol [60], and silicate melts [61]. The development of the maximally localized Wannier function method [62–66] allowed to obtain the individual dipole moments of the molecules in the simulation cell, so solute and solvent contributions could be separated, and the sampling was improved. This has been used to investigate the IR spectra of uracil in aqueous solution [67], *N*-methylacetamide

in aqueous solution [68, 69], liquid water [70–74], completely dissociated mineral acids in water [75, 76], hydrogen chloride hydrates [77–79], sodium chloride solutions in water [80], glycine in aqueous solution [81, 82], an alanine dipeptide analog in aqueous solution [83], a bridged cyclic diamide in aqueous solution [84], liquid methanol [85], and three bioionic liquids [86]. Recently, an alternative approach to individual molecular dipole moments has been implemented on the basis of subsystem embedding, and it has been applied to study the IR spectra of liquid ethylene carbonate and dimethyl carbonate [87]. Even more recently, another partitioning scheme relying on nonorthogonal generalized Wannier functions has been used to revisit the alanine dipeptide [88]. It should be noted that also the gas phase IR spectra of several peptide systems [69, 88–100], sugars [101–103], protonated methane [104], hydrogen chloride–acetonitrile clusters [105], 2-amino-1-phenylethanol clusters [106], water [88], carbon dioxide [88], and ethanol [88] have successfully been simulated by AIMD and Fourier transform of the dipole autocorrelation function.

While the IR spectra rely on the dipole moment, Raman spectra can be calculated in AIMD simulations as the Fourier transform of the polarizability autocorrelation function. The polarizability of the simulation cell under periodic boundary conditions can be obtained by density functional perturbation theory [107–113]. This technique has been employed to study the Raman spectra of ice under high pressure [114], naphthalene crystals [115], amorphous germanium telluride [116], spodumene crystals [117], arsenic sulfides [118], liquid water [119], water under high pressure [120], and liquid propylene oxide [121]. The polarizability of the simulation cell can also be calculated by applying a finite electric field [113, 122, 123], and this has been used for water under high pressure [120]. Due to the computational cost of the perturbation theory calculation for the whole cell in each simulation step, clavulanic acid and tazobactam in aqueous solution and a protein environment have been simulated by combining quantum chemistry with classical force fields (QM/MM) and relying on static calculations for the Raman spectra [124, 125]. Also for the investigation of vitreous systems, it is common to obtain only the model structures by AIMD and to perform static calculations for the spectra (see, e.g., Refs. [126–128]). Similar to the dipole moments, it is of general interest to obtain individual molecular polarizabilities in the bulk phase [129, 130]. A model based on maximally localized Wannier function centers [129, 130] has been employed for the Raman spectra in the studies of liquid water [119] and water under high pressure [120]. An alternative approach assigning polarizabilities to atom-centered basis functions has been developed in the investigation of liquid propylene oxide [121].

For the interpretation of the simulated spectra, it is desirable to assign the bands to particular molecular vibrations. While this information is intrinsically available in static calculations within the harmonic approximation as the normal modes of a molecule are the coordinate system in which the Hessian is diagonal, the extraction of normal modes from MD simulations is more involved. Several methods have been developed in this regard, including the technique of driven molecular dynamics [131, 132], the instantaneous normal mode analysis where the Hessian is calculated in certain steps along the trajectory [133–140], as well as principal mode analysis

[139–143], effective normal modes [69, 144], and generalized normal coordinates [145, 146] where the eigenvalue problem of a cross-correlation matrix is solved.

The general aim of this thesis is to collect the approaches to the simulation of IR and Raman spectra by AIMD, to improve their efficiency regarding the calculation of molecular dipole moments and polarizabilities, to extend them toward a simulation of VCD spectra, and to implement these methods in the software package TRAVIS [147]. The program TRAVIS intends to provide a wide variety of trajectory analysis algorithms under a common interface to enable an easy post-processing and visualization of MD simulations. In the course of this thesis, it is considerably extended regarding its capabilities to calculate vibrational spectra.

The thesis starts with an explanation of the general theoretical background in terms of the Schrödinger equation in Chap. 2. On the one hand, this is needed to understand the basic principles of vibrational spectroscopy and the influence of the most important approximation in the simulation of vibrational spectra by AIMD, which is the assumption of the nuclei as classical particles. On the other hand, this is necessary to elucidate the meaning of the parameters for the treatment of the electronic structure in *ab initio* calculations. In Chap. 3, all the algorithms important for the implementation in TRAVIS are described. At first, the equations are derived that define the vibrational spectra in AIMD simulations as Fourier transforms of correlation functions. While this is usually started from the Heisenberg picture of quantum mechanics in the literature [51, 148], where the quantum correlation functions are approximated by classical correlation functions and quantum correction factors are introduced, an alternative way is chosen here: the central model system is the harmonic oscillator and everything is defined in such a way that the MD approach provides the same spectra as quantum mechanics in this case. Except for constant prefactors, the resulting equations are the same as the ones known in the literature, but this clarifies the close relation of AIMD simulations and static calculations concerning the vibrational properties of a system. Afterwards, it is studied how the methodology transfers to anharmonic systems. Although it is often stated without further explanation in articles presenting vibrational spectra from AIMD that anharmonicity is included, it has to be recognized that the assumption of classical nuclei imposes certain restrictions on the effects that can be observed. The differences between quantum mechanics and the classical approximation of the nuclei are discussed in detail for several anharmonic model systems.

As soon as the basic equations for the spectra are known, it is important to obtain molecular dipole moments and polarizabilities. As the first approach, the well-known scheme of maximally localized Wannier functions is realized. Concerning the polarizabilities, the implementation is very similar to the idea in Refs. [129, 130], but it uses a simplification that significantly reduces the computational demand without an unacceptable distortion of the resulting Raman spectra. It should be noted that the first Raman spectra based on these molecular polarizabilities have already been published by the author in Ref. [149], prior to the above mentioned articles [119, 120].

A major drawback of the Wannier functions is the required computational effort. In particular, if the localization procedure suffers from convergence problems, this becomes the most expensive part of an AIMD simulation. A new approach that avoids the huge impact on the computation time is presented in this thesis. It is based on a radical Voronoi tessellation [150] of the total electron density, and its applicability is tested for several organic molecules. This reveals that it constitutes a good method to study also aromatic compounds such as benzene, for which the Wannier localization shows severe problems that prevent especially the simulation of Raman spectra.

To date, the application of MD simulations to VCD spectroscopy is limited. It has been derived that the VCD spectrum can be computed as the Fourier transform of the cross-correlation of dipole moment and magnetic moment [151–153], but the calculation of the magnetic moment needed for this approach is a major issue in AIMD. In Ref. [152], the MD force field was parametrized with atomic axial tensors from magnetic field perturbation theory [154–157], so this is a combination of MD with static calculations. In Refs. [151, 153, 158], the classical definition of the magnetic moment caused by point charges was employed. The atomic partial charges were either fixed [151] or they were obtained from population analyses [153, 158]. Although a good agreement with the experiment could be achieved in the latter examples, it has to be noted that atomic partial charges are not unique and the result strongly depends on the particular population analysis that is selected. Recently, atomic axial tensors on the basis of nuclear velocity perturbation theory [159–163] have been implemented and the authors directly aim for the application in AIMD simulations [164, 165]. In this thesis, a novel method to calculate magnetic moments in AIMD is presented. It is also based on the classical definition of the magnetic moment, but it does not resort to atomic partial charges. Instead, the electron density from the AIMD is directly processed to obtain the electric current density in the simulation cell. This allows to compute molecular magnetic moments in combination with the abovementioned Voronoi tessellation. In several examples, this proves to be a reasonable approach to VCD spectra in the liquid phase, which does not require any changes in the electronic structure code and can be used with any electronic structure method that is able to provide the electron density.

Since the major focus of this thesis is the development and the implementation of methods to simulate vibrational spectra by AIMD, the algorithms are primarily tested with simple organic molecules for which experimental data are readily available to compare the results (see Chap. 4). To cover a certain range of functional groups, the implementation to process the Wannier function centers is applied to methanol, acetone, and nitromethane in the gas phase, as well as to methanol in the bulk. Methanol is a small molecule, allowing to carry out AIMD simulations with little computational effort. However, methanol also contains a hydroxyl group that is able to form intermolecular hydrogen bonds, so it shows significant bulk phase effects and the suitability of AIMD simulations to treat such cases can be demonstrated. Anharmonicity effects are shown using the examples of cyanofornyl chloride, cyanofornyl bromide,

and carbon tetrachloride, where they are clearly visible in the experiment. The newly developed dissection of the electron density on the basis of a Voronoi tessellation for molecular dipole moments and polarizabilities is tested with methanol, benzene, and phenol in the bulk phase. The aromatic compounds have been selected to show the issues of the Wannier localization in this case. The novel method to simulate VCD spectra is applied to 2-butanol, which is the smallest chiral alkanol, propylene oxide, which is one of the smallest chiral molecules in general, and α -pinene as an important natural product.

Beside the implementation of the methodology in TRAVIS, another focus of this thesis is the application to ionic liquid systems. In general, ionic liquids are ionic compounds with such a low melting point that they are liquid at room temperature. In the last decades, they became an extensively studied type of substances since they often combine good thermal stability, nonflammability, and low volatility with excellent solvating properties, allowing for a wide variety of applications (see, e.g., the review articles [166–168]). Since the structure of ionic liquids is governed by a large diversity of interactions that range from electrostatic forces [169] through dispersion interactions [170, 171] to specific directional atom contacts such as hydrogen bonds [172–182], they show strong bulk phase effects in their vibrational spectra that are hard to model by static calculations of single ion pairs or clusters of a few ion pairs. Nevertheless, several studies in this sense of ionic liquids that contain the 1-ethyl-3-methylimidazolium ($[\text{C}_2\text{C}_1\text{Im}]^+$) cation have appeared in the literature [183–193]. Although they restrict the number of conformers of the ion pair and neglect the influence of the dynamic surrounding in the liquid, they provide a good general insight into some of the spectroscopic features. However, a major issue occurs, e.g., in 1-ethyl-3-methylimidazolium acetate ($[\text{C}_2\text{C}_1\text{Im}][\text{OAc}]$). Beside its good solvation properties for strongly hydrogen bonding materials such as cellulose [194] or chitin [195], this ionic liquid is able to form an N-heterocyclic carbene by a proton transfer between cation and anion. It has been shown that this reaction is favored in the gas phase [177] while the ion network [196, 197] stabilizes the ions and suppresses the carbene formation in the liquid [181, 198, 199]. As a direct consequence, a static calculation of a single ion pair, which resembles the situation in the gas phase, offers only a limited ability to describe the behavior in the liquid state.

The detailed settings of the AIMD simulations and the static calculations discussed in Chap. 4 are gathered in Appendix A. Furthermore, most of the mathematical derivations that are not primarily relevant to understand the argumentation in Chap. 3 can be found in Appendix B. In Appendix C, the method of imaginary time propagation is shortly explained, which allows to solve the nuclear Schrödinger equation without the approximation of the nuclei as classical particles. The description of this technique is not included in Chap. 2, since it is not needed for the modeling of vibrational spectra by AIMD presented in this thesis, and it only serves to provide the reference spectra for the discussion of anharmonicity effects in Sect. 3.2.3.

References

1. C. Krafft, J. Popp, *Anal. Bioanal. Chem.* **407**, 699–717 (2015)
2. C.K. Muro, K.C. Doty, J. Bueno, L. Halámková, I.K. Lednev, *Anal. Chem.* **87**, 306–327 (2015)
3. S. Devpura, K.N. Barton, S.L. Brown, O. Palyvoda, S. Kalkanis, V.M. Naik, F. Siddiqui, R. Naik, I.J. Chetty, *Med. Phys.* **41**, 050901 (2014)
4. R.E. Kast, S.C. Tucker, K. Killian, M. Trexler, K.V. Honn, G.W. Auner, *Cancer Metastasis Rev.* **33**, 673–693 (2014)
5. D.-W. Li, W.-L. Zhai, Y.-T. Li, Y.-T. Long, *Microchim. Acta* **181**, 23–43 (2014)
6. M. López-López, C. García-Ruiz, *TrAC Trends Anal. Chem.* **54**, 36–44 (2014)
7. M. Manley, *Chem. Soc. Rev.* **43**, 8200–8214 (2014)
8. A.L. Mitchell, K.B. Gajjar, G. Theophilou, F.L. Martin, P.L. Martin-Hirsch, *J. Biophotonics* **7**, 153–165 (2014)
9. O.J. Old, L.M. Fullwood, R. Scott, G.R. Lloyd, L.M. Almond, N.A. Shepherd, N. Stone, H. Barr, C. Kendall, *Anal. Methods* **6**, 3901–3917 (2014)
10. A. Savara, E. Weitz, *Annu. Rev. Phys. Chem.* **65**, 249–273 (2014)
11. S. Schmitt, S. Garrigues, M. de la Guardia, *Crit. Rev. Anal. Chem.* **44**, 186–197 (2014)
12. J. Sulé-Suso, N. Forsyth, V. Untereiner, G. Sockalingum, *Trends Biotechnol.* **32**, 254–262 (2014)
13. F. Zaera, *Chem. Soc. Rev.* **43**, 7624–7663 (2014)
14. A.P. Craig, A.S. Franca, J. Irudayaraj, *Annu. Rev. Food Sci. Technol.* **4**, 369–380 (2013)
15. A. López, S. Arazuri, I. Garcí, J. Mangado, C. Jarén, *J. Agric. Food Chem.* **61**, 5413–5424 (2013)
16. D. Drescher, J. Kneipp, *Chem. Soc. Rev.* **41**, 5780–5799 (2012)
17. A.B.S. Elliott, R. Horvath, K.C. Gordon, *Chem. Soc. Rev.* **41**, 1929–1946 (2012)
18. S. Pahlow, A. März, B. Seise, K. Hartmann, I. Freitag, E. Kämmer, R. Böhme, V. Deckert, K. Weber, D. Cialla, J. Popp, *Eng. Life Sci.* **12**, 131–143 (2012)
19. I. Levine, *Quantum Chemistry* (Pearson Prentice Hall, Upper Saddle River, 2009)
20. F. Jensen, *Introduction to Computational Chemistry* (Wiley, Chichester, 2006)
21. F. Neese, *Coord. Chem. Rev.* **253**, 526–563 (2009)
22. J.P. Merrick, D. Moran, L. Radom, *J. Phys. Chem. A* **111**, 11683–11700 (2007)
23. I.M. Alecu, J. Zheng, Y. Zhao, D.G. Truhlar, *J. Chem. Theory Comput.* **6**, 2872–2887 (2010)
24. P. Borowski, *J. Phys. Chem. A* **116**, 3866–3880 (2012)
25. H.H. Nielsen, *Rev. Mod. Phys.* **23**, 90–136 (1951)
26. D.A. Clabo, W.D. Allen, R.B. Remington, Y. Yamaguchi, H.F. Schaefer, *Chem. Phys.* **123**, 187–239 (1988)
27. J. Neugebauer, B.A. Hess, *J. Chem. Phys.* **118**, 7215–7225 (2003)
28. V. Barone, *J. Phys. Chem. A* **108**, 4146–4150 (2004)
29. J.M. Bowman, *Acc. Chem. Res.* **19**, 202–208 (1986)
30. J.O. Jung, R.B. Gerber, *J. Chem. Phys.* **105**, 10332–10348 (1996)
31. G.M. Chaban, J.O. Jung, R.B. Gerber, *J. Chem. Phys.* **111**, 1823–1829 (1999)
32. K.M. Christoffel, J.M. Bowman, *Chem. Phys. Lett.* **85**, 220–224 (1982)
33. S. Carter, J.M. Bowman, N.C. Handy, *Theor. Chem. Acc.* **100**, 191–198 (1998)
34. V. Nagalakshmi, V. Lakshminarayana, G. Sumithra, M.D. Prasad, *Chem. Phys. Lett.* **217**, 279–282 (1994)
35. O. Christiansen, *J. Chem. Phys.* **120**, 2149–2159 (2004)
36. F. Culot, J. Liévin, *Theor. Chim. Acta* **89**, 227–250 (1994)
37. S. Heislbeitz, G. Rauhut, *J. Chem. Phys.* **132**, 124102 (2010)
38. F. Pfeiffer, G. Rauhut, *J. Chem. Phys.* **140**, 064110 (2014)
39. O. Christiansen, *Phys. Chem. Chem. Phys.* **9**, 2942–2953 (2007)
40. O. Christiansen, *Phys. Chem. Chem. Phys.* **14**, 6672–6687 (2012)
41. V. Barone, M. Biczysko, J. Bloino, *Phys. Chem. Chem. Phys.* **16**, 1759–1787 (2014)

42. T. Weymuth, M.P. Haag, K. Kiewisch, S. Luber, S. Schenk, C.R. Jacob, C. Herrmann, J. Neugebauer, M. Reiher, *J. Comput. Chem.* **33**, 2186–2198 (2012)
43. C. Herrmann, M. Reiher, in *Atomistic Approaches in Modern Biology*, ed. by M. Reiher. Topics in Current Chemistry, vol. 268 (Springer, Heidelberg, 2007), pp. 85–132
44. S. Miertuš, E. Scrocco, J. Tomasi, *Chem. Phys.* **55**, 117–129 (1981)
45. A. Klamt, G. Schüürmann, *J. Chem. Soc. Perkin Trans.* **2**, 799–805 (1993)
46. J. Tomasi, B. Mennucci, R. Cammi, *Chem. Rev.* **105**, 2999–3094 (2005)
47. J.E. Rode, J.C. Dobrowolski, J. Sadlej, *J. Phys. Chem. B* **117**, 14202–14214 (2013)
48. T. Weymuth, M. Reiher, *J. Phys. Chem. B* **117**, 11943–11953 (2013)
49. A.M. Wright, A.A. Howard, J.C. Howard, G.S. Tschumper, N.I. Hammer, *J. Phys. Chem. A* **117**, 5435–5446 (2013)
50. P. Allen, D.J. Tildesley, *Computer Simulation of Liquids* (Clarendon Press, Oxford, 1989)
51. D. Marx, J. Hutter, *Ab Initio Molecular Dynamics: Basic Theory and Advanced Methods* (Cambridge University Press, Cambridge, 2009)
52. P.L. Silvestrelli, M. Bernasconi, M. Parrinello, *Chem. Phys. Lett.* **277**, 478–482 (1997)
53. R.D. King-Smith, D. Vanderbilt, *Phys. Rev. B* **47**, 1651–1654 (1993)
54. R. Resta, *Rev. Mod. Phys.* **66**, 899–915 (1994)
55. R. Resta, *Phys. Rev. Lett.* **80**, 1800–1803 (1998)
56. A. Debernardi, M. Bernasconi, M. Cardona, M. Parrinello, *Appl. Phys. Lett.* **71**, 2692–2694 (1997)
57. A. Pasquarello, R. Car, *Phys. Rev. Lett.* **79**, 1766–1769 (1997)
58. M. Bernasconi, P.L. Silvestrelli, M. Parrinello, *Phys. Rev. Lett.* **81**, 1235–1238 (1998)
59. Z. Zhu, M.E. Tuckerman, *J. Phys. Chem. B* **106**, 8009–8018 (2002)
60. J.-W. Handgraaf, E.J. Meijer, M.-P. Gaigeot, *J. Chem. Phys.* **121**, 10111–10119 (2004)
61. R. Vuilleumier, N. Sator, B. Guillot, *Geochim. Cosmochim. Acta* **73**, 6313–6339 (2009)
62. N. Marzari, D. Vanderbilt, *Phys. Rev. B* **56**, 12847–12865 (1997)
63. P.L. Silvestrelli, M. Parrinello, *Phys. Rev. Lett.* **82**, 3308–3311 (1999)
64. P.L. Silvestrelli, M. Parrinello, *J. Chem. Phys.* **111**, 3572–3580 (1999)
65. B. Kirchner, J. Hutter, *J. Chem. Phys.* **121**, 5133–5142 (2004)
66. R. Iftimie, J.W. Thomas, M.E. Tuckerman, *J. Chem. Phys.* **120**, 2169–2181 (2004)
67. M.-P. Gaigeot, M. Sprik, *J. Phys. Chem. B* **107**, 10344–10358 (2003)
68. M.-P. Gaigeot, R. Vuilleumier, M. Sprik, D. Borgis, *J. Chem. Theory Comput.* **1**, 772–789 (2005)
69. M.-P. Gaigeot, M. Martinez, R. Vuilleumier, *Mol. Phys.* **105**, 2857–2878 (2007)
70. M. Sharma, R. Resta, R. Car, *Phys. Rev. Lett.* **95**, 187401 (2005)
71. W. Chen, M. Sharma, R. Resta, G. Galli, R. Car, *Phys. Rev. B* **77**, 245114 (2008)
72. C. Zhang, D. Donadio, G. Galli, *J. Phys. Chem. Lett.* **1**, 1398–1402 (2010)
73. C. Zhang, D. Donadio, F. Gygi, G. Galli, *J. Chem. Theory Comput.* **7**, 1443–1449 (2011)
74. M. Heyden, J. Sun, S. Funkner, G. Mathias, H. Forbert, M. Havenith, D. Marx, *Proc. Natl. Acad. Sci. USA* **107**, 12068–12073 (2010)
75. R. Iftimie, M.E. Tuckerman, *J. Chem. Phys.* **122**, 214508 (2005)
76. R. Iftimie, M.E. Tuckerman, *Angew. Chem. Int. Ed.* **45**, 1144–1147 (2006)
77. J.P. Devlin, V. Buch, F. Mohamed, M. Parrinello, *Chem. Phys. Lett.* **432**, 462–467 (2006)
78. V. Buch, F. Mohamed, M. Parrinello, J.P. Devlin, *J. Chem. Phys.* **126**, 021102 (2007)
79. V. Buch, F. Mohamed, M. Parrinello, J.P. Devlin, *J. Chem. Phys.* **126**, 074503 (2007)
80. D.A. Schmidt, R. Scipioni, M. Boero, *J. Phys. Chem. A* **113**, 7725–7729 (2009)
81. J. Sun, D. Bousquet, H. Forbert, D. Marx, *J. Chem. Phys.* **133**, 114508 (2010)
82. J. Sun, G. Niehues, H. Forbert, D. Decka, G. Schwaab, D. Marx, M. Havenith, *J. Am. Chem. Soc.* **136**, 5031–5038 (2014)
83. M.-P. Gaigeot, *Phys. Chem. Chem. Phys.* **12**, 10198–10209 (2010)
84. M.-P. Gaigeot, N.A. Besley, J.D. Hirst, *J. Phys. Chem. B* **115**, 5526–5535 (2011)
85. N. Sieffert, M. Bühl, M.-P. Gaigeot, C.A. Morrison, *J. Chem. Theory Comput.* **9**, 106–118 (2013)
86. L. Tanzi, P. Benassi, M. Nardone, F. Ramondo, *J. Phys. Chem. A* **118**, 12229–12240 (2014)

87. S. Luber, *J. Chem. Phys.* **141**, 234110 (2014)
88. V. Vitale, J. Dziedzic, S.M.-M. Dubois, H. Fangohr, C.-K. Skylaris, *J. Chem. Theory Comput.* **11**, 3321–3332 (2015)
89. D.C. Marinica, G. Grégoire, C. Desfrancois, J.P. Schermann, D. Borgis, M.-P. Gaigeot, *J. Phys. Chem. A* **110**, 8802–8810 (2006)
90. G. Grégoire, M.-P. Gaigeot, D.C. Marinica, J. Lemaire, J.P. Schermann, C. Desfrancois, *Phys. Chem. Chem. Phys.* **9**, 3082–3097 (2007)
91. M.-P. Gaigeot, *J. Phys. Chem. A* **112**, 13507–13517 (2008)
92. A. Cimas, T.D. Vaden, T.S.J.A. de Boer, L.C. Snoek, M.-P. Gaigeot, *J. Chem. Theory Comput.* **5**, 1068–1078 (2009)
93. A. Cimas, P. Maitre, G. Ohanessian, M.-P. Gaigeot, *J. Chem. Theory Comput.* **5**, 2388–2400 (2009)
94. M.-P. Gaigeot, *Phys. Chem. Chem. Phys.* **12**, 3336–3359 (2010)
95. A. Cimas, M.-P. Gaigeot, *Phys. Chem. Chem. Phys.* **12**, 3501–3510 (2010)
96. M. Rossi, V. Blum, P. Kupser, G. von Helden, F. Bierau, K. Pagel, G. Meijer, M. Scheffler, *J. Phys. Chem. Lett.* **1**, 3465–3470 (2010)
97. A. Sediki, L.C. Snoek, M.-P. Gaigeot, *Int. J. Mass Spectrom.* **308**, 281–288 (2011)
98. J.P. Beck, M.-P. Gaigeot, J.M. Lisy, *Phys. Chem. Chem. Phys.* **15**, 16736–16745 (2013)
99. S. Jaeqx, J. Oomens, A. Cimas, M.-P. Gaigeot, A.M. Rijs, *Angew. Chem. Int. Ed.* **53**, 3663–3666 (2014)
100. E. Pluhařová, M.D. Baer, C.J. Mundy, B. Schmidt, P. Jungwirth, *J. Phys. Chem. Lett.* **5**, 2235–2240 (2014)
101. B. Brauer, M. Pincu, V. Buch, I. Bar, J.P. Simons, R.B. Gerber, *J. Phys. Chem. A* **115**, 5859–5872 (2011)
102. M. Pincu, E.J. Cocinero, N. Mayorkas, B. Brauer, B.G. Davis, R.B. Gerber, J.P. Simons, *J. Phys. Chem. A* **115**, 9498–9509 (2011)
103. H. bin Xie, M. Pincu, B. Brauer, R.B. Gerber, I. Bar, *Chem. Phys. Lett.* **514**, 284–290 (2011)
104. S.D. Ivanov, A. Witt, D. Marx, *Phys. Chem. Chem. Phys.* **15**, 10270–10299 (2013)
105. N. Bork, V. Loukonen, H.G. Kjaergaard, H. Vehkamäki, *Phys. Chem. Chem. Phys.* **16**, 24685–24690 (2014)
106. V. Brites, A.L. Nicely, N. Sieffert, M.-P. Gaigeot, J.M. Lisy, *Phys. Chem. Chem. Phys.* **16**, 13086–13095 (2014)
107. S. Baroni, P. Giannozzi, A. Testa, *Phys. Rev. Lett.* **58**, 1861–1864 (1987)
108. X. Gonze, *Phys. Rev. A* **52**, 1096–1114 (1995)
109. X. Gonze, *Phys. Rev. B* **55**, 10337–10354 (1997)
110. X. Gonze, C. Lee, *Phys. Rev. B* **55**, 10355–10368 (1997)
111. A. Putrino, D. Sebastiani, M. Parrinello, *J. Chem. Phys.* **113**, 7102–7109 (2000)
112. S. Baroni, S. de Gironcoli, A. Dal Corso, P. Giannozzi, *Rev. Mod. Phys.* **73**, 515–562 (2001)
113. P. Umari, A. Pasquarello, *Phys. Rev. B* **68**, 085114 (2003)
114. A. Putrino, M. Parrinello, *Phys. Rev. Lett.* **88**, 176401 (2002)
115. M. Pagliai, C. Cavazzoni, G. Cardini, G. Erbacci, M. Parrinello, V. Schettino, *J. Chem. Phys.* **128**, 224514 (2008)
116. R. Mazzarello, S. Caravati, S. Angioletti-Uberti, M. Bernasconi, M. Parrinello, *Phys. Rev. Lett.* **104**, 085503 (2010)
117. M. Pagliai, M. Muniz-Miranda, G. Cardini, V. Schettino, *J. Mol. Struct.* **993**, 151–154 (2011)
118. M. Pagliai, P. Bonazzi, L. Bindi, M. Muniz-Miranda, G. Cardini, *J. Phys. Chem. A* **115**, 4558–4562 (2011)
119. Q. Wan, L. Spanu, G.A. Galli, F. Gygi, *J. Chem. Theory Comput.* **9**, 4124–4130 (2013)
120. T. Ikeda, *J. Chem. Phys.* **141**, 044501 (2014)
121. S. Luber, M. Iannuzzi, J. Hutter, *J. Chem. Phys.* **141**, 094503 (2014)
122. I. Souza, J. Íñiguez, D. Vanderbilt, *Phys. Rev. Lett.* **89**, 117602 (2002)
123. P. Umari, A. Pasquarello, *Phys. Rev. Lett.* **89**, 157602 (2002)
124. A. Miani, S. Raugei, P. Carloni, M.S. Helfand, *J. Phys. Chem. B* **111**, 2621–2630 (2007)
125. A. Miani, M.S. Helfand, S. Raugei, *J. Chem. Theory Comput.* **5**, 2158–2172 (2009)

126. P. Umari, A. Pasquarello, Phys. Rev. Lett. **95**, 137401 (2005)
127. P. Umari, A. Pasquarello, Diamond Relat. Mater. **14**, 1255–1261 (2005)
128. L. Giacomazzi, P. Umari, A. Pasquarello, Phys. Rev. Lett. **95**, 075505 (2005)
129. R.J. Heaton, P.A. Madden, S.J. Clark, S. Jahn, J. Chem. Phys. **125**, 144104 (2006)
130. M. Salanne, R. Vuilleumier, P.A. Madden, C. Simon, P. Turq, B. Guillot, J. Phys. Condens. Matter **20**, 494207 (2008)
131. J.M. Bowman, X. Zhang, A. Brown, J. Chem. Phys. **119**, 646–650 (2003)
132. M. Kaledin, A. Brown, A.L. Kaledin, J.M. Bowman, J. Chem. Phys. **121**, 5646–5653 (2004)
133. M. Buchner, B.M. Ladanyi, R.M. Stratt, J. Chem. Phys. **97**, 8522–8535 (1992)
134. M. Cho, G.R. Fleming, S. Saito, I. Ohmine, R.M. Stratt, J. Chem. Phys. **100**, 6672–6683 (1994)
135. R.M. Stratt, Acc. Chem. Res. **28**, 201–207 (1995)
136. T. Keyes, J. Phys. Chem. A **101**, 2921–2930 (1997)
137. T. Kalbfleisch, T. Keyes, J. Chem. Phys. **108**, 7375–7383 (1998)
138. M. Nonella, G. Mathias, P. Tavan, J. Phys. Chem. A **107**, 8638–8647 (2003)
139. M. Schmitz, P. Tavan, J. Chem. Phys. **121**, 12233–12246 (2004)
140. M. Schmitz, P. Tavan, J. Chem. Phys. **121**, 12247–12258 (2004)
141. R.A. Wheeler, H. Dong, S.E. Boesch, ChemPhysChem **4**, 382–384 (2003)
142. R.A. Wheeler, H. Dong, ChemPhysChem **4**, 1227–1230 (2003)
143. A. Strachan, J. Chem. Phys. **120**, 1–4 (2004)
144. M. Martinez, M.-P. Gaigeot, D. Borgis, R. Vuilleumier, J. Chem. Phys. **125**, 144106 (2006)
145. G. Mathias, M.D. Baer, J. Chem. Theory Comput. **7**, 2028–2039 (2011)
146. G. Mathias, S.D. Ivanov, A. Witt, M.D. Baer, D. Marx, J. Chem. Theory Comput. **8**, 224–234 (2012)
147. M. Brehm, B. Kirchner, J. Chem. Inf. Model. **51**, 2007–2023 (2011)
148. D. McQuarrie, *Statistical Mechanics* (University Science Books, Sausalito, 2000)
149. M. Thomas, M. Brehm, R. Fligg, P. Vöhringer, B. Kirchner, Phys. Chem. Chem. Phys. **15**, 6608–6622 (2013)
150. B. Gellatly, J. Finney, J. Mol. Biol. **161**, 305–322 (1982)
151. S. Abbate, G. Longhi, K. Kwon, A. Moscovitz, J. Chem. Phys. **108**, 50–62 (1998)
152. J. Horníček, P. Kaprálová, P. Bouř, J. Chem. Phys. **127**, 084502 (2007)
153. S. Yang, M. Cho, J. Chem. Phys. **131**, 135102 (2009)
154. P.J. Stephens, J. Phys. Chem. **89**, 748–752 (1985)
155. P.J. Stephens, J. Phys. Chem. **91**, 1712–1715 (1987)
156. J. Cheeseman, M. Frisch, F. Devlin, P. Stephens, Chem. Phys. Lett. **252**, 211–220 (1996)
157. V.P. Nicu, J. Neugebauer, S.K. Wolff, E.J. Baerends, Theor. Chem. Acc. **119**, 245–263 (2008)
158. J.-H. Choi, M. Cho, J. Chem. Theory Comput. **7**, 4097–4103 (2011)
159. L.A. Nafie, T.B. Freedman, J. Chem. Phys. **78**, 7108–7116 (1983)
160. L.A. Nafie, J. Chem. Phys. **79**, 4950–4957 (1983)
161. A. Buckingham, P. Fowler, P. Galwas, Chem. Phys. **112**, 1–14 (1987)
162. L.A. Nafie, J. Chem. Phys. **96**, 5687–5702 (1992)
163. L.A. Nafie, J. Phys. Chem. A **108**, 7222–7231 (2004)
164. A. Scherrer, R. Vuilleumier, D. Sebastiani, J. Chem. Theory Comput. **9**, 5305–5312 (2013)
165. A. Scherrer, F. Agostini, D. Sebastiani, E.K.U. Gross, R. Vuilleumier, J. Chem. Phys. **143**, 074106 (2015)
166. T. Welton, Chem. Rev. **99**, 2071–2084 (1999)
167. T. Welton, Coord. Chem. Rev. **248**, 2459–2477 (2004)
168. J.P. Hallett, T. Welton, Chem. Rev. **111**, 3508–3576 (2011)
169. S. Tsuzuki, H. Tokuda, M. Mikami, Phys. Chem. Chem. Phys. **9**, 4780–4784 (2007)
170. S. Zahn, F. Uhlig, J. Thar, C. Spickermann, B. Kirchner, Angew. Chem. Int. Ed. **47**, 3639–3641 (2008)
171. S. Grimme, W. Hujo, B. Kirchner, Phys. Chem. Chem. Phys. **14**, 4875–4883 (2012)
172. M. Bühl, A. Chaumont, R. Schurhammer, G. Wipff, J. Phys. Chem. B **109**, 18591–18599 (2005)

173. P.A. Hunt, B. Kirchner, T. Welton, *Chem. Eur. J.* **12**, 6762–6775 (2006)
174. P.A. Hunt, I.R. Gould, B. Kirchner, *Aust. J. Chem.* **60**, 9–14 (2007)
175. R. Lungwitz, S. Spange, *New J. Chem.* **32**, 392–394 (2008)
176. S.B.C. Lehmann, M. Roatsch, M. Schöppke, B. Kirchner, *Phys. Chem. Chem. Phys.* **12**, 7473–7486 (2010)
177. O. Hollóczki, D. Gerhard, K. Massone, L. Szarvas, B. Németh, T. Veszprémi, L. Nyulászi, *New J. Chem.* **34**, 3004–3009 (2010)
178. O. Hollóczki, L. Nyulászi, *Org. Biomol. Chem.* **9**, 2634–2640 (2011)
179. M. Kohagen, M. Brehm, Y. Lingscheid, R. Giernoth, J. Sangoro, F. Kremer, S. Naumov, C. Iacob, J. Kärger, R. Valiullin, B. Kirchner, *J. Phys. Chem. B* **115**, 15280–15288 (2011)
180. I. Skarmoutsos, D. Dellis, R.P. Matthews, T. Welton, P.A. Hunt, *J. Phys. Chem. B* **116**, 4921–4933 (2012)
181. M. Brehm, H. Weber, A.S. Pensado, A. Stark, B. Kirchner, *Phys. Chem. Chem. Phys.* **14**, 5030–5044 (2012)
182. R.P. Matthews, T. Welton, P.A. Hunt, *Phys. Chem. Chem. Phys.* **16**, 3238–3253 (2014)
183. S. Katsyuba, P. Dyson, E. Vandyukova, A. Chernova, A. Vidiš, *Helv. Chim. Acta* **87**, 2556–2565 (2004)
184. E.R. Talaty, S. Raja, V.J. Storhaug, A. Dölle, W.R. Carper, *J. Phys. Chem. B* **108**, 13177–13184 (2004)
185. N.E. Heimer, R.E.D. Sesto, Z. Meng, J.S. Wilkes, W.R. Carper, *J. Mol. Liq.* **124**, 84–95 (2006)
186. S.A. Katsyuba, E.E. Zvereva, A. Vidiš, P.J. Dyson, *J. Phys. Chem. A* **111**, 352–370 (2007)
187. J. Kiefer, J. Fries, A. Leipertz, *Appl. Spectrosc.* **61**, 1306–1311 (2007)
188. N.R. Dhumal, H.J. Kim, J. Kiefer, *J. Phys. Chem. A* **113**, 10397–10404 (2009)
189. N. Akai, A. Kawai, K. Shibuya, *J. Phys. Chem. A* **114**, 12662–12666 (2010)
190. N.R. Dhumal, H.J. Kim, J. Kiefer, *J. Phys. Chem. A* **115**, 3551–3558 (2011)
191. J.X. Mao, A.S. Lee, J.R. Kitchin, H.B. Nulwala, D.R. Luebke, K. Damodaran, *J. Mol. Struct.* **1038**, 12–18 (2013)
192. N.R. Dhumal, K. Noack, J. Kiefer, H.J. Kim, *J. Phys. Chem. A* **118**, 2547–2557 (2014)
193. J.A. Fournier, C.T. Wolke, C.J. Johnson, A.B. McCoy, M.A. Johnson, *J. Chem. Phys.* **142**, 064306 (2015)
194. H. Wang, G. Gurau, R.D. Rogers, *Chem. Soc. Rev.* **41**, 1519–1537 (2012)
195. P.S. Barber, C.S. Griggs, G. Gurau, Z. Liu, S. Li, Z. Li, X. Lu, S. Zhang, R.D. Rogers, *Angew. Chem. Int. Ed.* **52**, 12350–12353 (2013)
196. J.P. Hallett, C.L. Liotta, G. Ranieri, T. Welton, *J. Org. Chem.* **74**, 1864–1868 (2009)
197. M.Y. Lui, L. Crowhurst, J.P. Hallett, P.A. Hunt, H. Niedermeyer, T. Welton, *Chem. Sci.* **2**, 1491–1496 (2011)
198. M. Brehm, H. Weber, A.S. Pensado, A. Stark, B. Kirchner, *Z. Phys. Chem.* **227**, 177–204 (2013)
199. O. Hollóczki, D.S. Firaha, J. Friedrich, M. Brehm, R. Cybik, M. Wild, A. Stark, B. Kirchner, *J. Phys. Chem. B* **117**, 5898–5907 (2013)

Chapter 2

Theoretical Background

2.1 The Schrödinger Equation

Any computational approach to study the properties of molecular systems needs to deal with the Schrödinger equation [1], which describes the dynamics in non-relativistic quantum mechanics. A brief summary of the approximations necessary to run molecular simulations within reasonable periods of time is given in the following sections. It follows several standard textbooks [2–5], so the educated reader might directly continue with Chap. 3.

The general time-dependent form of the Schrödinger equation in Dirac notation reads as

$$\mathcal{H}|\Phi(t)\rangle = i\hbar\frac{\partial}{\partial t}|\Phi(t)\rangle, \quad (2.1)$$

where \mathcal{H} is the Hamiltonian and $|\Phi(t)\rangle$ is a state vector in the Hilbert space of all possible quantum states of the particular system. If the Hamiltonian does not explicitly depend on the time t and $|\Phi(t)\rangle$ is a stationary state, the time dependence can be separated by the ansatz

$$|\Phi(t)\rangle = \exp\left(-\frac{i}{\hbar}Et\right)|\Psi\rangle, \quad (2.2)$$

where $|\Psi\rangle$ is an eigenstate of \mathcal{H} , so it fulfills the time-independent Schrödinger equation

$$\mathcal{H}|\Psi\rangle = E|\Psi\rangle \quad (2.3)$$

with the energy eigenvalue E .

In a molecular system that consists of N electrons and M nuclei, the Hamiltonian is commonly chosen to include the kinetic energy of the electrons \mathcal{T}_e , the kinetic energy of the nuclei \mathcal{T}_n , the Coulomb repulsion between the electrons \mathcal{V}_{ee} , the Coulomb attraction of the nuclei and the electrons \mathcal{V}_{ne} , and the Coulomb repulsion between the nuclei \mathcal{V}_{nn} :

$$\begin{aligned}
\mathcal{H} &= \mathcal{T}_e + \mathcal{T}_n + \mathcal{V}_{ee} + \mathcal{V}_{ne} + \mathcal{V}_{nn} \\
&= - \sum_{i=1}^N \frac{\hbar^2}{2m_e} \nabla_i^2 - \sum_{A=1}^M \frac{\hbar^2}{2M_A} \nabla_A^2 + \frac{e^2}{4\pi\epsilon_0} \left(\sum_{i=1}^N \sum_{j=i+1}^N \frac{1}{r_{ij}} - \sum_{i=1}^N \sum_{A=1}^M \frac{Z_A}{r_{iA}} + \sum_{A=1}^M \sum_{B=A+1}^M \frac{Z_A Z_B}{r_{AB}} \right).
\end{aligned} \tag{2.4}$$

In this equation, M_A and Z_A denote the mass and the atomic number of nucleus A , respectively, as well as $r_{ij} = |\mathbf{r}_i - \mathbf{r}_j|$, $r_{iA} = |\mathbf{r}_i - \mathbf{R}_A|$, and $r_{AB} = |\mathbf{R}_A - \mathbf{R}_B|$ represent the respective distances between electrons and nuclei. The coordinates of electron i and nucleus A are given by \mathbf{r}_i and \mathbf{R}_A , respectively.

The electronic and the nuclear motion can be separated within the Born–Oppenheimer approximation [6]. The total molecular wave function $\Psi(\mathbf{r}, \mathbf{R})$, which depends on the sets of all electronic coordinates $\mathbf{r} = \{\mathbf{r}_i\}$ and nuclear coordinates $\mathbf{R} = \{\mathbf{R}_i\}$, is expanded by

$$\Psi(\mathbf{r}, \mathbf{R}) = \sum_{k=0}^{\infty} \psi_k(\mathbf{r}; \mathbf{R}) \chi_k(\mathbf{R}), \tag{2.5}$$

where the electronic wave functions $\psi_k(\mathbf{r}; \mathbf{R})$ are assumed to form a complete set of eigenfunctions of the electronic Hamiltonian $\mathcal{H}_e = \mathcal{T}_e + \mathcal{V}_{ee} + \mathcal{V}_{ne} + \mathcal{V}_{nn}$ and fulfill—for fixed nuclear positions \mathbf{R} —the electronic Schrödinger equation

$$\mathcal{H}_e \psi_k(\mathbf{r}; \mathbf{R}) = E_k(\mathbf{R}) \psi_k(\mathbf{r}; \mathbf{R}) \tag{2.6}$$

with the electronic energy $E_k(\mathbf{R})$. The nuclear wave functions $\chi_k(\mathbf{R})$ can be seen as expansion coefficients that depend on the nuclear positions. Using this ansatz for the time-independent Schrödinger equation (2.3) with the molecular Hamiltonian (2.4) and integrating out the electronic coordinates, leads to the set of coupled equations

$$\left(- \sum_{A=1}^M \frac{\hbar^2}{2M_A} \nabla_A^2 + E_k(\mathbf{R}) \right) \chi_k(\mathbf{R}) + \sum_{l=0}^{\infty} C_{kl} \chi_l(\mathbf{R}) = \varepsilon_k \chi_k(\mathbf{R}) \tag{2.7}$$

with the energy ε_k and the coupling operator

$$C_{kl} = - \sum_{A=1}^M \frac{\hbar^2}{2M_A} \langle \psi_k(\mathbf{r}; \mathbf{R}) | \nabla_A^2 | \psi_l(\mathbf{r}; \mathbf{R}) \rangle_{\mathbf{r}} - \sum_{A=1}^M \frac{\hbar^2}{M_A} \langle \psi_k(\mathbf{r}; \mathbf{R}) | \nabla_A | \psi_l(\mathbf{r}; \mathbf{R}) \rangle_{\mathbf{r}} \nabla_A. \tag{2.8}$$

Within the Born–Oppenheimer approximation, all coupling terms are neglected, resulting in the nuclear Schrödinger equation

$$\left(- \sum_{A=1}^M \frac{\hbar^2}{2M_A} \nabla_A^2 + E_k(\mathbf{R}) \right) \chi_k(\mathbf{R}) = \varepsilon_k \chi_k(\mathbf{R}). \tag{2.9}$$

This effectively means to assume that the gradients of the electronic wave function along the nuclear coordinates in Eq. (2.8) vanish, so the the electronic wave function is influenced only by the positions of the nuclei but not by their momenta, and the nuclei move without changing the quantum state of the electrons. This is usually justifiable if the electronic states are separated well in energy. However, the approximation breaks down if two potential energy surfaces get close. This is often important, e.g., for photochemical processes, but such phenomena are not investigated in this thesis.

By the separation of electronic and nuclear motion, the Schrödinger equation is divided into two individual problems. For each nuclear configuration \mathbf{R} , the electronic energy $E_k(\mathbf{R})$ can be calculated by solving the electronic Schrödinger equation (2.6). This defines a potential energy surface, on which the nuclei behave according to the nuclear Schrödinger equation (2.9). A common method to solve the electronic Schrödinger equation is density functional theory (DFT), which is discussed in Sect. 2.2. Afterwards, the obtained electronic energy is used to treat the nuclear Schrödinger equation with further approximations that are described in Sect. 2.3.

2.2 Density Functional Theory

2.2.1 Hohenberg–Kohn Theorems and Kohn–Sham Method

Density functional theory (DFT) is a widely used method to solve the electronic Schrödinger equation, and it is founded on the Hohenberg–Kohn theorems [7]. The first Hohenberg–Kohn theorem states that the electronic ground-state wave function is uniquely determined by the ground-state electron density. The unique determination of the wave function also defines any further molecular property such as, e.g., the electronic ground-state energy. Thus, it is sufficient to calculate the electron density instead of the wave function. The advantage of the electron density is that it only depends on three spatial coordinates, whereas the wave function depends on the spatial and the spin coordinates of all N electrons.

In analogy to the electronic Hamiltonian \mathcal{H}_e defined for Eq. (2.6), the electronic energy is written as a functional of the electron density:

$$E[\rho(\mathbf{r})] = T[\rho(\mathbf{r})] + V_{ee}[\rho(\mathbf{r})] + V_n[\rho(\mathbf{r})]. \quad (2.10)$$

The last term in this sum,

$$V_n[\rho(\mathbf{r})] = \int \rho(\mathbf{r}) v_{\text{ext}}(\mathbf{r}) \, d\mathbf{r}, \quad (2.11)$$

is the only one that depends on the nuclear coordinates, as it contains the Coulomb attraction of the nuclei and the electrons as well as the nuclear Coulomb repulsion in the external potential

$$v_{\text{ext}}(\mathbf{r}) = \frac{e^2}{4\pi\epsilon_0} \left(- \sum_{A=1}^M \frac{Z_A}{|\mathbf{r} - \mathbf{R}_A|} + \sum_{A=1}^M \sum_{B=A+1}^M \frac{Z_A Z_B}{|\mathbf{R}_A - \mathbf{R}_B|} \right). \quad (2.12)$$

The other two functionals, the kinetic energy $T[\rho(\mathbf{r})]$ and the electron–electron interaction $V_{\text{ee}}[\rho(\mathbf{r})]$, are universal expressions that are valid for any system. Unfortunately, their general form is hitherto unknown.

The second Hohenberg–Kohn theorem introduces the variational principle to DFT. According to that, the energy of any trial electron density is never lower than the exact ground-state energy. It is therefore possible to find the exact ground-state electron density by varying a trial electron density until the energy reaches the global minimum.

A widely used approach to actually calculate the electron density in DFT is the Kohn–Sham method [8]. Within this technique, a fictitious system of noninteracting electrons is considered, the electron density $\rho_s(\mathbf{r})$ of which is equal to the one of the real system $\rho(\mathbf{r})$. The noninteracting electrons occupy the auxiliary Kohn–Sham orbitals $\theta_i(\mathbf{r})$, and the electron density is formed according to

$$\rho_s(\mathbf{r}) = \rho(\mathbf{r}) = e \sum_{i=1}^N |\theta_i(\mathbf{r})|^2. \quad (2.13)$$

Since the overall wave function of this system is exactly given by a single Slater determinant of Kohn–Sham orbitals, the kinetic energy is equal to

$$T_s[\{\theta_i(\mathbf{r})\}] = - \frac{\hbar^2}{2m_e} \sum_{i=1}^N \langle \theta_i(\mathbf{r}) | \nabla^2 | \theta_i(\mathbf{r}) \rangle. \quad (2.14)$$

If also the classical Coulomb repulsion

$$J[\rho(\mathbf{r})] = \frac{1}{4\pi\epsilon_0} \frac{1}{2} \iint \frac{\rho(\mathbf{r}_1)\rho(\mathbf{r}_2)}{|\mathbf{r}_1 - \mathbf{r}_2|} d\mathbf{r}_1 d\mathbf{r}_2 \quad (2.15)$$

is separated from the total electron–electron interaction $V_{\text{ee}}[\rho(\mathbf{r})]$, the electronic energy (2.10) can be rewritten as

$$E[\{\theta_i(\mathbf{r})\}] = T_s[\{\theta_i(\mathbf{r})\}] + J[\rho(\mathbf{r})] + E_{\text{xc}}[\rho(\mathbf{r})] + V_{\text{n}}[\rho(\mathbf{r})]. \quad (2.16)$$

The exchange–correlation energy functional $E_{\text{xc}}[\rho(\mathbf{r})]$ collects all unknown contributions to the energy, in particular the kinetic correlation energy, the exchange energy, the Coulombic correlation energy and the self–interaction correction.

Based on the second Hohenberg–Kohn theorem, the Kohn–Sham orbitals are found by minimizing the electronic energy with respect to the orbitals. As a constraint to this minimization, the orbitals are required to be orthonormal. Applying the method of Lagrange multipliers, this leads to the Kohn–Sham equations

$$\left(-\frac{\hbar^2}{2m_e} \nabla^2 + v_{\text{ext}}(\mathbf{r}) + \frac{1}{4\pi\epsilon_0} \int \frac{\rho(\mathbf{r}_1)}{|\mathbf{r} - \mathbf{r}_1|} d\mathbf{r}_1 + \frac{\delta E_{\text{xc}}[\rho(\mathbf{r})]}{\delta\rho(\mathbf{r})} \right) \theta_i(\mathbf{r}) = \epsilon_i \theta_i(\mathbf{r}) \quad (2.17)$$

with the orbital energies ϵ_i . Because the Coulomb potential and the exchange–correlation energy depend through the electron density on the orbitals, the Kohn–Sham equations are nonlinear and are, therefore, commonly solved iteratively. The traditional diagonalization approach to this problem is discussed in Sect. 2.2.3. Another method that relies on a direct minimization of the electronic energy is mentioned in Sect. 2.2.4.

2.2.2 Approximate Exchange–Correlation Functionals

Up to this point, DFT would provide an exact solution of the electronic Schrödinger equation. However, the correct exchange–correlation functional $E_{\text{xc}}[\rho(\mathbf{r})]$ is hitherto unknown, so approximations have to be made. For this purpose, the functional is usually divided into an exchange part and a correlation part:

$$E_{\text{xc}}[\rho(\mathbf{r})] = E_{\text{x}}[\rho(\mathbf{r})] + E_{\text{c}}[\rho(\mathbf{r})]. \quad (2.18)$$

In principle, it would be possible to evaluate the exchange part in the same way as in the Hartree–Fock method using the Kohn–Sham orbitals, but in connection with approximations to the correlation part, this exact exchange often yields poor results for the molecular properties. Other approaches that benefit from a successful cancellation of errors and, furthermore, avoid the evaluation of costly exchange integrals are therefore very popular.

A simple model for the exchange–correlation energy is the local density approximation (LDA), which assumes that the electron density is a slowly varying function, so it can locally be treated as a uniform electron gas. In this case, an exact expression for the exchange energy can be derived [9, 10]:

$$E_{\text{x}}^{\text{LDA}}[\rho(\mathbf{r})] = -\frac{9\alpha}{8} \left(\frac{3}{\pi} \right)^{\frac{1}{3}} \int \rho^{\frac{4}{3}}(\mathbf{r}) d\mathbf{r}, \quad \text{where} \quad \alpha = \frac{2}{3}. \quad (2.19)$$

Even for this simple system, it is impossible to give an analytic expression for the correlation energy, but it can accurately be determined by quantum Monte Carlo simulations. An analytic fitting formula to the results of these simulations has been developed by Vosko, Wilk, and Nusair (VWN) [11]. Neglecting the correlation part and taking only the exchange part (2.19) results in the X_{α} method proposed by Slater [12], where differing prefactors of $\alpha = 1$ and $\alpha = 3/4$ are used for better agreement with experimental results. The LDA is easily extended to open shell systems in terms of the local spin density approximation (LSDA) [11, 12].

Because the assumption of a uniform electron gas does not provide a good description of typical molecular systems, more advanced exchange-correlation functionals depend on the gradient of the electron density. This is called generalized gradient approximation (GGA). Common examples of GGA functionals are Becke's exchange functional (B) [13] and the correlation functional of Lee, Yang, and Parr (LYP) [14], which can be combined to form the exchange-correlation functional BLYP. Both parts of this functional contain empirical parameters fitted to Hartree–Fock data of noble gases. In the exchange-correlation functional of Perdew and Wang (PW91) [15] and its successor functional of Perdew, Burke, and Ernzerhof (PBE) [16], no fitting to existing data is performed and the parameters are chosen to fulfill some general theoretical requirements instead. The basic idea of GGA functionals is extended in meta-GGA functionals, which depend on higher derivatives of the electron density, such as, e.g., the exchange-correlation functional of Tao, Perdew, Staroverov, and Scuseria (TPSS) [17].

As mentioned before, it is in principle possible to use the Kohn–Sham orbitals for calculating the exchange part as in Hartree–Fock theory. In a system of noninteracting electrons, this would provide the exact exchange-correlation energy as there is no correlation energy. Based on the adiabatic connection method, hybrid functionals take the exact exchange for a part of the exchange-correlation energy while the remainder is calculated using the pure functionals from above. The amount of exact exchange constitutes another empirical parameter that has to be chosen. Very common are Becke's three-parameter functionals (B3). The originally proposed one utilized the B exchange and the correlation part of PW91. Its general form reads as

$$E_{xc}^{B3PW91} = (1 - a - b)E_x^{LSDA} + aE_x^{\text{exact}} + bE_x^B + (1 - c)E_c^{LSDA} + cE_c^{PW91}. \quad (2.20)$$

The parameters were optimized to $a = 0.20$, $b = 0.72$ and $c = 0.81$ by fitting to experimental data [18]. Later on, PW91 was replaced by LYP in the correlation part to create the B3LYP functional, but the parameters a , b , and c were kept at the same values [19]. In the same way as B3LYP is connected to the BLYP functional, the PBE0 functional has been developed as a hybrid version of PBE [20]. However, in PBE0 the amount of exact exchange is fixed at 25 % according to arguments from perturbation theory. Therefore, it does not contain any parameters fitted to experimental data and is given by

$$E_{xc}^{PBE0} = \frac{1}{4}E_x^{\text{exact}} + \frac{3}{4}E_x^{PBE} + E_c^{PBE}. \quad (2.21)$$

Also hybrid versions of meta-GGA functionals have been developed, such as, e.g., TPSSh that combines TPSS with 10% of exact exchange [21].

A common deficiency of the above mentioned exchange-correlation functionals is the lack of a proper description of dispersion interactions. Several approaches to include also these effects have been proposed. Beside, e.g., nonlocal van der Waals functionals [22, 23] and dispersion-corrected atom-centered potentials [24, 25], the DFT-D technique [26–28] is widely applied. In this method, an empirical correction term is added to the final energy of the system, which has the general form

$$E_{\text{disp}} = - \sum_{A=1}^M \sum_{B=A+1}^M \sum_{n=6,8,10,\dots} C_n^{AB} s_n \frac{C_n^{AB}}{r_{AB}^n} f_{\text{damp}}(r_{AB}), \quad (2.22)$$

where the sum over all atom pairs (A, B) is taken, C_n^{AB} denotes the averaged n th-order dispersion coefficient of atom pair (A, B) , $r_{AB} = |\mathbf{R}_A - \mathbf{R}_B|$ is the distance of the atoms A and B , s_n is a global scaling factor adjusted to the exchange-correlation functional, and f_{damp} is a damping function to avoid near-singularities at small distances and double-counting effects at intermediate distances. In DFT-D3 [27], the sum over n is truncated after $n = 8$, and the dispersion coefficients are calculated by time-dependent density functional theory.

2.2.3 Basis Set Expansion

The Kohn–Sham equations (2.17) are usually solved by representing the Kohn–Sham orbitals $\theta_i(\mathbf{r})$ as linear combinations of a finite set of n known basis functions $\phi_j(\mathbf{r})$:

$$\theta_i(\mathbf{r}) = \sum_{j=1}^n C_{ij} \phi_j(\mathbf{r}). \quad (2.23)$$

This allows to transform the Kohn–Sham equations from their integro-differential form into a matrix representation:

$$\mathbf{K}\mathbf{C} = \mathbf{S}\mathbf{C}\epsilon. \quad (2.24)$$

In this equation, \mathbf{K} is the Kohn–Sham matrix with the elements

$$K_{ij} = \left\langle \phi_i(\mathbf{r}) \left| -\frac{\hbar^2}{2m_e} \nabla^2 + v_{\text{ext}}(\mathbf{r}) + \frac{1}{4\pi\epsilon_0} \int \frac{\rho(\mathbf{r}_1)}{|\mathbf{r} - \mathbf{r}_1|} d\mathbf{r}_1 + \frac{\delta E_{\text{xc}}[\rho(\mathbf{r})]}{\delta\rho(\mathbf{r})} \right| \phi_j(\mathbf{r}) \right\rangle, \quad (2.25)$$

\mathbf{S} is the overlap matrix with the elements

$$S_{ij} = \langle \phi_i(\mathbf{r}) | \phi_j(\mathbf{r}) \rangle, \quad (2.26)$$

\mathbf{C} is the matrix of the coefficients C_{ij} from the basis expansion (2.23), and ϵ is a diagonal matrix with the orbital energies ϵ_i on the main diagonal. In doing so, the problem of finding the Kohn–Sham orbitals $\theta_i(\mathbf{r})$ is reduced to the task of determining the coefficients C_{ij} . Equation (2.24) possesses the form of a generalized eigenvalue problem, but since the Kohn–Sham matrix \mathbf{K} depends on the coefficients \mathbf{C} , an iterative procedure is needed: An initial guess for the coefficients \mathbf{C} is taken, the Kohn–Sham matrix \mathbf{K} is evaluated using these coefficients, new coefficients \mathbf{C} are calculated by solving the generalized eigenvalue problem, and this process is repeated

until the coefficients do not change anymore. This means that they are self-consistent, and the approach is, therefore, called self-consistent field (SCF) method.

Several choices for the basis functions $\phi_i(\mathbf{r})$ have been proposed. Very common in quantum chemistry are contracted Gaussian type orbitals (GTOs) of the general form

$$\phi(\mathbf{r}) = N\xi(\mathbf{r} - \mathbf{r}_0) \sum_{k=1}^m d_k \exp(-\zeta_k |\mathbf{r} - \mathbf{r}_0|^2), \quad (2.27)$$

which try to mimic the atomic orbitals of the individual atoms. Here, N is a normalization constant, $\xi(\mathbf{r} - \mathbf{r}_0)$ contains the angular momentum dependence, and \mathbf{r}_0 is the center of the basis function, which usually coincides with the position of the corresponding nucleus. The orbital exponents ζ_k and the expansion coefficients d_k are optimized once when the basis set is created, but they remain fixed in the SCF procedure to solve Eq. (2.24). Advantages of GTO basis sets are the good results with small set sizes and the straight description of all electrons in the system. However, the basis functions are not generally orthogonal, which can lead to linear dependencies that cause problems in the SCF procedure. Moreover, one has to take care of the basis set superposition error and Pulay forces [29] due to the position dependence of the basis functions.

Another approach, which is very common in solid state physics, is the use of plane wave basis sets. The periodicity of a crystalline solid imposes the same periodicity on the electron density, suggesting to use basis functions of the general form

$$\phi(\mathbf{r}) = \frac{1}{\sqrt{\Omega}} \exp(i\mathbf{G} \cdot \mathbf{r}), \quad (2.28)$$

where Ω is the volume of the periodic cell, and the wave vector \mathbf{G} has to satisfy the periodic boundary conditions. Usually, the basis set expansion (2.23) contains all wave vectors up to a certain cutoff. Since the plane waves are independent of the nuclear positions, Pulay forces and the basis set superposition error do not occur. Furthermore, all basis functions are orthogonal, making the overlap matrix trivial. Although a plane wave basis set implies periodic boundary conditions, molecular calculations in the gas phase are possible by applying such a large cell that the periodic images do not interact. The drawback of this approach is that a large number of basis functions is actually used to describe the empty part of the system.

A major issue of plane waves is the very high cutoff that is required to describe the rapid oscillations of the wave function due to the nodal structure of the valence orbitals near the nuclei. To overcome this problem, it is very common to apply pseudopotentials. A pseudopotential combines the Coulomb potential of the nuclei and the effective interaction potential of the core electrons with the valence electrons, and it replaces the sole Coulomb attraction of the nuclei in the external potential (2.12). This softens the potential the valence electrons move in, and lower cutoffs are sufficient for an adequate description. On the other hand, the core electrons are not

treated explicitly anymore, but this is only a minor restriction for most chemical applications.

2.2.4 *The Gaussian and Plane Waves Method*

The Gaussian and plane waves method [30, 31] is a particular implementation of DFT available in the CP2K software package [32], aiming for efficient calculations of large systems containing several thousand atoms. Within this approach, the Kohn–Sham orbitals are expanded in terms of GTO basis functions, but an auxiliary basis of plane waves is used for a second representation of the electron density. To convert between these representations, the electron density in the GTO basis is mapped onto a real-space grid with a spacing determined by the plane wave cutoff, and the plane wave coefficients are obtained by a discrete Fourier transform. The pseudopotentials of Goedecker, Teter, and Hutter (GTH) [33–35] are employed to reduce the necessary cutoff in the plane wave basis (see Sect. 2.2.3). These pseudopotentials are norm-conserving and separable, and their dual-space Gaussian form allows for an analytic calculation of the corresponding matrix elements in the GTO basis set. Also the kinetic energy contributions to the Kohn–Sham matrix are evaluated in the GTO basis, but the Coulomb interaction and the exchange–correlation potential are more efficiently calculated in the plane wave representation of the electron density. This leads to a construction scheme of the Kohn–Sham matrix that scales linearly with the system size.

Due to the application of GTH pseudopotentials, the electron density vanishes at the positions of the nuclei except for hydrogen atoms. Since many GGA exchange–correlation functionals contain terms with the electron density in the denominator, this gives rise to numerical problems in the evaluation of the exchange–correlation potential near the nuclei, making the total energy dependent on the atom positions relative to the real-space grid imposed by the plane wave basis. To reduce this effect, several smoothing procedures have been developed [31].

The SCF method described in Sect. 2.2.3 relies on the diagonalization of a matrix. An alternative approach is the direct minimization of the electronic energy (2.16), rewritten with the basis set expansion (2.23). In this formulation, the energy $E(\mathbf{C})$ is a function of the expansion coefficients, and the orthonormality constraint is given by $\mathbf{C}^T \mathbf{S} \mathbf{C} = \mathbf{I}$, where \mathbf{C} and \mathbf{S} are defined in Sect. 2.2.3, and \mathbf{I} is the identity matrix of the appropriate size. A minimization with this nonlinear constraint would require to follow a curved geodesic, but this can be avoided [36] by introducing a new set of variables \mathbf{X} that fulfill the linear constraint

$$\mathbf{X}^T \mathbf{S} \mathbf{C}_0 = \mathbf{0}, \quad (2.29)$$

where \mathbf{C}_0 are constant initial coefficients that satisfy the original constraint $\mathbf{C}_0^T \mathbf{S} \mathbf{C}_0 = \mathbf{I}$. The coefficients \mathbf{C} are related to the new variables \mathbf{X} by

$$\mathbf{C} = \mathbf{C}_0 \cos(\mathbf{U}) + \mathbf{X}\mathbf{U}^{-1} \sin(\mathbf{U}), \quad \text{with} \quad \mathbf{U} = (\mathbf{X}^T \mathbf{S} \mathbf{X})^{\frac{1}{2}}. \quad (2.30)$$

With a linear constraint, any standard minimization algorithm such as the conjugate gradient method or direct inversion in the iterative subspace (DIIS) [37] can be employed.

In the CP2K software package, this approach is available as orbital transformation (OT) method. If conjugate gradients are used with an extensive line search, convergence is guaranteed, leading to a procedure that can handle also cases which are problematic within the traditional diagonalization approach. Furthermore, the OT method is often faster than diagonalization [36].

2.3 Molecular Dynamics

Within the Born–Oppenheimer approximation, the nuclei obey the nuclear Schrödinger equation, which was given in its time-independent form in Eq. (2.9). The time-dependent form reads as

$$\left(- \sum_{A=1}^M \frac{\hbar^2}{2M_A} \nabla_A^2 + E_k(\mathbf{R}) \right) \chi_k(\mathbf{R}, t) = i\hbar \frac{\partial}{\partial t} \chi_k(\mathbf{R}, t). \quad (2.31)$$

For basic cases such as, e.g., the harmonic oscillator (see Sect. 2.4.1), it can be solved analytically. For larger systems, it can be simplified by approximating the nuclei as classical point particles. For this purpose, the complex nuclear wave function is rewritten as

$$\chi_k(\mathbf{R}, t) = B_k(\mathbf{R}, t) \exp\left(i \frac{S_k(\mathbf{R}, t)}{\hbar}\right) \quad (2.32)$$

with real functions $B_k(\mathbf{R}, t)$ (amplitude) and $S_k(\mathbf{R}, t)$ (phase). Applying this ansatz to Eq. (2.31) and separating the real and imaginary parts results in two coupled equations for amplitude and phase:

$$\frac{\partial}{\partial t} B_k(\mathbf{R}, t) + \sum_{A=1}^M \frac{1}{M_A} \left(\nabla_A B_k(\mathbf{R}, t) \nabla_A S_k(\mathbf{R}, t) + \frac{1}{2} B_k(\mathbf{R}, t) \nabla_A^2 S_k(\mathbf{R}, t) \right) = 0, \quad (2.33)$$

$$\frac{\partial}{\partial t} S_k(\mathbf{R}, t) + \sum_{A=1}^M \frac{1}{2M_A} (\nabla_A S_k(\mathbf{R}, t))^2 + E_k(\mathbf{R}) = \hbar^2 \sum_{A=1}^M \frac{1}{2M_A} \frac{\nabla_A^2 B_k(\mathbf{R}, t)}{B_k(\mathbf{R}, t)}. \quad (2.34)$$

Equation (2.33) can be interpreted as a continuity equation that ensures the conservation of the probability density $|\chi_k(\mathbf{R}, t)|^2$. In Eq. (2.34), the right-hand side vanishes in the classical limit $\hbar \rightarrow 0$, and the Hamilton–Jacobi equation of classical

mechanics remains:

$$\frac{\partial}{\partial t} S_k(\mathbf{R}, t) + \sum_{A=1}^M \frac{1}{2M_A} (\nabla_A S_k(\mathbf{R}, t))^2 + E_k(\mathbf{R}) = \frac{\partial}{\partial t} S_k(\mathbf{R}, t) + H_k(\mathbf{R}, \mathbf{P}) = 0 \quad (2.35)$$

with the momenta $\mathbf{P} = \{\mathbf{P}_A\}$, $\mathbf{P}_A(t) = \nabla_A S_k(\mathbf{R}, t)$, and the Hamilton function $H_k(\mathbf{R}, \mathbf{P}) = T(\mathbf{P}) + E_k(\mathbf{R})$, where $T(\mathbf{P})$ is the kinetic energy. This can be transformed to the Newtonian equations of motion

$$\frac{d}{dt} \mathbf{P}_A(t) = M_A \frac{d^2}{dt^2} \mathbf{R}_A(t) = -\nabla_A E_k(\mathbf{R}(t)). \quad (2.36)$$

This means that the nuclei move according to classical mechanics in the potential that is provided by the electronic energy $E_k(\mathbf{R})$, suggesting the following procedure to study the time evolution of a molecular system: the nuclei are propagated according to Eq. (2.36), and at any particular time t , the electronic energy and its gradient are obtained by solving the time-independent electronic Schrödinger equation (2.6) for the current nuclear configuration $\mathbf{R}(t)$. This approach is called Born–Oppenheimer molecular dynamics (BOMD). The AIMD simulations performed in the course of this thesis are BOMD simulations.

The Newtonian equations of motion (2.36) are usually solved by numerical methods that introduce a discrete timestep Δt . In the Verlet algorithm [38], the nuclear coordinates are expanded in Taylor series up to third order:

$$\mathbf{R}_A(t + \Delta t) = \mathbf{R}_A(t) + \Delta t \frac{d}{dt} \mathbf{R}_A(t) + \frac{1}{2} \Delta t^2 \frac{d^2}{dt^2} \mathbf{R}_A(t) + \frac{1}{6} \Delta t^3 \frac{d^3}{dt^3} \mathbf{R}_A(t) + \mathcal{O}(\Delta t^4), \quad (2.37)$$

$$\mathbf{R}_A(t - \Delta t) = \mathbf{R}_A(t) - \Delta t \frac{d}{dt} \mathbf{R}_A(t) + \frac{1}{2} \Delta t^2 \frac{d^2}{dt^2} \mathbf{R}_A(t) - \frac{1}{6} \Delta t^3 \frac{d^3}{dt^3} \mathbf{R}_A(t) + \mathcal{O}(\Delta t^4). \quad (2.38)$$

Adding these two equations and rearranging the terms leads to

$$\mathbf{R}_A(t + \Delta t) = 2\mathbf{R}_A(t) - \mathbf{R}_A(t - \Delta t) + \frac{1}{M_A} \Delta t^2 \mathbf{F}_A(t) + \mathcal{O}(\Delta t^4), \quad (2.39)$$

where the forces $\mathbf{F}_A(t) = M_A \ddot{\mathbf{R}}(t) = -\nabla_A E_k(\mathbf{R}(t))$ are introduced. The nuclear velocities $\mathbf{V}_A(t) = \dot{\mathbf{R}}_A(t)$ are eliminated in this derivation, but it is often desirable to know them, e.g., to calculate the kinetic energy. Therefore, it is more convenient to apply the velocity form of the Verlet algorithm [39], where coordinates and velocities are given by

$$\mathbf{R}_A(t + \Delta t) = \mathbf{R}_A(t) + \Delta t \mathbf{V}_A(t) + \frac{1}{2M_A} \Delta t^2 \mathbf{F}_A(t), \quad (2.40)$$

$$\mathbf{V}_A(t + \Delta t) = \mathbf{V}_A(t) + \frac{1}{2M_A} \Delta t (\mathbf{F}_A(t) + \mathbf{F}_A(t + \Delta t)). \quad (2.41)$$

It can be shown that this formulation is equivalent to the original Verlet method, but it directly delivers the velocities in each step of the simulation. The complete BOMD procedure starting from certain initial coordinates $\mathbf{R}(0)$ and velocities $\mathbf{V}(0)$ now reads as follows: The coordinates $\mathbf{R}(t)$ are used to calculate the forces $\mathbf{F}(t)$ by solving the time-independent electronic Schrödinger equation for these coordinates (e.g., by applying DFT, see Sect. 2.2), the new coordinates $\mathbf{R}(t + \Delta t)$ are calculated by Eq. (2.40), they are used to obtain the new forces $\mathbf{F}(t + \Delta t)$ by solving again the electronic Schrödinger equation, and the new velocities $\mathbf{V}(t + \Delta t)$ are finally given by Eq. (2.41). This procedure has to be repeated until a reasonable part of the nuclear phase space is sampled.

Since BOMD on the basis of the Newtonian equations of motion (2.36) conserves the total energy, a trajectory in the microcanonical or NVE ensemble is generated. For comparison with experiments, where usually the temperature is controlled, it is, however, desirable to run simulations in the canonical or NVT ensemble. For this purpose, a thermostat has to be applied. A very common choice is the Nosé–Hoover thermostat [40–42], which adds a heat bath by introducing an additional degree of freedom to the system. This “heat bath particle” follows a specific potential so that the original degrees of freedom sample the NVT ensemble. To handle also difficult cases, the concept has been extended to the Nosé–Hoover thermostat chain [43], where the heat bath is coupled to another heat bath. Introducing further heat baths that are successively connected to each other finally leads to a linear chain of K thermostats with the following equations of motion:

$$M_A \ddot{\mathbf{R}}_A(t) = -\nabla_A E_k(\mathbf{R}(t)) - M_A \dot{\xi}_1(t) \dot{\mathbf{R}}_A(t), \quad (2.42)$$

$$Q_1 \ddot{\xi}_1(t) = \sum_{A=1}^M M_A \dot{\mathbf{R}}_A(t)^2 - g k_B T - Q_1 \dot{\xi}_1(t) \dot{\xi}_2(t), \quad (2.43)$$

$$Q_i \ddot{\xi}_i(t) = Q_{i-1} \dot{\xi}_{i-1}(t)^2 - k_B T - Q_i \dot{\xi}_i(t) \dot{\xi}_{i+1}(t), \quad i = 2, \dots, K-1, \quad (2.44)$$

$$Q_K \ddot{\xi}_K(t) = Q_{K-1} \dot{\xi}_{K-1}(t)^2 - k_B T. \quad (2.45)$$

Here, T is the desired average temperature, and g is the number of degrees of freedom to which the thermostat chain is coupled ($g = 3M$ if no constraints are imposed on the nuclear coordinates). Each thermostat has a coordinate $\xi_i(t)$ and a mass-like parameter Q_i , which is chosen as

$$Q_1 = g k_B T \tau^2, \quad Q_i = k_B T \tau^2, \quad i = 2, \dots, K. \quad (2.46)$$

The coupling time constant τ should be in the order of the timescale of the nuclear motions. Since the forces in the equations of motion explicitly depend on the

velocities, the velocity Verlet algorithm cannot be applied directly. It is possible to solve Eq. (2.41) iteratively, but also explicit reversible integrators have been developed [44] on the basis of the Liouville operator, multiple timestep schemes, and higher order Yoshida–Suzuki integration [45, 46]. For the NVE ensemble, these reduce to the velocity Verlet method.

For the equilibration of an MD simulation, it is convenient to use an individual Nosé–Hoover thermostat chain for each degree of freedom (massive thermostat). This significantly reduces the equilibration time and helps to excite even stiff vibrational modes that are only loosely coupled to all other modes of the system, as it is required to fulfill the equipartition theorem.

2.4 Vibrational Spectroscopy

2.4.1 The Harmonic Oscillator

As discussed in Sect. 2.1, the Born–Oppenheimer approximation decouples the electronic from the nuclear motion in a molecular system. The nuclei move on the $3M$ -dimensional potential energy surface that is determined by the electronic structure. In a typical stable molecule, this potential has distinct minima and the molecule performs oscillations around these minima.

For simplicity, a one-dimensional potential $V(x)$ with a minimum at $x = 0$ is considered in the following. The Taylor series around $x = 0$ reads as

$$V(x) = V(0) + V'(0)x + \frac{1}{2}V''(0)x^2 + \frac{1}{6}V'''(0)x^3 + \dots \quad (2.47)$$

The first term is a constant offset and the potential can always be transformed to make this offset vanish by choosing an appropriate energy zero point. Since the potential has a minimum at $x = 0$, also the second term is zero. The first non-vanishing term is the harmonic potential

$$V(x) = \frac{1}{2}kx^2, \quad (2.48)$$

where the second derivative of the potential is identified with the force constant k . This means that the first approximation to an arbitrarily shaped potential is given by (2.48) in the vicinity of a minimum. In particular, also the nuclear motion in a molecule can approximately be described within a multidimensional harmonic potential.

In classical mechanics (cf. Eq. (2.36)), a particle of mass m moving in the harmonic potential (2.48) fulfills the differential equation

$$m\ddot{x}(t) + kx(t) = 0. \quad (2.49)$$

It can be shown that the general solution of this differential equation is

$$x(t) = x_0 \cos\left(\sqrt{\frac{k}{m}}t + \varphi\right) = x_0 \cos(\omega_0 t + \varphi), \quad (2.50)$$

where the eigenfrequency $\omega_0 = \sqrt{k/m}$ is introduced. This means that the particle performs a harmonic vibration with the constant angular frequency ω_0 . The amplitude x_0 and the phase φ are determined by the initial conditions.

In quantum mechanics (cf. Eq. (2.9)), the corresponding differential equation reads as

$$\left(-\frac{\hbar^2}{2m} \frac{d^2}{dx^2} + \frac{1}{2}kx^2\right) \chi_n(x) = \varepsilon_n \chi_n(x). \quad (2.51)$$

If $\omega_0 = \sqrt{k/m}$ is set as in the classical case, the eigenfunctions of the quantum harmonic oscillator are given by

$$\chi_n(x) = \frac{1}{\sqrt{2^n n!}} \sqrt{\frac{m\omega_0}{\pi \hbar}} H_n\left(\sqrt{\frac{m\omega_0}{\hbar}}x\right) \exp\left(-\frac{1}{2} \frac{m\omega_0}{\hbar} x^2\right) \quad (2.52)$$

with the Hermite polynomials

$$H_n(x) = (-1)^n \exp(x^2) \frac{d^n}{dx^n} \exp(-x^2). \quad (2.53)$$

The energy eigenvalues are

$$\varepsilon_n = \hbar\omega_0 \left(n + \frac{1}{2}\right), \quad n \geq 0. \quad (2.54)$$

The quantum harmonic oscillator can only take discrete energy values with a constant spacing of $\hbar\omega_0$. Even the ground state has the non-vanishing energy $\varepsilon_0 = \hbar\omega_0/2$, which is called zero-point energy.

Both types of harmonic oscillators are easily extended to the multidimensional case, since the multidimensional harmonic potential

$$V(\mathbf{x}) = \frac{1}{2} \mathbf{x}^T \mathbf{k} \mathbf{x} \quad (2.55)$$

can always be written as a sum of one-dimensional harmonic potentials if the force matrix \mathbf{k} is diagonal. If the force matrix \mathbf{k} is not diagonal, an appropriate transformation to the system of normal coordinates has to be applied beforehand. In such a separable potential, the classical harmonic oscillator performs a harmonic vibration (2.50) along each normal coordinate. The total wave function of the quantum harmonic oscillator is the product of the one-dimensional wave functions (2.52), and its energy is the sum of the one-dimensional energy eigenvalues (2.54).

2.4.2 Infrared Absorption

The nuclei in a molecule generally follow the laws of quantum mechanics, so they can only take discrete eigenstates with certain energy values, as discussed for the harmonic approximation to the potential energy surface in Sect. 2.4.1. A change from one eigenstate to another one is possible by the absorption or emission of electromagnetic radiation, the energy of which is equal to the energy difference between the two states. For the nuclear vibrations in a molecule, these energy differences are typically in the range of 10^{-21} to 10^{-19} J, corresponding to the IR region of the electromagnetic spectrum. This leads to the experimental technique of IR spectroscopy: a chemical substance is irradiated with IR radiation and its absorption is measured in dependence of its energy. The resulting spectrum shows peaks at positions characteristic for the molecular structure. For a harmonic oscillator, e.g., the peak is located at the difference $\hbar\sqrt{k/m}$ between two subsequent states, so its position is directly related to the force constant.

Beside the peak positions, also the intensities are an important property of IR spectra. Their theoretical values can be derived [47] by applying Fermi's golden rule [48, 49]

$$W_{i \rightarrow f} = \frac{1}{\hbar^2} |\langle v_f | \mathcal{H}' | v_i \rangle|^2 \rho_N(v_f), \quad (2.56)$$

which gives the transition rate $W_{i \rightarrow f}$ for the transition from state $|v_i\rangle$ to state $|v_f\rangle$ when the perturbation \mathcal{H}' by electromagnetic radiation with a density of photon states per frequency range $\rho_N(\nu)$ is applied to the system. Within the dipole approximation, the perturbation is

$$\langle v_f | \mathcal{H}' | v_i \rangle = -\langle v_f | \bar{\boldsymbol{\mu}}(\mathbf{Q}) \cdot \mathbf{E} | v_i \rangle = -\langle v_f | \bar{\boldsymbol{\mu}}(\mathbf{Q}) | v_i \rangle \cdot \mathbf{E}_0 \quad (2.57)$$

where $\bar{\boldsymbol{\mu}}(\mathbf{Q})$ is the molecular dipole moment depending on the mass-weighted normal coordinates \mathbf{Q} (the overbar indicates the expectation value over the electronic coordinates), and \mathbf{E} is the electric field vector of the radiation, which is assumed to be constant over the extent of the molecule with an average amplitude \mathbf{E}_0 . For the evaluation of the transition dipole matrix elements, the translational and rotational degrees of freedom are separated and the classical average over all rotational states is taken. Within the harmonic approximation, the harmonic oscillator wave functions (2.52) are used for the remaining $g = 3M - 6$ ($g = 3M - 5$ in a linear molecule) vibrational degrees of freedom. The molecular dipole moment is expanded in a Taylor series around the minimum of the potential energy surface up to first order:

$$\bar{\boldsymbol{\mu}}(\mathbf{Q}) = \bar{\boldsymbol{\mu}}_0 + \sum_{k=1}^g \left(\frac{\partial \bar{\boldsymbol{\mu}}(\mathbf{Q})}{\partial Q_k} \right)_0 Q_k. \quad (2.58)$$

With all these assumptions, analytic expressions for the transition dipole matrix elements can be found, and the integral absorption coefficient for the transition from

the ground state to the first excited state in the harmonic oscillator corresponding to mode k is given by [47]

$$A_k = \frac{1}{4 \pi \epsilon_0} \frac{N_A \pi}{3c^2} \left(\frac{\partial \bar{\boldsymbol{\mu}}(\mathbf{Q})}{\partial Q_k} \right)_0^2. \quad (2.59)$$

This shows that a particular vibrational mode appears as a peak in the IR spectrum of a molecule if the dipole moment changes along this mode.

Equation (2.59) can be used to estimate IR spectra by static quantum chemical calculations within the harmonic approximation to the potential energy surface: a geometry optimization is performed to find the minimum of the potential energy surface, the Hessian matrix of the potential energy at this point is the force matrix in (2.55), the force matrix is diagonalized to get the normal coordinates and the vibrational frequencies, and the dipole moment derivatives along the normal coordinates are calculated to obtain IR intensities according to (2.59).

For chiral molecules, the absorption is not the same if left and right circularly polarized IR radiation are compared. The difference between these two cases is measured in VCD spectroscopy. For a theoretical model of VCD intensities, the interaction of the molecular magnetic moment \mathbf{m} with the magnetic field of the electromagnetic radiation has to be taken into account. In this way, it is found that the VCD intensity for the transition from state $|i\rangle$ to state $|f\rangle$ is proportional to the rotational strength [50]

$$R_{i \rightarrow f} = \text{Im} \left(\langle i | \hat{\boldsymbol{\mu}} | f \rangle \langle f | \hat{\mathbf{m}} | i \rangle \right), \quad (2.60)$$

where $\hat{\boldsymbol{\mu}}$ and $\hat{\mathbf{m}}$ are the electric dipole and magnetic dipole operators, respectively. The magnetic transition moment needs special care, since the matrix elements $\langle f | \hat{\mathbf{m}} | i \rangle$ always vanish within the Born–Oppenheimer approximation. This can be circumvented by magnetic field perturbation theory [51–54] or nuclear velocity perturbation theory [55–61], allowing to calculate VCD spectra by static calculations within the harmonic approximation.

2.4.3 Raman Scattering

Beside absorption and emission, the scattering of electromagnetic radiation is another physical process that can change the quantum state of a molecule. When photons interact with molecules, most of them are scattered elastically, so the scattered photons have the same energy as the incident photons and the molecular quantum state remains unchanged (Rayleigh scattering). However, a small fraction of the photons is scattered inelastically, meaning that the molecule switches to another quantum state and the photon energy changes by the energy difference of the two molecular states. This effect is named Raman scattering after Chandrasekhara Raman, who first verified it experimentally [62], five years after the theoretical prediction by Adolf

Smekal [63]. If the molecule switches to a state higher in energy and the photon energy is reduced, the process is called Stokes Raman scattering. If the molecule switches to a state lower in energy and the photon energy is increased, the process is called anti-Stokes Raman scattering.

The effect of Raman scattering is used in Raman spectroscopy as an alternative to IR spectroscopy for the investigation of molecular vibrations. Due to the low efficiency of the Raman scattering process and the dependence of the scattering cross section on the fourth power of the photon energy, it is common to use high intensity lasers in the visible region of the electromagnetic spectrum for the irradiation of the sample. The intensity of the scattered radiation is measured in dependence of its energy, and the peak positions are recorded relative to the incident radiation, so they relate to energy differences between vibrational states, and Raman spectra can directly be compared to IR spectra.

Theoretical values for Raman intensities can be obtained from Placzek's classical theory of polarizability [64]. The electric field of the incident radiation induces a dipole moment in the molecule, and within classical electrodynamics, the scattered intensity is proportional to the square of the induced dipole moment. The expectation value of the induced dipole moment μ_{fi}^{ind} is determined quantum mechanically by evaluation of the corresponding polarizability matrix elements,

$$\langle \mu_{fi}^{\text{ind}} \rangle = \langle v_f | \bar{\alpha}(\mathbf{Q}) | v_i \rangle \mathbf{E}_0, \quad (2.61)$$

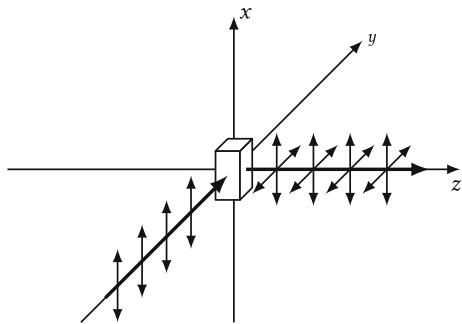
where it is assumed again that the electric field is constant over the extent of the molecule with an average amplitude \mathbf{E}_0 . The polarizability tensor $\bar{\alpha}(\mathbf{Q})$ (the overbar indicates the expectation value over the electronic coordinates) is expanded in a Taylor series analogous to (2.58):

$$\bar{\alpha}(\mathbf{Q}) = \bar{\alpha}_0 + \sum_{k=1}^g \left(\frac{\partial \bar{\alpha}(\mathbf{Q})}{\partial Q_k} \right)_0 Q_k. \quad (2.62)$$

This allows to derive analytic expressions for the Raman intensities of individual vibrational modes [47]. An important parameter is, however, the scattering geometry employed in the measurement setup. A common choice for theoretical investigations is shown in Fig. 2.1: the incident light beam propagates along the y axis and is polarized along the x axis. The detector for the scattered light is located on the z axis and is equipped with a polarization filter to measure the x polarized intensity I^{\parallel} and the y polarized intensity I^{\perp} . If the molecule is fixed with respect to the laboratory coordinate system, the differential Raman scattering cross sections for the Stokes line of vibrational mode k in this setup are given by

$$I_k^{\parallel} = \frac{\pi^2}{\varepsilon_0^2} (\tilde{\nu}_{\text{in}} - \tilde{\nu}_k)^4 \frac{h}{8 \pi^2 c \tilde{\nu}_k} \left(\frac{\partial \bar{\alpha}_{xx}(\mathbf{Q})}{\partial Q_k} \right)_0^2 \frac{1}{1 - \exp\left(-\frac{hc\tilde{\nu}_k}{k_{\text{B}}T}\right)} \quad (2.63)$$

Fig. 2.1 Measurement setup for Raman spectra. The incident light beam propagates along the y axis and is polarized along the x axis. The light scattered along the z axis is detected with a polarization filter for either x polarized or y polarized light



and

$$I_k^\perp = \frac{\pi^2}{\varepsilon_0^2} (\tilde{\nu}_{\text{in}} - \tilde{\nu}_k)^4 \frac{h}{8 \pi^2 c \tilde{\nu}_k} \left(\frac{\partial \bar{\alpha}_{xy}(\mathbf{Q})}{\partial Q_k} \right)_0^2 \frac{1}{1 - \exp\left(-\frac{hc\tilde{\nu}_k}{k_B T}\right)}, \quad (2.64)$$

where $\tilde{\nu}_{\text{in}}$ is the wavenumber of the incident radiation, $\tilde{\nu}_k$ is the wavenumber corresponding to vibrational mode k , and T is the temperature. This shows that a particular vibrational mode appears as a peak in the Raman spectrum of a molecule if the polarizability changes along this mode. If the molecule is randomly orientated with respect to the laboratory frame, the classical averages of the polarizability tensor components have to be taken. This results in

$$I_k^\parallel = \frac{\pi^2}{\varepsilon_0^2} (\tilde{\nu}_{\text{in}} - \tilde{\nu}_k)^4 \frac{h}{8 \pi^2 c \tilde{\nu}_k} \frac{45a_k^2 + 4\gamma_k^2}{45} \frac{1}{1 - \exp\left(-\frac{hc\tilde{\nu}_k}{k_B T}\right)} \quad (2.65)$$

and

$$I_k^\perp = \frac{\pi^2}{\varepsilon_0^2} (\tilde{\nu}_{\text{in}} - \tilde{\nu}_k)^4 \frac{h}{8 \pi^2 c \tilde{\nu}_k} \frac{3\gamma_k^2}{45} \frac{1}{1 - \exp\left(-\frac{hc\tilde{\nu}_k}{k_B T}\right)} \quad (2.66)$$

with the isotropic polarizability derivative

$$a_k = \frac{1}{3} \left(\left(\frac{\partial \bar{\alpha}_{xx}(\mathbf{Q})}{\partial Q_k} \right)_0 + \left(\frac{\partial \bar{\alpha}_{yy}(\mathbf{Q})}{\partial Q_k} \right)_0 + \left(\frac{\partial \bar{\alpha}_{zz}(\mathbf{Q})}{\partial Q_k} \right)_0 \right) \quad (2.67)$$

and the anisotropy

$$\begin{aligned} \gamma_k^2 = & \frac{1}{2} \left(\left(\frac{\partial \bar{\alpha}_{xx}(\mathbf{Q})}{\partial Q_k} \right)_0 - \left(\frac{\partial \bar{\alpha}_{yy}(\mathbf{Q})}{\partial Q_k} \right)_0 \right)^2 + \frac{1}{2} \left(\left(\frac{\partial \bar{\alpha}_{yy}(\mathbf{Q})}{\partial Q_k} \right)_0 - \left(\frac{\partial \bar{\alpha}_{zz}(\mathbf{Q})}{\partial Q_k} \right)_0 \right)^2 \\ & + \frac{1}{2} \left(\left(\frac{\partial \bar{\alpha}_{zz}(\mathbf{Q})}{\partial Q_k} \right)_0 - \left(\frac{\partial \bar{\alpha}_{xx}(\mathbf{Q})}{\partial Q_k} \right)_0 \right)^2 + 3 \left(\frac{\partial \bar{\alpha}_{xy}(\mathbf{Q})}{\partial Q_k} \right)_0^2 + 3 \left(\frac{\partial \bar{\alpha}_{yz}(\mathbf{Q})}{\partial Q_k} \right)_0^2 + 3 \left(\frac{\partial \bar{\alpha}_{zx}(\mathbf{Q})}{\partial Q_k} \right)_0^2. \end{aligned} \quad (2.68)$$

An important quantity related to the scattering intensities is the depolarization ratio

$$\rho_k = \frac{I_k^\perp}{I_k^\parallel}. \quad (2.69)$$

For vibrations that transform as the totally symmetric irreducible representation of the molecular point group, it can be lower than 0.75, but it is 0.75 in all other cases.

Analogous to IR spectra, these expressions can be used to estimate Raman spectra by static quantum chemical calculations within the harmonic approximation. They just require the calculation of the polarizability derivatives along the normal coordinates.

References

1. E. Schrödinger, *Phys. Rev.* **28**, 1049–1070 (1926)
2. I. Levine, *Quantum Chemistry* (Pearson Prentice Hall, Upper Saddle River, 2009)
3. A. Szabo, N. Ostlund, *Modern Quantum Chemistry: Introduction to Advanced Electronic Structure Theory*, Dover Books on Chemistry Series (Dover Publications, Mineola, 1996)
4. F. Jensen, *Introduction to Computational Chemistry* (Wiley, Chichester, 2006)
5. D. Marx, J. Hutter, *Ab Initio Molecular Dynamics: Basic Theory and Advanced Methods* (Cambridge University Press, Cambridge, 2009)
6. M. Born, R. Oppenheimer, *Ann. Phys.* **389**, 457–484 (1927)
7. P. Hohenberg, W. Kohn, *Phys. Rev.* **136**, B864–B871 (1964)
8. W. Kohn, L.J. Sham, *Phys. Rev.* **140**, A1133–A1138 (1965)
9. F. Bloch, *Z. Phys.* **57**, 545–555 (1929)
10. P.A.M. Dirac, *Math. Proc. Camb.* **26**, 376–385 (1930)
11. S.H. Vosko, L. Wilk, M. Nusair, *Can. J. Phys.* **58**, 1200–1211 (1980)
12. J.C. Slater, *Phys. Rev.* **81**, 385–390 (1951)
13. A.D. Becke, *Phys. Rev. A* **38**, 3098–3100 (1988)
14. C. Lee, W. Yang, R.G. Parr, *Phys. Rev. B* **37**, 785–789 (1988)
15. J.P. Perdew, J.A. Chevary, S.H. Vosko, K.A. Jackson, M.R. Pederson, D.J. Singh, C. Fiolhais, *Phys. Rev. B* **46**, 6671–6687 (1992)
16. J.P. Perdew, K. Burke, M. Ernzerhof, *Phys. Rev. Lett.* **77**, 3865–3868 (1996)
17. J. Tao, J.P. Perdew, V.N. Staroverov, G.E. Scuseria, *Phys. Rev. Lett.* **91**, 146401 (2003)
18. A.D. Becke, *J. Chem. Phys.* **98**, 5648–5652 (1993)
19. P.J. Stephens, F.J. Devlin, C.F. Chabalowski, M.J. Frisch, *J. Phys. Chem.* **98**, 11623–11627 (1994)
20. C. Adamo, V. Barone, *J. Chem. Phys.* **110**, 6158–6170 (1999)
21. V.N. Staroverov, G.E. Scuseria, J. Tao, J.P. Perdew, *J. Chem. Phys.* **119**, 12129–12137 (2003)
22. D.C. Langreth, M. Dion, H. Rydberg, E. Schröder, P. Hyldgaard, B.I. Lundqvist, *Int. J. Quantum Chem.* **101**, 599–610 (2005)
23. T. Sato, T. Tsuneda, K. Hirao, *Mol. Phys.* **103**, 1151–1164 (2005)
24. O.A. von Lilienfeld, I. Tavernelli, U. Rothlisberger, D. Sebastiani, *Phys. Rev. Lett.* **93**, 153004 (2004)
25. Y.Y. Sun, Y.-H. Kim, K. Lee, S.B. Zhang, *J. Chem. Phys.* **129**, 154102 (2008)
26. S. Grimme, *J. Comput. Chem.* **27**, 1787–1799 (2006)
27. S. Grimme, J. Antony, S. Ehrlich, H. Krieg, *J. Chem. Phys.* **132**, 154104 (2010)
28. S. Grimme, S. Ehrlich, L. Goerigk, *J. Comput. Chem.* **32**, 1456–1465 (2011)
29. P. Pulay, *Mol. Phys.* **17**, 197–204 (1969)

30. G. Lippert, M. Parrinello, J. Hutter, *Mol. Phys.* **92**, 477–488 (1997)
31. J. VandeVondele, M. Krack, F. Mohamed, M. Parrinello, T. Chassaing, J. Hutter, *Comput. Phys. Commun.* **167**, 103–128 (2005)
32. J. Hutter, M. Iannuzzi, F. Schiffmann, J. VandeVondele, *WIREs Comput. Mol. Sci.* **4**, 15–25 (2014)
33. S. Goedecker, M. Teter, J. Hutter, *Phys. Rev. B* **54**, 1703–1710 (1996)
34. C. Hartwigsen, S. Goedecker, J. Hutter, *Phys. Rev. B* **58**, 3641–3662 (1998)
35. M. Krack, *Theor. Chem. Acc.* **114**, 145–152 (2005)
36. J. VandeVondele, J. Hutter, *J. Chem. Phys.* **118**, 4365–4369 (2003)
37. P. Pulay, *J. Comput. Chem.* **3**, 556–560 (1982)
38. L. Verlet, *Phys. Rev.* **159**, 98–103 (1967)
39. W.C. Swope, H.C. Andersen, P.H. Berens, K.R. Wilson, *J. Chem. Phys.* **76**, 637–649 (1982)
40. S. Nosé, *J. Chem. Phys.* **81**, 511–519 (1984)
41. S. Nosé, *Mol. Phys.* **52**, 255–268 (1984)
42. W.G. Hoover, *Phys. Rev. A* **31**, 1695–1697 (1985)
43. G.J. Martyna, M.L. Klein, M. Tuckerman, *J. Chem. Phys.* **97**, 2635–2643 (1992)
44. G.J. Martyna, M.E. Tuckerman, D.J. Tobias, M.L. Klein, *Mol. Phys.* **87**, 1117–1157 (1996)
45. H. Yoshida, *Phys. Lett. A* **150**, 262–268 (1990)
46. M. Suzuki, *J. Math. Phys.* **32**, 400–407 (1991)
47. J. Neugebauer, M. Reiher, C. Kind, B.A. Hess, *J. Comput. Chem.* **23**, 895–910 (2002)
48. P.A.M. Dirac, *Proc. R. Soc. Lond. Ser. A* **114**, 243–265 (1927)
49. J. Orear, E. Fermi, *Nuclear Physics: A Course Given by Enrico Fermi at the University of Chicago, of Midway reprint*, University of Chicago Press (1950)
50. C. Herrmann, M. Reiher, in *Atomistic Approaches in Modern Biology*, ed. by M. Reiher. *Topics in Current Chemistry*, vol. 268 (Springer, Heidelberg, 2007), pp. 85–132
51. P.J. Stephens, *J. Phys. Chem.* **89**, 748–752 (1985)
52. P.J. Stephens, *J. Phys. Chem.* **91**, 1712–1715 (1987)
53. J. Cheeseman, M. Frisch, F. Devlin, P. Stephens, *Chem. Phys. Lett.* **252**, 211–220 (1996)
54. V.P. Nicu, J. Neugebauer, S.K. Wolff, E.J. Baerends, *Theor. Chem. Acc.* **119**, 245–263 (2008)
55. L.A. Nafie, T.B. Freedman, *J. Chem. Phys.* **78**, 7108–7116 (1983)
56. L.A. Nafie, *J. Chem. Phys.* **79**, 4950–4957 (1983)
57. A. Buckingham, P. Fowler, P. Galwas, *Chem. Phys.* **112**, 1–14 (1987)
58. L.A. Nafie, *J. Chem. Phys.* **96**, 5687–5702 (1992)
59. L.A. Nafie, *J. Phys. Chem. A* **108**, 7222–7231 (2004)
60. A. Scherrer, R. Vuilleumier, D. Sebastiani, *J. Chem. Theory Comput.* **9**, 5305–5312 (2013)
61. A. Scherrer, F. Agostini, D. Sebastiani, E.K.U. Gross, R. Vuilleumier, *J. Chem. Phys.* **143**, 074106 (2015)
62. C. Raman, *Indian J. Phys.* **2**, 387–398 (1928)
63. A. Smekal, *Naturwissenschaften* **11**, 873–875 (1923)
64. G. Placzek, *Z. Phys.* **70**, 84–103 (1931)

Chapter 3

Methodological Developments

3.1 The TRAVIS Program Package

The most important output of an MD simulation (see Sect. 2.3) is a trajectory that contains the coordinates of all atoms in each simulation step. When there are M atoms, this is a path through the $3M$ -dimensional configuration space of the system. Since this high-dimensional object is not directly accessible for interpretation and extraction of chemical characteristics, methods to reduce the dimensionality need to be applied. These can be simple structural analyses such as, e.g., radial pair distribution functions, or more involved dynamical analyses such as, e.g., dimer lifetime distribution functions.

From the wide variety of trajectory analyses, some common ones are integrated in publicly available simulation software packages. In more specific cases however, research groups often create their own private tools. To provide a more convenient approach, the development of the TRAVIS (*T*rajectory *A*nalyzer and *V*isualizer) program package was initiated in the research group of Prof. Dr. Barbara Kirchner in 2009. The aim of TRAVIS is to collect a large range of analyses and to support many different trajectory file formats, providing a stand-alone program package for the analysis of results from the most popular simulation software packages. The analyses are presented through an interactive user interface in a text-mode terminal asking questions about all necessary parameters and suggesting reasonable default values in most cases. TRAVIS is written in the C++ programming language and it is released as open-source software under the GNU General Public License. To make it easily portable to a wide range of operating systems, external software is either directly incorporated in the source code or can optionally be linked only for better performance. The latest version is currently available from the website <http://www.travis-analyzer.de>. A general documentation of TRAVIS can be found in a scientific article published in 2011 [1] and in the Ph.D. thesis of Dr. Martin Brehm [2].

The topic of this thesis are trajectory analyses to obtain vibrational spectra from MD simulations. In the following sections, methods known from the literature are studied, their general applicability is assessed, and new ideas to extend or improve

these methods are presented. Applications to several example systems are discussed in Chap. 4. All algorithms mentioned in this thesis were implemented in TRAVIS [3–5], turning TRAVIS into a versatile tool for the extraction of vibrational spectra from MD. Furthermore, the new ideas developed in the course of this thesis are available to the scientific community for immediate application.

3.2 Vibrational Frequencies

3.2.1 Power Spectra of Harmonic Oscillators

The first step in the simulation of molecular vibrational spectra by theoretical methods is the calculation of vibrational frequencies. The most basic approach, which is available in most quantum chemistry software packages, relies on static calculations within the harmonic approximation: a geometry optimization is performed to find a minimum of the potential energy surface, and the Hessian matrix at this point is diagonalized to get the force constants of a multidimensional harmonic potential in the neighborhood of the minimum. For a quantum harmonic oscillator of mass m , the force constant k determines the eigenfrequency $\omega_0 = \sqrt{k/m}$ and the energy spacing $\Delta\varepsilon = \hbar\omega_0$ of the eigenstates (see Sect. 2.4.1). Therefore, the band positions in the vibrational spectrum can directly be deduced from the force constants.

A classical harmonic oscillator that is subject to the same harmonic potential performs a vibration with an eigenfrequency ω_0 equal to the quantum eigenfrequency (see Sect. 2.4.1). This means that the model of a classical harmonic oscillator can be used to find the spectrum of a quantum harmonic oscillator, suggesting the following alternative procedure for the estimation of vibrational frequencies: instead of a geometry optimization and the calculation of the Hessian matrix, an MD simulation is performed for a certain time, and the oscillation frequencies are extracted from the resulting trajectory by a Fourier transform. The spectrum provided by the Fourier transform is equal to the quantum vibrational spectrum in the case of harmonic oscillators.

The MD approach bears the advantage that it does not require a geometry optimization. Such a geometry optimization always restricts the analysis to a single conformational isomer. For a single molecule in gas phase, this is often not a major problem, as a limited number of conformers can be studied by static calculations one after another and the spectra can be averaged properly. In the liquid phase, however, the potential energy surface is usually quite flat along the coordinates of the intermolecular orientation, featuring a huge number of indistinct minima with low barriers. In this case, it is hard to reach convergence of a geometry optimization, and a comprehensive search for all minima is not feasible. An MD simulation, on the other hand, can easily sample the accessible conformational space, and inherently provides properly averaged spectra.

Although the MD approach seems to be straightforward, it has to be stressed that the absorption spectrum of a quantum oscillator and the frequency of a classical oscillator are actually completely different physical phenomena. The equality of the eigenfrequencies of the classical and the quantum harmonic oscillator is a fortunate coincidence of classical and quantum physics. MD simulations are not able to describe, e.g., rotational spectra: The energy eigenvalues of a quantum mechanical linear rigid rotor with the moment of inertia I are $\varepsilon_J = J(J+1)\hbar^2/(2I)$, so the energy spacing of two adjacent eigenstates is $\Delta\varepsilon_J = \varepsilon_{J+1} - \varepsilon_J = (J+1)\hbar^2/I$, and the spectrum has an infinite number of bands with equal distances of \hbar^2/I . The classical linear rigid rotor, however, is not constrained to any particular angular velocity. Its rotational frequency is proportional to the square root of its energy, but the latter can take an arbitrary value. This means that the Fourier transform of a classical trajectory provides a spectrum with a single peak at an arbitrary position in the NVE ensemble and a continuous spectrum in the NVT ensemble. The crucial difference between the linear rigid rotor and the harmonic oscillator is that the vibrational frequency of the latter does not depend on the energy, but only its amplitude is determined by the energy.

For a more detailed mathematical insight, a one-dimensional classical harmonic oscillator with the coordinate x and the eigenfrequency ω_0 is considered in the following. Its trajectory is given by (see Sect. 2.4.1)

$$x(t) = x_0 \cos(\omega_0 t + \varphi), \quad (3.1)$$

where x_0 is the amplitude and φ is the phase. The amplitude is related to the energy (see below), but the phase is solely determined by the initial conditions of the MD simulation and is not connected to the eigenfrequency. It is therefore desirable to remove the phase information, as this also turns the trajectory into an even function and makes the Fourier transform real-valued. For this purpose, the autocorrelation function is calculated. In general, the autocorrelation of a time-dependent quantity $A(\tau)$ is the expected value over τ of the product $A^*(\tau)A(\tau + t)$ as a function of the time difference t . For a periodic function, this is given by

$$R_A(t) = \langle A^*(\tau)A(\tau + t) \rangle_\tau = \lim_{T \rightarrow \infty} \frac{1}{2T} \int_{-T}^T A^*(\tau)A(\tau + t) d\tau. \quad (3.2)$$

This means to take the complex conjugated value of A at a certain time, multiply it by the value of A at time t later, and average over all possible pairs of values with time difference t . For the harmonic oscillator (3.1), the autocorrelation of the coordinate $x(t)$ yields (see Appendix B.1)

$$R_x(t) = \frac{1}{2} x_0^2 \cos(\omega_0 t). \quad (3.3)$$

The cosine function with the frequency ω_0 is retained, but the phase φ is removed. The Fourier transform of this expression can be written as

$$\mathcal{F}(R_x)(\omega) = \int_{-\infty}^{\infty} R_x(t) \exp(-i\omega t) dt = \frac{1}{2} x_0^2 \pi (\delta(\omega - \omega_0) + \delta(\omega + \omega_0)), \quad (3.4)$$

where δ denotes the Dirac delta distribution. This means that the spectrum is real-valued, and it possesses infinitely sharp peaks at $\omega = \omega_0$ and $\omega = -\omega_0$, so the eigenfrequency of the oscillator can directly be read off.

Beside the peak positions, the spectrum also delivers intensity information. Due to the properties of the delta distribution, the total integral of the spectrum is

$$\int_{-\infty}^{\infty} \mathcal{F}(R_x)(\omega) d\omega = \frac{1}{2} x_0^2 \pi \cdot 2 = \pi x_0^2. \quad (3.5)$$

The intensity is proportional to the square of the oscillator amplitude, which is in turn related to the energy of the oscillator. At the maximum elongation $x = x_0$, there is only the potential energy $kx_0^2/2$, and the kinetic energy vanishes. At the equilibrium position $x = 0$, the potential energy is zero, and the kinetic energy is $kx_0^2/2$. On average, the kinetic energy takes half of its maximum value, $\langle E_{\text{kin}} \rangle = kx_0^2/4$. Using the definition of the eigenfrequency ω_0 , the oscillator amplitude is therefore connected to the average kinetic energy by $x_0 = \sqrt{4 \langle E_{\text{kin}} \rangle / m} / \omega_0$, and the integral of the total spectrum is

$$\int_{-\infty}^{\infty} \mathcal{F}(R_x)(\omega) d\omega = \frac{4 \pi \langle E_{\text{kin}} \rangle}{m \omega_0^2}, \quad (3.6)$$

showing that the intensity provides information about the average kinetic energy of the oscillator in the MD simulation. In the microcanonical ensemble, this is the half of the constant total energy. In the canonical ensemble, this average is related to the temperature T by $\langle E_{\text{kin}} \rangle = k_B T / 2$ according to the equipartition theorem. The reason why the integral is expressed in terms of the average kinetic energy is that the latter relation holds also for anharmonic oscillators, while there is usually no simple connection between average potential energy and temperature then.

For a general comparison of MD simulations, it is unsatisfactory that the intensity depends on the intrinsic oscillator properties, namely the mass m and the eigenfrequency ω_0 . This suggests to multiply the spectrum (3.4) by $m\omega^2$, creating the mass-weighted power spectrum

$$P(\omega) = m\omega^2 \mathcal{F}(R_x)(\omega) = \frac{1}{2} \pi m\omega^2 x_0^2 (\delta(\omega - \omega_0) + \delta(\omega + \omega_0)) \quad (3.7)$$

with the total integral

$$\int_{-\infty}^{\infty} P(\omega) d\omega = \pi m\omega_0^2 x_0^2 = 4 \pi \langle E_{\text{kin}} \rangle, \quad (3.8)$$

which only depends on the oscillator energy $E = 2 \langle E_{\text{kin}} \rangle$ in the microcanonical ensemble, or the temperature T in the canonical ensemble.

It should be noted that the power spectrum can also be calculated from the autocorrelation of the velocity $\dot{x}(t) = dx(t)/dt$. As shown in Appendix B.1, this autocorrelation is given by

$$R_{\dot{x}}(t) = \langle \dot{x}^*(\tau) \dot{x}(\tau + t) \rangle_{\tau} = -\frac{d^2}{dt^2} R_x(t). \quad (3.9)$$

Since the Fourier transform of a function's derivative is the Fourier transform of the function multiplied by $i\omega$, the Fourier transform of the velocity autocorrelation yields

$$\mathcal{F}(R_{\dot{x}})(\omega) = -i^2 \omega^2 \mathcal{F}(R_x)(\omega) = \omega^2 \mathcal{F}(R_x)(\omega), \quad (3.10)$$

and the mass-weighted power spectrum can be written as

$$P(\omega) = m \mathcal{F}(R_{\dot{x}})(\omega). \quad (3.11)$$

The concept of the power spectrum as the Fourier transform of the velocity autocorrelation has been known in the literature for a long time [6–9], although the mass-weighting has sometimes been omitted. Further names commonly used are, e.g., velocity spectrum [10] or vibrational density of states [11]. Although the position representation and the velocity representation of the power spectrum are formally equivalent, experience shows that the latter is advantageous for numerical reasons. In practice (see also Sect. 3.2.2), the spectrum obtained from the Fourier transform always contains a certain level of noise, and multiplying the spectrum by ω^2 enhances the noise level at high frequencies. Furthermore, taking the autocorrelation of the velocity clarifies the relation between the total integral of the spectrum and the average kinetic energy of the oscillator.

MD simulations are usually performed in the three-dimensional space, so the atom positions are three-dimensional vectors. In this case, the power spectrum is calculated by applying the vector autocorrelation. For a time-dependent vector $\mathbf{A}(\tau)$, this is the expected value over τ of the scalar product $\mathbf{A}^*(\tau) \cdot \mathbf{A}(\tau + t)$ as a function of the time difference t . Due to the linearity of the integral, this is the sum of the autocorrelations in each coordinate in an orthonormal basis (see Appendix B.1). For a three-dimensional harmonic oscillator

$$\mathbf{x}(t) = \mathbf{x}_0 \cos(\omega_0 t + \varphi), \quad (3.12)$$

this leads to the autocorrelation

$$R_{\mathbf{x}}(t) = \frac{1}{2} \mathbf{x}_0^2 \cos(\omega_0 t). \quad (3.13)$$

As \mathbf{x}_0^2 is the squared value of the amplitude, all derivations from above remain valid, and the power spectrum

$$P(\omega) = m\mathcal{F}(R_{\dot{\mathbf{x}}})(\omega) \quad (3.14)$$

carries the same information as in the one-dimensional case. For each atom in the MD simulation, the power spectrum can be calculated according to Eq. (3.14) using its particular mass m . The total power spectrum of the system is the sum of all atomic power spectra.

Up to this point, a single harmonic oscillator was considered. An atom in a typical molecule, however, is bonded to several other atoms and therefore participates in the motion of several oscillators with different eigenfrequencies. For a one-dimensional coordinate, this can be written as

$$x(t) = \sum_{i=1}^k x_i(t) = \sum_{i=1}^k x_i \cos(\omega_i t + \varphi_i), \quad (3.15)$$

where k is the number of oscillators, and the ω_i are mutually different. If the frequencies ω_i are integer multiples of a base frequency, this expression can also be understood as a Fourier expansion, which allows to describe the trajectory of an anharmonic oscillator. For this case, it has to be investigated later on, how the frequencies ω_i and amplitudes x_i are related to the absorption spectrum of a quantum anharmonic oscillator (see Sect. 3.2.3). At the moment, only the effect of the autocorrelation on the expansion (3.15) shall be studied. Applying the definition of the autocorrelation yields

$$\begin{aligned} R_x(t) &= \lim_{T \rightarrow \infty} \frac{1}{2T} \int_{-T}^T \left(\sum_{i=1}^k x_i \cos(\omega_i \tau + \varphi_i) \right) \left(\sum_{j=1}^k x_j \cos(\omega_j(\tau + t) + \varphi_j) \right) d\tau \\ &= \sum_{i=1}^k \sum_{j=1}^k \lim_{T \rightarrow \infty} \frac{1}{2T} \int_{-T}^T x_i x_j \cos(\omega_i \tau + \varphi_i) \cos(\omega_j(\tau + t) + \varphi_j) d\tau \\ &= \sum_{i=1}^k \sum_{j=1}^k R_{x_i x_j}(t), \end{aligned} \quad (3.16)$$

where the cross-correlations $R_{x_i x_j}(t)$ are introduced. In general, the cross-correlation of two time-dependent quantities $A(\tau)$ and $B(\tau)$ is the expected value over τ of the product $A^*(\tau)B(\tau + t)$ as a function of the time difference t :

$$R_{AB}(t) = \langle A^*(\tau)B(\tau + t) \rangle_\tau = \lim_{T \rightarrow \infty} \frac{1}{2T} \int_{-T}^T A^*(\tau)B(\tau + t) d\tau. \quad (3.17)$$

Evaluating the cross-correlations $R_{x_i x_j}(t)$ of harmonic vibrations (see Appendix B.1) shows that they vanish if $\omega_i \neq \omega_j$. The total autocorrelation

$$R_x(t) = \sum_{i=1}^k R_{x_i x_i}(t) = \sum_{i=1}^k R_{x_i}(t) = \sum_{i=1}^k \frac{1}{2} x_i^2 \cos(\omega_i t) \quad (3.18)$$

is therefore the sum of the autocorrelations in each harmonic component. Since the Fourier transform is a linear operation, also the total power spectrum is the sum of the power spectra of the harmonic components, so it has peaks at all the harmonic frequencies ω_i . The total integral of the power spectrum is proportional to the sum of the oscillator energies. In the canonical ensemble, where the temperature measures the average energy over all oscillators, the total integral is proportional to the temperature times the number of oscillators. The integrals of individual bands can be used to inquire if the simulation is in equilibrium. In this case, each oscillator— or vibrational mode—of the system gives a band of the same intensity.

3.2.2 Power Spectra of Molecular Dynamics Simulations

In the last section, the power spectrum of the harmonic oscillator was studied by using a continuous function as trajectory. In a practical MD simulation, however, a discrete timestep Δt is employed and the coordinates are only known at certain points in time. Furthermore, the trajectory is of finite length. In this case, the autocorrelation has to be defined in a different way. If $(A_i)_{i=0}^{N-1}$ are the values of quantity A in the N snapshots of the MD simulation, where i numbers the step, the value of the autocorrelation at time $t = n\Delta t$ is given by

$$R_A(n\Delta t) = \frac{1}{N-n} \sum_{i=0}^{N-n-1} A_i^* A_{i+n}, \quad \text{with } n = 0, \dots, N-1. \quad (3.19)$$

This means to calculate the product $A_i^* A_{i+n}$ from two snapshots that are n steps apart, and take the average over all possible pairs of this kind in the trajectory.

Since also the autocorrelation is a discrete function now, a discrete Fourier transform has to be applied to obtain the power spectrum. Efficient algorithms for this purpose are available as “fast Fourier transforms” [12], which can also be used to efficiently calculate the autocorrelation (3.19) as shown in Appendix B.2. Employing a discrete Fourier transform has certain implications on the shape of the spectrum. Since it works on a discrete data set of finite length, this effectively means to take the Fourier transform of the underlying periodic function multiplied by a rectangle function. According to the convolution theorem, a multiplication in the time domain is equivalent to a convolution in the frequency domain, so the spectrum of the periodic function is convolved with the Fourier transform of a rectangle function. As the latter is a sinc function, the spectrum shows bands with a certain width and an infinite number of side lobes instead of infinitely sharp peaks. A very common technique to reduce the intensity of the undesired side lobes is the multiplication of the data set by a window function before the application of the Fourier transform. Plenty of

window functions can be found in the literature. By default, TRAVIS uses the Hann function, the discrete values of which are given by

$$W_n = \cos^2 \left(\frac{\pi n}{2(N-1)} \right), \quad (3.20)$$

but exponential and Gaussian functions are also available in TRAVIS. Since the total integral of the discrete Fourier transform of a data set $(A_i)_{i=0}^{N-1}$ only depends on the first value A_0 (see Appendix B.2), the multiplication by a window function does not influence the integral as long as $W_0 = 1$ is fulfilled. Thus, the peak shapes in the power spectrum are altered, but the integral band intensities are not influenced by the windowing procedure.

Two other techniques common in connection with discrete Fourier transforms are data mirroring and zero padding. In general, the continuous Fourier transform of an even function such as the autocorrelation is purely real, but this is not necessarily fulfilled in the discrete case. However, also the discrete Fourier transform can be guaranteed to be real-valued by data mirroring. This means to append the data set in reverse order to the original data set and apply the discrete Fourier transform to this new data set. Again, this procedure does not influence the integral of the spectrum, but as the number of data points is doubled, it also doubles the resolution of the spectrum. This resolution can be increased even further by zero padding, meaning to insert an arbitrary number of zeros between the original data set and its mirror image. This does not change anything in the spectrum, but it leads to a finer frequency mesh with a spacing that is generally given by $\Delta\omega = 2\pi/(N'\Delta t)$, where N' is the total number of data points after mirroring and zero padding. In this context, it should also be noted that the highest observable frequency is always restricted by the timestep to $\omega_{\max} = \pi/\Delta t$ according to the Nyquist–Shannon sampling theorem [13].

The discrete autocorrelation (3.19) is only an approximation to the continuous autocorrelation function (3.2). For the discretized harmonic oscillator trajectory

$$A_i = x_0 \cos(i\omega_0\Delta t + \varphi), \quad (3.21)$$

it can be shown (see Appendix B.2) that the discrete autocorrelation is

$$R_A(n\Delta t) = \frac{1}{2}x_0^2 \cos(n\omega_0\Delta t) + \frac{x_0^2 \cos((N-1)\omega_0\Delta t + 2\varphi)}{2(N-n) \sin(\omega_0\Delta t)} \sin((N-n)\omega_0\Delta t). \quad (3.22)$$

Beside the first term known from the continuous case (see Eq. (3.3)), it contains an error term with a complicated dependence on the trajectory length N , the timestep Δt , and the phase φ . The essential features for a qualitative discussion are the proportionality to $1/(N-n)$ and $1/\sin(\omega_0\Delta t)$, so $N-n$ and $\sin(\omega_0\Delta t)$ should be large to minimize the error. For the former, this can be achieved in two ways: As N is the number of steps in the trajectory, the MD simulation should be as long as possible. Moreover, since n numbers the discrete points of the autocorrelation, only its first part

up to a certain correlation depth n_{\max} should be considered for the Fourier transform and everything else should be cut. However, although the resolution of the power spectrum can arbitrarily be increased by zero padding, this correlation depth is the only parameter that determines the width of the bands, and thus, how well vibrations with similar frequency can be separated, so it has to be chosen carefully. The dependence on $\sin(\omega_0 \Delta t)$ effectively means that the spectrum is distorted for very low frequencies and for frequencies close to the limit given by the Nyquist–Shannon theorem. Therefore, a long trajectory is needed to accurately detect low frequencies and the timestep should always be chosen in such a way that also the highest frequencies of the system are reasonably sampled. Also the cross-correlations introduced in Eq. (3.16) for a linear combination of harmonic oscillators do not exactly vanish in the discrete case (see Appendix B.2), but with two frequencies ω_A and ω_B , they are proportional to $1/(N-n)$ and to $1/((\cos((\omega_B - \omega_A)\Delta t) - 1)(\cos((\omega_B + \omega_A)\Delta t) - 1))$. Similar conclusions as for the autocorrelation also hold for these expressions.

To calculate the power spectrum in the preferable velocity representation, the atoms' velocities are needed. Although software packages usually allow to output the velocities during the simulation, they can also be obtained by approximate derivation of the atoms' positions from the trajectory afterwards. Choosing the second-order central finite difference

$$\mathbf{V}_A(i\Delta t) = \frac{\mathbf{R}_A((i+1)\Delta t) - \mathbf{R}_A((i-1)\Delta t)}{2\Delta t} \quad (3.23)$$

provides even the exact velocities if the velocity Verlet algorithm has been used to perform the MD (this can be shown by inserting Eqs. (2.40) and (2.41) into Eq. (3.23)).

3.2.3 Comparison of Classical Oscillators and Quantum Oscillators

In Sect. 3.2.1, it was shown that power spectra from trajectories of classical harmonic oscillators can be used to find the eigenfrequencies of the corresponding quantum harmonic oscillators. It was also discussed that the approach is easily extended to find the frequencies of anharmonic oscillators performing a linear combination of harmonic vibrations in the sense of a Fourier expansion as in Eq. (3.15). However, it remains to be clarified how the power spectrum is related to the absorption spectrum of the quantum system in this case. To this end, the power spectra of classical dynamics and the quantum spectra are investigated for several one-dimensional and two-dimensional potentials. The discussion does not aim to systematically deal with all possible kinds of potentials, but several examples are selected to demonstrate the facts important for the comparison to experimental data later on.

For a harmonic potential, analytical solutions of the corresponding differential equations are available (see Sect. 2.4.1), but numerical solutions have to be found in the general case. For this purpose, two specialized programs were implemented

in the course of this thesis. The first one is able to perform MD in arbitrary one-dimensional and two-dimensional potentials. It relies on the velocity Verlet algorithm to integrate the equations of motion, and it provides a Nosé–Hoover thermostat chain to carry out NVT simulations (see Sect. 2.3). The second program is able to solve the time-independent nuclear Schrödinger equation (2.9) for arbitrary one-dimensional and two-dimensional potentials. It relies on the method of imaginary time propagation (see Appendix C for an explanation), and it provides the energy eigenvalues ε_i with the corresponding eigenfunctions $|\chi_i\rangle$. Power spectra of the MD simulations are obtained as described in the last section with an exponential window function. As the Fourier transform of an exponential function is a Lorentzian function, this yields spectra with Lorentzian bands. To get the quantum absorption spectra, the transition moments $\langle\chi_j|x|\chi_i\rangle$ (and $\langle\chi_j|y|\chi_i\rangle$ in the two-dimensional case) are calculated by numerical integration, and Lorentzian functions with areas equal to the squared transition moments are placed at the transition frequencies in the spectra. The squared transition moment of a harmonic oscillator with an eigenfrequency ω_0 for the transition from the ground state to the first excited state is given by (see Appendix B.3)

$$|\langle\chi_1|x|\chi_0\rangle|^2 = \frac{\hbar}{2m\omega_0}. \quad (3.24)$$

The integral of the power spectrum for the corresponding classical harmonic oscillator is $4\pi\langle E_{\text{kin}}\rangle$ (see Sect. 3.2.1). Thus, a dimensionless spectrum $S(\omega)$ for easy comparison is obtained by dividing the power spectrum by $4\pi\langle E_{\text{kin}}\rangle$ (or $2\pi k_B\langle T\rangle$) and the quantum transition moments by $\hbar/(2m\omega)$. As it is very common to plot experimental vibrational spectra as a function of the wavenumber $\tilde{\nu} = \omega/(2\pi c)$, where c is the speed of light in vacuum, this quantity is used instead of the frequency ω in all figures. The oscillator mass is set to $m = 1.661 \cdot 10^{-27}$ kg (equal to 1 u), and all MD simulations are run for 100 ps. The correlation depth for the power spectra is always chosen as 8.192 ps (so the number of data points is a power of two, making “fast Fourier transform” algorithms more efficient), and the decay of the exponential window function is selected to produce a Lorentzian band with a full width at half maximum (FWHM) of 15 cm^{-1} . The same FWHM is used to broaden the quantum spectra.

The first system to be considered is a one-dimensional harmonic oscillator. For the quantum case, this essentially tests the correctness of the implementation as the analytical solution is known. If the force constant k in Eq. (2.48) is chosen to give a target wavenumber of $\tilde{\nu}_t = 1000\text{ cm}^{-1}$, the eigenfunctions shown in Fig. 3.1 are obtained. These coincide with the analytical expression (2.52). Calculating the transition matrix elements confirms the strict selection rule $\Delta n = \pm 1$, so dipole transitions are only allowed between adjacent eigenstates in the harmonic oscillator. For that reason, the spectrum possesses a single peak at 1000 cm^{-1} with an integral intensity of 1 due to the abovementioned normalization.

Also for the classical case, the analytical solution is known, so this allows to investigate the influence of the discrete timestep in the integration of the equations of motion. The results for two different target wavenumbers $\tilde{\nu}_t$ of 1000 and 3000 cm^{-1}

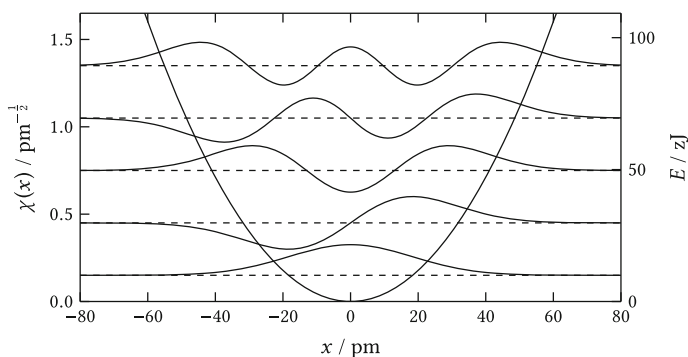


Fig. 3.1 Five lowest energy eigenvalues and eigenfunctions of a harmonic oscillator with a target wavenumber of $\tilde{\nu}_t = 1000 \text{ cm}^{-1}$. For convenience, the eigenfunctions are shifted to match the energy levels

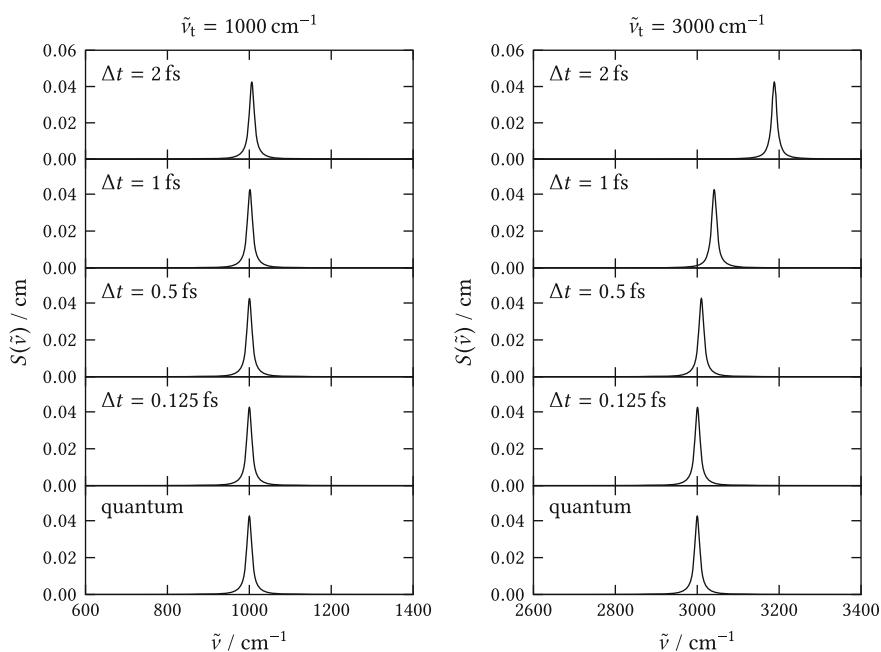


Fig. 3.2 Power spectra of harmonic oscillators with two different target wavenumbers $\tilde{\nu}_t$, applying four different timesteps Δt ; comparison to the spectra of the corresponding quantum oscillators

are presented in Fig. 3.2. Four different timesteps Δt of 2, 1, 0.5, and 0.125 fs were applied, and all simulations were run with a constant energy chosen to give an average temperature of 400 K. The spectra clearly demonstrate that the timestep influences the observed vibrational frequencies. If it is too large, the vibrations are significantly blue-shifted. The effect also depends on the underlying exact frequency. With the same timestep, smaller frequencies are shifted less. This means that the timestep of an MD simulation cannot be chosen just on the basis of the Nyquist–Shannon theorem, which would require $\Delta t < 5.6$ fs for the 3000 cm^{-1} oscillator, but the error in the velocity Verlet method makes much smaller timesteps necessary to accurately reproduce vibrational frequencies. A common choice for AIMD simulations, which was used for all systems presented in Chap. 4, is a timestep of 0.5 fs. This is a reasonable compromise between accuracy and computational resources needed for a proper trajectory length. For the 1000 cm^{-1} oscillator, the error in the wavenumber is less than 1 cm^{-1} . However, it has to be kept in mind that the blueshift already amounts to ca. 10 cm^{-1} for the 3000 cm^{-1} oscillator, which is a wavenumber typical for CH stretching vibrations. A timestep of 0.5 fs is also used for all further examples in this section.

It should be noted that the influence on the frequency can be expressed quantitatively. As shown in Appendix B.4, the Verlet integration of the equations of motion for a harmonic oscillator with the target frequency ω_t yields a harmonic vibration with the frequency

$$\omega_v = \frac{1}{\Delta t} \arccos \left(1 - \frac{1}{2} \omega_t^2 \Delta t^2 \right) \quad (3.25)$$

as long as the condition $\omega_t \Delta t < 2$ is fulfilled. With even larger timesteps, the algorithm usually diverges. The Verlet integration also modifies the amplitude of the vibration, but this effect is canceled in the spectra here due to the normalization by the average kinetic energy.

The next system to be considered is the one-dimensional Morse potential. The Morse potential is a model for the potential energy curve of a diatomic molecule along the coordinate of the interatomic distance. It is given by

$$V(x) = D(1 - \exp(-ax))^2 \quad (3.26)$$

with the dissociation energy D and the width parameter a . For large values of x , this function converges to D , so the reachable coordinate is not limited and the molecule can dissociate if the energy is sufficient. For the investigation here, a dissociation energy of $D = 99.6\text{ zJ}$ (corresponding to 60 kJ/mol) was chosen. Compared to typical intramolecular bonds, this value is quite low, but it is suitable to highlight the anharmonicity effects. Furthermore, the oscillator should have a target wavenumber of $\tilde{\nu}_t = 1000\text{ cm}^{-1}$ within the harmonic approximation to the potential. Since the second derivative of the Morse potential at the equilibrium position is $V''(0) = 2Da^2$, this request leads to a width parameter of $a = 0.0172\text{ pm}^{-1}$. The five lowest energy eigenvalues with the corresponding eigenfunctions for this parameter choice are shown in Fig. 3.3. In contrast to the harmonic potential, the eigenstates are not equally

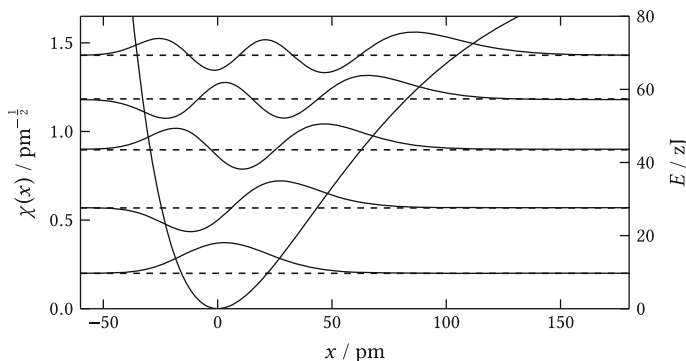


Fig. 3.3 Five lowest energy eigenvalues and eigenfunctions in a Morse potential with a harmonic target wavenumber of $\tilde{\nu}_t = 1000 \text{ cm}^{-1}$. For convenience, the eigenfunctions are shifted to match the energy levels

spaced in energy, but the distance decreases at higher quantum numbers. Also the selection rule $\Delta n = \pm 1$ is not strictly valid anymore, as the transition moments between nonadjacent states do not vanish. This has several consequences for the spectrum: The transitions from the ground state $n = 0$ to higher excited states $n = 2, 3, \dots$ appear as overtones. Moreover, transitions from excited states that are thermally populated at finite temperature to higher excited states show up as hot bands. Such hot bands are also present in the quantum spectrum of the harmonic oscillator, but they are not distinguishable from the fundamental band due to the equal spacing of all eigenstates in this case.

The quantum absorption spectrum of the Morse oscillator at 0 K (so without any hot bands) is shown at the bottom of Fig. 3.4. Due to the anharmonicity, the fundamental transition is shifted from the harmonic target wavenumber down to 900 cm^{-1} . The first overtone is visible as a small peak at 1701 cm^{-1} , and the second overtone shows up with very low intensity at 2402 cm^{-1} . The higher overtones are located beyond 3000 cm^{-1} . At finite temperature, the most intense hot band would appear at 801 cm^{-1} for the transition from $n = 1$ to $n = 2$.

Classical MD simulations for the Morse potential were performed in the microcanonical ensemble with four different energies of 0.1, 10.0, 18.9, and 50.0 zJ. The resulting power spectra are shown in Fig. 3.4 together with the average temperatures (proportional to the average kinetic energies) that correspond to these energies. Since the potential is not a purely quadratic function of the coordinate, the average kinetic energy is not exactly the half of the total energy anymore, and even the ratio is not a constant, but it depends on the total energy itself.

The most important finding is the dependence of the peak positions on the total energy. With increasing energy, the bands are shifted to lower wavenumbers. This is a consequence of the fact that the classical MD samples only a certain part of the potential curve. If the energy is low, the amplitude of the oscillations is very small, so the classical particle only experiences the potential in the vicinity of the minimum. Since this can be approximated by a harmonic potential very well, the fundamental

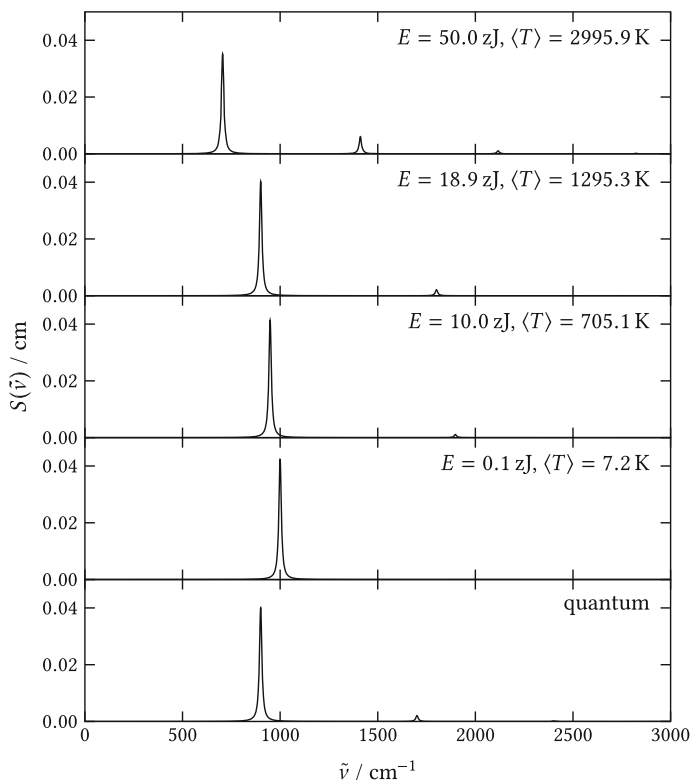


Fig. 3.4 Power spectra of an oscillator in a Morse potential with a harmonic target wavenumber of $\tilde{\nu}_t = 1000 \text{ cm}^{-1}$ at four different total energies E ; comparison to the spectrum of the corresponding quantum oscillator

transition appears at the harmonic target wavenumber of 1000 cm^{-1} with $E = 0.1 \text{ zJ}$ (see Fig. 3.4). If the energy is increased, the trajectory of the classical particle reaches more and more the anharmonic region of the potential curve, leading to a successive redshift of the fundamental band. In the limiting case where the total energy exceeds the dissociation energy D , the particle continuously moves in positive x direction and never returns to the minimum, so the fundamental band effectively arrives at zero wavenumber. An interesting point is the energy, where the band position coincides with the quantum spectrum. This is the case for $E = 18.9 \text{ zJ}$ (see Fig. 3.4). The average temperature connected to this total energy is $\langle T \rangle = 1295.3 \text{ K}$, corresponding to an average kinetic energy of $\langle E_{\text{kin}} \rangle = 8.9 \text{ zJ}$. This value is the half of the transition energy from $n = 0$ to $n = 1$ in the quantum system. However, this is just an accidental coincidence for this special choice of the potential. The next example shows that this is not a strictly valid rule.

Another important finding is the occurrence of overtone bands in the power spectra. Analogous to the shift of the fundamental peak position, their intensity increases

with higher total energies (see Fig. 3.4). If the amplitude is small, a single harmonic frequency is sufficient to describe the particle oscillation. The more the vibration reaches into the anharmonic part of the potential, the higher is the fraction of other frequencies required to represent the motion. As the power spectra are normalized to the average kinetic energy, the total integral is always 1, so the intensity of the fundamental band is reduced to the same degree as the intensity of the overtones rises. The wavenumbers where the overtone peaks are located are always integer multiples of the fundamental wavenumber, so the overtone bands have a constant spacing. This is an important difference to the quantum spectrum, where the spacing of the overtones continuously decreases. The simulation with $E = 18.9$ zJ, which reproduces the fundamental wavenumber of the quantum spectrum, yields the first overtone at 1801 cm^{-1} , so 100 cm^{-1} above the value in the quantum spectrum. Similarly, the second overtone is located at 2702 cm^{-1} , which differs by 300 cm^{-1} from the quantum spectrum. Nevertheless, the intensity ratios of the fundamental transition and the overtones are equal in the power spectrum and the quantum spectrum. This means that classical MD is in principle able to give at least a qualitative insight into the overtone spectrum of a system.

Further important phenomena can be observed in two-dimensional systems. For this purpose, a potential surface of the general form

$$V(x, y) = k_{xx}x^2 + k_{yy}y^2 + k_{xxx}x^3 + k_{xxy}x^2y + k_{xyy}xy^2 + k_{yyy}y^3 + k_{xxxx}x^4 + k_{yyyy}y^4 \quad (3.27)$$

is employed. It contains the harmonic terms $k_{xx}x^2$ and $k_{yy}y^2$, as well as third power terms to introduce anharmonicities. The fourth power terms are added to obtain a bound potential, as they guarantee that the function approaches positive infinity in all directions. Three different parameter sets were applied (see Table 3.1). In the first set, the cross terms $k_{xxy}x^2y$ and $k_{xyy}xy^2$ are zero, so the two coordinates are uncoupled. The remaining parameters were chosen to match the coefficients of Taylor polynomials that approximate Morse potentials with a dissociation energy of $D = 99.6$ zJ and harmonic target wavenumbers $\tilde{\nu}_t$ of 1000 cm^{-1} along the x axis and 1200 cm^{-1} along the y axis. The second set consists of the same parameters, but it adds the coupling factors k_{xxy} and k_{xyy} . Their values do not have a specific background, they were just chosen as 10^{-2} in atomic units, which are employed internally in the program. The third parameter set preserves the coupling of the coordinates, but it changes the

Table 3.1 Three parameter sets applied within the two-dimensional potential in Eq. (3.27)

No.	k_{xx}	k_{yy}	k_{xxx}	k_{xxy}	k_{xyy}	k_{yyy}	k_{xxxx}	k_{yyyy}
	$10^{-2} \text{ zJ pm}^{-2}$		$10^{-4} \text{ zJ pm}^{-3}$			$10^{-6} \text{ zJ pm}^{-4}$		
1	2.946	4.242	-5.066	0	0	-8.753	5.081	10.54
2	2.946	4.242	-5.066	-2.942	2.942	-8.753	5.081	10.54
3	2.946	11.20	-5.066	-2.942	2.942	-37.56	5.081	73.47

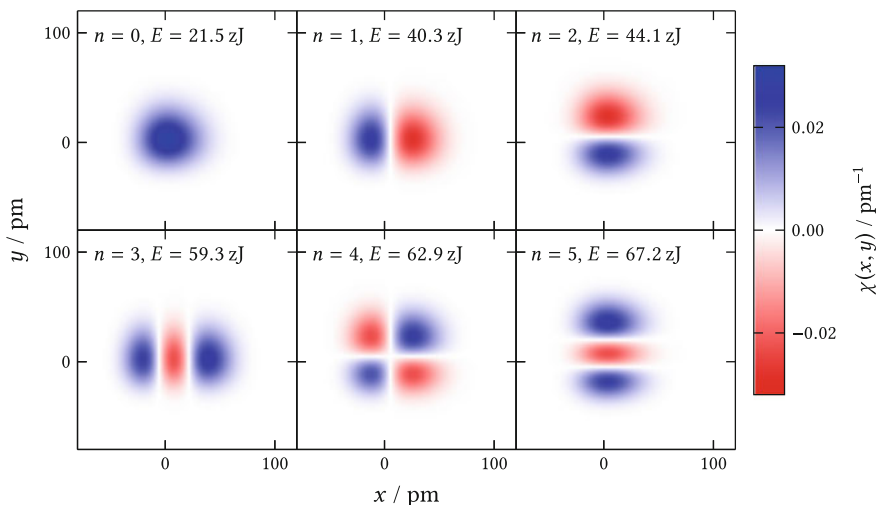


Fig. 3.5 Wave functions and energy eigenvalues of the six lowest eigenstates in the two-dimensional potential (3.27) with parameter set 1 from Table 3.1

harmonic target wavenumber of the underlying Morse potential along the y axis to 1950 cm^{-1} . This value was selected in such a way that the first overtone in the first coordinate coincides with the fundamental transition in the second coordinate.

The six lowest eigenfunctions of a quantum oscillator with parameter set 1 are shown in Fig. 3.5, and the resulting spectrum can be found at the bottom of Fig. 3.6. Due to the absence of coupling terms between the coordinates, this system behaves like two independent one-dimensional oscillators. The two-dimensional wave functions are just the products of the corresponding one-dimensional wave functions (cf. Fig. 3.3). Thus, the first excited two-dimensional state ($n = 1$) corresponds to an excitation in the x coordinate while the second excited two-dimensional state ($n = 2$) arises from an excitation in the y coordinate. Analogously, the subsequent three two-dimensional states can be assigned to a double excitation in the x coordinate ($n = 3$), a simultaneous excitation in both coordinates ($n = 4$), and a double excitation in the y coordinate ($n = 5$), respectively. Considering the spectrum, the transition from $n = 0$ to $n = 4$ is a special case, as it is forbidden by symmetry and has zero intensity, so no band is found at 2082 cm^{-1} . Nevertheless, all the other possible transitions from the ground state show up as in the corresponding one-dimensional cases, and the spectrum of the two-dimensional system is just the sum of the one-dimensional spectra. In particular, the fundamental peaks appear at 947 and 1136 cm^{-1} , respectively, and the first overtones give rise to weak bands at 1901 and 2299 cm^{-1} , respectively.

The power spectra obtained from classical MD simulations are compared to the quantum spectrum in Fig. 3.6. The simulations were performed in the microcanonical ensemble with four different energies of 0.2 , 28.5 , 68.7 , and 150.0 zJ . As for the one-dimensional Morse potential, a dependence of the peak positions on the energy is

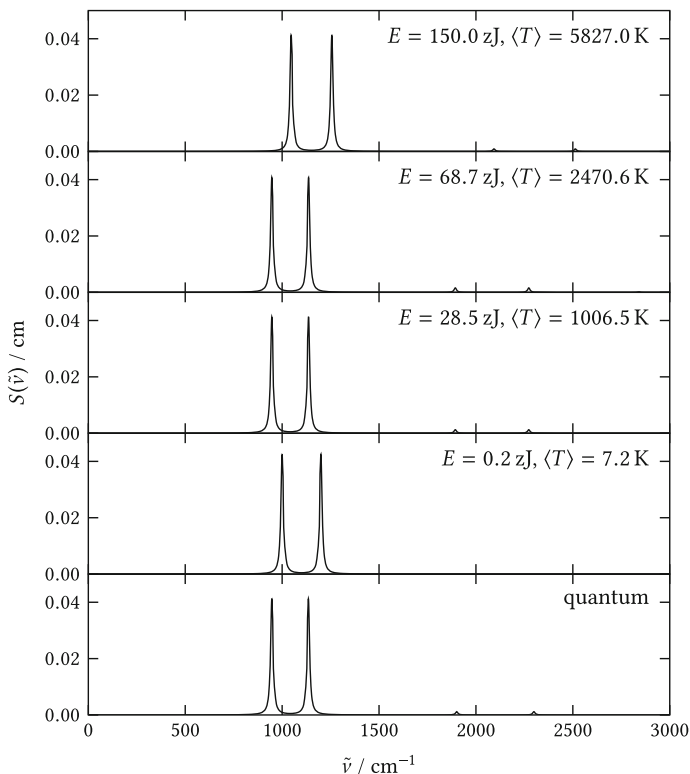


Fig. 3.6 Power spectra of a classical oscillator in the two-dimensional potential (3.27) with parameter set 1 from Table 3.1 at four different total energies E ; comparison to the spectrum of the corresponding quantum oscillator

observed again. This time, however, the bands are not shifted monotonically, but their wavenumbers decrease up to a certain energy while they increase at higher energies. This is a consequence of the potential form: In contrast to the Morse oscillator, which dissociates at high energies, the particle mainly experiences the quartic terms of the potential here. Since these rise more steeply than a harmonic potential, the oscillation wavenumber increases more and more at high energies. With the very low energy of $E = 0.2$ zJ in the MD simulation, the bands show up at the harmonic target wavenumbers of the potential. It is possible to find two energy values where the wavenumber of the first fundamental band at 947 cm^{-1} in the quantum spectrum is exactly reproduced, $E = 28.5$ and $E = 68.7$ zJ. The turning point of the shifting direction is located in between at $E = 47.1$ zJ. One can also find two further energy values where the wavenumber of the second fundamental transition exactly coincides with the quantum system. Since this energy of coincidence is, however, an individual property of each mode, it is impossible to match both bands at the same time. In contrast to the Morse potential, the average kinetic energy at the point of coincidence

is not related to the quantum transition energy in a simple manner here. If the energy is not too low, also the overtones appear in the power spectrum. As seen before, the wavenumbers of the first overtones are always twice as large as the wavenumbers of the corresponding fundamental bands, meaning that they are underestimated by 7 and 27 cm^{-1} compared to the quantum spectrum if the total energy is chosen to reproduce the first fundamental band. This demonstrates that the incomplete description of the quantum anharmonicity by classical dynamics does not generally lead to an overestimation of the overtone wavenumbers as in the case of a Morse potential. The intensity ratios of fundamental and overtone bands are in good agreement with the quantum spectrum if the total energy is $E = 28.5 \text{ zJ}$.

It is important to note that the power spectra actually show a strong dependence on the initial conditions of the MD simulation. Since the two coordinates are not coupled, energy cannot be exchanged between them. For all the spectra shown here, the same energy was put into both coordinates in the beginning. However, it is easily possible to create arbitrary intensity ratios of the two fundamental bands by choosing different initial conditions. As the complete decoupling of all coordinates is a very special case, this is not a major issue with regard to later applications, but it has to be kept in mind that setting up MD simulations requires some attention in this respect.

Parameter set 2 (see Table 3.1) allows to study the effect of coupling the coordinates, as it introduces the cross terms $k_{xy}x^2y$ and $k_{xy}xy^2$. The eigenfunctions of a quantum oscillator in this potential are shown in Fig. 3.7 and the corresponding spectrum considering only transitions from the ground state can be found at the bottom of Fig. 3.8. In contrast to the uncoupled system (see Fig. 3.5), the wave functions are slightly distorted and the nodal lines are not straight anymore. Still, it is possible to

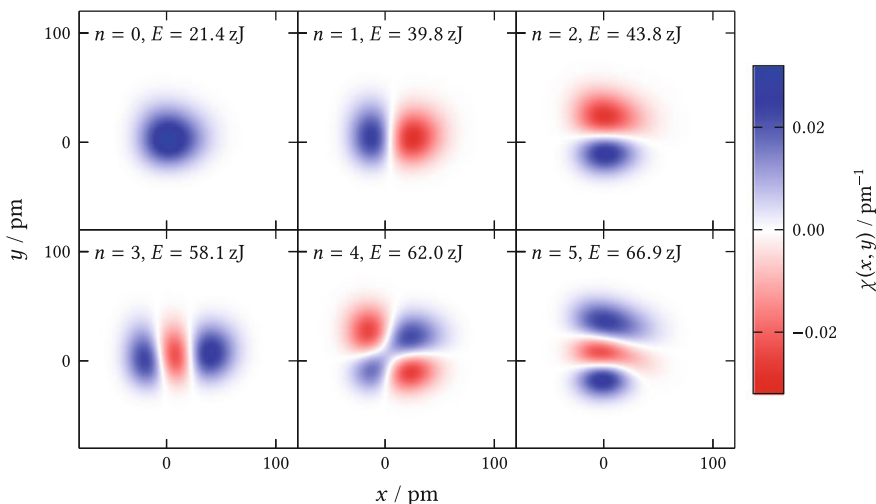


Fig. 3.7 Wave functions and energy eigenvalues of the six lowest eigenstates in the two-dimensional potential (3.27) with parameter set 2 from Table 3.1

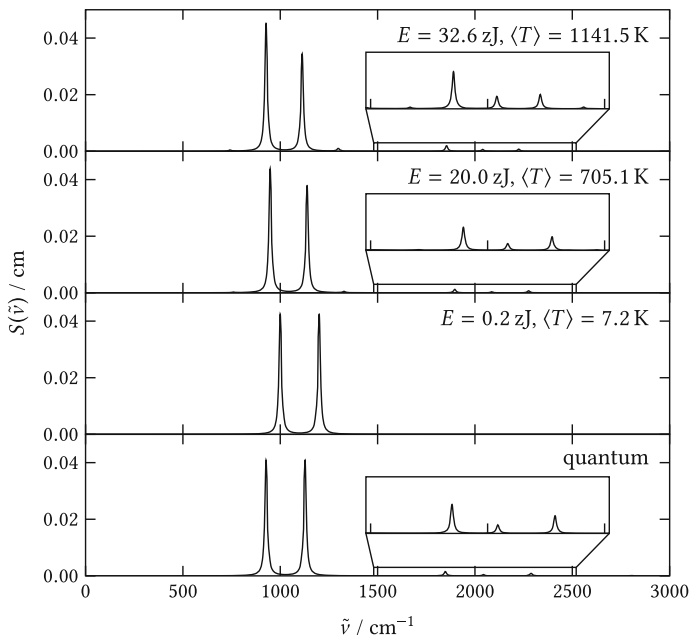


Fig. 3.8 Power spectra of a classical oscillator in the two-dimensional potential (3.27) with parameter set 2 from Table 3.1 at three different total energies E ; comparison to the spectrum of the corresponding quantum oscillator. The insets magnify the region of overtone and combination bands between 1500 and 2500 cm^{-1}

interpret the states as single excitations in each coordinate ($n = 1, n = 2$), double excitations in each coordinate ($n = 3, n = 5$), and a simultaneous excitation in both coordinates ($n = 4$). Of particular importance is the distortion of the $n = 4$ state, as a transition from the ground state to this state is not strictly forbidden anymore. In addition to the fundamental bands (927, 1127 cm^{-1}) and the overtones (1848, 2288 cm^{-1}) known from the uncoupled system, this yields a combination band at 2044 cm^{-1} in the spectrum.

Classical MD simulations with parameter set 2 were performed in the micro-canonical ensemble with energies of 0.2, 20.0, and 32.6 zJ. The resulting power spectra are compared to the quantum spectrum in Fig. 3.8. With the lowest energy, the fundamental bands appear at the harmonic target wavenumbers in the same way as before. Within this parameter set, an energy of $E = 32.6$ zJ exactly reproduces the wavenumber of the first fundamental band in the quantum spectrum. The most important finding is the emergence of several additional peaks at higher energies. Beside the first overtones showing up at the doubled wavenumbers of the fundamental peaks, one can also find a combination band exactly at the sum of the two fundamental wavenumbers. With $E = 32.6$ zJ, it almost matches the combination band in the quantum spectrum, showing a difference of only 4 cm^{-1} . On the other hand, the intensity ratios of the two overtones and the combination band are bet-

ter reproduced with $E = 20.0$ zJ. Again, this indicates that classical power spectra are not fully consistent with the spectrum of the corresponding quantum system. However, they provide a good qualitative insight not only for overtones, but also for combination bands.

It has to be noted that the classical simulations do not only show the desired combination band, but they add several more peaks to the spectrum. The most distinct ones are the satellite peaks of the two fundamental bands, the intensity of which is similar to the real combination band. The distance of these satellite peaks to the fundamental bands is equal to the distance of the fundamental bands, so the four bands are equally spaced. The satellite peaks might be interpreted as higher combination transitions starting from excited states, i.e., double excitations in one coordinate and simultaneous disexcitations in the other coordinate. However, as they are exactly located at the sum of the involved transition wavenumbers, they suffer from the same deviations as normal overtones and combination bands, making an assignment to the finite temperature quantum spectrum very hard. In any case, this interpretation would be inconsistent with the absence of other hot bands, e.g., no such peaks could be observed with parameter set 1 at any energy, so the satellite peaks should be regarded as artifacts.

Another important point is the intensity shifting between the fundamental bands at higher energies. Although the initial conditions were chosen in such a way that both coordinates contain the same energy in all cases, the first fundamental peak becomes more intense than the second one. This indicates that the intensity in power spectra cannot strictly be used to justify whether a simulation is in equilibrium when modes are coupled to each other.

In parameter set 3 (see Table 3.1), the first overtone wavenumber in the x coordinate is near the fundamental wavenumber in the y coordinate. This allows to observe the phenomenon of Fermi resonance. The corresponding eigenfunctions of the quantum oscillator are shown in Fig. 3.9 and the resulting spectrum is given at the bottom of Fig. 3.10. Comparing to the uncoupled system (see Fig. 3.5), the distinct distortion of the wave functions with $n \geq 2$ is obvious. In particular the second excited state ($n = 2$) and the third excited state ($n = 3$) are strongly mixed, and a clear assignment of the single excitation in the y coordinate and the double excitation in the x coordinate is not possible anymore. As a consequence, a transition to both states is equally possible from the ground state by dipole interaction, and the spectrum shows two bands of similar intensity at 1830 and 1898 cm^{-1} instead of a strong peak for the fundamental transition and a weak peak for the overtone.

The power spectra from classical MD simulations within the microcanonical ensemble and with energies of 0.2, 10.0, and 20.0 zJ are compared to the quantum spectrum in Fig. 3.10. Applying parameter set 3, it is impossible to find an energy where the wavenumber of the first fundamental band is exactly reproduced. The wavenumber in the power spectrum at the turning point of the band shifting direction is still higher than in the quantum spectrum. As before, the power spectrum with $E = 0.2$ zJ provides the harmonic target wavenumbers of the potential. The most important finding is, however, that intensity shifts similar to the Fermi resonance also occur in the classical system, so two peaks of similar intensity can be found at the

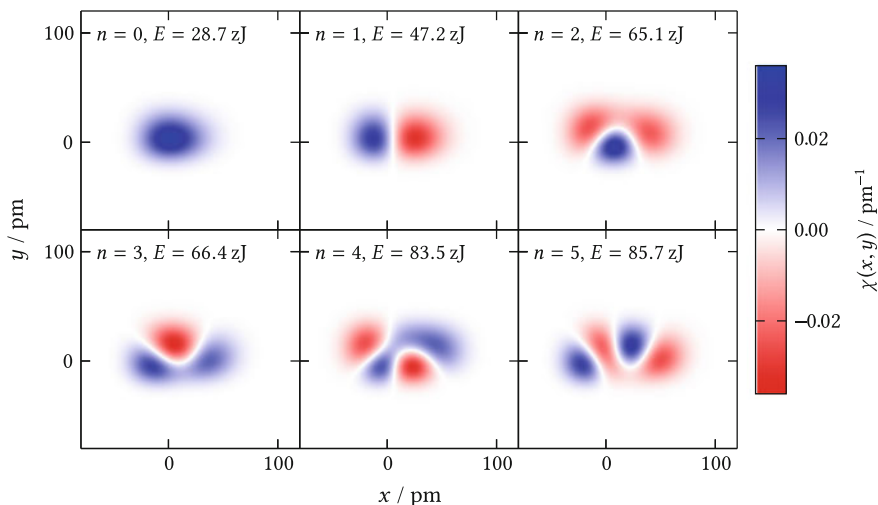


Fig. 3.9 Wave functions and energy eigenvalues of the six lowest eigenstates in the two-dimensional potential (3.27) with parameter set 3 from Table 3.1

position of the second fundamental transition with higher energies. As the intensity ratio of the two bands clearly depends on the energy, classical dynamics provides again not a quantitative estimation of the quantum spectrum, but a qualitative insight even into special effects like Fermi resonance is possible. Similar to parameter set 2, a small side peak at the first fundamental band appears as an artifact. Also the intensity of the first fundamental band increases again, although the initial conditions were still chosen to provide the same energy in both coordinates.

Summarizing the results observed in the five examples selected for this section, the following conclusions can be drawn: In general, MD simulations with classical particles contain a description of anharmonicity effects in qualitative agreement with the corresponding quantum particles. This allows to observe overtones and combination bands in the power spectra, but always at integer multiples or exact sums and differences of the fundamental wavenumbers. The intensity ratios of these bands are usually in good accordance with the quantum system. Even intensity shifts due to Fermi resonance are found in the classical spectra, but this requires matching wavenumbers of a fundamental band and an overtone, and this is usually prevented in later applications by the just mentioned shifts of overtone wavenumbers. The most important issue, however, is the dependence of the effects on the energy (or the temperature) of the simulation. Thus, it is usually impossible to determine quantitatively to which extent anharmonicity effects are included. Nevertheless, a qualitative insight can always be gained as long as the energy (or the temperature) is not too low.

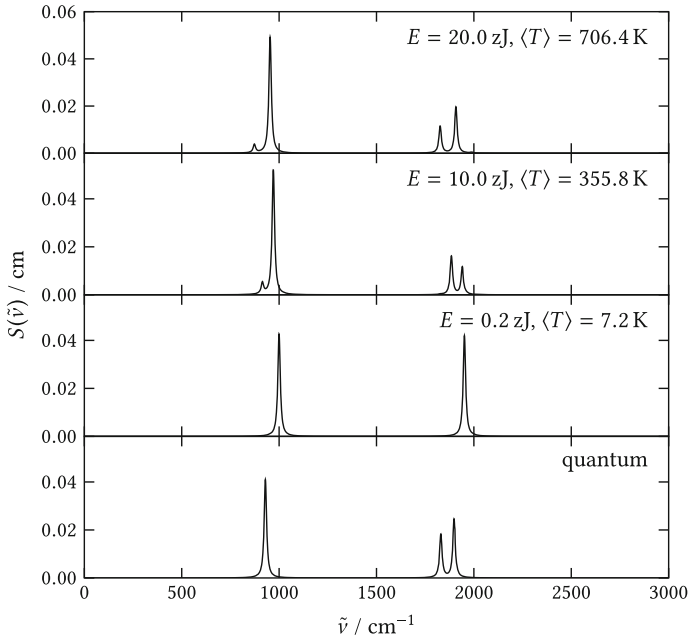


Fig. 3.10 Power spectra of a classical oscillator in the two-dimensional potential (3.27) with parameter set 3 from Table 3.1 at three different total energies E ; comparison to the spectrum of the corresponding quantum oscillator

3.2.4 Influence of a Thermostat

For the comparison of classical oscillators and quantum oscillators in the last section, the MD simulations were performed in the microcanonical ensemble, i.e., with constant energy. A constant energy is, however, difficult to realize experimentally, and measurements are usually carried out at constant temperature. For that reason, it is very common to conduct MD simulations in the canonical ensemble by applying a Nosé–Hoover thermostat chain (see Sect. 2.3). Thus, the question arises how the power spectrum is influenced by the thermostat. To avoid thermostat artifacts in the first place, it has been reported in the literature (see, e.g., references [14–17]) to perform multiple NVE simulations and to average the resulting spectra. The initial conditions for these NVE simulations are drawn from an NVT trajectory with the desired temperature. To compare this approach with a straightforward calculation of the power spectrum from the NVT trajectory, MD simulations were carried out in the model potential (3.27) employing parameter set 2 from Table 3.1. An NVT simulation at $T = 400 \text{ K}$ was conducted for 100 ps with a timestep of $\Delta t = 0.5 \text{ fs}$, applying a Nosé–Hoover thermostat chain of length 3 and a coupling time constant of $\tau = 100 \text{ fs}$. From the resulting 200000 snapshots, a certain number was selected by a uniform random distribution and NVE simulations were started with each of

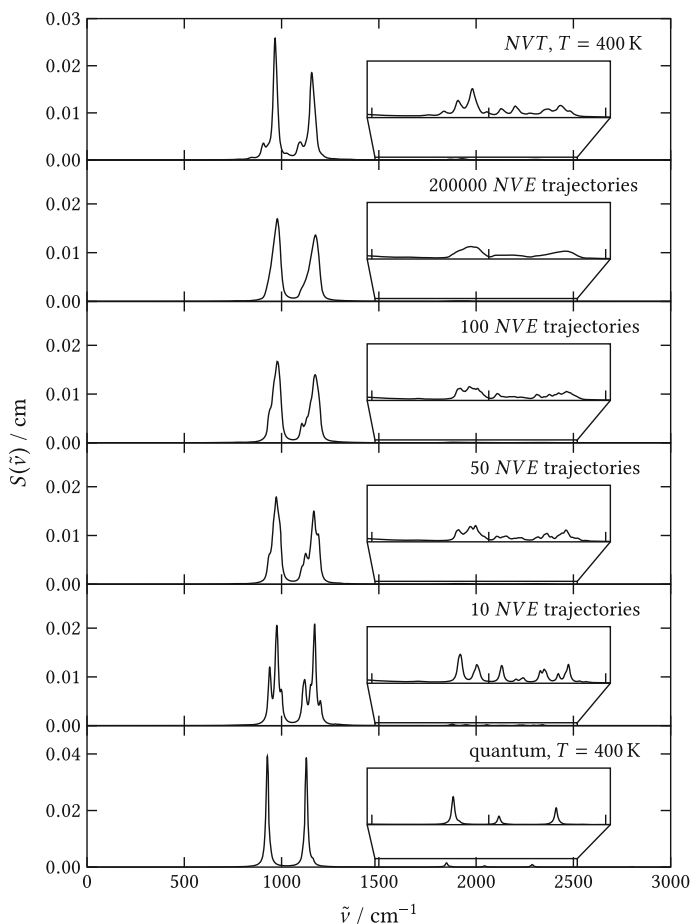


Fig. 3.11 Power spectra of a classical oscillator in the two-dimensional potential (3.27) with parameter set 2 from Table 3.1, employing an *NVT* simulation ($\tau = 100$ fs) at 400 K and different numbers of *NVE* trajectories with initial conditions randomly drawn from the *NVT* simulation; comparison to the spectrum of the corresponding quantum oscillator at 400 K, assuming state populations according to a Boltzmann distribution. The insets magnify the region of overtone and combination bands

them. The power spectra obtained by averaging over the *NVE* trajectories are shown together with the power spectrum from the *NVT* simulation in Fig. 3.11. This figure also contains the spectrum of the quantum system at finite temperature modeled by assuming a population of the states according to a Boltzmann distribution. The quantum spectrum hardly differs from the spectrum at 0 K discussed in Fig. 3.8, the only notable change is the appearance of a hot band as a small shoulder of the second fundamental peak.

It is obvious that the direct *NVT* spectrum and the average over a sufficient number of *NVE* trajectories are not equal. The peaks in the averaged *NVE* spectra are broader, but the *NVT* spectrum shows artificial satellite peaks at all bands. The broad asymmetric bands with a flat edge to low wavenumbers of the *NVE* spectra can be regarded as substituted by stairs of peaks in the *NVT* spectrum. In this way, the overtone region between 1500 and 2500 cm^{-1} can be interpreted to actually consist of three underlying bands, which correspond to the two overtones and the combination band visible in the quantum spectrum. It should be noted that the satellite peaks in the *NVT* spectrum are influenced by the coupling time constant of the thermostat chain. If the latter is reduced, the satellite peaks are shifted further apart from the real bands. The satellite peaks are an undesired drawback of the *NVT* spectrum, but as discussed in the last section, the thermostat is not the only source of artificial bands in a coupled potential. On the other hand, in the order of 100 *NVE* simulations are needed till the average over a set of *NVE* trajectories can be considered as converged. For the application to large bulk phase AIMD simulations, this poses a tremendous increase of the required computational resources. Therefore, the spectra are directly obtained from *NVT* trajectories for all systems in Chap. 4. Due to the finite simulation times and system sizes, the correlation depth has to be chosen smaller than here, so the bands are slightly broadened and the satellite peaks are mostly indistinguishable in the investigated systems. This might also be connected to the fact that a two-dimensional model potential is considered here while the systems in Chap. 4 have many more degrees of freedom. Moreover, the approximations to treat the electronic structure (see Sect. 2.2) and the numerical limitations to converge the forces acting on the nuclei add further artifacts to the spectra. Nevertheless, a more detailed comparison of *NVT* spectra and *NVE* spectra for real systems could be subject of future work.

3.2.5 Normal Coordinates

It was mentioned in Sect. 3.2.1 that the atoms in a molecule usually move according to a linear combination of several harmonic vibrations with different frequencies when they are bonded to other atoms. If all internal degrees of freedom in the molecule follow a harmonic potential, it is possible to find a coordinate transform such that only a single harmonic vibration with a clearly defined frequency is performed in each coordinate. These new coordinates, which are called normal coordinates, do not describe the motion of single atoms, but collective displacements of all atoms in the molecule that do not change the center of mass. The normal coordinates allow to describe the bands observed in experimental spectra as specific molecular vibrations.

In the basic approach of static quantum chemistry, the normal coordinates are inherently available, as this method relies on the harmonic approximation to the potential energy surface. In this case, the normal coordinates are just the coordinate system in which the Hessian matrix is diagonal at the potential minimum. In contrast, the normal coordinates cannot strictly be defined in MD, since the harmonic approximation is not applied and the minima of the potential energy surface do not

enter directly. Nevertheless, it is desirable to find a similar quantity with regard to the interpretation of experimental spectra in the liquid phase. For this purpose, several techniques have been proposed in the literature [11, 18–31]. For this thesis, the generalized normal coordinate scheme of Mathias et al. [14, 15] was adopted and implemented in TRAVIS [4]. The underlying ideas are described in the remainder of this section.

In the three-dimensional space, all atoms of a molecule have three coordinates, and in each coordinate, the power spectrum can be calculated according to the definition (3.11). Summing the three spectra belonging to the same atom gives the atomic power spectrum (3.14). The sum of all these atomic power spectra defines the power spectrum of the molecule. As the atoms are usually involved in several different vibrational modes of the molecule, the atomic power spectra show peaks at several different frequencies and the power spectra of different atoms overlap. These overlaps can be characterized by the mass-weighted cross-correlation spectra

$$\begin{aligned} P_{ij}(\omega) &= \sqrt{m_i m_j} \operatorname{Re} \left(\mathcal{F} (R_{\dot{x}_i \dot{x}_j}) (\omega) \right) \\ &= \sqrt{m_i m_j} \operatorname{Re} \left(\int_{-\infty}^{\infty} \langle \dot{x}_i^*(\tau) \dot{x}_j(\tau + t) \rangle_{\tau} \exp(-i\omega t) dt \right), \end{aligned} \quad (3.28)$$

where i and j subsequently number the coordinates of all atoms, so in a molecule with M atoms, they run from 1 to $3M$. The mass m_i is the mass of the atom corresponding to coordinate i . The real part of the Fourier transform is taken to guarantee that the spectra are real-valued. This corresponds to averaging over the time forward and the time backward trajectory [14]. In the TRAVIS implementation, the same effect is achieved by the mirroring technique described in Sect. 3.2.2.

As the coordinates are real, the cross-correlation spectra (3.28) constitute a symmetric matrix $\mathbf{P}(\omega)$ of functions, the trace of which is the power spectrum of the molecule. If the matrix $\mathbf{P}(\omega)$ was calculated in the normal coordinates of a purely harmonic system, it would be diagonal (all off-diagonal elements would be zero functions) as long as there are no degenerate modes. With an MD trajectory of finite length that contains anharmonicity effects, also the spectral peaks have a finite width and the off-diagonal elements usually do not vanish completely. Still, this suggests to search for a set of coordinates where the off-diagonal elements of $\mathbf{P}(\omega)$ are minimal. The magnitude of the off-diagonal elements is measured by

$$o = \sqrt{\sum_{i=1}^{3M} \sum_{j=i+1}^{3M} \int_{-\infty}^{\infty} (P_{ij}(\omega))^2 d\omega}. \quad (3.29)$$

The new coordinates that minimize this expression are called generalized normal coordinates [14].

If $\mathbf{P}(\omega)$ was a regular matrix, it could simply be diagonalized. But since it depends on the frequency, a modified Jacobi algorithm is used for the minimization. In principle, the Jacobi algorithm finds an orthogonal transformation matrix \mathbf{C} that diago-

nalizes a general matrix \mathbf{A} by $\mathbf{A}' = \mathbf{CAC}^T$. The transformation matrix \mathbf{C} is written as a product of j Givens rotations $\mathbf{G}(k, l, \theta)$:

$$\mathbf{C} = \prod_{i=1}^j \mathbf{G}(k_i, l_i, \theta_i). \quad (3.30)$$

A Givens rotation is defined as

$$\mathbf{G}(k, l, \theta) = \begin{pmatrix} 1 & \cdots & 0 & \cdots & 0 & \cdots & 0 \\ \vdots & \ddots & \vdots & & \vdots & & \vdots \\ 0 & \cdots & \cos \theta & \cdots & \sin \theta & \cdots & 0 \\ \vdots & & \vdots & \ddots & \vdots & & \vdots \\ 0 & \cdots & -\sin \theta & \cdots & \cos \theta & \cdots & 0 \\ \vdots & & \vdots & & \vdots & \ddots & \vdots \\ 0 & \cdots & 0 & \cdots & 0 & \cdots & 1 \end{pmatrix}, \quad (3.31)$$

where $\sin \theta$ and $\cos \theta$ appear in columns and rows k and l . For each rotation, the angle θ is chosen in such a way that the element A_{kl} of the matrix \mathbf{A} is zero after the transformation. The number of rotation matrices j is determined iteratively by applying rotations until all off-diagonal elements of \mathbf{A} are smaller than a certain threshold.

For the spectra matrix $\mathbf{P}(\omega)$, the angle θ cannot generally be chosen in such a way that the off-diagonal spectrum $P_{kl}(\omega)$ vanishes completely. Instead, it is requested that the integral of its square gets minimal, yielding the condition

$$\frac{\partial}{\partial \theta} \left(\int_{-\infty}^{\infty} (\mathbf{G}(k, l, \theta) \mathbf{P}(\omega) \mathbf{G}(k, l, \theta)^T)_{kl}^2 d\omega \right) = 0. \quad (3.32)$$

It can be shown [14] that this leads to a fourth order equation with the roots for $t = \sin \theta / \cos \theta$ given by

$$t_{mn} = \frac{1}{4} \left(-\eta + (-1)^m \sqrt{16 + \eta^2} + (-1)^n \sqrt{2} \sqrt{16 + \eta^2 - (-1)^m \eta \sqrt{16 + \eta^2}} \right), \quad (3.33)$$

where $m, n \in \{1, 2\}$ number the roots and $\eta = (4\chi_1 - \chi_3)/\chi_2$ with the integrals

$$\chi_1 = \int_{-\infty}^{\infty} (P_{kl}(\omega))^2 d\omega, \quad (3.34)$$

$$\chi_2 = \int_{-\infty}^{\infty} P_{kl}(\omega) (P_{kk}(\omega) - P_{ll}(\omega)) d\omega, \quad (3.35)$$

$$\chi_3 = \int_{-\infty}^{\infty} (P_{kk}(\omega) - P_{ll}(\omega))^2 d\omega. \quad (3.36)$$

The root with $|t_{mn}| \leq 1$ and

$$-\frac{2\chi_2}{(t_{mn}^2 + 1)^4} (2t_{mn} (t_{mn}^4 - 14t_{mn}^2 + 9) + \eta (3t_{mn}^4 - 8t_{mn}^2 + 1)) > 0 \quad (3.37)$$

is selected (the left-hand side of (3.37) is the second derivative of the integral in (3.32), so the condition ensures that a minimum is found), and the rotation matrix is collocated by using $\cos \theta = 1/\sqrt{1+t^2}$ and $\sin \theta = t \cos \theta$. Applying such a rotation matrix once to each pair of k and l with $k < l$ means to perform a Jacobi sweep. Such sweeps are carried out until the off-diagonal norm (3.29) changes less than a certain threshold. The final transformation matrix \mathbf{C} , which is the product of all rotation matrices according to Eq. (3.30), contains the generalized normal coordinate vectors. The diagonal elements of the transformed spectra matrix $\mathbf{P}'(\omega) = \mathbf{C}\mathbf{P}(\omega)\mathbf{C}^T$ are the corresponding mode spectra that should be localized well in frequency space. Since the trace of a matrix is not changed by an orthogonal transformation, the sum of these mode spectra is equal to the power spectrum of the molecule. This means that just another dissection of the power spectrum in terms of normal mode spectra instead of atomic spectra is calculated.

The concept of normal coordinates is based on the assumption that the molecule performs small oscillations around a minimum of the potential energy surface. Therefore, rotational and translational motion in an MD trajectory have to be removed beforehand. For this purpose, the coordinates are transformed to the Eckart frame of reference [32]. This requires to provide an external reference structure with the coordinates \mathbf{r}_k^0 , which is obtained, e.g., by a geometry optimization of the isolated molecule. In each snapshot of the trajectory, the rotation matrix \mathbf{R} and the translation vector \mathbf{T} that minimize the mass-weighted root-mean-square distance

$$d = \sqrt{\sum_{k=1}^M m_k (\mathbf{R}\mathbf{r}_k + \mathbf{T} - \mathbf{r}_k^0)^2} \quad (3.38)$$

have to be found, where \mathbf{r}_k is the position vector of atom k in the trajectory. The TRAVIS implementation of this problem follows reference [33]. At first, the centroids in both coordinate systems are calculated:

$$\bar{\mathbf{r}} = \frac{\sum_{k=1}^M m_k \mathbf{r}_k}{\sum_{k=1}^M m_k}, \quad \bar{\mathbf{r}}^0 = \frac{\sum_{k=1}^M m_k \mathbf{r}_k^0}{\sum_{k=1}^M m_k}. \quad (3.39)$$

Using the centered vectors

$$\mathbf{x}_k = \mathbf{r}_k - \bar{\mathbf{r}}, \quad \mathbf{y}_k = \mathbf{r}_k^0 - \bar{\mathbf{r}}^0, \quad k = 1, \dots, M, \quad (3.40)$$

the 3×3 covariance matrix

$$\mathbf{S} = \mathbf{XMY}^T \quad (3.41)$$

is computed, where \mathbf{X} and \mathbf{Y} are $3 \times M$ matrices with the \mathbf{x}_k and \mathbf{y}_k as columns, respectively, and $\mathbf{M} = \text{diag}(m_1, \dots, m_k)$. With the singular value decomposition

$$\mathbf{S} = \mathbf{U}\mathbf{\Sigma}\mathbf{V}^T \quad (3.42)$$

of \mathbf{S} , the optimal rotation matrix is given by [33]

$$\mathbf{R} = \mathbf{V} \begin{pmatrix} 1 & 0 & 0 \\ 0 & 1 & 0 \\ 0 & 0 & \det(\mathbf{VU}^T) \end{pmatrix} \mathbf{U}^T. \quad (3.43)$$

Finally, the optimal translation vector is [33]

$$\mathbf{T} = \bar{\mathbf{r}}^0 - \mathbf{R}\bar{\mathbf{r}}. \quad (3.44)$$

The projection onto a single reference structure breaks down if there are conformational changes in the trajectory. In this context, the procedure has to be extended to several reference structures [15]. Two cases that need to be handled differently can occur: On the one hand, the reference structures can differ only in the ordering of equivalent atoms. This happens, e.g., if a methyl group rotates, as their hydrogen atoms are indistinguishable. On the other hand, the reference structures can correspond to conformationally different minima on the potential energy surface. This applies, e.g., to *trans* and *gauche* conformations of a butyl group. In the former case, all reference structures can be mapped to the same minimum by appropriately permuting the equivalent atoms, resulting in a single set of normal coordinates. In the latter case, different normal coordinates are obtained for each structure.

To assign the molecular conformation from a trajectory to the reference structures, a probability $p_m(t)$ giving the fitness of structure m has to be introduced. The general form of a possible choice [15] reads as

$$p_m(t) = N \exp\left(-\frac{d(\mathbf{r}(t), \mathbf{r}^{0m})}{2\sigma^2}\right), \quad (3.45)$$

where N is a normalization factor ensuring that the sum of all probabilities is 1, and σ determines the width of the switching region between two reference structures. The distance function $d(\mathbf{r}(t), \mathbf{r}^{0m})$ measures the distance between the coordinates from the trajectory transformed to the Eckart frame and the coordinates of reference structure m . The simplest choice is the mass-weighted root-mean-square distance as in Eq.(3.38). In many cases, however, the reference structures differ only in a few angles while the rest of the molecule has the same conformation. Under these circumstances, it is more convenient to use the root-mean-square deviation in certain internal coordinates [15]. At the moment, the TRAVIS implementation provides

the possibility to employ the root-mean-square deviation of an arbitrary number of dihedral angles δ_k :

$$d = \sqrt{\sum_{k=1}^l (\delta_k - \delta_k^0)^2}. \quad (3.46)$$

With the probabilities $p_m(t)$, a spectra matrix $\mathbf{P}_m(\omega)$ can be calculated for each reference structure using the definition

$$P_{mij}(\omega) = \sqrt{m_i m_j} \operatorname{Re} \left(\int_{-\infty}^{\infty} \langle p_m(\tau) \dot{x}_i^*(\tau) \dot{x}_j(\tau + t) \rangle_{\tau} \exp(-i\omega t) dt \right). \quad (3.47)$$

As opposed to (3.28), a modified cross-correlation enters the Fourier transform. Whereas the normal cross-correlation equally averages over all products $\dot{x}_i^*(\tau) \dot{x}_j(\tau + t)$ with timeshift t , the modified cross-correlation weights by $p_m(\tau)$, so each product gives a large contribution to the average only if the molecule is closest to reference structure m at time τ . Since the sum of all probabilities is 1, the sum of all matrices $\mathbf{P}_m(\omega)$ is equal to the matrix $\mathbf{P}(\omega)$ with only one reference structure, so the matrix $\mathbf{P}(\omega)$ is just split into the contributions of the different molecular conformations. At this point, the matrices that belong to reference structures differing only in the ordering of equivalent atoms can be added after properly permuting the corresponding entries. The minimization of the off-diagonal elements is carried out for each of the remaining matrices, yielding one set of normal coordinates for each conformationally different reference structure.

3.3 Infrared and Raman Intensities

In static quantum chemistry, IR spectra are calculated as described in Sect. 2.4.2. As soon as the normal modes of a molecule are known, the IR intensities can be computed by taking the derivatives of the dipole moment along the normal coordinates. In an MD simulation, these derivatives are not directly accessible. An alternative approach is, however, possible by the following line of thought: If the MD simulation is in equilibrium, all modes are excited at once, so the oscillation of the dipole moment contains contributions from all modes at the same time. Each of these contributions oscillates at the frequency of the corresponding mode, suggesting to employ a Fourier transform to obtain a frequency-resolved representation of these oscillations. In the same manner as power spectra (see Sect. 3.2.1), these spectra show peaks at all vibrational frequencies of the molecule, but this time, the intensity is proportional to the amplitudes of the dipole oscillations at these frequencies. In linear approximation, the latter are proportional to the derivatives of the dipole moment along the normal coordinates (cf. Eq. 2.58), so the result of the Fourier transform is just the IR spectrum of the system.

For a more detailed mathematical insight, the one-dimensional classical harmonic oscillator is considered again. Using the mass-weighted coordinate $q = \sqrt{m}x$, its trajectory is given by (see Sect. 2.4.1)

$$q(t) = \sqrt{m}x_0 \cos(\omega_0 t + \varphi), \quad (3.48)$$

where x_0 is the amplitude, ω_0 is the eigenfrequency, and φ is the phase. The dipole moment μ is assumed to depend linearly on the coordinate, so the Taylor expansion around the equilibrium position can be truncated after the linear term:

$$\mu(q) = \mu_0 + \left(\frac{\partial \mu}{\partial q} \right)_0 q, \quad (3.49)$$

where μ_0 is the dipole moment at the equilibrium position. Inserting the trajectory yields for the time-dependent dipole moment

$$\mu(t) = \mu_0 + \left(\frac{\partial \mu}{\partial q} \right)_0 \sqrt{m}x_0 \cos(\omega_0 t + \varphi). \quad (3.50)$$

For power spectra (see Sect. 3.2.1), it was discussed that it is more convenient to use the time derivative of the coordinate instead of the coordinate itself. Transferring this to the dipole moment bears the additional advantage that the equilibrium dipole moment, which does not carry information relevant for the IR intensities, is removed:

$$\dot{\mu}(t) = - \left(\frac{\partial \mu}{\partial q} \right)_0 \sqrt{m}x_0 \omega_0 \sin(\omega_0 t + \varphi). \quad (3.51)$$

To remove also the dependence on the initial conditions of the MD simulation in terms of the phase φ , the autocorrelation function is calculated (see Appendix B.1):

$$R_{\dot{\mu}}(t) = \frac{1}{2} \left(\frac{\partial \mu}{\partial q} \right)_0^2 m x_0^2 \omega_0^2 \cos(\omega_0 t). \quad (3.52)$$

The Fourier transform of this expression can be written as

$$\mathcal{F}(R_{\dot{\mu}})(\omega) = \int_{-\infty}^{\infty} R_{\dot{\mu}}(t) \exp(-i\omega t) dt = \frac{1}{2} \left(\frac{\partial \mu}{\partial q} \right)_0^2 m x_0^2 \omega_0^2 \pi (\delta(\omega - \omega_0) + \delta(\omega + \omega_0)). \quad (3.53)$$

Due to the properties of the delta distribution, the total integral of the spectrum is

$$\int_{-\infty}^{\infty} \mathcal{F}(R_{\dot{\mu}})(\omega) d\omega = \left(\frac{\partial \mu}{\partial q} \right)_0^2 m x_0^2 \omega_0^2 \pi. \quad (3.54)$$

Recalling that the amplitude is related to the average kinetic energy by $x_0 = \sqrt{4 \langle E_{\text{kin}} \rangle / m} / \omega_0$ (see Sect. 3.2.1), this is equal to

$$\int_{-\infty}^{\infty} \mathcal{F}(R_{\dot{\mu}})(\omega) d\omega = \left(\frac{\partial \mu}{\partial q} \right)_0^2 \cdot 4 \pi \langle E_{\text{kin}} \rangle = \left(\frac{\partial \mu}{\partial q} \right)_0^2 \cdot 2 \pi k_{\text{B}} T. \quad (3.55)$$

This means that the integral of the Fourier transform of the dipole moment autocorrelation in a harmonic oscillator is proportional to the average kinetic energy (or the temperature) and the squared derivative of the dipole moment along the mass-weighted coordinate at the equilibrium position. The latter is the same term as the one appearing in static quantum chemistry (see Eq. 2.59). Comparing these two expressions leads to the following definition of the IR spectrum in MD simulations:

$$A(\omega) = \frac{N_{\text{A}}}{24 \pi \varepsilon_0 c^2 k_{\text{B}} T} \int_{-\infty}^{\infty} \langle \dot{\boldsymbol{\mu}}(\tau) \cdot \dot{\boldsymbol{\mu}}(\tau + t) \rangle_{\tau} \exp(-i\omega t) dt. \quad (3.56)$$

In this expression, the vector autocorrelation of the dipole moment is introduced to switch over to the general three-dimensional case. The prefactor ensures that—for a harmonic oscillator with a linear dependence of the dipole moment on the position—the integral of the spectrum is equal to the integral absorption coefficient in static quantum chemistry. For comparison to experimental data later on, it is more convenient to use the wavenumber-dependent representation

$$A(\tilde{\nu}) = \frac{N_{\text{A}}}{12 \varepsilon_0 c k_{\text{B}} T} \int_{-\infty}^{\infty} \langle \dot{\boldsymbol{\mu}}(\tau) \cdot \dot{\boldsymbol{\mu}}(\tau + t) \rangle_{\tau} \exp(-2 \pi i c \tilde{\nu} t) dt, \quad (3.57)$$

which is the one actually calculated in the TRAVIS implementation.

The concept of IR spectra from the Fourier transform of the dipole moment autocorrelation function has been known in the literature for a long time [34]. The usual derivation starts with Fermi’s golden rule (2.56) and transforms the formula for the IR absorption coefficient from the Schrödinger picture to the Heisenberg picture of quantum mechanics [35, 36]. In the resulting expressions, the quantum correlation functions are approximated by classical correlation functions. Since these do not satisfy the detailed balance condition [37], several quantum correction factors have been discussed [28, 29, 38–42], and it has been concluded that the best choice is the factor called “harmonic correction”. Although different variants of the constant prefactor have been applied, this correction factor yields the same frequency dependence as in Eq. (3.56). Here, this formula is directly derived in an alternative fashion by comparing the results for a harmonic oscillator. This clarifies the close relation of MD and static calculations regarding vibrational spectra.

Replacing the dipole moment by the polarizability, the same derivation can in principle be carried out for Raman spectra. The only point requiring special attention is that the polarizability is a second-order tensor and the static quantum chemistry formulas contain various combinations of its elements (see Sect. 2.4.3). The general rule is to replace each quadratic term containing polarizability derivatives along the normal coordinates by the corresponding autocorrelation function of the polarizability time derivatives. Choosing the prefactor in such a way that the integral of the MD spectrum agrees with the differential Raman scattering cross section in static quantum

chemistry (for a harmonic oscillator with a linear dependence of the polarizability on the position), the polarized frequency-dependent differential Raman scattering cross sections for fixed molecular orientation with respect to the laboratory coordinate system are given by

$$I^{\parallel}(\omega) = \frac{\hbar}{64 \pi^3 \varepsilon_0^2 c^4 k_B T} \frac{(\omega_{\text{in}} - \omega)^4}{\omega \left(1 - \exp\left(-\frac{\hbar\omega}{k_B T}\right)\right)} \int_{-\infty}^{\infty} \langle \dot{\alpha}_{xx}(\tau) \dot{\alpha}_{xx}(\tau + t) \rangle_{\tau} \exp(-i\omega t) dt \quad (3.58)$$

and

$$I^{\perp}(\omega) = \frac{\hbar}{64 \pi^3 \varepsilon_0^2 c^4 k_B T} \frac{(\omega_{\text{in}} - \omega)^4}{\omega \left(1 - \exp\left(-\frac{\hbar\omega}{k_B T}\right)\right)} \int_{-\infty}^{\infty} \langle \dot{\alpha}_{xy}(\tau) \dot{\alpha}_{xy}(\tau + t) \rangle_{\tau} \exp(-i\omega t) dt. \quad (3.59)$$

For random molecular orientation with respect to the laboratory coordinate system, the expressions read as

$$I^{\parallel}(\omega) = \frac{\hbar}{64 \pi^3 \varepsilon_0^2 c^4 k_B T} \frac{(\omega_{\text{in}} - \omega)^4}{\omega \left(1 - \exp\left(-\frac{\hbar\omega}{k_B T}\right)\right)} \frac{45a(\omega) + 4\gamma(\omega)}{45} \quad (3.60)$$

and

$$I^{\perp}(\omega) = \frac{\hbar}{64 \pi^3 \varepsilon_0^2 c^4 k_B T} \frac{(\omega_{\text{in}} - \omega)^4}{\omega \left(1 - \exp\left(-\frac{\hbar\omega}{k_B T}\right)\right)} \frac{3\gamma(\omega)}{45} \quad (3.61)$$

with the isotropic contribution

$$a(\omega) = \int_{-\infty}^{\infty} \left\langle \frac{\dot{\alpha}_{xx}(\tau) + \dot{\alpha}_{yy}(\tau) + \dot{\alpha}_{zz}(\tau)}{3} \frac{\dot{\alpha}_{xx}(\tau + t) + \dot{\alpha}_{yy}(\tau + t) + \dot{\alpha}_{zz}(\tau + t)}{3} \right\rangle_{\tau} \exp(-i\omega t) dt \quad (3.62)$$

and the anisotropic contribution

$$\begin{aligned} \gamma(\omega) = \int_{-\infty}^{\infty} \left[\frac{1}{2} \langle (\dot{\alpha}_{xx}(\tau) - \dot{\alpha}_{yy}(\tau)) (\dot{\alpha}_{xx}(\tau + t) - \dot{\alpha}_{yy}(\tau + t)) \rangle_{\tau} \right. \\ + \frac{1}{2} \langle (\dot{\alpha}_{yy}(\tau) - \dot{\alpha}_{zz}(\tau)) (\dot{\alpha}_{yy}(\tau + t) - \dot{\alpha}_{zz}(\tau + t)) \rangle_{\tau} \\ + \frac{1}{2} \langle (\dot{\alpha}_{zz}(\tau) - \dot{\alpha}_{xx}(\tau)) (\dot{\alpha}_{zz}(\tau + t) - \dot{\alpha}_{xx}(\tau + t)) \rangle_{\tau} \\ + 3 \langle \dot{\alpha}_{xy}(\tau) \dot{\alpha}_{xy}(\tau + t) \rangle_{\tau} + 3 \langle \dot{\alpha}_{yz}(\tau) \dot{\alpha}_{yz}(\tau + t) \rangle_{\tau} \\ \left. + 3 \langle \dot{\alpha}_{zx}(\tau) \dot{\alpha}_{zx}(\tau + t) \rangle_{\tau} \right] \exp(-i\omega t) dt. \quad (3.63) \end{aligned}$$

Similar to the IR spectrum (3.56), these formulas can be transferred to the wavenumber-dependent representation, which is the one actually calculated in TRAVIS. For fixed molecular orientation with respect to the laboratory coordinate system, this yields

$$I^{\parallel}(\tilde{\nu}) = \frac{h}{8\varepsilon_0^2 k_B T} \frac{(\tilde{\nu}_{\text{in}} - \tilde{\nu})^4}{\tilde{\nu} \left(1 - \exp\left(-\frac{hc\tilde{\nu}}{k_B T}\right)\right)} \int_{-\infty}^{\infty} \langle \dot{\alpha}_{xx}(\tau) \dot{\alpha}_{xx}(\tau + t) \rangle_{\tau} \exp(-2\pi ic\tilde{\nu}t) dt \quad (3.64)$$

and

$$I^{\perp}(\tilde{\nu}) = \frac{h}{8\varepsilon_0^2 k_B T} \frac{(\tilde{\nu}_{\text{in}} - \tilde{\nu})^4}{\tilde{\nu} \left(1 - \exp\left(-\frac{hc\tilde{\nu}}{k_B T}\right)\right)} \int_{-\infty}^{\infty} \langle \dot{\alpha}_{xy}(\tau) \dot{\alpha}_{xy}(\tau + t) \rangle_{\tau} \exp(-2\pi ic\tilde{\nu}t) dt. \quad (3.65)$$

The formulas for random molecular orientation with respect to the laboratory coordinate system are given by

$$I^{\parallel}(\tilde{\nu}) = \frac{h}{8\varepsilon_0^2 k_B T} \frac{(\tilde{\nu}_{\text{in}} - \tilde{\nu})^4}{\tilde{\nu} \left(1 - \exp\left(-\frac{hc\tilde{\nu}}{k_B T}\right)\right)} \frac{45a(\tilde{\nu}) + 4\gamma(\tilde{\nu})}{45} \quad (3.66)$$

and

$$I^{\perp}(\tilde{\nu}) = \frac{h}{8\varepsilon_0^2 k_B T} \frac{(\tilde{\nu}_{\text{in}} - \tilde{\nu})^4}{\tilde{\nu} \left(1 - \exp\left(-\frac{hc\tilde{\nu}}{k_B T}\right)\right)} \frac{3\gamma(\tilde{\nu})}{45} \quad (3.67)$$

with the isotropic contribution

$$a(\tilde{\nu}) = \int_{-\infty}^{\infty} \left\langle \frac{\dot{\alpha}_{xx}(\tau) + \dot{\alpha}_{yy}(\tau) + \dot{\alpha}_{zz}(\tau)}{3} \frac{\dot{\alpha}_{xx}(\tau + t) + \dot{\alpha}_{yy}(\tau + t) + \dot{\alpha}_{zz}(\tau + t)}{3} \right\rangle_{\tau} \cdot \exp(-2\pi ic\tilde{\nu}t) dt \quad (3.68)$$

and the anisotropic contribution

$$\begin{aligned} \gamma(\tilde{\nu}) = \int_{-\infty}^{\infty} & \left[\frac{1}{2} \langle (\dot{\alpha}_{xx}(\tau) - \dot{\alpha}_{yy}(\tau)) (\dot{\alpha}_{xx}(\tau + t) - \dot{\alpha}_{yy}(\tau + t)) \rangle_{\tau} \right. \\ & + \frac{1}{2} \langle (\dot{\alpha}_{yy}(\tau) - \dot{\alpha}_{zz}(\tau)) (\dot{\alpha}_{yy}(\tau + t) - \dot{\alpha}_{zz}(\tau + t)) \rangle_{\tau} \\ & + \frac{1}{2} \langle (\dot{\alpha}_{zz}(\tau) - \dot{\alpha}_{xx}(\tau)) (\dot{\alpha}_{zz}(\tau + t) - \dot{\alpha}_{xx}(\tau + t)) \rangle_{\tau} \\ & + 3 \langle \dot{\alpha}_{xy}(\tau) \dot{\alpha}_{xy}(\tau + t) \rangle_{\tau} + 3 \langle \dot{\alpha}_{yz}(\tau) \dot{\alpha}_{yz}(\tau + t) \rangle_{\tau} \\ & \left. + 3 \langle \dot{\alpha}_{zx}(\tau) \dot{\alpha}_{zx}(\tau + t) \rangle_{\tau} \right] \exp(-2\pi ic\tilde{\nu}t) dt. \end{aligned} \quad (3.69)$$

The quotient $I^\perp(\tilde{\nu})/I^\parallel(\tilde{\nu})$ provides the depolarization ratio $\rho(\tilde{\nu})$ as a function of the wavenumber. The result, however, is only meaningful in the region of Raman bands. Anywhere else, it is just numerical noise due to the division of two very small numbers.

3.4 Dipole Moments and Polarizabilities

3.4.1 Maximally Localized Wannier Functions

In the last section, it was shown how IR and Raman intensities can be obtained from the temporal development of dipole moments and polarizabilities. Now, it is discussed how these quantities can be calculated in AIMD simulations.

In principle, the dipole moment is easily computed as the expectation value of the dipole operator after the wave function is known by the electronic structure method. This approach works very well for isolated molecules in the gas phase, and it is available in most quantum chemistry software packages. An AIMD simulation of a liquid, however, suffers from the problem that the standard dipole operator is ill-defined when periodic boundary conditions are applied. This issue has been solved by the Berry phase approach to polarization [43–45], which can provide the dipole moment of the whole simulation cell under periodic boundary conditions. Combining this method with perturbation theory, it is also possible to calculate the polarizability [46].

In many applications, it is desirable to assign an individual dipole moment to each molecule of the system. This improves the sampling of the spectra, but more importantly, it also allows to separate the spectral contributions of the components in a mixture and it provides the possibility to study the individual spectrum of a solute molecule. For this purpose, the scheme of maximally localized Wannier functions [47–51] can be used in DFT. By a unitary transformation of the occupied Kohn–Sham orbitals, a set of localized Wannier orbitals is created. The particular form of this transformation is chosen in such a way that a specific spread functional of the Wannier orbitals (see the references for details) is minimized. The position expectation values \mathbf{r}_i of these Wannier orbitals are called Wannier function centers, and they can be interpreted in a chemical sense as the locations of electron pairs. In a bulk phase AIMD simulation, the Wannier function centers are usually located near the molecules, allowing for a distinct assignment of each center to one molecule on the basis of a minimum distance criterion. For each molecule I , the dipole moment is given by the classical definition summing over the point charges:

$$\boldsymbol{\mu}_I = -2e \sum_{i=1}^N \mathbf{r}_i + e \sum_{A=1}^M Z_A \mathbf{R}_A, \quad (3.70)$$

where e is the elementary charge, the first sum is over all Wannier function centers assigned to the molecule, and the second sum is over all nuclei of the molecule with

the positions \mathbf{R}_A and the charges Z_A . If pseudopotentials are employed, the number of electrons in the pseudopotential has to be subtracted from the nuclear charge to obtain Z_A . The sum of all molecular dipole moments calculated in this way is a good approximation to the total dipole moment of the simulation cell [50]. It should be noted that the Wannier localization itself is required to be performed by the simulation software package while TRAVIS takes the resulting Wannier function centers as input to carry out the assignment to the molecules and to calculate the dipole moments.

A possible calculation scheme for polarizabilities is found by recalling that the dipole moment induced by an electric field \mathbf{E} is given in linear approximation as

$$\boldsymbol{\mu}_{\text{ind}} = \boldsymbol{\alpha}\mathbf{E}, \quad (3.71)$$

where $\boldsymbol{\alpha}$ is the second-order polarizability tensor. This suggests to perform additional single-point calculations with an external electric field for each step of the AIMD simulation and to record the dipole moment changes. The polarizability is the dipole moment change divided by the electric field strength. If the Wannier function centers are used for the dipole moment, this approach provides individual polarizabilities for each molecule. To obtain the complete polarizability tensor, this has to be carried out using three linear independent polarization vectors for the electric field. In the simplest case, these are the three Cartesian coordinate axes with the same field strength, since this makes the inversion of Eq. (3.71) trivial. If the complete polarizability tensor is available, Raman spectra can be calculated for random orientation of the simulation cell with respect to the laboratory coordinate system as in Eqs. (3.66) and (3.67). However, this is not necessarily needed as long as isotropic systems are studied, since the molecules rotate in a typical MD simulation and they will adopt all possible orientations with respect to the cell coordinate system by themselves if the trajectory is sufficiently long. This allows to identify the cell coordinate system with the laboratory coordinate system, so that only α_{xx} and α_{yy} (see Eqs. (3.64) and (3.65)) are needed to calculate the Raman spectrum. These two components of the polarizability tensor can be found by only one additional single-point calculation with an external electric field along the x axis. Experience shows that the complete polarizability tensor provides only minor improvements to this approach, and it is normally not necessary to invest three times the computational resources as long as depolarization ratios are not needed.

The calculation of polarizabilities on the basis of Eq. (3.71) neglects changes in the local electric field of a molecule by the polarization of the neighboring molecules. These can be included by considering dipole–dipole interaction tensors computed by Ewald summation under periodic boundary conditions as explained in references [52, 53]. This method always requires to spend the computational resources for applying the electric field with three linear independent polarization directions. A recent study of water has shown that this has only a minor influence on the resulting Raman spectra [54].

Another important way to save computational resources is to calculate the polarizability not in all steps of the trajectory. According to the Nyquist–Shannon theorem, e.g., sampling the polarizability with a timestep of 4 fs is sufficient to obtain the

Raman spectrum up to a wavenumber of 4170 cm^{-1} . IR spectra benefit in a similar manner from this fact, since already the Wannier localization to calculate the dipole moments can be very costly. The only point that needs special attention is the computation of the time derivative that enters the autocorrelation functions (see Sect. 3.3). This derivative is never known exactly, but it has to be calculated by finite differences. Taking a larger timestep makes this approximation worse. Fortunately, the error made by the finite difference can be quantified in an easy way. For a cosine function $\cos(\omega t + \varphi)$, it can be shown (see Appendix B.5) that the second-order central finite difference derivative is given by

$$D \cos(\omega t + \varphi) = \frac{\cos(\omega(t + \Delta t) + \varphi) - \cos(\omega(t - \Delta t) + \varphi)}{2\Delta t} = -\omega \sin(\omega t + \varphi) \frac{\sin(\omega\Delta t)}{\omega\Delta t}, \quad (3.72)$$

meaning that the exact derivative $d(\cos(\omega t + \varphi))/dt = -\omega \sin(\omega t + \varphi)$ is multiplied by the sinc function $\sin(\omega\Delta t)/(\omega\Delta t)$. In other words, the amplitude of a harmonic vibration is modified but its frequency is not affected. This allows to correct the finite difference error by a simple factor in the final spectra. Since the product of two time derivatives enters the autocorrelation, the final spectra have to be divided by the square $(\sin(\omega\Delta t)/(\omega\Delta t))^2$ of the sinc function.

3.4.2 Voronoi Tessellation of the Electron Density

A major issue of the maximally localized Wannier function scheme is the computational effort required for the localization. In systems with several hundred atoms, this easily takes much longer than the actual electronic structure calculation, in particular when the convergence is slow. To avoid this huge impact on the computation time to get IR and Raman spectra from an AIMD simulation, an alternative idea was implemented in the course of this thesis. It relies on the fact that it is sufficient to know the total electron density to calculate the dipole moment by integration according to the classical definition. The Wannier function centers allow to assign each orbital to a molecule, but this is actually unnecessary, as it is only needed to divide the total electron density into molecular contributions. Any scheme to partition the electron density, which is inherently available in each AIMD snapshot, should be applicable for this purpose. Many such techniques are known [55–65], mainly to assign atomic partial charges in molecules.

A simple method to generally partition the space of a simulation cell is the Voronoi tessellation [66]. The Voronoi tessellation takes a set of n sites \mathbf{s}_i as input, and it creates n Voronoi cells C_i according to

$$C_i = \{ \mathbf{x} \in \mathbb{R}^3 \mid (\mathbf{x} - \mathbf{s}_i)^2 \leq (\mathbf{x} - \mathbf{s}_j)^2 \forall j \neq i \}, \quad i, j = 1, \dots, n. \quad (3.73)$$

This means that cell C_i consists of all points that are closer to site \mathbf{s}_i than to any other site. The Voronoi tessellation is unique and it assigns each point in space to exactly

one cell. The cell faces are always placed midway between two atoms, which has already been used to assign atomic partial charges on the basis of the electron density [67].

It contradicts chemical intuition that the Voronoi tessellation equally divides the space between two atoms irrespective of their kind. In later applications to the calculation of atomic partial charges [68–70] and the molecular multipole moments of water clusters [71], the boundary planes were shifted therefore. In reference [69], radii were assigned to the atoms, and the position of the cell face between two atoms was determined by the ratio of their radii. This approach, however, suffers from the vertex error [72], meaning that not all points in space are assigned to a cell, and the tessellation contains holes. For the separation of the water molecules in reference [71], the original Voronoi tessellation was employed, but the Voronoi sites of the hydrogen atoms were shifted along the O-H bonds toward the oxygen atoms until the boundary between two water molecules was approximately located in the minimum of the electron density. This approach is not generally transferable to arbitrary systems.

An extended partitioning scheme that allows to keep the Voronoi sites at the atom positions and does not suffer from the vertex error is the radical Voronoi tessellation [73]. In this method, a radius r_i is assigned to each site and the cells are defined by

$$C_i^r = \{ \mathbf{x} \in \mathbb{R}^3 \mid (\mathbf{x} - \mathbf{s}_i)^2 - r_i^2 \leq (\mathbf{x} - \mathbf{s}_j)^2 - r_j^2 \forall j \neq i \}, \quad i, j = 1, \dots, n. \quad (3.74)$$

This means that the distance to the sites themselves from the original Voronoi tessellation is replaced by the power distance to spheres around the sites with the corresponding radii. The position of the cell face between two atoms is determined by the difference of the squared radii. For each cell, it is possible to calculate the charge

$$q_i = \int_{C_i^r} \rho(\mathbf{r}) \, d\mathbf{r} \quad (3.75)$$

and the dipole moment

$$\boldsymbol{\mu}_i = \int_{C_i^r} \mathbf{r} \rho(\mathbf{r}) \, d\mathbf{r} \quad (3.76)$$

according to the classical definitions, where the integration has to be carried out over the volume of the cell. The cells belonging to atoms of the same molecule can be joined to gain a molecular cell, and the charges and dipole moments of the atomic cells can be added to obtain a molecular charge and a molecular dipole moment. The general idea of the Voronoi tessellation is illustrated in Fig. 3.12.

In practice, the electron density is usually output on a regular grid by simulation software packages, and the integration is most easily performed by the rectangle method. For the radical Voronoi tessellation, the VORO++ library of Chris Rycroft [74] was adopted in TRAVIS. This library takes the Voronoi sites with their radii as input and it provides separately for each site the vertex coordinates of the corresponding Voronoi cell. The straightforward approach to the integration would be to check

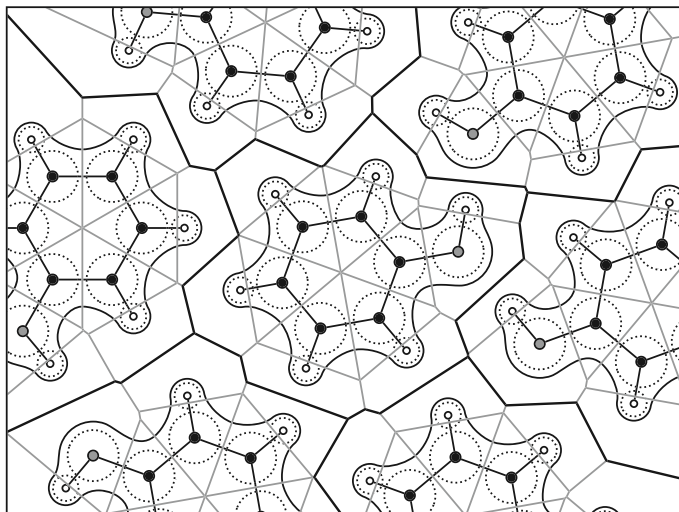


Fig. 3.12 Schematic illustration of the radical Voronoi tessellation at the example of phenol. The electron density is indicated by *black isolines*, the Voronoi radii are denoted by *dotted circles*, and the radical Voronoi cells are shown by *gray lines*. Combining the cells of atoms in the same molecule yields the molecular cells drawn in *black*

for each electron density grid point one after another to which cell it belongs and to add it to the integral of this cell. A more efficient method, however, is as follows¹: The electron density grid is stored internally in memory such that adjacent points along the first cell vector \mathbf{h}_1 (the x axis in an orthorhombic cell) appear contiguously. This means that the grid is mapped to a number of ordered point sets, where in each set, the points share the same coordinates along the second cell vector \mathbf{h}_2 and the third cell vector \mathbf{h}_3 (the y and z axes in an orthorhombic cell). After the Voronoi tessellation is known, the maximum extent along \mathbf{h}_2 and \mathbf{h}_3 (bounding box) is determined for each cell first. This reduces the number of point sets possibly contributing to the cell, as all point sets outside of this coordinate range do not need to be considered further. For each of the remaining point sets, the intersections of a straight line parallel to \mathbf{h}_1 with the corresponding coordinates along \mathbf{h}_2 and \mathbf{h}_3 are computed. Since Voronoi cells are always convex, this line hits either none or two of the cell faces. In the latter case, it follows easily from the coordinates of the intersections along \mathbf{h}_1 , which points of the set are located inside of the cell and have to be added to the integral (see Fig. 3.13 for an illustration in two dimensions, where the cell faces are straight lines).

The calculation of the intersections of the cell faces and a line through the point set requires some elementary vector algebra. The Hesse normal form of a cell face plane reads as

$$\mathbf{n} \cdot (\mathbf{x} - \mathbf{c}) = 0, \quad \mathbf{x} \in \mathbb{R}^3, \quad (3.77)$$

¹I would like to thank Dr. Martin Brehm for the initial idea of this algorithm and the initial implementation for orthorhombic simulation cells.

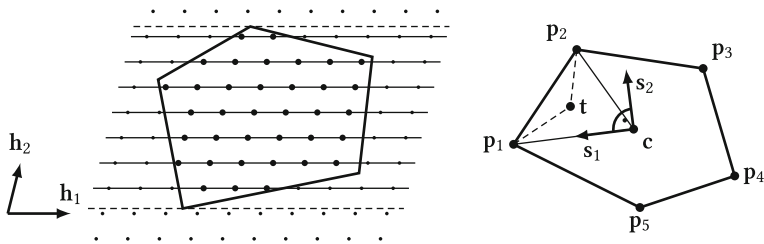


Fig. 3.13 *Left*: Illustration of the discrete integration over Voronoi cells in two dimensions. The *dashed lines* mark the maximum extent of the cell along \mathbf{h}_2 , the *thin solid lines* connect the point sets sharing the same coordinate along \mathbf{h}_2 , and the *large circles* indicate the grid points between the intersections that are added to the integral. *Right*: Local coordinate system of a Voronoi cell face used to calculate the intersection \mathbf{t} with a line. The normal vector \mathbf{n} is perpendicular to the paper plane

where \mathbf{n} is the normal vector of the plane and \mathbf{c} is the centroid of the face. The straight line through the point set can be written as

$$\mathbf{x} = \lambda \mathbf{h}_1 + b \mathbf{h}_2 + c \mathbf{h}_3, \quad \lambda \in \mathbb{R}, \quad (3.78)$$

with the common coordinates b and c of the point set along \mathbf{h}_2 and \mathbf{h}_3 . Combining these two equations allows to determine λ and yields

$$\mathbf{t} = \frac{\mathbf{n} \cdot (\mathbf{c} - b \mathbf{h}_2 - c \mathbf{h}_3)}{\mathbf{n} \cdot \mathbf{h}_1} \mathbf{h}_1 + b \mathbf{h}_2 + c \mathbf{h}_3 \quad (3.79)$$

for the intersection \mathbf{t} of the line with the plane in Cartesian coordinates. To find out whether this intersection is located inside of the cell face, a local coordinate system is defined (see Fig. 3.13), which consists of the normal vector \mathbf{n} and two vectors \mathbf{s}_1 and \mathbf{s}_2 in the plane. The centroid \mathbf{c} is the origin of the coordinate system. Starting from the vertex coordinates $\{\mathbf{p}_1, \dots, \mathbf{p}_n\}$ provided by the Voronoi tessellation, the centroid \mathbf{c} is calculated and the basis vectors are constructed by:

$$\mathbf{s}_1 = \frac{\mathbf{p}_1 - \mathbf{c}}{|\mathbf{p}_1 - \mathbf{c}|}, \quad \mathbf{n} = \frac{\mathbf{s}_1 \times (\mathbf{p}_2 - \mathbf{c})}{|\mathbf{s}_1 \times (\mathbf{p}_2 - \mathbf{c})|}, \quad \mathbf{s}_2 = \mathbf{s}_1 \times \mathbf{n}. \quad (3.80)$$

(Since \mathbf{n} is needed to compute the intersection in Eq.(3.79), this step is actually performed beforehand.) Calculating the scalar products $(\mathbf{p}_i - \mathbf{c}) \cdot \mathbf{s}_1$ and $(\mathbf{p}_i - \mathbf{c}) \cdot \mathbf{s}_2$ as well as $(\mathbf{t} - \mathbf{c}) \cdot \mathbf{s}_1$ and $(\mathbf{t} - \mathbf{c}) \cdot \mathbf{s}_2$ provides the coordinates of the vertices \mathbf{p}'_i and the intersection \mathbf{t}' in the local face coordinate system. The coordinate along \mathbf{n} is always zero by construction. According to the shoelace formula, the signed area of the triangle $(\mathbf{t}', \mathbf{p}'_i, \mathbf{p}'_{i+1})$ with $i \in \mathbb{Z}/n\mathbb{Z}$ is given by

$$A_1 = \frac{1}{2} \left[(\mathbf{t}'_1 \mathbf{p}'_{i2}) + (\mathbf{p}'_{i1} \mathbf{p}'_{i+12}) + (\mathbf{p}'_{i+11} \mathbf{t}'_{i2}) - (\mathbf{p}'_{i1} \mathbf{t}'_{i2}) - (\mathbf{p}'_{i+11} \mathbf{p}'_{i2}) - (\mathbf{t}'_{i1} \mathbf{p}'_{i+12}) \right], \quad (3.81)$$

where the subscripts 1 and 2 at the parentheses denote the coordinates along \mathbf{s}_1 and \mathbf{s}_2 , respectively. Considering that the centroid is the origin of the local face coordinate system, the area of the triangle $(\mathbf{c}', \mathbf{p}'_i, \mathbf{p}'_{i+1})$ is similarly given by

$$A_2 = \frac{1}{2} [(\mathbf{p}'_i)_1(\mathbf{p}'_{i+1})_2 - (\mathbf{p}'_{i+1})_1(\mathbf{p}'_i)_2]. \quad (3.82)$$

If both areas have the same sign, \mathbf{t} and \mathbf{c} are located on the same side of the edge between \mathbf{p}_i and \mathbf{p}_{i+1} . Only if this condition is fulfilled for all edges, the intersection is located inside of the cell face, and its coordinate along \mathbf{h}_1 reads as

$$a = \frac{\mathbf{n} \cdot (\mathbf{c} - b\mathbf{h}_2 - c\mathbf{h}_3)}{\mathbf{n} \cdot \mathbf{h}_1}. \quad (3.83)$$

Taking this coordinate for both intersections with the Voronoi cell, rounding up the smaller value, and rounding down the larger value provides the indices of the first and the last point in the point set that have to be added to the integral.

The internal design of the VORO++ library can sometimes cause numerical problems with this approach. As each Voronoi cell is computed independently on the basis of the Voronoi sites, the coordinates of a common vertex shared by several cells can differ between the cells in the order of the machine precision. This means that very small volumes of the simulation cell are actually assigned to two Voronoi cells while other very small volumes do not belong to any Voronoi cell. Although the spacing of the grid points is by orders larger than the machine precision, it can accidentally happen that grid points are located within these small volumes. To avoid an assignment of any grid point either to two cells or to no cell, grid points very close to a cell face are shifted temporarily by a small positive displacement along the cell vectors until they can unambiguously be assigned to exactly one cell.

It is apparent in Fig. 3.13 that the accuracy of the integration depends on the grid spacing, since the shape of the Voronoi cell is rasterized to the electron density data grid. Also if the Voronoi cell moves smoothly during an AIMD simulation, the integral shows finite jumps over time, as grid points can only enter or leave the cell completely at once. Moreover, the assignment of each grid point to exactly one cell can introduce a systematic error in highly ordered systems such as crystals, where many grid points might be close to cell faces. To avoid these distortions, it would be desirable to have some kind of equitable binning [1]. Along \mathbf{h}_1 , this is easily implemented by weighting the grid points adjacent to the cell faces by the relative distance to the intersection. A suitable algorithm in this sense for the other cell vectors has, however, not been found yet. Applying the equitable binning only for \mathbf{h}_1 turned out to make the results worse, probably because one of the cell vectors is favored and the rotational invariance is disturbed even more. As an alternative approach, a linear interpolation of the grid is therefore available in TRAVIS. This allows to create an arbitrary number of intermediate points in the data grid provided by the simulation software. The linear interpolation is consistent with the rectangle method, so the total integral of the grid is not changed, but the finer mesh allows for a more appropriate

representation of the cell shape. In the limit of infinitely many intermediate points this would provide a true equitable binning. This interpolation can be carried out on the fly, so the memory requirements are not increased.

For the dipole moment, it is important to note that it generally depends on the reference point. Choosing \mathbf{r}' as the reference point or, equivalently, calculating the dipole moment in a shifted coordinate system with \mathbf{r}' as origin yields

$$\boldsymbol{\mu}'_i = \int_{C'_i} (\mathbf{r} - \mathbf{r}') \rho(\mathbf{r}) \, d\mathbf{r} = \int_{C'_i} \mathbf{r} \rho(\mathbf{r}) \, d\mathbf{r} - \mathbf{r}' \int_{C'_i} \rho(\mathbf{r}) \, d\mathbf{r} = \boldsymbol{\mu}_i - q_i \mathbf{r}'. \quad (3.84)$$

Only if the charge q_i is zero, the dipole moment is independent of \mathbf{r}' . This leads to the general issue that the dipole moment of a molecular ion cannot be defined uniquely. Several possibilities to select the reference point have been discussed in the context of ionic liquids [75]. In connection with vibrational spectra, the most reasonable choice is the center of mass, which remains fixed in all normal modes, so that the reference point becomes independent of the internal degrees of freedom. In all other cases, translational motion can show up in the spectra (see Appendix B.6).

It remains to discuss how the radii for the radical Voronoi tessellation should be chosen. For the calculation of spectra, which rely on molecular dipole moments, the most important aim is a reasonable separation of the molecules in the bulk, whereas the intramolecular partitioning of the electron density is of minor interest. This suggests to employ van der Waals radii [76–78], since these were fitted to reproduce intermolecular distances. For the assignment of atomic partial charges, on the other hand, it would be more important to get a proper distribution of the electron density within the molecule, and minor deficiencies in the partitioning of the low electron density between the molecules can be accepted. This suggests to apply covalent radii [79], as these were fitted to reflect intramolecular bond lengths. A further justification of these choices is given in Sect. 4.5.1 by an investigation of the standard deviations in the charge distribution functions that were implemented in TRAVIS.

3.5 Magnetic Moments and Vibrational Circular Dichroism

VCD is a spectroscopic technique closely related to IR spectroscopy. It measures the difference in the absorption of left and right circularly polarized IR radiation, so it is a prominent method to investigate chiral molecules. Both enantiomers of a chiral molecule show the same VCD intensities but with opposite sign, meaning that their spectra are mirror images with respect to the wavenumber axis. If theoretical methods are used to predict the VCD spectrum of a chiral molecule, this allows to determine the absolute configuration of an experimental sample.

A few quantum chemistry software packages provide the possibility to obtain VCD intensities by static calculations with DFT. These implementations compute

rotational strengths relying either on magnetic field perturbation theory [80–83] or on nuclear velocity perturbation theory [84–90]. Alternatively, it has been shown in the context of MD simulations [91–93] that the VCD spectrum can be calculated by Fourier transforming the cross-correlation of the dipole moment and the magnetic moment. (The terms dipole moment and magnetic moment are used throughout this thesis to refer to the electric dipole moment and the magnetic dipole moment, respectively.) A derivation starting with the one-dimensional harmonic oscillator analogous to Sect. 3.3 is not possible here, since this system does not possess a magnetic moment. Nevertheless, the expressions for IR and VCD spectra in reference [91] can be compared, revealing that the prefactors—in SI units—just differ by the speed of light c . The same result is found with the formulas in reference [93]. Following Eq. (3.56) for the IR intensity, the VCD spectrum is therefore defined as

$$\Delta A(\omega) = \frac{N_A}{24 \pi \epsilon_0 c^3 k_B T} \int_{-\infty}^{\infty} [\langle \dot{\boldsymbol{\mu}}(\tau) \cdot \dot{\mathbf{m}}(\tau + t) \rangle_{\tau} - \langle \dot{\mathbf{m}}(\tau) \cdot \dot{\boldsymbol{\mu}}(\tau + t) \rangle_{\tau}] \exp(-i\omega t) dt, \quad (3.85)$$

where \mathbf{m} is the magnetic moment. The corresponding wavenumber-dependent representation reads as

$$\Delta A(\tilde{\nu}) = \frac{N_A}{12 \epsilon_0 c^2 k_B T} \int_{-\infty}^{\infty} [\langle \dot{\boldsymbol{\mu}}(\tau) \cdot \dot{\mathbf{m}}(\tau + t) \rangle_{\tau} - \langle \dot{\mathbf{m}}(\tau) \cdot \dot{\boldsymbol{\mu}}(\tau + t) \rangle_{\tau}] \exp(-2 \pi i c \tilde{\nu} t) dt. \quad (3.86)$$

The crucial point in this approach is the calculation of the magnetic moments. While dipole moments are readily accessible in AIMD by the methods described in Sect. 3.4, this is not the case for magnetic moments so far. Previous applications of the time-correlation formalism applied atomic axial tensors by magnetic field perturbation theory to parametrize the MD force field [92], or they used atomic partial charges to calculate the magnetic moment according to the classical definition for point charges:

$$\mathbf{m}_I = \frac{1}{2} \sum_{A=1}^M q_A \mathbf{R}_A \times \mathbf{V}_A. \quad (3.87)$$

Either the charges were fixed [91], or they were obtained by population analyses in a QM/MM setup [93, 94]. The utilization of atomic partial charges is perfectly suited for MD simulations with classical force fields. However, it poses a clear restriction for AIMD where the complete electron density is known, and computing atomic partial charges drops information that is actually present. Furthermore, the charges always depend on the method chosen for the population analysis, so they are not uniquely defined. Therefore, an important aim in the course of this thesis was the development of a model for magnetic moments in AIMD that directly relies on the electron density.

In the Wannier center approach, dipole moments are calculated by a classical sum over point charges (see Eq. (3.70)). This suggests to extend Eq. (3.87) for magnetic moments to include the Wannier centers as equivalents of electron pairs:

$$\mathbf{m}_I = -2e \cdot \frac{1}{2} \sum_{i=1}^N \mathbf{r}_i \times \mathbf{v}_i + e \cdot \frac{1}{2} \sum_{A=1}^M Z_A \mathbf{R}_A \times \mathbf{V}_A, \quad (3.88)$$

where the first sum is over all Wannier centers and the second sum is over all nuclei with the effective charges Z_A accounting for pseudopotentials. This expression includes the velocities \mathbf{v}_i of the Wannier centers. In principle, these can readily be computed by finite difference derivation of the Wannier center coordinates \mathbf{r}_i analogous to the nuclear velocities in Eq. (3.23). In practice, this is hampered by the fact that there is no specific ordering of the Wannier centers, so they are arbitrarily mixed in each step of the trajectory. This requires to sort the Wannier centers in each snapshot, so that they can be followed along the trajectory before the velocities are calculated. A reasonable criterion for this purpose is that the sum of the squared distances between the Wannier centers in two subsequent steps should become minimal. To this end, the Kuhn–Munkres algorithm [95, 96] was implemented in TRAVIS.

Another issue is the jumping of the Wannier centers in certain cases. In aromatic rings, e.g., the Wannier localization produces an alternating pattern of single and double bonds (see Sect. 4.5.3 for further details). Switching between the two possible ways to form this pattern yields large velocities of the corresponding Wannier centers, leading to unphysically large magnetic moments. Effects of this kind cannot generally be avoided, and are probably the reason, why it turned out to be impossible to obtain reasonable magnetic moments or meaningful VCD spectra with the Wannier center technique according to Eq. (3.88). Neither did the spectra coincide with experimental data, nor were they stable with respect to simulation parameters such as the timestep.

In the more general definition of the dipole moment, the sum over point charges is replaced by an integration over the electron density (see Eq. (3.76)). The corresponding classical definition of the magnetic moment reads as

$$\mathbf{m}_i = \frac{1}{2} \int_{C_i} \mathbf{r} \times \mathbf{j}(\mathbf{r}) \, d\mathbf{r}, \quad (3.89)$$

where $\mathbf{j}(\mathbf{r})$ is the electric current density. If the electric current density is known, molecular magnetic moments can be calculated in the same manner as molecular dipole moments by integration over Voronoi cells. However, the computation of the current density on the basis of the electron density requires further assumptions. In principle, these two quantities are connected by the continuity equation

$$\frac{\partial \rho(\mathbf{r})}{\partial t} + \nabla \cdot \mathbf{j}(\mathbf{r}) = 0. \quad (3.90)$$

This means that changes in the electron density act as sources and sinks of an electric current. If the electron density is saved in each snapshot of the trajectory, the time derivative can be calculated by finite difference derivation after the simulation. This allows to find the divergence of the current density in each step, but this is not sufficient for a unique definition of the current density itself. Any arbitrary solenoidal

vector field can be added to the current density without violating the continuity equation. This is equivalent to the statement that arbitrary eddy currents cannot be seen as changes in the electron density. Furthermore, it is closely related to the abovementioned jumping of the Wannier centers, e.g., the switching of the Wannier localization between the two patterns of alternating single and double bonds in an aromatic ring is just a particular eddy current. The more general concept on the basis of the current density allows to avoid these effects explicitly.

The naive ansatz to avoid eddy currents would be to demand that the current density is an irrotational vector field, so it could be expressed as the gradient of a scalar field. It is appealing that this would turn the continuity Eq. (3.90) into the Poisson equation, which can be solved under periodic boundary conditions by Fourier transform very efficiently. However, it becomes easily apparent that this would not yield the desired result: Substituting the electric field for the current density and the charge density for the density derivative, the Poisson equation also describes the electric field caused by a charge distribution. If a small electron density distribution moves with constant speed along a straight line, the density derivative looks like a dipole, being negative where the density distribution moves away and positive where it moves to. Thus, the current density of this system would look like the electric field of a dipole, ranging far into the empty space. However, it is expected that the current density of this system points into the moving direction and is zero outside of the charge distribution. For that reason, it is assumed instead that the current density is the product of the electron density $\rho(\mathbf{r})$ and a conservative velocity field $\mathbf{v}(\mathbf{r})$ which is expressed as the negative gradient of a scalar field $\alpha(\mathbf{r})$:

$$\mathbf{j}(\mathbf{r}) = \rho(\mathbf{r})\mathbf{v}(\mathbf{r}) = -\rho(\mathbf{r})\nabla\alpha(\mathbf{r}). \quad (3.91)$$

In this way, the current can only flow in spatial regions with finite electron density, but still it follows an irrotational vector field. The same ansatz is employed, e.g., to describe a potential flow in fluid dynamics, which is used to model the irrotational flow of a homogeneous fluid with negligible frictional forces. This is a reasonable analogon of the molecular electron density in the classical limit.

Inserting ansatz (3.91) into the continuity equation (3.90) yields

$$\begin{aligned} \frac{\partial\rho(\mathbf{r})}{\partial t} &= -\nabla \cdot \mathbf{j}(\mathbf{r}) \\ &= -\nabla \cdot (-\rho(\mathbf{r})\nabla\alpha(\mathbf{r})) \\ &= (\nabla\rho(\mathbf{r})) \cdot (\nabla\alpha(\mathbf{r})) + \rho(\mathbf{r})\Delta\alpha(\mathbf{r}). \end{aligned} \quad (3.92)$$

As the electron density is known from the AIMD, and its time derivative and its gradient can be calculated by finite difference derivation, this constitutes a second-order partial differential equation that needs to be solved to find the scalar field $\alpha(\mathbf{r})$ which provides the current density $\mathbf{j}(\mathbf{r})$ according to Eq. (3.91).

For a numerical solution of the differential equation (3.92), a finite difference method is used in TRAVIS. This means that the differential equation is discretized on a regular grid, replacing it by a system of linear equations. Most easily, the already present grid of the electron density data is used as discretization grid. The derivatives of $\alpha(\mathbf{r})$ are approximated by second-order central finite differences, so the current implementation only works for orthorhombic simulation cells where the cell vectors are the Cartesian coordinate axes. If the grid consists of $n_x \times n_y \times n_z$ points with spacings of h_x , h_y , and h_z along the three axes, the components of the gradient are given by

$$(D_x \alpha)_{i,j,k} = \frac{\alpha_{i+1,j,k} - \alpha_{i-1,j,k}}{2h_x}, \quad (3.93)$$

$$(D_y \alpha)_{i,j,k} = \frac{\alpha_{i,j+1,k} - \alpha_{i,j-1,k}}{2h_y}, \quad (3.94)$$

$$(D_z \alpha)_{i,j,k} = \frac{\alpha_{i,j,k+1} - \alpha_{i,j,k-1}}{2h_z}, \quad (3.95)$$

and the Laplacian reads as

$$(L\alpha)_{i,j,k} = \frac{\alpha_{i+1,j,k} - 2\alpha_{i,j,k} + \alpha_{i-1,j,k}}{h_x^2} + \frac{\alpha_{i,j+1,k} - 2\alpha_{i,j,k} + \alpha_{i,j-1,k}}{h_y^2} + \frac{\alpha_{i,j,k+1} - 2\alpha_{i,j,k} + \alpha_{i,j,k-1}}{h_z^2}, \quad (3.96)$$

where i, j , and k number the points along the x, y , and z axes, respectively. The periodic boundary conditions are properly taken into account by $i \in \mathbb{Z}/n_x\mathbb{Z}$, $j \in \mathbb{Z}/n_y\mathbb{Z}$, and $k \in \mathbb{Z}/n_z\mathbb{Z}$, so, e.g., the successor of $i = n_x - 1$ is $i = 0$ and the predecessor of $i = 0$ is $i = n_x - 1$. The grid is linearized in such a way that x lines and then xy planes of the grid follow one after another, so $l = i + jn_x + kn_xn_y$ becomes the new index in the one-dimensional arrays. This leads to the following matrix representation of the system of linear equations that emerges from the discretization of Eq. (3.92):

$$\mathbf{A} \begin{pmatrix} \alpha_0 \\ \vdots \\ \alpha_{n_x n_y n_z - 1} \end{pmatrix} = \begin{pmatrix} \left(\frac{\partial \rho}{\partial r}\right)_0 \\ \vdots \\ \left(\frac{\partial \rho}{\partial r}\right)_{n_x n_y n_z - 1} \end{pmatrix}, \quad (3.97)$$

where $\mathbf{A} = \mathbf{B} + \mathbf{G} \in \mathbb{R}^{n_x n_y n_z \times n_x n_y n_z}$ with the definitions

$$h_2 = \frac{1}{h_x^2} + \frac{1}{h_y^2} + \frac{1}{h_z^2}, \quad (3.98)$$

$$\mathbf{B} = \begin{pmatrix} \mathbf{C}_0 & \mathbf{F}_0 & \mathbf{0} & & \mathbf{F}_0 \\ \mathbf{F}_1 & \mathbf{C}_1 & \mathbf{F}_1 & \ddots & \\ \mathbf{0} & \mathbf{F}_2 & \mathbf{C}_2 & \ddots & \mathbf{0} \\ & \ddots & \ddots & \ddots & \mathbf{F}_{n_z-2} \\ \mathbf{F}_{n_z-1} & \mathbf{0} & \mathbf{F}_{n_z-1} & \mathbf{C}_{n_z-1} & \end{pmatrix} \in \mathbb{R}^{n_x n_y n_z \times n_x n_y n_z}, \quad (3.99)$$

$$\mathbf{C}_m = \begin{pmatrix} \mathbf{D}_{mn_y} & \mathbf{E}_{mn_y} & \mathbf{0} & & \mathbf{E}_{mn_y} \\ \mathbf{E}_{mn_y+1} & \mathbf{D}_{mn_y+1} & \mathbf{E}_{mn_y+1} & \ddots & \\ \mathbf{0} & \mathbf{E}_{mn_y+2} & \mathbf{D}_{mn_y+2} & \ddots & \mathbf{0} \\ & \ddots & \ddots & \ddots & \mathbf{E}_{mn_y+n_y-2} \\ \mathbf{E}_{mn_y+n_y-1} & \mathbf{0} & \mathbf{E}_{mn_y+n_y-1} & \mathbf{D}_{mn_y+n_y-1} & \end{pmatrix} \in \mathbb{R}^{n_x n_y \times n_x n_y}, \quad (3.100)$$

$$\mathbf{D}_n = \begin{pmatrix} -2h_2 \rho_{nn_x} & \frac{\rho_{nn_x}}{h_x^2} & 0 & & \frac{\rho_{nn_x}}{h_x^2} \\ \frac{\rho_{nn_x+1}}{h_x^2} & -2h_2 \rho_{nn_x+1} & \frac{\rho_{nn_x+1}}{h_x^2} & \ddots & \\ 0 & \frac{\rho_{nn_x+2}}{h_x^2} & -2h_2 \rho_{nn_x+2} & \ddots & 0 \\ & \ddots & \ddots & \ddots & \frac{\rho_{nn_x+n_x-2}}{h_x^2} \\ \frac{\rho_{nn_x+n_x-1}}{h_x^2} & 0 & \frac{\rho_{nn_x+n_x-1}}{h_x^2} & -2h_2 \rho_{nn_x+n_x-1} & \end{pmatrix} \in \mathbb{R}^{n_x \times n_x}, \quad (3.101)$$

$$\mathbf{E}_n = \begin{pmatrix} \frac{\rho_{nn_x}}{h_y^2} & 0 & \cdots & 0 \\ 0 & \frac{\rho_{nn_x+1}}{h_y^2} & \ddots & \vdots \\ \vdots & \ddots & \ddots & 0 \\ 0 & \cdots & 0 & \frac{\rho_{nn_x+n_x-1}}{h_y^2} \end{pmatrix} \in \mathbb{R}^{n_x \times n_x}, \quad (3.102)$$

$$\mathbf{F}_m = \begin{pmatrix} \frac{\rho_{mn_x n_y}}{h_z^2} & 0 & \cdots & 0 \\ 0 & \frac{\rho_{mn_x n_y+1}}{h_z^2} & \ddots & \vdots \\ \vdots & \ddots & \ddots & 0 \\ 0 & \cdots & 0 & \frac{\rho_{mn_x n_y+n_x n_y-1}}{h_z^2} \end{pmatrix} \in \mathbb{R}^{n_x n_y \times n_x n_y}, \quad (3.103)$$

$$\mathbf{G} = \begin{pmatrix} \mathbf{H}_0 & \mathbf{K}_0 & \mathbf{0} & & -\mathbf{K}_0 \\ -\mathbf{K}_1 & \mathbf{H}_1 & \mathbf{K}_1 & \ddots & \\ \mathbf{0} & -\mathbf{K}_2 & \mathbf{H}_2 & \ddots & \mathbf{0} \\ & \ddots & \ddots & \ddots & \mathbf{K}_{n_z-2} \\ \mathbf{K}_{n_z-1} & \mathbf{0} & -\mathbf{K}_{n_z-1} & \mathbf{H}_{n_z-1} & \end{pmatrix} \in \mathbb{R}^{n_x n_y n_z \times n_x n_y n_z}, \quad (3.104)$$

$$\mathbf{H}_m = \begin{pmatrix} \mathbf{I}_{mn_y} & \mathbf{J}_{mn_y} & \mathbf{0} & & -\mathbf{J}_{mn_y} \\ -\mathbf{J}_{mn_y+1} & \mathbf{I}_{mn_y+1} & \mathbf{J}_{mn_y+1} & \ddots & \\ \mathbf{0} & -\mathbf{J}_{mn_y+2} & \mathbf{I}_{mn_y+2} & \ddots & \mathbf{0} \\ & \ddots & \ddots & \ddots & \mathbf{J}_{mn_y+n_y-2} \\ \mathbf{J}_{mn_y+n_y-1} & \mathbf{0} & -\mathbf{J}_{mn_y+n_y-1} & \mathbf{I}_{mn_y+n_y-1} & \end{pmatrix} \in \mathbb{R}^{n_x n_y \times n_x n_y}, \quad (3.105)$$

$$\mathbf{I}_n = \begin{pmatrix} 0 & \frac{(\frac{\partial \rho}{\partial x})_{mn_x}}{2h_x} & 0 & & -\frac{(\frac{\partial \rho}{\partial x})_{mn_x}}{2h_x} \\ -\frac{(\frac{\partial \rho}{\partial x})_{mn_x+1}}{2h_x} & 0 & \frac{(\frac{\partial \rho}{\partial x})_{mn_x+1}}{2h_x} & \ddots & \\ 0 & -\frac{(\frac{\partial \rho}{\partial x})_{mn_x+2}}{2h_x} & 0 & \ddots & 0 \\ & \ddots & \ddots & \ddots & \frac{(\frac{\partial \rho}{\partial x})_{mn_x+n_x-2}}{2h_x} \\ \frac{(\frac{\partial \rho}{\partial x})_{mn_x+n_x-1}}{2h_x} & 0 & -\frac{(\frac{\partial \rho}{\partial x})_{mn_x+n_x-1}}{2h_x} & 0 & \end{pmatrix} \in \mathbb{R}^{n_x \times n_x}, \quad (3.106)$$

$$\mathbf{J}_n = \begin{pmatrix} \frac{(\frac{\partial \rho}{\partial y})_{mn_y}}{2h_y} & 0 & \dots & 0 \\ 0 & \frac{(\frac{\partial \rho}{\partial y})_{mn_y+1}}{2h_y} & \ddots & \vdots \\ \vdots & \ddots & \ddots & 0 \\ 0 & \dots & 0 & \frac{(\frac{\partial \rho}{\partial y})_{mn_y+n_y-1}}{2h_y} \end{pmatrix} \in \mathbb{R}^{n_x \times n_x}, \quad (3.107)$$

$$\mathbf{K}_m = \begin{pmatrix} \frac{(\frac{\partial \rho}{\partial z})_{mn_x n_y}}{2h_z} & 0 & \dots & 0 \\ 0 & \frac{(\frac{\partial \rho}{\partial z})_{mn_x n_y+1}}{2h_z} & \ddots & \vdots \\ \vdots & \ddots & \ddots & 0 \\ 0 & \dots & 0 & \frac{(\frac{\partial \rho}{\partial z})_{mn_x n_y+n_x n_y-1}}{2h_z} \end{pmatrix} \in \mathbb{R}^{n_x n_y \times n_x n_y}. \quad (3.108)$$

The square matrix \mathbf{A} is sparse, and for the applications studied in this thesis, it has in the order of 10^6 rows and columns. Several iterative algorithms have been developed to solve systems of linear equations with this size [97]. As \mathbf{A} is not symmetric, the extended biconjugate gradient stabilized method BiCGstab(l) [98–101] was selected for TRAVIS. A FORTRAN implementation of this method is available in reference [102], which was transferred to C++ to be used in TRAVIS. The conver-

gence of the algorithm is improved by using an incomplete LU factorization [103] of \mathbf{A} for preconditioning. To exploit the sparsity of \mathbf{A} and its incomplete LU factorization for memory efficiency, the TRAVIS implementation relies on the compressed row storage format [97] to store the matrices. This means that not the whole matrices are kept in memory, but only the value and the position of each nonzero entry are saved.

Experience shows that the convergence behavior of the BiCGstab(l) algorithm needs special attention due to numerical issues. Apart from the fact that the residual is not smoothly reduced but oscillates, the algorithm usually reaches a minimum after some iterations and strongly diverges then. Furthermore, it is not easy to estimate how small the absolute value of the residual has to be to obtain reasonably converged magnetic moments. Therefore, the following way is taken to select a convergence threshold: In the first snapshot, the solution guess for $\alpha(\mathbf{r})$ is set to zero on the whole grid. The threshold for all steps is calculated relative to the residual in the first snapshot with this initial guess. Relative convergence criteria of 0.005 or 0.01 proved to be sufficient to converge the final magnetic moments within a few percent in typical bulk phase simulations studied here (see also Sect. 4.6.1). With these values and $l = 4$, about 10–20 iterations are usually needed to solve the system of linear equations in the first step. Subsequently, the solution of the previous step is used as guess for the next step, reducing the number of iterations to less than 10 in most cases. The following check is incorporated to facilitate the application in a black-box manner: if the algorithm diverges before the threshold is reached, it is restarted and the threshold is temporarily increased to the lowest residual that occurred in the first run for the snapshot. Future work could focus on other solution algorithms for the system of linear equations (3.97) that might be more stable in this regard.

The integral of the density time derivative over the whole grid, which is the sum of all elements on the right-hand-side of (3.97), has to vanish. Otherwise, this would mean that the total electron density changes and that a current flows out of or into the grid, but this is incompatible with periodic boundary conditions and would imply that the total number of electrons is not conserved in the AIMD. Caused by the error of the finite difference approximation to the time derivative, this condition is not necessarily fulfilled in practice. For that reason, the values of the density time derivative are shifted by their average before the system of linear equations (3.97) is solved.

Another issue occurs in regions with vanishing electron density. In principle, $\alpha(\mathbf{r})$ can take arbitrary values there without violating the differential equation (3.92). To improve the stability of the solution algorithm in this case, the TRAVIS implementation provides the possibility to add a constant background electron density. Since this is done only for the determination of $\alpha(\mathbf{r})$, other quantities such as the dipole moment are not modified. Experience shows that densities in the order of $10^{-3} e/\text{nm}^3$ are necessary for gas phase calculations with large empty regions of the simulation cell. However, this is not needed at all for the bulk phase simulations investigated here.

Analogous to the dipole moment, the magnetic moment depends on the choice of the reference point. However, not only the position of the reference point, but also its velocity are important. For an arbitrary electron density distribution with the centroid $\mathbf{s}(t)$ that internally vibrates and globally moves, it can be shown (see Appendix B.6) that the magnetic moment is given by

$$\mathbf{m}(t) = \mathbf{m}^s(t) + \frac{1}{2}\mathbf{s}(t) \times \mathbf{J}^s(t) + \frac{1}{2}\boldsymbol{\mu}^s(t) \times \frac{\partial \mathbf{s}(t)}{\partial t} + \frac{1}{2}q(t)\mathbf{s}(t) \times \frac{\partial \mathbf{s}(t)}{\partial t}. \quad (3.109)$$

Here, $\mathbf{m}^s(t)$, $\mathbf{J}^s(t)$, and $\boldsymbol{\mu}^s(t)$ are the magnetic moment, the total current, and the dipole moment, respectively, in the centroid coordinate system. The total current is the integral over the current density,

$$\mathbf{J} = \int_{C_i^e} \mathbf{j}(\mathbf{r}) \, d\mathbf{r}, \quad (3.110)$$

just as the charge is the integral over the electron density. Thus, the second term of the sum in Eq. (3.109) is similar to the dependence of the dipole moment on the reference point in Eq. (3.84). The time-dependence of $\mathbf{m}^s(t)$ and $\mathbf{J}^s(t)$ just stems from the internal vibrations of the electron density, but similar to $\mathbf{m}(t)$, a general total current is given by (see Appendix B.6)

$$\mathbf{J}(t) = \mathbf{J}^s(t) + q(t) \frac{\partial \mathbf{s}(t)}{\partial t}, \quad (3.111)$$

where the translational motion appears too. The grid used to solve the partial differential equation (3.92) is fixed with respect to the simulation cell and the molecules move around during the simulation. Based on the same justification as for dipole moments, however, the molecular center of mass is the most reasonable choice for the reference point when VCD spectra are calculated. Thus, the molecular magnetic moments and the total currents obtained by integration of the current density solving Eq. (3.92) are transformed according to Eqs. (3.109) and (3.111) in TRAVIS.

References

1. M. Brehm, B. Kirchner, *J. Chem. Inf. Model.* **51**, 2007–2023 (2011)
2. M. Brehm, *Analyzing trajectories from molecular simulation* (Universität Leipzig, Leipzig, 2014)
3. M. Thomas, M. Brehm, R. Fligg, P. Vöhringer, B. Kirchner, *Phys. Chem. Chem. Phys.* **15**, 6608–6622 (2013)
4. M. Thomas, M. Brehm, O. Hollóczki, Z. Kelemen, L. Nyulászi, T. Pasinszki, B. Kirchner, *J. Chem. Phys.* **141**, 024510 (2014)
5. M. Thomas, M. Brehm, B. Kirchner, *Phys. Chem. Chem. Phys.* **17**, 3207–3213 (2015)
6. J.M. Dickey, A. Paskin, *Phys. Rev.* **188**, 1407–1418 (1969)
7. R. Futrelle, D. McGinty, *Chem. Phys. Lett.* **12**, 285–287 (1971)

8. E. Kestemont, J.V. Craen, J. Comput. Phys. **22**, 451–458 (1976)
9. D.W. Noid, M.L. Koszykowski, R.A. Marcus, J. Chem. Phys. **67**, 404–408 (1977)
10. P.H. Berens, D.H.J. Mackay, G.M. White, K.R. Wilson, J. Chem. Phys. **79**, 2375–2389 (1983)
11. M.-P. Gaigeot, M. Martinez, R. Vuilleumier, Mol. Phys. **105**, 2857–2878 (2007)
12. M. Frigo, S. Johnson, Proc. IEEE **93**, 216–231 (2005)
13. C.E. Shannon, Proc. IEEE **86**, 447–457 (1998)
14. G. Mathias, M.D. Baer, J. Chem. Theory Comput. **7**, 2028–2039 (2011)
15. G. Mathias, S.D. Ivanov, A. Witt, M.D. Baer, D. Marx, J. Chem. Theory Comput. **8**, 224–234 (2012)
16. S.D. Ivanov, A. Witt, D. Marx, Phys. Chem. Chem. Phys. **15**, 10270–10299 (2013)
17. J. Sun, G. Niehues, H. Forbert, D. Decka, G. Schwaab, D. Marx, M. Havenith, J. Am. Chem. Soc. **136**, 5031–5038 (2014)
18. J.M. Bowman, X. Zhang, A. Brown, J. Chem. Phys. **119**, 646–650 (2003)
19. M. Kaledin, A. Brown, A.L. Kaledin, J.M. Bowman, J. Chem. Phys. **121**, 5646–5653 (2004)
20. M. Buchner, B.M. Ladanyi, R.M. Stratt, J. Chem. Phys. **97**, 8522–8535 (1992)
21. M. Cho, G.R. Fleming, S. Saito, I. Ohmine, R.M. Stratt, J. Chem. Phys. **100**, 6672–6683 (1994)
22. R.M. Stratt, Acc. Chem. Res. **28**, 201–207 (1995)
23. T. Keyes, J. Phys. Chem. A **101**, 2921–2930 (1997)
24. T. Kalbfleisch, T. Keyes, J. Chem. Phys. **108**, 7375–7383 (1998)
25. M. Nonella, G. Mathias, P. Tavan, J. Phys. Chem. A **107**, 8638–8647 (2003)
26. R.A. Wheeler, H. Dong, S.E. Boesch, Chem. Phys. Chem. **4**, 382–384 (2003)
27. R.A. Wheeler, H. Dong, Chem. Phys. Chem. **4**, 1227–1230 (2003)
28. M. Schmitz, P. Tavan, J. Chem. Phys. **121**, 12233–12246 (2004)
29. M. Schmitz, P. Tavan, J. Chem. Phys. **121**, 12247–12258 (2004)
30. A. Strachan, J. Chem. Phys. **120**, 1–4 (2004)
31. M. Martinez, M.-P. Gaigeot, D. Borgis, R. Vuilleumier, J. Chem. Phys. **125**, 144106 (2006)
32. C. Eckart, Phys. Rev. **47**, 552–558 (1935)
33. O. Sorkine, Least-squares rigid motion using SVD, http://igl.ethz.ch/projects/ARAP/svd_rot.pdf. Accessed 7 June 2013
34. R.G. Gordon, J. Chem. Phys. **43**, 1307–1312 (1965)
35. D. McQuarrie, *Statistical Mechanics* (University Science Books, Sausalito, 2000)
36. D. Marx, J. Hutter, *Ab Initio Molecular Dynamics: Basic Theory and Advanced Methods* (Cambridge University Press, Cambridge, 2009)
37. J. Borysow, M. Moraldi, L. Frommhold, Mol. Phys. **56**, 913–922 (1985)
38. P.L. Silvestrelli, M. Bernasconi, M. Parrinello, Chem. Phys. Lett. **277**, 478–482 (1997)
39. M.-P. Gaigeot, M. Sprik, J. Phys. Chem. B **107**, 10344–10358 (2003)
40. R. Ramírez, T. López-Ciudad, P.P. Kumar, D. Marx, J. Chem. Phys. **121**, 3973–3983 (2004)
41. C.P. Lawrence, A. Nakayama, N. Makri, J.L. Skinner, J. Chem. Phys. **120**, 6621–6624 (2004)
42. R. Iftimie, M.E. Tuckerman, J. Chem. Phys. **122**, 214508 (2005)
43. R.D. King-Smith, D. Vanderbilt, Phys. Rev. B **47**, 1651–1654 (1993)
44. R. Resta, Rev. Mod. Phys. **66**, 899–915 (1994)
45. R. Resta, Phys. Rev. Lett. **80**, 1800–1803 (1998)
46. A. Putrino, D. Sebastiani, M. Parrinello, J. Chem. Phys. **113**, 7102–7109 (2000)
47. N. Marzari, D. Vanderbilt, Phys. Rev. B **56**, 12847–12865 (1997)
48. P.L. Silvestrelli, M. Parrinello, Phys. Rev. Lett. **82**, 3308–3311 (1999)
49. P.L. Silvestrelli, M. Parrinello, J. Chem. Phys. **111**, 3572–3580 (1999)
50. B. Kirchner, J. Hutter, J. Chem. Phys. **121**, 5133–5142 (2004)
51. R. Iftimie, J.W. Thomas, M.E. Tuckerman, J. Chem. Phys. **120**, 2169–2181 (2004)
52. R.J. Heaton, P.A. Madden, S.J. Clark, S. Jahn, J. Chem. Phys. **125**, 144104 (2006)
53. M. Salanne, R. Vuilleumier, P.A. Madden, C. Simon, P. Turq, B. Guillot, J. Phys. Condens. Matter **20**, 494207 (2008)
54. Q. Wan, L. Spanu, G.A. Galli, F. Gygi, J. Chem. Theory Comput. **9**, 4124–4130 (2013)
55. F. Hirshfeld, Theor. Chim. Acta **44**, 129–138 (1977)

56. M. Yáñez, R.F. Stewart, J.A. Pople, *Acta Cryst.* **A34**, 641–648 (1978)
57. R.F.W. Bader, *Chem. Rev.* **91**, 893–928 (1991)
58. K. Laasonen, M. Sprik, M. Parrinello, R. Car, *J. Chem. Phys.* **99**, 9080–9089 (1993)
59. P.M.W. Gill, *J. Phys. Chem.* **100**, 15421–15427 (1996)
60. L.D. Site, A. Alavi, R.M. Lynden-Bell, *Mol. Phys.* **96**, 1683–1693 (1999)
61. C. Fonseca Guerra, J.-W. Handgraaf, E.J. Baerends, F.M. Bickelhaupt, *J. Comput. Chem.* **25**, 189–210 (2004)
62. P. Bultinck, C. Van Alsenoy, P.W. Ayers, R. Carbó-Dorca, *J. Chem. Phys.* **126**, 144111 (2007)
63. T.C. Lillestolen, R.J. Wheatley, *Chem. Commun.* **50**, 5909–5911 (2008)
64. T.A. Manz, D.S. Sholl, *J. Chem. Theory Comput.* **8**, 2844–2867 (2012)
65. D. Geldof, A. Krishtal, F. Blockhuys, C. Van Alsenoy, *J. Chem. Phys.* **140**, 144104 (2014)
66. G. Voronoi, *J. Reine Angew. Math.* **134**, 198 (1908)
67. M. Pollak, R. Rein, *J. Chem. Phys.* **47**, 2045–2052 (1967)
68. P. Politzer, R.R. Harris, *J. Am. Chem. Soc.* **92**, 6451–6454 (1970)
69. B. Rousseau, A. Peeters, C.V. Alsenoy, *J. Mol. Struct.* **538**, 235–238 (2001)
70. M. Swart, P.T. Van Duijnen, *Int. J. Quantum Chem.* **111**, 1763–1772 (2011)
71. E.R. Batista, S.S. Xantheas, H. Jónsson, *J. Chem. Phys.* **111**, 6011–6015 (1999)
72. F.M. Richards, *J. Mol. Biol.* **82**, 1–14 (1974)
73. B. Gellatly, J. Finney, *J. Mol. Biol.* **161**, 305–322 (1982)
74. C.H. Rycroft, *Chaos* **19**, 041111 (2009)
75. M. Brehm, H. Weber, A.S. Pensado, A. Stark, B. Kirchner, *Phys. Chem. Chem. Phys.* **14**, 5030–5044 (2012)
76. A. Bondi, *J. Phys. Chem.* **68**, 441–451 (1964)
77. R.S. Rowland, R. Taylor, *J. Phys. Chem.* **100**, 7384–7391 (1996)
78. M. Mantina, A.C. Chamberlin, R. Valero, C.J. Cramer, D.G. Truhlar, *J. Phys. Chem. A* **113**, 5806–5812 (2009)
79. B. Cordero, V. Gómez, A.E. Platero-Prats, M. Revés, J. Echeverría, E. Cremades, F. Barragán, S. Alvarez, *Dalton Trans.* **21**, 2832–2838 (2008)
80. P.J. Stephens, *J. Phys. Chem.* **89**, 748–752 (1985)
81. P.J. Stephens, *J. Phys. Chem.* **91**, 1712–1715 (1987)
82. J. Cheeseman, M. Frisch, F. Devlin, P. Stephens, *Chem. Phys. Lett.* **252**, 211–220 (1996)
83. V.P. Nicu, J. Neugebauer, S.K. Wolff, E.J. Baerends, *Theor. Chem. Acc.* **119**, 245–263 (2008)
84. L.A. Nafie, T.B. Freedman, *J. Chem. Phys.* **78**, 7108–7116 (1983)
85. L.A. Nafie, *J. Chem. Phys.* **79**, 4950–4957 (1983)
86. A. Buckingham, P. Fowler, P. Galwas, *Chem. Phys.* **112**, 1–14 (1987)
87. L.A. Nafie, *J. Chem. Phys.* **96**, 5687–5702 (1992)
88. L.A. Nafie, *J. Phys. Chem. A* **108**, 7222–7231 (2004)
89. A. Scherrer, R. Vuilleumier, D. Sebastiani, *J. Chem. Theory Comput.* **9**, 5305–5312 (2013)
90. A. Scherrer, F. Agostini, D. Sebastiani, E.K.U. Gross, R. Vuilleumier, *J. Chem. Phys.* **143**, 074106 (2015)
91. S. Abbate, G. Longhi, K. Kwon, A. Moscowitz, *J. Chem. Phys.* **108**, 50–62 (1998)
92. J. Horníček, P. Kaprálová, P. Bouř, *J. Chem. Phys.* **127**, 084502 (2007)
93. S. Yang, M. Cho, *J. Chem. Phys.* **131**, 135102 (2009)
94. J.-H. Choi, M. Cho, *J. Chem. Theory Comput.* **7**, 4097–4103 (2011)
95. H.W. Kuhn, *Nav. Res. Logist.* **2**, 83–97 (1955)
96. J. Munkres, *J. Soc. Indust. Appl. Math.* **5**, 32–38 (1957)
97. R. Barrett, M. Berry, T. Chan, J. Demmel, J. Donato, J. Dongarra, V. Eijkhout, R. Pozo, C. Romine, H. van der Vorst, *Templates for the Solution of Linear Systems: Building Blocks for Iterative Methods*, Society for Industrial and Applied Mathematics, 1994, Electronic version: <http://www.netlib.org/templates/templates.pdf>. Accessed 12 Sep 2014
98. H. van der Vorst, *SIAM. J. Sci. Stat. Comput.* **13**, 631–644 (1992)
99. G.L. Sleijpen, D.R. Fokkema, *Electron. Trans. Numer. Anal.* **1**, 11–32 (1993)
100. G.L. Sleijpen, H.A. van der Vorst, *Numer. Algorithms* **10**, 203–223 (1995)
101. G. Sleijpen, H. van der Vorst, *Computing* **56**, 141–163 (1996)
102. M. Botchev, D. Fokkema, <http://www.staff.science.uu.nl/~vorst102/software.html>. Accessed 7 Nov 2014
103. J.A. Meijerink, H.A. van der Vorst, *Math. Comp.* **31**, 148–162 (1977)

Chapter 4

Applications

4.1 Spectra of Single Molecules

4.1.1 *Comparison of Molecular Dynamics and Static Calculations*

In Chap. 3, the theoretical foundations to calculate vibrational spectra from AIMD simulations were discussed. Several derivations are based on the idea that the MD approach and static quantum chemical calculations should provide the same spectra for a system of harmonic oscillators. The general success of the harmonic approximation for the prediction of vibrational spectra of real molecules suggests to compare these two techniques for single molecules in the gas phase, which are readily accessible in both ways. In addition, this allows to present all the basic spectra analysis features available in TRAVIS and to discuss some general points that need to be considered for AIMD spectra. For this purpose, the three small organic molecules methanol, acetone, and nitromethane were selected as test cases to cover a certain range of functional groups. Computational details and a discussion of the dipole moments from the AIMD simulations at 400 K and the static calculations within the harmonic approximation can be found in Appendix A. Except for the normal coordinate analysis, the results in this section have been published in Ref. [1]. The Raman spectra shown here are slightly different due to a mistake in TRAVIS that was fixed shortly after publication of Ref. [1].

The comparison of the spectra for methanol (see Fig. 4.1) is divided into six parts. The first part shows the power spectrum as solid line and its integral as dotted line. The spectrum is normalized in such a way that the total integral is equal to the number of 18 degrees of freedom, meaning that it was divided by the average simulation temperature. The gray dashed lines indicate the vibrational wavenumbers from the static calculation. At each of these wavenumbers, the power spectrum would feature a band of the same intensity in the harmonic case. Obviously, this is not strictly fulfilled as some of the bands are shifted and the peak integrals are not exactly equal to the num-

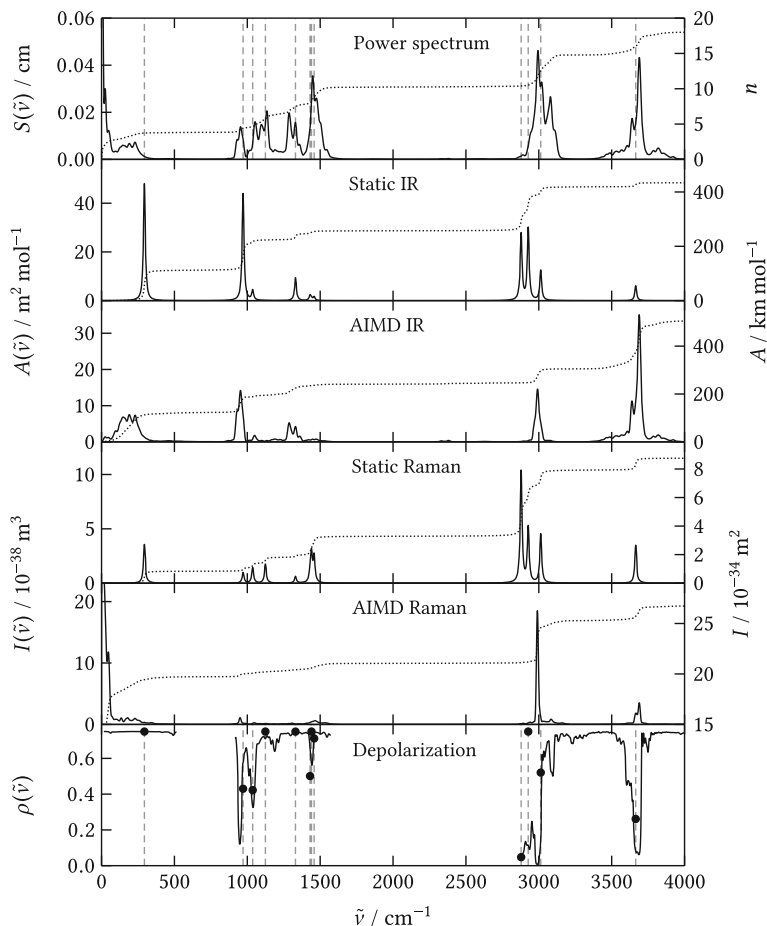


Fig. 4.1 Spectra of methanol in the gas phase: power spectrum, IR spectrum, and Raman spectrum from an AIMD simulation, IR spectrum and Raman spectrum from a static calculation. The *gray dashed lines* denote the vibrational frequencies from the static calculation, and the *dotted lines* show the integrals with the scales on the *right* side. The Raman depolarization ratios from the static calculation are shown as *circles*

ber of underlying modes. Several reasons have to be considered for these deviations. First of all, the system is not purely harmonic as the potential of a real molecule is applied. Furthermore, the finite simulation timestep introduces a certain blueshift that is particularly important in the region of higher wavenumbers (see Sect. 3.2.3). Moreover, the simulation is not fully in equilibrium and some modes carry more energy than others on average. Finally, the electronic structure methods in the AIMD and the static calculations are not fully consistent due to the restrictions imposed by the employed software packages. Although the same exchange-correlation functional is used, the basis sets are only of similar quality but not equal.

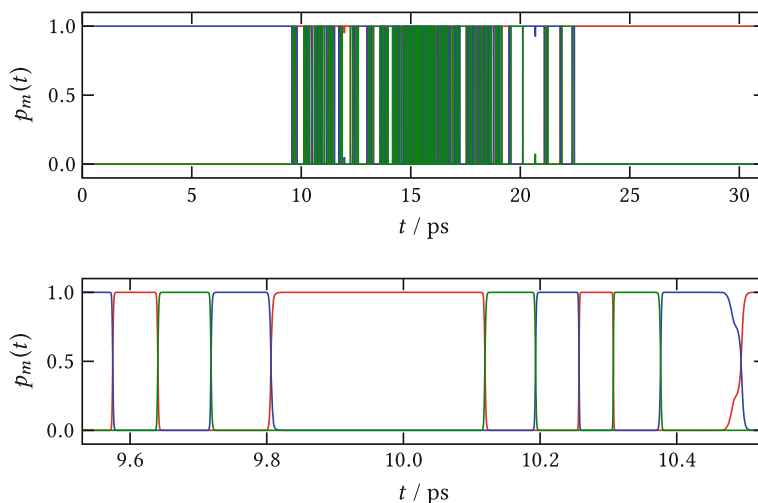


Fig. 4.2 Fitness of the reference structures employed in the normal coordinate analysis of methanol in the gas phase. The three probabilities are shown in different colors over the whole trajectory (*above*) and 1 ps of the trajectory (*below*)

For a more detailed discussion of the power spectrum, a normal coordinate analysis was carried out (see Figs. 4.2 and 4.3, and Table 4.1). A geometry optimization was performed using the electronic structure method of the AIMD and the three cyclic permutations of the methyl hydrogen atoms were employed as reference structures to account for the rotation of the methyl group in the trajectory. (Only one optimized structure has to be entered in TRAVIS, and the permutations are created within the program.) As the distance function, the sum of the three dihedral angles over the C–O bond was applied, and a width parameter of $\sigma = 15^\circ$ was used for the switching region. The resulting probabilities (see Fig. 4.2) clearly show that the methyl group undergoes regular rotations in the middle of the simulation while it stays in one minimum in the beginning and in the end. The magnified part of 1 ps demonstrates how the exponential probability function (3.45) in connection with the chosen width parameter provides for smooth transitions between the reference structures.

The power spectrum in the normal coordinate analysis (see Fig. 4.3) differs from the original power spectrum (see Fig. 4.1) due to the transformation of the trajectory to the Eckart frame of reference. The former possesses narrower bands and it does not show an intense peak at zero wavenumber because global rotation and translation of the molecule are removed and only the 12 internal degrees of freedom remain. In particular the global rotation is responsible for the broadening of the bands in the original power spectrum while the translation appears as a strong peak close to zero. For all internal degrees of freedom, the normal coordinate analysis provides individual mode spectra which are shown in different colors. Each of the spectra consists of a well defined single peak that can be characterized by its maximum (see Table 4.1). Other quantities such as the centroid of the spectrum are less suitable

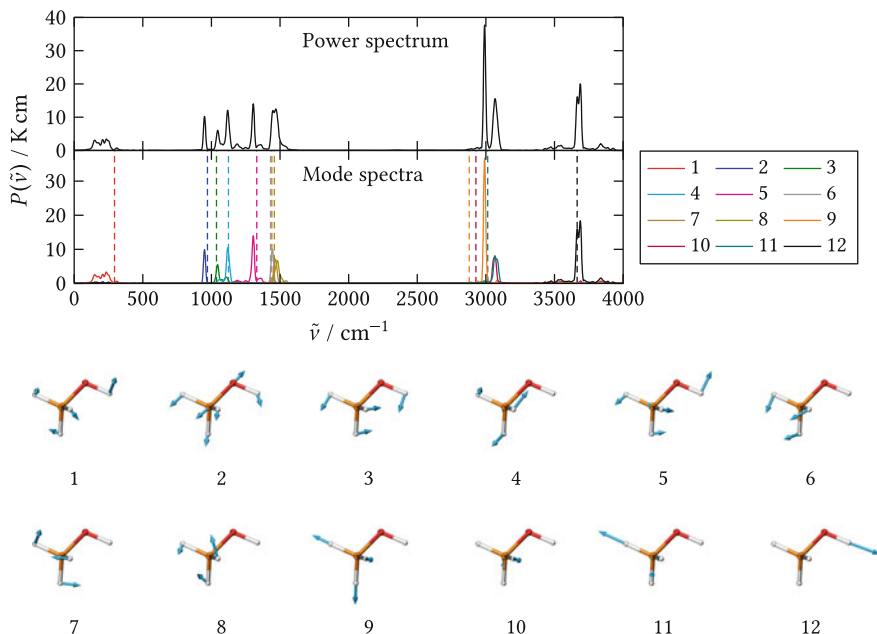


Fig. 4.3 Normal coordinate spectra of methanol in the gas phase: total power spectrum and dissection into mode spectra. The *colored dashed lines* indicate the corresponding vibrational frequencies in the static calculation. Graphical representations of the normal coordinate vectors obtained from the AIMD simulation

since misleading values can be obtained if the separation is not perfect and other modes slightly contribute at vastly different wavenumbers. The normal mode vectors corresponding to the spectra are in very good agreement with the ones from the static calculation, allowing to assign a wavenumber from the static calculation to each mode as indicated by the colored dashed lines. The largest differences concern the CH stretching modes, which are significantly blue-shifted in the AIMD simulation. At least to a certain amount, this is caused by the finite timestep, but it is interesting to note that not all three modes are affected in the same way and the AIMD gives almost equal wavenumbers for the two antisymmetric vibrations (modes 10 and 11). Thus, a significant coupling of these modes also plays a role. In contrast, almost no blueshift is observed for the OH stretching vibration (mode 12) though it occurs at even higher wavenumbers. This is likely related to the anharmonicity of the bond potential. According to the observations in Sect. 3.2.3, the temperature is clearly too low to fully recover this anharmonicity, but the induced redshift at least cancels the blueshift due to the finite timestep. Another effect are the side lobes of the OH stretching band. Their distance to the main peak exactly matches the wavenumber of the HCOH torsion (mode 1), so these are combination bands of the two modes. Also the torsional mode shows a significant deviation from the static calculation as a consequence of the regularly rotating methyl group. The AIMD simulation samples

Table 4.1 Normal coordinates of methanol in the gas phase: Wavenumbers $\tilde{\nu}_{\text{static}}$ from the static calculation, peak maxima $\tilde{\nu}_{\text{AIMD}}$ and average mode temperatures $\langle T \rangle$ from the AIMD simulation

No.	$\tilde{\nu}_{\text{static}}/\text{cm}^{-1}$	$\tilde{\nu}_{\text{AIMD}}/\text{cm}^{-1}$	$\langle T \rangle/\text{K}$	Description
1	294	199	474	HCOH torsion
2	971	950	203	CO stretching
3	1037	1044	257	CH ₃ bending + COH bending
4	1124	1120	382	CH ₃ bending
5	1330	1305	495	COH bending + CH ₃ bending
6	1431	1444	275	CH ₃ bending
7	1440	1466	246	CH ₃ bending
8	1459	1480	272	CH ₃ bending
9	2879	2991	800	Symmetric CH ₃ stretching
10	2927	3064	289	Antisymmetric CH ₃ stretching
11	3013	3066	393	Antisymmetric CH ₃ stretching
12	3665	3677	1015	OH stretching

the complete torsional potential while the static calculation approximates it by a clearly insufficient quadratic function around one minimum.

As the mode spectra are not normalized here, their integrals give the average temperature of each mode (see Table 4.1). It is immediately apparent that there are significant differences, confirming that the simulation is not fully in equilibrium. In particular the symmetric CH₃ stretching vibration (mode 9) and the OH stretching vibration carry an excess of energy. This phenomenon is a general issue of MD simulations of small molecules in the gas phase. If there is only a small number of degrees of freedom and if these are not strongly coupled, it takes a long time to exchange energy between them, making it hard to reach equipartition within the time affordable by AIMD. Also the technique of massive thermostatting, which was applied here, does not completely remedy this effect. In bulk phase simulations, for which the MD approach is primarily intended, this problem does not occur to that extent (see Sects. 4.2.1 and 4.3.1).

The IR spectra and the Raman spectra of methanol are shown as solid lines and their integrals are plotted as dotted lines (see Fig. 4.1). The static calculation actually provides only intensities for each mode, but for convenience, it is very common to broaden these line spectra. Lorentzian functions with a FWHM of 15 cm^{-1} were selected for this purpose here. In principle, the line width in the AIMD spectra is governed by the choice of the window function and the correlation depth, but it is clearly apparent that the AIMD simulation also contains information about peak shapes. In particular the HCOH torsion leads to a broader band than the other modes.

Due to these effects, it is important to compare the peak integrals and not only the peak heights in order to draw conclusions for the absolute intensities. Furthermore, it is important to note that the Raman spectra from AIMD always possess a large peak at zero wavenumber. Even if the full polarizability tensor is taken into account, the anisotropy $\gamma(\tilde{\nu})$ is not formally invariant under rotations of the molecule. This is amplified in practice by the finite difference approximations in the application of the electric field and in the time derivative of the polarizability. This means that also the rotational motion of the molecule contributes at low wavenumbers, and this part of the spectrum is exaggerated by the factor $1/\tilde{\nu}$ in Eqs. (3.66) and (3.67). To facilitate the comparison of the vibrational bands in the spectrum, the integral axis on the right side of the Raman spectrum (see Fig. 4.1) does not start at zero, and the integral of the low wavenumber band is cut.

While the IR intensities agree very well below 2000 cm^{-1} , the comparison of AIMD and static spectra reveals certain differences in the high-wavenumber region. In contrast to the static calculation, which assigns significant intensity to all three CH stretching modes, the AIMD simulation yields only a peak for the symmetric vibration. Furthermore, the AIMD predicts a much larger OH stretching intensity. Comparison with experimental gas phase data of methanol [2–4] shows that the latter is clearly overestimated, but this is a direct consequence of the excess energy in this mode. Considering that also the symmetric CH_3 stretching vibration carries excess energy, the reasonable agreement of this mode with the experimental intensity is probably caused by a cancellation of errors.

In the Raman spectra, the AIMD yields very broad bands below 2000 cm^{-1} , but the peak integrals agree reasonably well with the static calculation. The high wavenumber region shows a similar effect as the IR spectra: while the static calculation predicts significant intensities for all three CH stretching modes, the AIMD estimates much less intensity for the antisymmetric vibrations. However, considering the excess energies of the symmetric CH_3 stretching and OH stretching modes, the overall agreement of the AIMD and the static calculation is very reasonable. The CH stretching region of methanol is generally a complex task for theoretical methods, as it is governed by several Fermi resonances with bending overtones [5], which are included only to some extent in the AIMD (see Sect. 3.2.3) and not at all in the static calculation.

The last quantity to be analyzed is the Raman depolarization ratio. In the AIMD, this is calculated as the ratio of two spectra (see Sect. 3.3), so it has a certain value in the whole wavenumber range. In parts of the spectrum without Raman intensity, however, this is just noise, so the depolarization ratio is shown as a solid line only in the range of Raman bands (see Fig. 4.1). The static calculation provides a value for each mode as indicated by the black circles. Considering the shift of the CH stretching modes, their depolarization ratios coincide very well. Also the value of 0.75 for the depolarized bands below 2000 cm^{-1} is predicted by the AIMD simulation. For the polarized bands, the values are at least in qualitative agreement. The AIMD depolarization ratio probably suffers from too much noise in the Raman spectra to allow for quantitative estimations. Although the Raman spectrum itself does not change considerably when the rotational averaging of the polarizability tensor is omitted,

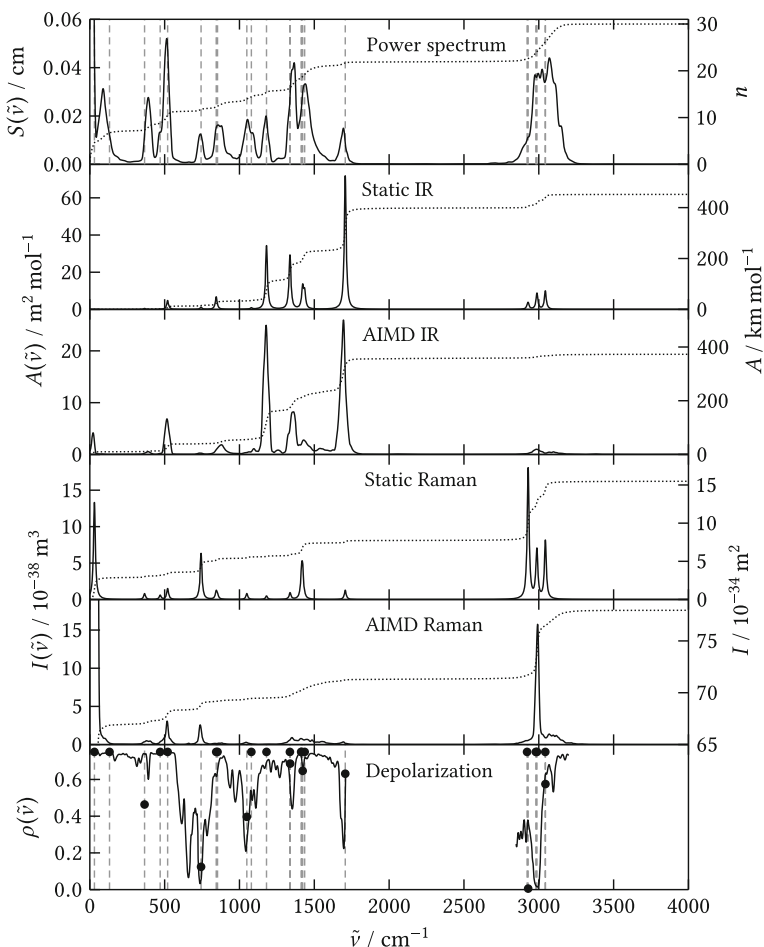


Fig. 4.4 Spectra of acetone in the gas phase: power spectrum, IR spectrum, and Raman spectrum from an AIMD simulation, IR spectrum and Raman spectrum from a static calculation. The *gray dashed lines* denote the vibrational frequencies from the static calculation, and the *dotted lines* show the integrals with the scales on the *right side*. The Raman depolarization ratios from the static calculation are shown as *circles*

the depolarization ratio becomes much more noisy then, so it is more sensitive to numerical errors.

Similar conclusions as for methanol can be drawn from the simulation of acetone (see Fig. 4.4). The peak positions in the power spectrum agree very well with the vibrational wavenumbers from the static calculation, only the CH stretching modes around 3000 cm^{-1} are significantly blue-shifted again. Furthermore, the integral of this band is equal to eight modes instead of six, indicating that equipartition is not fully reached. Another vibration that carries excess energy according to the integral curve is the in-plane CCO bending at 520 cm^{-1} . This is directly transferred to the

IR and Raman spectra: the intensities of AIMD simulation and static calculation are in very good agreement below 2000 cm^{-1} except for the in-plane CCO bending mode, for which the AIMD predicts a significantly larger intensity in both spectra. The CH stretching modes behave similar to methanol: despite their excess energy, the AIMD provides much lower IR intensities, and it assigns less Raman intensity to the antisymmetric vibrations, but the depolarization ratios agree very well. The depolarization ratios below 2000 cm^{-1} show stronger differences, but at least for most of the depolarized bands, the AIMD estimates a value of 0.75 too.

An important point to note is the peak at 20 cm^{-1} in the AIMD IR spectrum. Analogous to the intense zero wavenumber band in the Raman spectra, it is connected to the global rotation of the molecule. In general, if the molecule possesses a permanent dipole moment, already a simple rotation changes the dipole moment vector with respect to the space-fixed coordinate system, and a peak appears at the wavenumber of the rotation in the IR spectrum. In the case of methanol, however, this effect is covered by the broad band of the HCOH torsional mode.

The last example to be discussed is nitromethane (see Fig. 4.5), which shows in principle the same effects as methanol and acetone. It is clearly apparent in the power spectrum that the in-plane NO_2 bending mode at 846 cm^{-1} carries a significant excess of energy. As a direct consequence, the AIMD simulation predicts much larger IR and Raman intensities for this vibration. All other intensities below 2000 cm^{-1} coincide very well. As seen before, less Raman intensity is assigned to the antisymmetric CH_3 stretching modes above 3000 cm^{-1} in the AIMD, but the depolarization ratios of these vibrations are reproduced well. Both methods agree about the very low IR intensity of the CH stretching modes. The depolarization ratios show some deviations for the polarized bands below 2000 cm^{-1} again.

4.1.2 *Temperature Dependence of Molecular Dynamics Spectra*

In Sect. 3.2.3, it was discussed that MD based spectra show a temperature dependent shift of the vibrational wavenumbers since the temperature determines the extent to which the anharmonicity of the potential is sampled. To investigate this effect for a real molecule, the simulation of a single methanol molecule was carried out at 10, 100, and 1000 K in addition to the simulation at 400 K analyzed in the last section. The comparison of the power spectra (see Fig. 4.6) clearly shows the expected shifts. They are mostly apparent for the OH stretching vibration and the HCOH torsion. While the peak position of the torsional mode perfectly matches the wavenumber from the static calculation at 10 K, it appears at significantly lower wavenumber in the 400 K simulation. A temperature of 10 K is certainly too low to overcome the barrier of the torsion as it is easily verified by a visual inspection of the trajectory. In this case, the AIMD just samples the torsional potential in the close vicinity of one minimum, which is approximated very well by the harmonic potential of the static calculation, so both approaches yield the same wavenumber. At 400 K, the barrier is regularly

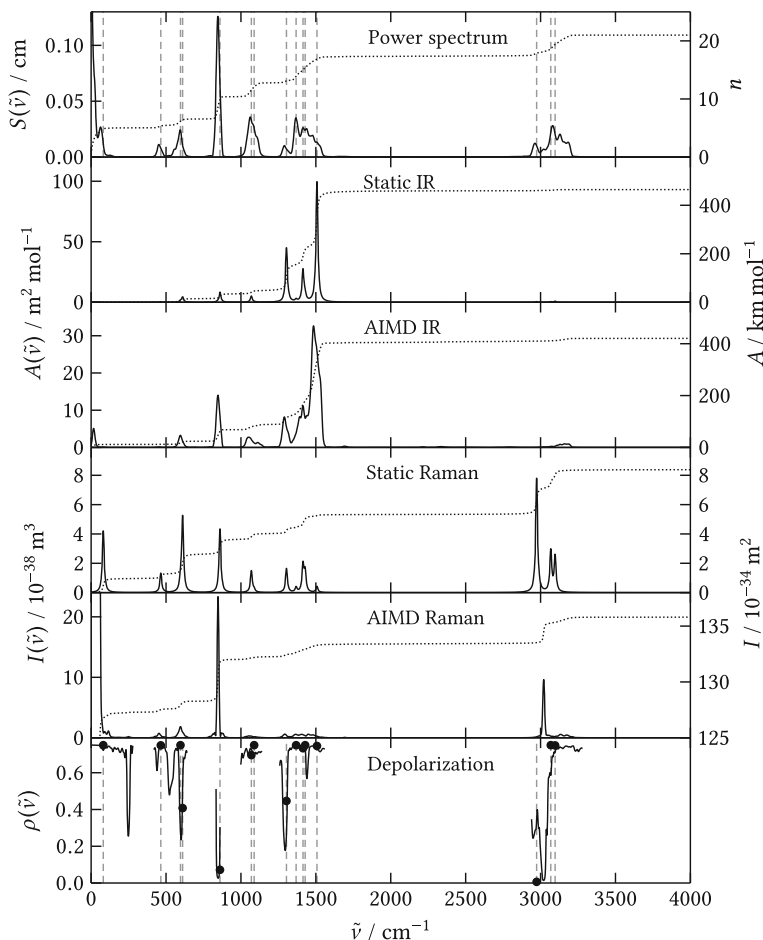


Fig. 4.5 Spectra of nitromethane in the gas phase: power spectrum, IR spectrum, and Raman spectrum from an AIMD simulation, IR spectrum and Raman spectrum from a static calculation. The *gray dashed lines* denote the vibrational frequencies from the static calculation, and the *dotted lines* show the integrals with the scales on the *right* side. The Raman depolarization ratios from the static calculation are shown as *circles*

passed (see Fig. 4.2) and the AIMD samples the complete torsional potential, leading to a strong redshift of the band. In contrast, the OH stretching wavenumber from the AIMD is almost equal to the static calculation at 400 K, while it is somewhat higher at 10 K. This supports the conclusion from the last section that the anharmonicity-induced redshift just cancels the blueshift caused by the finite timestep for this mode. Moreover, the side lobes of the OH stretching band do not appear at 10 and 100 K. This is totally in line with their identification as combination bands with the torsional

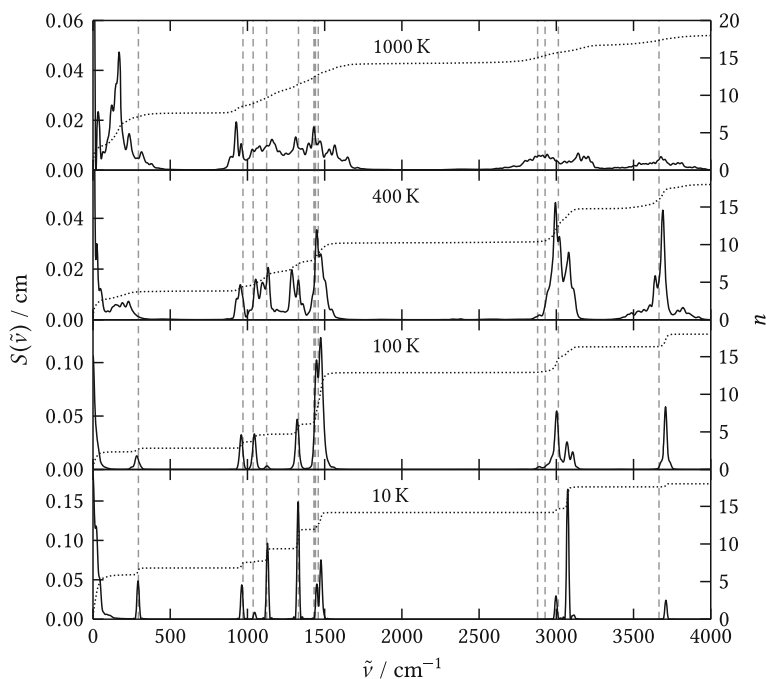


Fig. 4.6 Power spectra of methanol in the gas phase at four different temperatures. The *gray dashed lines* denote the vibrational frequencies from a static calculation, and the *dotted lines* show the integrals with the scale on the *right side*

mode, as a certain temperature is needed to sample the corresponding anharmonic region of the potential energy surface.

Beside the band shifts, it is also important to note the intensities. In particular at 10 K, the integral curve immediately indicates strong differences between the modes, so equipartition of the energy is not achieved. The almost complete decoupling of the vibrational degrees of freedom and the slow dynamics at this temperature make it very hard to reach equilibrium even with massive thermostating. In the case of ideal harmonic potentials, there would not be any coupling, and the modes could not exchange energy at all. As a direct consequence, the IR and Raman intensities are strongly distorted and the low temperature simulation does not provide reliable IR and Raman spectra. An advantage of the AIMD at 10 K is, however, that the peaks are very sharp, while they are significantly broadened at higher temperatures. This is related to the global rotation of the molecule. At higher temperatures, the amplitude of the vibrations is so large that the moments of inertia are substantially influenced, introducing a strong coupling between rotational and vibrational degrees of freedom that broadens the vibrational bands.

4.1.3 Anharmonicity Effects in Molecular Dynamics Spectra

The investigation of the two-dimensional model potentials in Sect. 3.2.3 revealed that it is in principle possible to observe overtones and combination bands in MD based vibrational spectra. To demonstrate this effect for real molecules, cyanoformyl chloride (ClC(O)CN) and cyanoformyl bromide (BrC(O)CN) were selected as example systems. The gas phase IR spectra of these molecules have recently been measured [6], and they show several distinct bands that could be assigned to overtones and combination bands. This marks cyanoformyl chloride and cyanoformyl bromide as ideal example systems, since it is easily validated if AIMD simulations also produce these distinct bands. Simulations of the single molecules were performed as detailed in Appendix A.

The comparison of the IR spectrum from the AIMD simulation with the experimental data (see Fig. 4.7) shows a very good coincidence except for the slight redshift of all AIMD bands. In particular, this is not only true for the fundamental transitions but also for the distinct overtones and combination bands that are marked by arrows. The experimental peak at 1025 cm^{-1} is not fully resolved in the AIMD spectrum, but it is clearly visible as a shoulder at 987 cm^{-1} . The normal coordinate analysis (see Fig. 4.7 and Table 4.2) allows to assign a particular vibrational mode to each fundamental peak. According to that, the intense experimental bands at 2242 and 1774 cm^{-1} are connected to the CN stretching (ν_1) and CO stretching (ν_2) modes, respectively. The mode vector of the most intense experimental band at 986 cm^{-1} is best described as CC stretching (ν_3), but it is significantly mixed with the in-plane CCO bending (ν_4), CCl stretching (ν_5), and in-plane OCCl bending (ν_6) vibrations that occur with further peaks at wavenumbers of 654 , 510 , and 422 cm^{-1} . The out-of-plane OCCl bending (ν_8) is found as a small shoulder at 677 cm^{-1} in the experiment, but it is hard to distinguish it in the AIMD spectrum where it is covered by ν_4 due to a more pronounced wavenumber shift. Altogether, this assignment is in full agreement with Ref. [6]. In this article, the experimental satellite bands at 1074 , 907 , and 1025 cm^{-1} have been attributed to the combination bands $\nu_4 + \nu_6$ and $\nu_5 + \nu_6$, and the first overtone of ν_5 , respectively, which gain intensity by Fermi resonance with ν_3 [6]. For MD based spectra, it was found in Sect. 3.2.3 that overtones and combination bands always appear at integer multiples or exact sums, respectively, of the corresponding fundamental wavenumbers. Although this is a general deficiency of the model, it is a big advantage for the assignment of the bands: it is just necessary to calculate the corresponding sums of the fundamental wavenumbers found in the normal coordinate analysis and to check for peaks in the IR spectrum. This analysis reveals that the satellite bands in the AIMD spectrum perfectly match the expected positions of $\nu_4 + \nu_6$, $\nu_5 + \nu_6$, and $2\nu_5$. This also holds for $2\nu_2$, which is not shown in the experimental spectrum, but is mentioned in Ref. [6] too. Therefore, the AIMD spectrum is totally in line with the experimental assignment of the overtones and combination bands.

It is interesting to note how the normal coordinate analysis treats the combination bands. From the viewpoint of this analysis, the combination peaks are artifacts, as

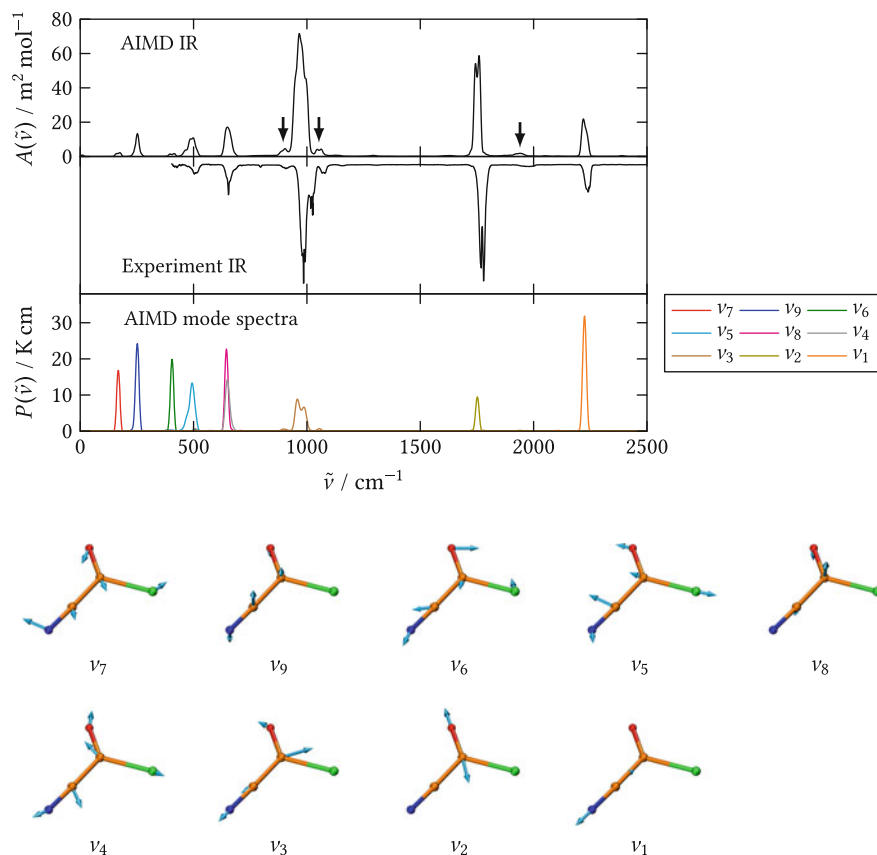


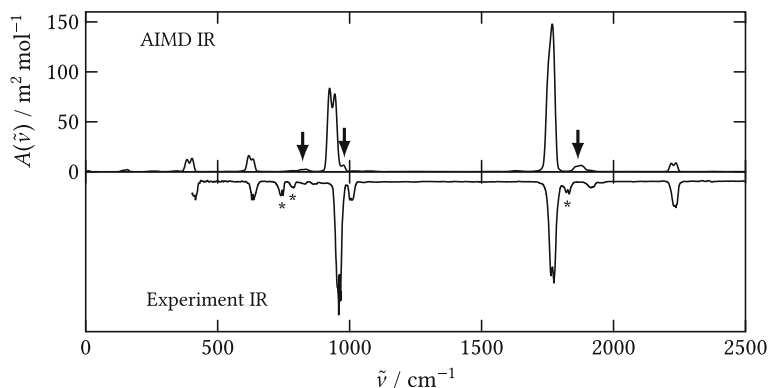
Fig. 4.7 IR spectra and normal coordinate analysis of cyanofornyl chloride. The *arrows* mark overtones and combination bands. The experimental spectrum and the mode numbering are taken from Ref. [6]

they cannot be separated into individual modes. Since the normal coordinate analysis performs a unitary transformation that does not change the total power spectrum, it also cannot remove these peaks, so they have to remain as satellite bands in some of the fundamental mode spectra. It is not generally predictable where they appear. Here, they show up as satellite peaks and a shoulder in the mode spectrum of ν_3 .

Another point to note is the splitting of the bands in the experiment due to the rotational transitions. In particular for ν_2 , this splitting is partially reproduced by the AIMD simulation. However, this agreement can only be of qualitative nature, and the AIMD will not resolve individual rotational bands for the reason given in Sect. 3.2.1.

Table 4.2 Vibrational wavenumbers of cyanofornyl chloride from experiment ($\tilde{\nu}_{\text{exp}}$) and AIMD (peak maxima $\tilde{\nu}_{\text{AIMD}}$). The experimental values and the mode numbering are taken from Ref. [6]

Assignment	$\tilde{\nu}_{\text{exp}}/\text{cm}^{-1}$	$\tilde{\nu}_{\text{AIMD}}/\text{cm}^{-1}$	Description
$2\nu_2$	3525	3503	
ν_1	2242	2225	CN stretching
ν_2	1774	1752	CO stretching
$\nu_4 + \nu_6$	1074	1054	
$2\nu_5$	1025	987	
ν_3	986	958	CC stretching
$\nu_5 + \nu_6$	907	897	
ν_8	677	645	Out-of-plane OCCl bending
ν_4	654	649	In-plane CCO bending
ν_5	510	493	CCl stretching
ν_6	422	405	In-plane OCCl bending
ν_9	–	252	Out-of-plane CCN bending
ν_7	–	168	In-plane CCN bending

**Fig. 4.8** IR spectra of cyanofornyl bromide. The *arrows* mark overtones and combination bands. The experimental spectrum is taken from Ref. [6]. The *asterisks* mark Br_2CO impurity bands

Based on the simulation of cyanofornyl bromide (see Fig. 4.8), similar conclusions can be drawn as for cyanofornyl chloride. Again, a slight redshift of the bands is observed, but all fundamental transitions as well as all overtones and combination bands indicated by the arrows are reproduced. Only the intensity ratios are less accurate here, since equipartition is not completely fulfilled in this simulation.

4.2 Spectra of Molecular Liquids

4.2.1 Methanol

In Sect. 4.1, some general properties of MD based vibrational spectra were discussed on the basis of several gas phase simulations. However, the main purpose of the MD approach to vibrational spectroscopy is the application to bulk phase systems that are not readily accessible by static calculations. As the first example, methanol is studied in this section. Methanol is a polar molecule and the hydroxyl group provides for the possibility to form intermolecular hydrogen bonds. This raises the expectation of strong differences in the spectra between gas phase and liquid phase, and an AIMD simulation should be particularly suited to model these effects. An AIMD simulation of 16 methanol molecules under periodic boundary conditions was carried out as detailed in Appendix A. Except for the normal coordinate analysis, the spectra have been published in Ref. [1].

For the comparison of simulation and experiment, the power, IR, and Raman spectra from the AIMD as well as two experimental IR spectra¹ and one experimental Raman spectrum are given (see Fig. 4.9). Already the power spectrum indicates the changes when passing from the gas phase to the bulk phase: the sharp peak of the OH stretching mode at 3677 cm^{-1} is replaced by a broad band centered around 3370 cm^{-1} , and another broad band appears, which is centered around 670 cm^{-1} . The remaining peaks of the gas phase spectrum are partially fused but mostly retain their positions. A more detailed insight is provided by the normal coordinate analysis (see Fig. 4.10 and Table 4.3), which clearly confirms that the broad band around 3370 cm^{-1} is connected to the OH stretching vibration. The shift and the broadening of this peak in contrast to the gas phase are a consequence of the strong hydrogen bonding network in liquid methanol. The formation of a hydrogen bond weakens the O–H bond in the donating molecule and, therefore, reduces its stretching wavenumber. The dynamic and flexible nature of the hydrogen bonding network leads to a wide distribution of the induced wavenumber shifts, so the band becomes very broad. Simultaneously, librational modes or bending modes of the hydrogen bond are added to the system. As the normal coordinate analysis relies on a separation into single molecules, it does not reproduce them as additional modes. Instead, the spectrum of the HCOH torsion (mode 1) possesses two peaks: a very broad one centered around 670 cm^{-1} , which can be assigned to the librations [8], and a narrower one at 106 cm^{-1} , which is the actual torsion of the C–O bond. The COH bending is much less affected by the hydrogen bonding network, but a blueshift and a slight broadening of the involved modes 3 and 5 compared to the gas phase are still recognizable. As mentioned before, the mode temperatures in the bulk indicate much less deviation from equipartition than in the gas phase.

¹I would like to thank Prof. Dr. Peter Vöhringer for providing several experimental IR spectra discussed throughout this thesis.

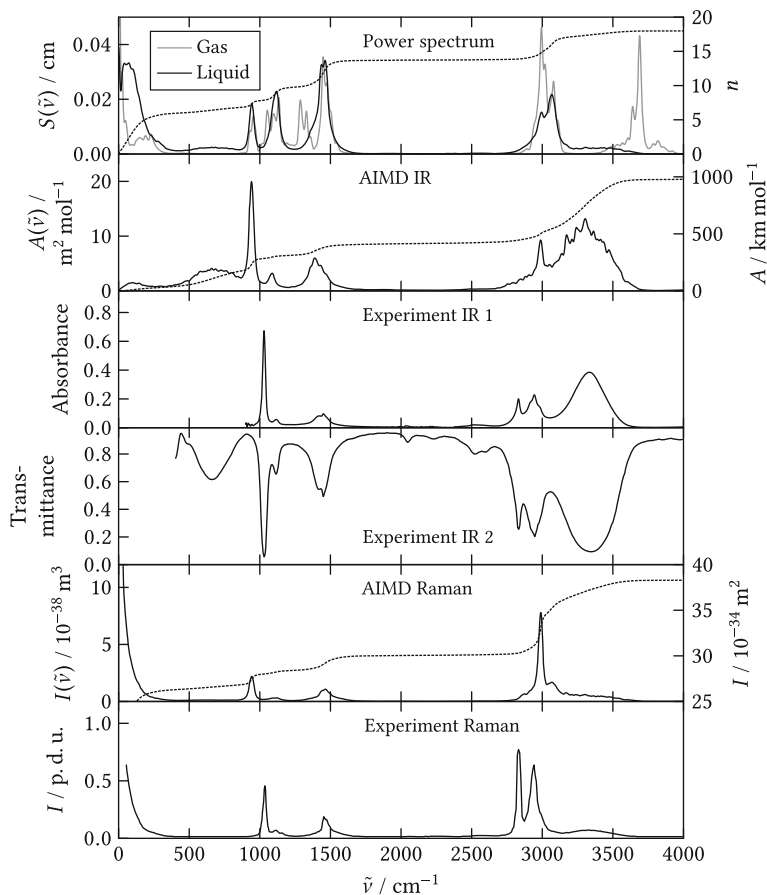


Fig. 4.9 Spectra of methanol in the liquid phase: power spectrum, IR spectrum, and Raman spectrum from an AIMD simulation of 16 methanol molecules, experimental IR and Raman spectra. The power spectrum of the gas phase is shown in *gray* for comparison. IR experiment 1 has been provided by the research group of Prof. Dr. Peter Vöhringer. IR experiment 2 and the Raman experiment are taken from Ref. [7]

A prominent feature of the experimental IR spectrum of methanol are the two broad and intense bands that are caused by the OH stretching vibration (around 3340 cm^{-1}) and the librational modes (around 660 cm^{-1}). It is an important result that the AIMD simulation reproduces them very well. They appear with some noise in the simulated spectrum, but this is caused by the limited size of the system and the finite length of the trajectory. In principle, it can be concluded that 16 molecules under periodic boundary conditions are sufficient to get the essential bulk phase effects on the vibrational spectra of methanol. Also the absolute intensities are in good agreement with further experimental data [9]. While the librational modes and the OH stretching vibration give rise to intense IR bands, they possess only a low

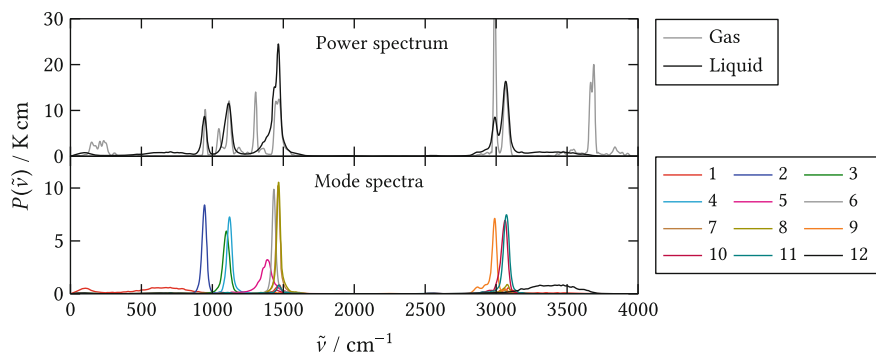


Fig. 4.10 Normal coordinate spectra of methanol in the liquid phase: total power spectrum and dissection into mode spectra. The power spectrum of the gas phase is shown in *gray* for comparison. See Fig. 4.3 for graphical representations of the normal coordinate vectors

Table 4.3 Normal coordinates of methanol in the liquid phase: peak maxima $\tilde{\nu}$ and average mode temperatures $\langle T \rangle$

No.	$\tilde{\nu}/\text{cm}^{-1}$	$\langle T \rangle/\text{K}$	Description
1	106, ≈ 670	371	HCOH torsion + libration
2	945	477	CO stretching
3	1099	396	CH ₃ bending + COH bending
4	1121	397	CH ₃ bending
5	1386	396	COH bending + CH ₃ bending
6	1433	382	CH ₃ bending
7	1464	484	CH ₃ bending
8	1467	540	CH ₃ bending
9	2989	408	Symmetric CH ₃ stretching
10	3063	509	Antisymmetric CH ₃ stretching
11	3073	548	Antisymmetric CH ₃ stretching
12	≈ 3370	421	OH stretching

Raman intensity. The librations are not visible in the spectra shown here, but the broadness of the weak OH stretching band is predicted very well by the AIMD also in the Raman spectrum. Also the other bands below 2000 cm^{-1} are reproduced well by the AIMD simulation. In the IR spectrum, these are the CO stretching (mode 2) and the modes involving COH bending (modes 3 and 5), while in the Raman spectrum, these are the CO stretching (mode 2) and several CH₃ bending vibrations (modes 4, 6, 7, and 8). As the latter occur at very similar wavenumbers, it is not possible to completely discern their individual contributions here. The only remarkable deviation is the slight redshift of the bands in the simulation, which is particularly apparent for the CO stretching vibration.

A stronger difference appears, however, for the CH stretching modes. Apart from the significant blueshift, the simulation yields only one intense band for the symmetric CH_3 stretching vibration in both spectra. The second band occurring in both experiments is connected to several Fermi resonances with overtones of bending modes [5], which also induce certain wavenumber shifts. It is obvious that the AIMD simulation insufficiently accounts for these Fermi resonances, so it underestimates the intensity of the second band. Thus, the band is covered by the OH stretching vibration in the IR spectrum and only a small peak shows up in the Raman spectrum.

4.2.2 Carbon Tetrachloride

As the second example for simple molecular liquids, carbon tetrachloride was simulated. Due to the absence of hydrogen bonds, less pronounced bulk phase effects than for methanol have to be expected, but carbon tetrachloride is interesting with regard to several distinct overtone and combination bands that are found in the IR and Raman spectra. An AIMD simulation of 32 carbon tetrachloride molecules was performed as detailed in Appendix A.

The comparison of IR and Raman spectra from simulation and experiment (see Fig. 4.11) shows a good general agreement. The normal coordinate analysis identifies four different fundamentals: the non-degenerate symmetric stretching ν_1 , the doubly degenerate symmetric deformation ν_2 , the triply degenerate antisymmetric stretching ν_3 , and the triply degenerate antisymmetric deformation ν_4 (see Table 4.4 and Ref. [11]). While ν_3 gives rise to an intense IR band, it appears only with low Raman intensity. In contrast, the other three modes show up as distinct Raman peaks, but possess a very low IR intensity. As long as isotope effects [11] are neglected, the symmetric modes ν_1 and ν_2 are even forbidden by symmetry in the IR spectrum. The most important differences between simulation and experiment concern the wavenumber shift of ν_3 and the Raman intensity ratios of ν_1 , ν_2 , and ν_4 . These deficiencies have to be attributed to the PBE exchange-correlation functional. Neglecting the solute influence on the solvent, it can be found in the solution spectra in Sect. 4.3 that BLYP provides a better estimate of the relative Raman intensities, but on the other hand, it introduces more pronounced wavenumber shifts for these modes. In general, the vibrational wavenumbers of carbon tetrachloride pose a challenge for DFT. A comparison of several exchange-correlation functionals (see Table 4.5 and Appendix A) shows that all of them underestimate the wavenumbers except for PBE0. Among the GGA functionals, which are the ones readily accessible for AIMD, PBE performs best.

In the experiment, the intense IR band at 786 cm^{-1} shows a splitting due to the Fermi resonance of ν_3 and the combination band $\nu_1 + \nu_4$ [11]. The AIMD simulation does not fully reproduce the intensity transfer between these transitions, but the combination band is clearly visible as a shoulder at 750 cm^{-1} . Further overtones and combination bands occur at higher wavenumbers. A detailed comparison in the range between 800 and 1600 cm^{-1} (see Fig. 4.12) reveals a qualitative agreement

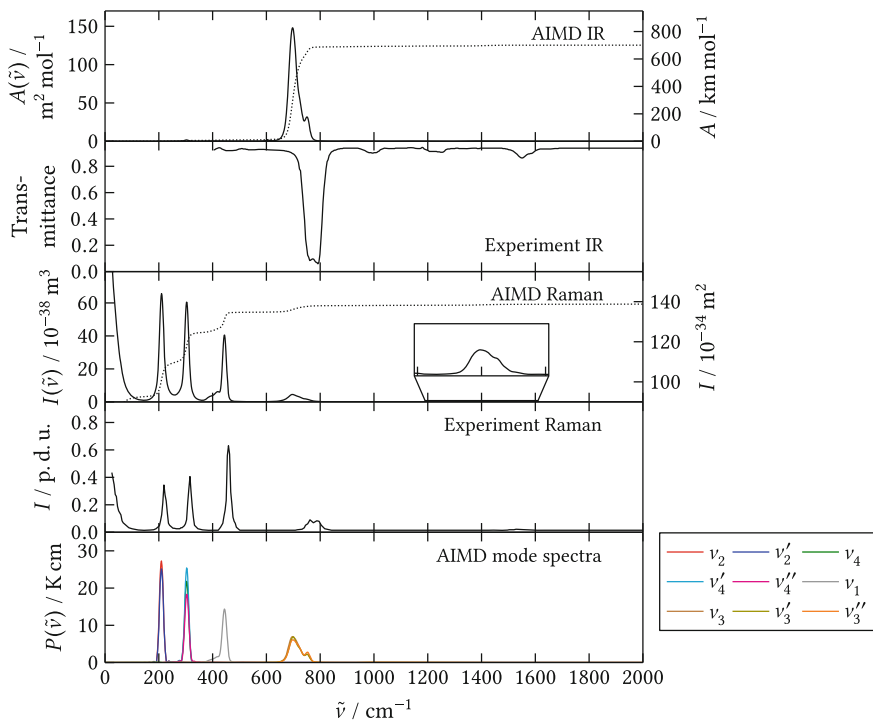


Fig. 4.11 Spectra of carbon tetrachloride in the liquid phase: IR spectrum, Raman spectrum, and normal coordinate analysis from an AIMD simulation of 32 carbon tetrachloride molecules. The experimental IR and Raman spectra are taken from Ref. [10]. The mode numbering is adopted from Ref. [11], and degenerate modes are denoted by primes. The *inset* magnifies the simulated Raman spectrum between 1200 and 1600 cm^{-1}

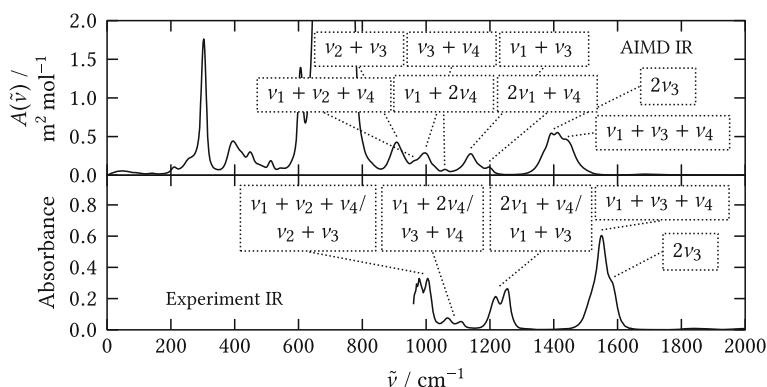
Table 4.4 Normal coordinates of carbon tetrachloride in the liquid phase: experimental wavenumbers $\tilde{\nu}_{\text{exp}}$ in the IR spectrum [11], AIMD peak maxima $\tilde{\nu}_{\text{AIMD}}$ and average mode temperatures $\langle T \rangle$. The mode descriptions are adopted from Ref. [11]. In the symmetric modes, the carbon atom remains fixed, while it is displaced in the antisymmetric modes

Mode	$\tilde{\nu}_{\text{exp}}/\text{cm}^{-1}$	$\tilde{\nu}_{\text{AIMD}}/\text{cm}^{-1}$	$\langle T \rangle/\text{K}$	Description
ν_2	218	210	475	Symmetric deformation
ν_4	314	304	422	Antisymmetric deformation
ν_1	456	444	361	Symmetric stretching
ν_3	786	700	382	Antisymmetric stretching

of simulation and experiment also for these transitions. The peaks that show up in this region are the combination bands of ν_3 and $\nu_1 + \nu_4$ with all the fundamentals, and Fermi resonances are responsible for the occurrence of these transitions as split double bands in the experiment [11]. Since the AIMD does not fully describe these effects, the intensity ratios are distorted, and the first-order combination transitions

Table 4.5 Comparison of several exchange-correlation functionals regarding the vibrational wavenumbers of carbon tetrachloride predicted by static calculations in the gas phase

Functional	$\tilde{\nu}_2/\text{cm}^{-1}$	$\tilde{\nu}_4/\text{cm}^{-1}$	$\tilde{\nu}_1/\text{cm}^{-1}$	$\tilde{\nu}_3/\text{cm}^{-1}$
BLYP	201	289	414	664
BP86	203	296	432	700
PBE	205	300	440	714
B97D	207	298	422	673
TPSS	202	295	434	708
B3LYP	212	306	443	734
PBE0	217	316	468	788
TPSSh	207	302	447	741
Experiment (liquid) [11]	218	314	456	786

**Fig. 4.12** Overtones and combination bands in the IR spectrum of carbon tetrachloride. The experimental spectrum has been provided by the research group of Prof. Dr. Peter Vöhringer. The assignment in the experimental spectrum is taken from Ref. [11]

are more intense than the second-order combination transitions. Nevertheless, all peaks of the experiment can be identified in the simulated spectrum by calculating the corresponding sums of the fundamental wavenumbers obtained from the normal coordinate analysis.

Similar effects can be observed in the Raman spectra: Also here, the Fermi resonance of ν_3 and $\nu_1 + \nu_4$ [11] causes a splitting of the band at 786 cm^{-1} in the experiment. The simulation shows a broader peak instead, which consists of both the fundamental transition and the combination band. The first overtone of ν_3 and the combination $\nu_1 + \nu_3 + \nu_4$, which are found as a weak band around 1540 cm^{-1} in the experiment, are also predicted by the AIMD, though with a significant redshift due to the underestimated fundamental wavenumber of ν_3 .

4.3 Spectra of Solute Molecules

4.3.1 Methanol in Carbon Tetrachloride

A major advantage of the MD approach to vibrational spectra is the possibility to separate the spectra of solvent and solute in a solution. As a first example, methanol in carbon tetrachloride is studied. The idea for this simulation originates from the measurement in the research group of Prof. Dr. Peter Vöhringer, where methanol was solved in carbon tetrachloride to obtain the spectrum of isolated methanol molecules, which should resemble the gas phase spectrum of methanol. The AIMD simulation of one methanol molecule in 32 carbon tetrachloride molecules was carried out as detailed in Appendix A.

A direct comparison of simulation and experiment (see Fig. 4.13) is only possible above 2000 cm^{-1} . Since methanol is hardly soluble in carbon tetrachloride and the formation of methanol clusters should be avoided, a thick solution layer with a low methanol concentration was measured. Thus, the region below 2000 cm^{-1} is totally covered by the carbon tetrachloride bands. The intensity ratios of the OH stretching and the symmetric CH_3 stretching vibrations are, however, in very good agreement. A blueshift of these modes in the simulation is observed in the same way as in the gas phase (see Sect. 4.1.1). As already mentioned before, the broader second peak of the CH stretching modes is largely influenced by Fermi resonances with bending

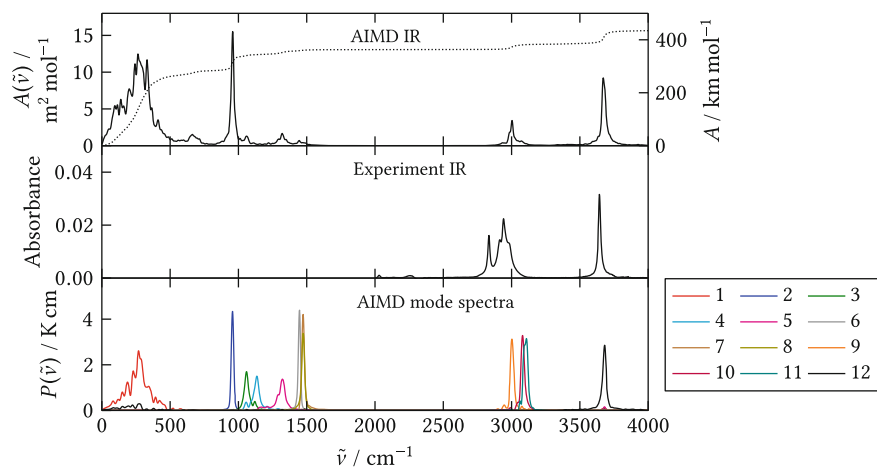


Fig. 4.13 Spectra of methanol in carbon tetrachloride: IR spectrum and normal coordinate analysis from an AIMD simulation of one methanol molecule in 32 carbon tetrachloride molecules. The experimental IR spectrum has been provided by the research group of Prof. Dr. Peter Vöhringer. Due to the strong absorption bands of carbon tetrachloride, it is shown only above 2000 cm^{-1} . See Fig. 4.1 for graphical representations of the normal coordinate vectors

overtone [5]. Since these are insufficiently included in the AIMD, the simulated spectrum does not show the second peak.

Compared to the gas phase simulation, the HCOH torsional mode gives rise to a broader band in the solution, showing that the torsion is significantly influenced by the surrounding carbon tetrachloride molecules. Furthermore, it possesses a much larger IR intensity, and the main reason for that is the significant excess energy of this mode in comparison with the other vibrations (see Table 4.6). However, as the simulation was performed with the thermostat temperature set to 400 K, the energy of the other vibrations is actually too low. This is a general artifact of the simulation: although massive thermostating was used to approximately equilibrate the system, the energy flows from the high-frequency modes of methanol to the low-frequency modes of the carbon tetrachloride. A potential solution would be the application of two thermostats, one for the carbon tetrachloride molecules and one for the methanol molecule. However, since the temperature of the CH stretching and OH stretching modes is similar, no major influence on the intensity ratios in the spectral region important for the comparison with the experiment is expected in the particular case studied here. Nevertheless, simulations of solute molecules have to be checked carefully for this issue in general. A side effect of the lowered methanol temperature is the slight blueshift of all bands with respect to the gas phase, since a smaller part of the anharmonic potential energy surface is sampled (see Sect. 4.1.2).

Table 4.6 Normal coordinates of methanol in carbon tetrachloride: peak maxima $\tilde{\nu}$ and average mode temperatures $\langle T \rangle$

No.	$\tilde{\nu}/\text{cm}^{-1}$	$\langle T \rangle/\text{K}$	Description
1	≈ 270	395	HCOH torsion
2	956	109	CO stretching
3	1059	93	CH ₃ bending + COH bending
4	1135	100	CH ₃ bending
5	1322	116	COH bending + CH ₃ bending
6	1447	101	CH ₃ bending
7	1473	111	CH ₃ bending
8	1474	108	CH ₃ bending
9	3002	117	Symmetric CH ₃ stretching
10	3080	131	Antisymmetric CH ₃ stretching
11	3109	145	Antisymmetric CH ₃ stretching
12	3681	179	OH stretching

4.3.2 Pinacol in Carbon Tetrachloride

The second example to be investigated is pinacol solved in carbon tetrachloride. Pinacol is studied in the research group of Prof. Dr. Peter Vöhringer as a model system for extended hydrogen bond wires [12, 13]. In the synclinal conformation, the two hydroxyl groups of pinacol form an intramolecular hydrogen bond where one hydroxyl group acts as donor while the other one is the acceptor. The solution in a nonpolar solvent such as carbon tetrachloride largely suppresses the influence of the surrounding molecules, allowing to study the hydrogen bond dynamics of the almost isolated system.

The comparison of simulation and experiment (see Fig. 4.14) shows a very good agreement of most bands. The five experimental lines between 1000 and 1500 cm^{-1} are reproduced very well by the simulation, only the intensity of the peak in the middle of the higher triplet is underestimated and the bands are slightly red-shifted. Also the lower-wavenumber region, which is covered by the carbon tetrachloride here, coincides with experimental data obtained in the gas phase and in a carbon disulfide solution [14, 15]. The OH stretching band around 3600 cm^{-1} clearly shows a splitting of 47 cm^{-1} in the experiment. The narrow peak at 3626 cm^{-1} is connected to the dangling hydroxyl group that acts as the hydrogen bond acceptor, while the slightly broader peak at 3579 cm^{-1} belongs to the donating hydroxyl group [12]. Due to the noise in the simulated spectrum, it is hard to exactly quantify the splitting there, but the width of the band indicates that it is in the order of 50 cm^{-1} , which is very similar to the experiment. A clear deficiency of the simulation is, however, the strong underestimation of the CH stretching vibrations around 3000 cm^{-1} . This is in line with earlier observations (see Sect. 4.1.1) though the effect is much more pronounced here. On the one hand, this might be caused by the underlying electronic structure method, but a static calculation within the harmonic approximation using the same

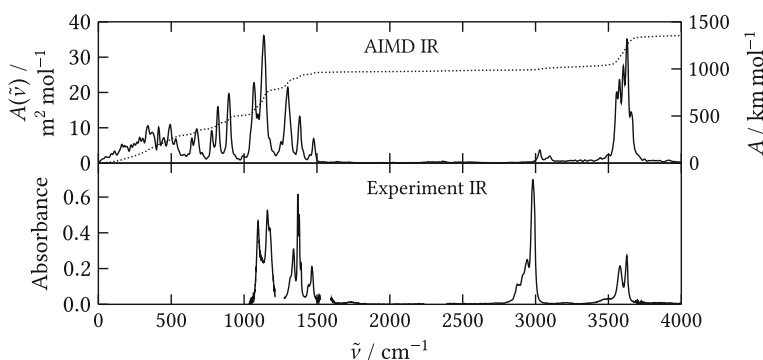


Fig. 4.14 Spectra of pinacol in carbon tetrachloride: IR spectrum from an AIMD simulation of one pinacol molecule in 32 carbon tetrachloride molecules. The experimental IR spectrum has been provided by the research group of Prof. Dr. Peter Vöhringer. Due to the strong absorption bands of carbon tetrachloride, certain regions of the experimental spectrum are cut out

method provides larger IR intensities for these modes. On the other hand, it is likely that anharmonicity effects in terms of Fermi resonances play a significant role similar to the methanol system, and these are insufficiently included in the AIMD, leading to the strongly reduced intensities. Moreover, the integral over the CH stretching bands in the power spectrum is equal to around nine modes instead of the expected twelve modes, so this is another reason for the underestimation of the IR intensity, but it cannot explain the complete effect.

It is important to note that the simulation of pinacol in carbon tetrachloride does not show the same temperature shifting effect as the simulation of methanol in carbon tetrachloride. The total integrals of the power spectra indicate that both the pinacol molecule and the carbon tetrachloride molecules have temperatures of approximately 400 K. A possible reason might be that pinacol, in contrast to methanol, possesses many modes at low wavenumbers close to carbon tetrachloride. This largely facilitates the exchange of energy between the solute and the solvent, allowing to maintain equipartition more easily.

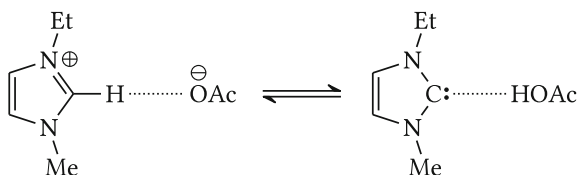
4.4 Spectra of Ionic Liquid Systems

4.4.1 Neat 1-Ethyl-3-Methylimidazolium Acetate

The examples discussed so far have shown that the MD approach to vibrational spectra is suited very well to model the effects of the molecular surrounding in the bulk phase. This is of particular interest for ionic liquids with a strong network of intermolecular interactions. As an important system of this kind, the ionic liquid 1-ethyl-3-methylimidazolium acetate ($[\text{C}_2\text{C}_1\text{Im}][\text{OAc}]$) was extensively studied in the course of this thesis. The discussion starts with the neat ionic liquid in this section. A $[\text{C}_2\text{C}_1\text{Im}][\text{OAc}]$ -water mixture follows in Sect. 4.4.2, and the absorption of carbon dioxide in $[\text{C}_2\text{C}_1\text{Im}][\text{OAc}]$ is presented in Sect. 4.4.3. All the results concerning the spectra of $[\text{C}_2\text{C}_1\text{Im}][\text{OAc}]$ have been published in Ref. [16]. The IR spectra shown here are slightly different since the molecular center of geometry has been used as dipole reference point in Ref. [16] while the molecular center of mass was employed here as suggested in Sect. 3.4.

An interesting property of $[\text{C}_2\text{C}_1\text{Im}][\text{OAc}]$ is the possibility to form an N-heterocyclic carbene by a proton transfer from the imidazolium ring to the basic acetate ion (see Fig. 4.15). Different spectroscopic experiments have revealed that

Fig. 4.15 Carbene formation by a proton transfer in $[\text{C}_2\text{C}_1\text{Im}][\text{OAc}]$



the equilibrium is shifted toward the hydrogen-bonded carbene–acetic acid complex in the gas phase, which can even dissociate under low pressure [17]. In the liquid, however, the ion network [18, 19] of the surrounding charged particles stabilizes the ionic state and suppresses the carbene formation [20–22]. Although trapping reactions with different chalcogens, benzaldehyde [23], and carbon dioxide [24] indicate its accessibility, the carbene has not yet been observed by any direct approach in the liquid phase.

Due to this difference between vapor and liquid, significant bulk phase effects have to be expected also in the vibrational spectra of $[\text{C}_2\text{C}_1\text{Im}][\text{OAc}]$. This is easily apparent in the IR spectra obtained by static calculations of a single ion pair and a cluster of five ion pairs (see Fig. 4.16), where the cluster provides a first approximation

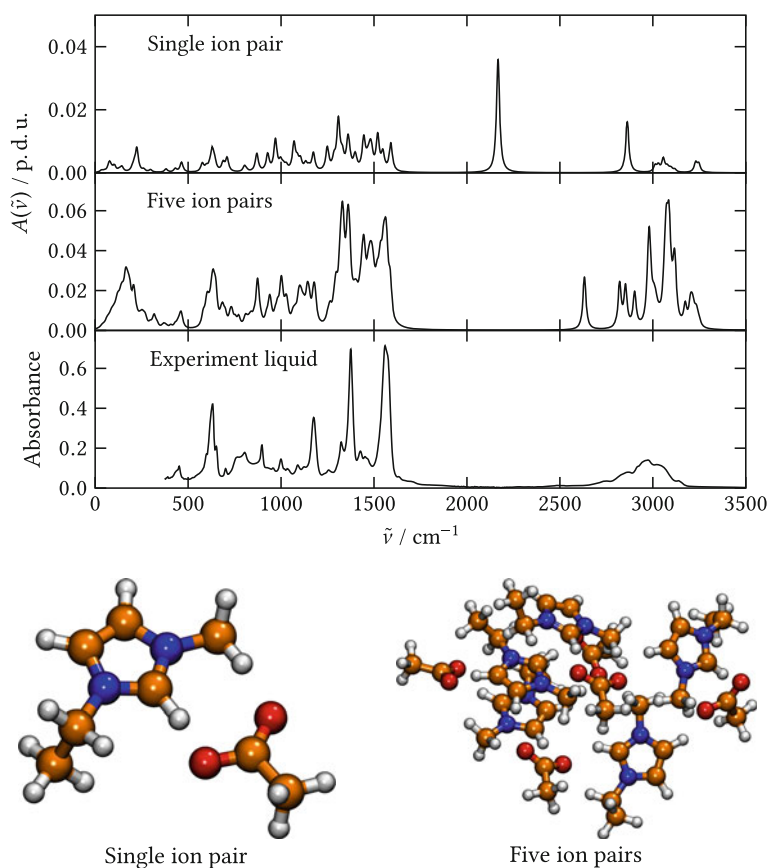


Fig. 4.16 IR spectra of $[\text{C}_2\text{C}_1\text{Im}][\text{OAc}]$ from static calculations of a single ion pair and a cluster of five ion pairs. The lines are broadened by Lorentzian functions with a FWHM of 20 cm^{-1} . The experimental IR spectrum of the liquid has been provided by Prof. Dr. Tibor Pasinszki. Adapted from reference [16], reprinted with the permission of AIP Publishing

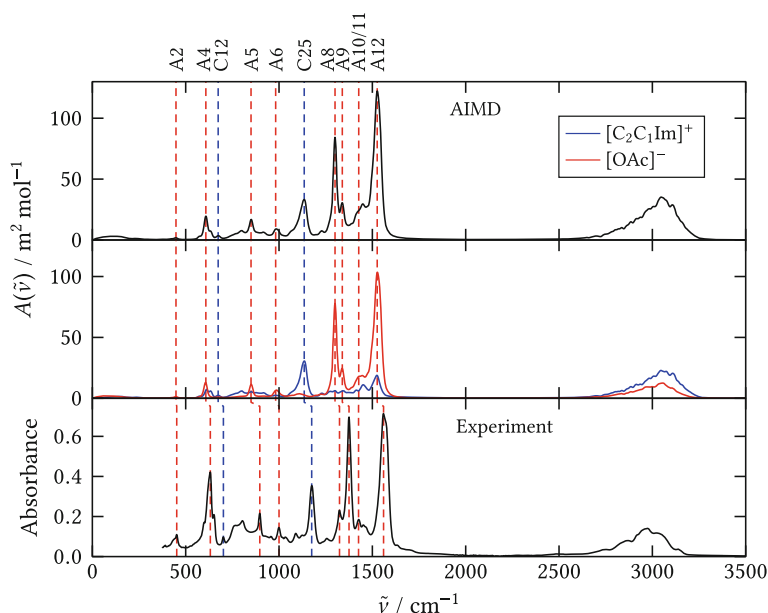


Fig. 4.17 IR spectra of neat $[\text{C}_2\text{C}_1\text{Im}][\text{OAc}]$: disentanglement of cation and anion contributions in an AIMD simulation of 36 $[\text{C}_2\text{C}_1\text{Im}][\text{OAc}]$ ion pairs. The experimental IR spectrum has been provided by Prof. Dr. Tibor Pasinszki. The dashed lines indicate the peak assignment to cation and anion

to the bulk phase as it models the influence of the surrounding on the central ions. Similar to the data previously reported in the literature on the basis of a different electronic structure method [25], the most intense band of the single ion pair is predicted at 2167 cm^{-1} where the experiment² shows almost no absorption in the liquid. The mode vector corresponding to this peak primarily consists of the ring proton shift between the cation and the anion that leads toward the carbene. Due to the facilitated carbene formation in the gas phase, the potential energy surface of the proton transfer becomes flatter, and the wavenumber of this mode is significantly reduced. For the cluster of five ion pairs, the spectrum is already closer to the liquid, but there are still several distinct peaks for the proton shifting modes between 2600 and 2900 cm^{-1} with no direct counterpart in the experiment. Aside from the difficulty to converge the geometry optimization of such a system, the single structure selected here is by far not sufficient to cover the whole range of possible cluster configurations. Thus, the application of clusters can only partially model the bulk phase and surface effects will always be present.

An AIMD simulation of 36 $[\text{C}_2\text{C}_1\text{Im}][\text{OAc}]$ ion pairs under periodic boundary conditions (see Appendix A for computational details) performs much better regard-

²I would like to thank Prof. Dr. Tibor Pasinszki for providing the experimental data of liquid $[\text{C}_2\text{C}_1\text{Im}][\text{OAc}]$.

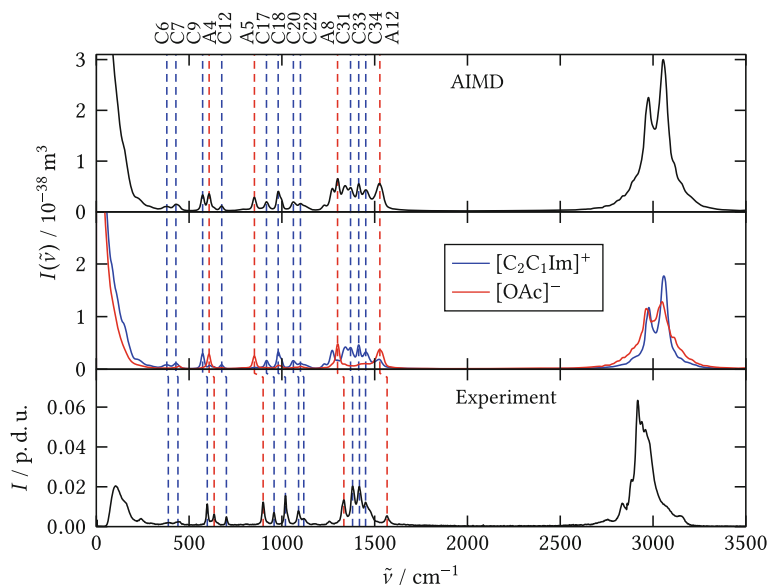


Fig. 4.18 Raman spectra of neat $[\text{C}_2\text{C}_1\text{Im}][\text{OAc}]$: disentanglement of cation and anion contributions in an AIMD simulation of 36 $[\text{C}_2\text{C}_1\text{Im}][\text{OAc}]$ ion pairs. The experimental Raman spectrum has been provided by Prof. Dr. Tibor Pasinszki. The *dashed lines* indicate the peak assignment to cation and anion

ing the comparison with experimental IR and Raman spectra (see Figs. 4.17 and 4.18). Similar to the examples discussed in the last sections, there is a slight redshift of almost all fingerprint bands by $(24 \pm 14) \text{ cm}^{-1}$, but most of the peak shapes and intensity ratios agree very well with the experiment. In contrast, the broad IR band feature around 3000 cm^{-1} is blue-shifted by ca. 70 cm^{-1} , but this is also in line with previous observations for CH stretching vibrations. Most importantly, its FWHM of 240 cm^{-1} is reproduced very well by the simulation. This broadening is a direct consequence of the hydrogen bonding network in the ionic liquid, which is proficiently modeled by the AIMD.

The first step toward a detailed analysis of the spectra is the separation of cation and anion contributions by considering only their individual dipole moments and polarizabilities. This leads to the classification indicated by the dashed lines, revealing that the IR spectrum is dominated by the $[\text{OAc}]^-$ anion while most of the Raman bands are connected to the 1-ethyl-3-methylimidazolium ($[\text{C}_2\text{C}_1\text{Im}]^+$) cation. Although most of the cation's IR spectrum between 1200 and 1700 cm^{-1} is covered in $[\text{C}_2\text{C}_1\text{Im}][\text{OAc}]$, it agrees well with experimental data of other ionic liquids that combine the $[\text{C}_2\text{C}_1\text{Im}]^+$ cation with anions that do not absorb in this wavenumber range [26–33].

An assignment of each peak to a particular molecular vibration is possible by a normal coordinate analysis. The reference structures for this purpose were obtained by geometry optimizations of the single ions (see Fig. 4.19). For the anion, the three

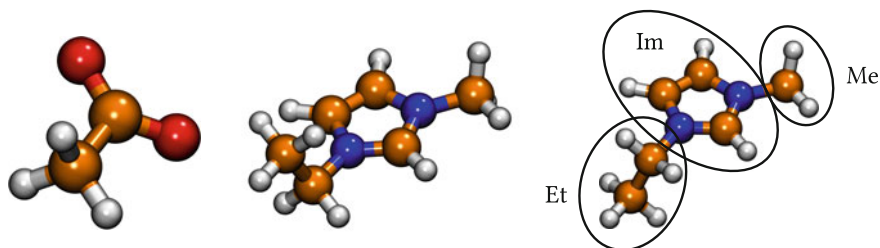


Fig. 4.19 Reference structures for the normal coordinate analysis in $[\text{C}_2\text{C}_1\text{Im}][\text{OAc}]$. The $[\text{C}_2\text{C}_1\text{Im}]^+$ cation is divided into three parts for the mode descriptions in Table 4.8. Adapted from reference [16], reprinted with the permission of AIP Publishing

cyclic permutations of the hydrogen atoms were employed as references to account for the rotation of the methyl group, and the root-mean-square deviation of all six $\text{H}-\text{C}-\text{C}-\text{O}$ dihedral angles was used as distance function with a width parameter of $\sigma = 15^\circ$. For the cation, two optimized structures are needed at first to take the rotation of the ethyl group into consideration. Although these are actually mirror images, they were treated as two structurally different minima, so that two sets of normal coordinates were obtained. As it should be expected, these are very similar, and only one of them is shown here. Future work could aim to extend the TRAVIS implementation to map the two structures onto a single minimum by appropriate mirroring operations. In each of the two structures, the respective three cyclic permutations of the methyl group's hydrogen atoms and the ethyl group's terminal hydrogen atoms were employed as references to account for rotations of the terminal methyl moieties. This results in nine references for each structure, and a total number of 18 references for the normal coordinate analysis of the cation. To distinguish between the permutations of the hydrogen atoms, the root-mean-square deviation of all six dihedral angles across the $\text{C}_{\text{Me}}-\text{N}$ bond and all nine dihedral angles across the $\text{C}_{\text{Et}}-\text{C}_{\text{Et}}$ bond was used as distance function with a width parameter of $\sigma = 20^\circ$. The two separate minima of the ethyl group orientation were discriminated by the root-mean-square deviation of all six dihedral angles across the $\text{C}_{\text{Et}}-\text{N}$ bond with a width parameter of $\sigma = 20^\circ$.

The mode spectra obtained from the normal coordinate analysis (see Figs. 4.20 and 4.21) show that the disentanglement of the power spectrum works very well even for the more complicated case of the $[\text{C}_2\text{C}_1\text{Im}]^+$ cation with 51 internal degrees of freedom. Some are very sharp and some are broader, but most of the mode spectra consist of one single peak. Only several alkyl CH stretching modes at 3000 cm^{-1} are slightly mixed with CH bending vibrations in the fingerprint region and torsional modes below 200 cm^{-1} . One reason for that are low rotational barriers: by definition, normal coordinates are always related to minima on the potential energy surface, but these are not well-defined anymore in the limiting case of a vanishing barrier. For example, the distinction of the torsional mode and the symmetric stretching mode of a methyl group is arbitrary in this situation.

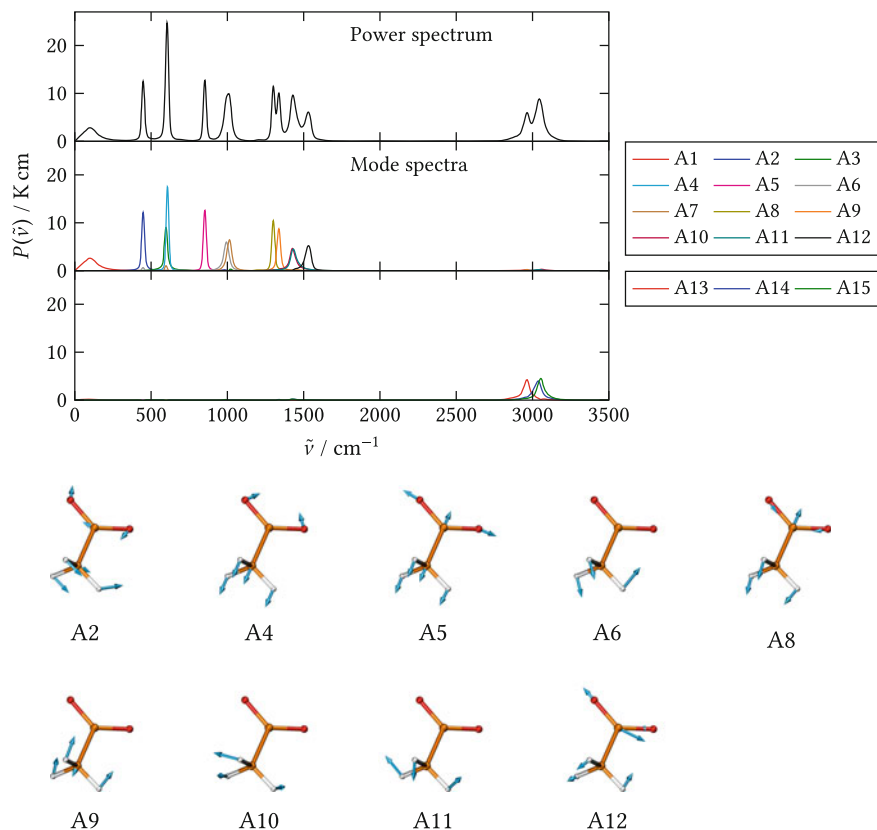


Fig. 4.20 Normal coordinate spectra of $[\text{OAc}]^-$ in $[\text{C}_2\text{C}_1\text{Im}][\text{OAc}]$: total power spectrum and dissection into mode spectra from the AIMD simulation. Graphical representations of the normal coordinate vectors assigned in the experiment

A detailed comparison of the peak positions in the mode spectra and in the simulated IR and Raman spectra allows to assign specific modes to the experimentally observed bands (see Tables 4.7 and 4.8). The most intense band in the IR spectrum is connected to the antisymmetric CO stretching mode of the anion (A12) as it is generally expected for carboxyl compounds. Two other important modes are the symmetric CO stretching (A8) and a methyl group bending (A9). For these two modes, the IR spectra show a notable difference between simulation and experiment as their intensity ratio is significantly distorted. Beside the assignment made in Ref. [16] that is shown here, it might also be possible that the wavenumber ordering of these vibrations is simply swapped. However, the Raman spectrum shows some deviations in this wavenumber region too, as the simulation predicts two peaks for the cation which are not separately visible in the experiment: a CN stretching mode at 1271 cm^{-1} and a CH bending mode at 1342 cm^{-1} . The experimental Raman band at 1334 cm^{-1} that was assigned to the anion's symmetric CO stretching (A8) simply on the basis of its

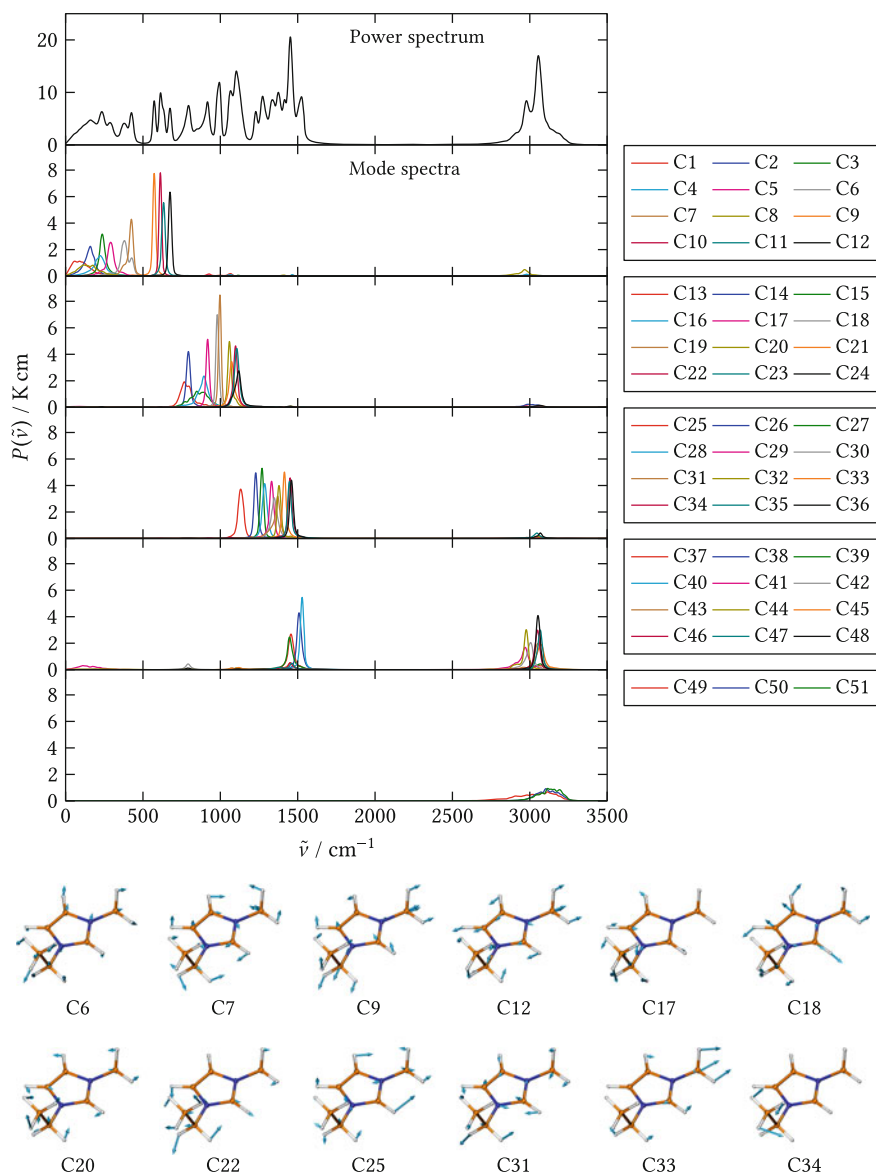


Fig. 4.21 Normal coordinate spectra of $[\text{C}_2\text{C}_1\text{Im}]^+$ in $[\text{C}_2\text{C}_1\text{Im}][\text{OAc}]$: total power spectrum and dissection into mode spectra from the AIMD simulation. Graphical representations of the normal coordinate vectors assigned in the experiment

Table 4.7 Normal coordinate assignment for $[\text{OAc}]^-$ in the spectra of neat $[\text{C}_2\text{C}_1\text{Im}][\text{OAc}]$. Simulated wavenumbers $\tilde{\nu}_{\text{AIMD}}$ from the AIMD and experimental wavenumbers $\tilde{\nu}_{\text{exp}}$ from the measured IR and Raman spectra

No.	$\tilde{\nu}_{\text{AIMD}}/\text{cm}^{-1}$	$\tilde{\nu}_{\text{exp}}/\text{cm}^{-1}$		Description
		IR	Raman	
A2	448	452		In-plane CCO bending
A4	608	632	635	OCO bending + CC stretching
A5	852	897	899	OCO bending + CC stretching
A6	995	1000		CH_3 bending
A8	1301	1323	1334	Symmetric CO stretching
A9	1338	1374		CH_3 bending
A10, A11	1430	1430		CH_3 bending
A12	1535	1559	1567	Antisymmetric CO stretching

Table 4.8 Normal coordinate assignment for $[\text{C}_2\text{C}_1\text{Im}]^+$ in the spectra of neat $[\text{C}_2\text{C}_1\text{Im}][\text{OAc}]$. Simulated wavenumbers $\tilde{\nu}_{\text{AIMD}}$ from the AIMD and experimental wavenumbers $\tilde{\nu}_{\text{exp}}$ from the measured IR and Raman spectra

No.	$\tilde{\nu}_{\text{AIMD}}/\text{cm}^{-1}$	$\tilde{\nu}_{\text{exp}}/\text{cm}^{-1}$		Description
		IR	Raman	
C6	381		388	$\text{C}_{\text{Et}}\text{C}_{\text{Et}}\text{N}$ bending
C7	424		440	$\text{C}_{\text{Et}}\text{NC}_{\text{Im}}$ bending + $\text{C}_{\text{Me}}\text{NC}_{\text{Im}}$ bending
C9	573		597	In-plane ring deformation + $\text{C}_{\text{Et}}\text{N}$ stretching + $\text{C}_{\text{Me}}\text{N}$ stretching
C12	674	702	701	In-plane ring deformation + $\text{C}_{\text{Et}}\text{N}$ stretching + $\text{C}_{\text{Me}}\text{N}$ stretching
C17	918		957	$\text{C}_{\text{Et}}\text{C}_{\text{Et}}$ stretching + in-plane ring deformation
C18	982		1019	In-plane ring deformation
C20	1059		1089	$\text{C}_{\text{Et}}\text{H}$ bending
C22	1097		1118	$\text{C}_{\text{Et}}\text{H}$ bending
C25	1135	1175		In-plane $\text{C}_{\text{Im}}\text{H}$ bending
C31	1373		1381	$\text{C}_{\text{Et}}\text{H}$ bending + $\text{C}_{\text{Im}}\text{N}$ stretching
C33	1414		1417	$\text{C}_{\text{Me}}\text{H}$ bending
C34	1452		1451	$\text{C}_{\text{Et}}\text{H}$ bending

simulated intensity, therefore, potentially contains significant cation contributions, and it is very likely that some anharmonic coupling effects insufficiently included in the AIMD are responsible for the differences in this wavenumber region.

Further deviations between simulation and experiment occur for the broad experimental IR peak feature between 750 and 800 cm^{-1} , which is significantly underestimated by the simulation, and the splitting of the CH stretching Raman band predicted

by the AIMD. The reason for the latter could be the insufficient modeling of Fermi resonances similar to the observations made for methanol (see Sect. 4.2.1). It should be noted that the role which Fermi resonances play for the CH stretching vibrations of imidazolium-based ionic liquids has been a matter of heavy debate in the literature [34–39].

An interesting feature of the normal coordinate analysis are the very broad mode spectra of the ring CH stretching modes in the cation (C49, C50, and C51). This result is absolutely in line with the general structural analysis of $[\text{C}_2\text{C}_1\text{Im}][\text{OAc}]$ on the basis of the AIMD simulation [20, 21], where it was demonstrated that the ring hydrogen atoms of the $[\text{C}_2\text{C}_1\text{Im}][\text{OAc}]$ cations are strongly involved in the network of intermolecular interactions by forming hydrogen bonds to the $[\text{OAc}]^-$ anions. The dynamic nature of this interaction network leads to a very broad distribution of the corresponding vibrational wavenumbers. This is discussed further at the end of the next section.

4.4.2 *1-Ethyl-3-Methylimidazolium Acetate–Water Mixture*

The ionic liquid $[\text{C}_2\text{C}_1\text{Im}][\text{OAc}]$ is a highly hygroscopic substance, so it always contains traces of moisture if it is handled without special care under ambient conditions. For that reason, it is very interesting to study the effect of water on the ionic liquid regarding its vibrational spectra. To clearly observe the effect, an AIMD simulation of 27 $[\text{C}_2\text{C}_1\text{Im}][\text{OAc}]$ ion pairs with 81 water molecules was carried out (see Appendix A for computational details), which corresponds to a water mass fraction of 24.1%. Furthermore, this demonstrates the applicability of the MD approach to vibrational spectra for binary mixtures of ionic liquids and molecular liquids.

The comparison of the IR spectra from simulation and experiment shows a very good agreement again (see Fig. 4.22). Apparently, the water molecules give rise to three broad bands in the spectrum. The OH stretching vibrations contribute to the peak of the CH stretching modes of cation and anion, making it even broader than in the neat ionic liquid. The HOH bending mode shows up at 1650 cm^{-1} and the librational motions appear below 1000 cm^{-1} with a maximum around 600 cm^{-1} . It is obvious that the water molecules significantly influence the spectral contributions of the ions. Many of the anion's bands are slightly blue-shifted in the experiment, and the simulation reproduces this shift in most cases (see Table 4.9). The intensity ratio of modes A8 and A9 is shifted in favor of A9. Although this is a step toward the experiment, the intensity of these two modes is still a deficiency as in the neat ionic liquid (see Sect. 4.4.1). The changes in the cation's spectrum are mostly indiscernible in the experiment due to the dominance of the anion and the water molecules. The only notable difference is the slight redshift of mode C25, which is also reproduced in the simulation.

The effects observed in the IR spectra are totally in line with the general structural analysis of this system [20, 21]. There, it was found that the water molecules weakly interact with the cations, but show a strong tendency to form hydrogen bonds with

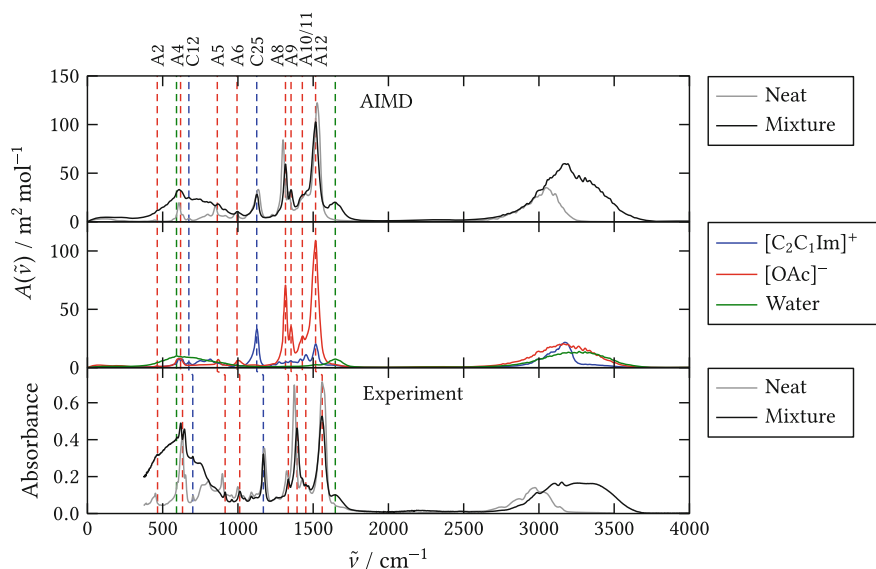


Fig. 4.22 IR spectra of a $[\text{C}_2\text{C}_1\text{Im}][\text{OAc}]$ -water mixture: disentanglement of cation, anion, and water contributions in an AIMD simulation of 27 $[\text{C}_2\text{C}_1\text{Im}][\text{OAc}]$ ion pairs and 81 water molecules. The experimental IR spectrum has been provided by Prof. Dr. Tibor Pasinszki. The *dashed lines* indicate the peak assignment to cation, anion, and water. The spectra of the neat ionic liquid (see Fig. 4.17) are drawn in *gray* for comparison

Table 4.9 Vibrational wavenumbers in neat $[\text{C}_2\text{C}_1\text{Im}][\text{OAc}]$ and in the $[\text{C}_2\text{C}_1\text{Im}][\text{OAc}]$ -water mixture: comparison of simulated wavenumbers $\tilde{\nu}_{\text{AIMD}}$ and experimental wavenumbers $\tilde{\nu}_{\text{exp}}$ in the IR spectra

No.	$\tilde{\nu}_{\text{AIMD}}/\text{cm}^{-1}$		$\tilde{\nu}_{\text{exp}}/\text{cm}^{-1}$	
	Neat	Mixture	Neat	Mixture
A2	448	464	452	466
A4	608	619	632	632
A5	852	863	897	915
A6	995	994	1000	1012
A8	1301	1316	1323	1335
A9	1338	1353	1374	1393
A10, A11	1430	1428	1430	1451
A12	1535	1516	1559	1560
C12	674	674	702	700
C25	1135	1125	1175	1169

the anions, heading toward a proton transfer and the generation of acetic acid. This disturbance of the cation–anion network significantly reduces the interaction between $[\text{OAc}]^-$ and the ring hydrogen atoms of $[\text{C}_2\text{C}_1\text{Im}]^+$, and it suppresses the proton shift from the cation to the anion. The strong interaction between water and $[\text{OAc}]^-$ directly transfers to the significant wavenumber shifts observed in the IR spectrum of the anion. Furthermore, it considerably changes also the bands of the water molecules: in an AIMD simulation of neat water with the same electronic structure method, the peak maxima are located at 3400 cm^{-1} for the OH stretching vibrations and 550 cm^{-1} for the librations (these values are taken from the power spectrum of system D in Refs. [20, 21]), while they are found at 3300 and 600 cm^{-1} , respectively, in the mixture with the ionic liquid. This means that the O–H bonds become weaker while the intermolecular hydrogen bonds get stronger, indicating that the strength of the anion–water interaction exceeds that of the hydrogen bonding network in pure water due to the polarization of the water molecules by the anions.

The influence on the cation is most obvious in the normal coordinate spectra of the ring hydrogen CH stretching modes around 3000 cm^{-1} (see Fig. 4.23). As mentioned before, these modes possess very broad mode spectra in the neat ionic liquid because the dynamic hydrogen bonding network between $[\text{OAc}]^-$ and $[\text{C}_2\text{C}_1\text{Im}]^+$ leads to a wide distribution of the vibrational wavenumbers. In the mixture with water, this broadening is much less pronounced and the wavenumber redshift is reduced. This

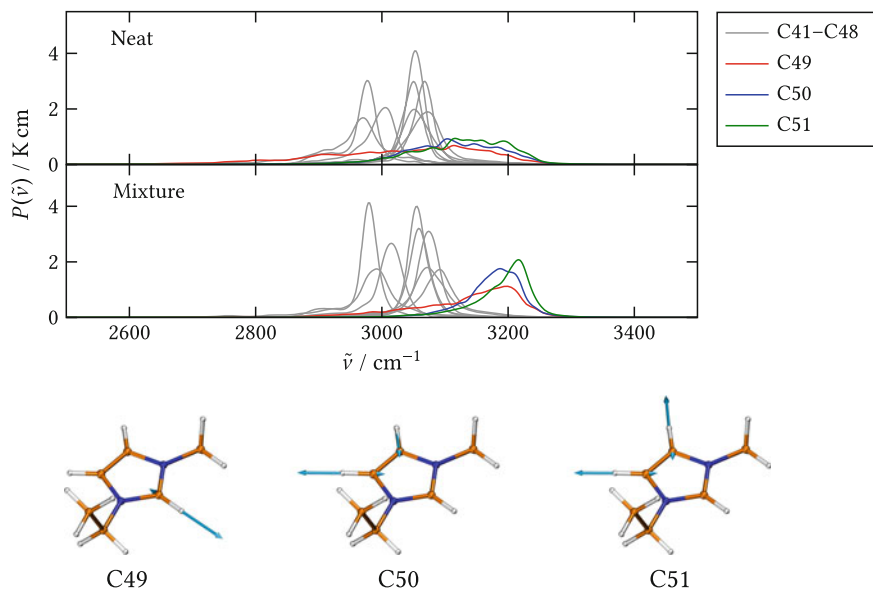


Fig. 4.23 CH stretching normal coordinate spectra of $[\text{C}_2\text{C}_1\text{Im}]^+$ in neat $[\text{C}_2\text{C}_1\text{Im}][\text{OAc}]$ and in the $[\text{C}_2\text{C}_1\text{Im}][\text{OAc}]$ –water mixture. Graphical representations of the normal coordinate vectors corresponding to the ring hydrogen atoms. Adapted from reference [16], reprinted with the permission of AIP Publishing

is a direct consequence of the decreased interaction between anion and cation, which transfers to a narrower wavenumber distribution of the ring hydrogen CH stretching vibrations.

4.4.3 Carbon Dioxide Absorption in 1-Ethyl-3-Methylimidazolium Acetate

The ability to physically absorb significant amounts of carbon dioxide is a general property of many ionic liquids [40–43]. In the case of $[\text{C}_2\text{C}_1\text{Im}][\text{OAc}]$ [44], however, the accessibility of a carbene (see Sect. 4.4.1) is of particular importance, as it also allows a chemical absorption by the formation of a bond between carbon dioxide and the carbene (see Fig. 4.24). This process has been proven by the X-ray structure of the resulting 1-ethyl-3-methylimidazolium-2-carboxylate $[\text{C}_2\text{C}_1\text{ImCO}_2]$ [24]. Later on, it has also been shown in the liquid phase of 1-butyl-3-methylimidazolium acetate by IR, Raman, and NMR spectroscopy with support by static calculations in the gas phase [45–47] and classical molecular dynamics simulations [48]. Here, the vibrational spectra of carbon dioxide in $[\text{C}_2\text{C}_1\text{Im}][\text{OAc}]$ are studied by AIMD. For this purpose, two simulations were performed (see Appendix A for computational details): one with a $[\text{C}_2\text{C}_1\text{ImCO}_2]$ molecule and an acetic acid molecule in 35 ion pairs of $[\text{C}_2\text{C}_1\text{Im}][\text{OAc}]$, and one containing a free carbon dioxide molecule in 36 ion pairs of $[\text{C}_2\text{C}_1\text{Im}][\text{OAc}]$ to model the physical absorption. The acetic acid in the first simulation is the byproduct of the carbene formation (see Fig. 4.15) needed for the chemical absorption process. It is tightly bound to an acetate anion forming a $[\text{H}(\text{OAc})_2]^-$ complex that persists during the whole simulation.

The carboxylate as the product of the chemical absorption can be identified by three very intense IR bands in the fingerprint region (see Fig. 4.25). To assign these bands to specific molecular vibrations, a normal coordinate analysis was carried out. Four different structures of $[\text{C}_2\text{C}_1\text{ImCO}_2]$ were found by geometry optimizations (see Fig. 4.26). Similar to the $[\text{C}_2\text{C}_1\text{Im}]^+$ cation, these are actually two pairs of mirror images, but they were treated as four structurally different minima. Analogous to the cation, the respective three cyclic permutations of the methyl group's hydrogen atoms and the ethyl group's terminal hydrogen atoms were used as references in each of the structures to account for rotations of the terminal methyl moieties. This results in a total number of 36 references for the normal coordinate analysis. The

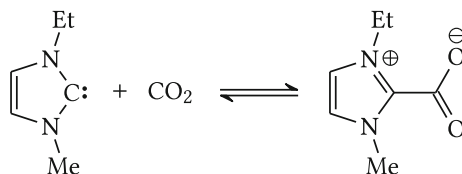


Fig. 4.24 Carbon dioxide absorption in $[\text{C}_2\text{C}_1\text{Im}][\text{OAc}]$ by the formation of $[\text{C}_2\text{C}_1\text{ImCO}_2]$

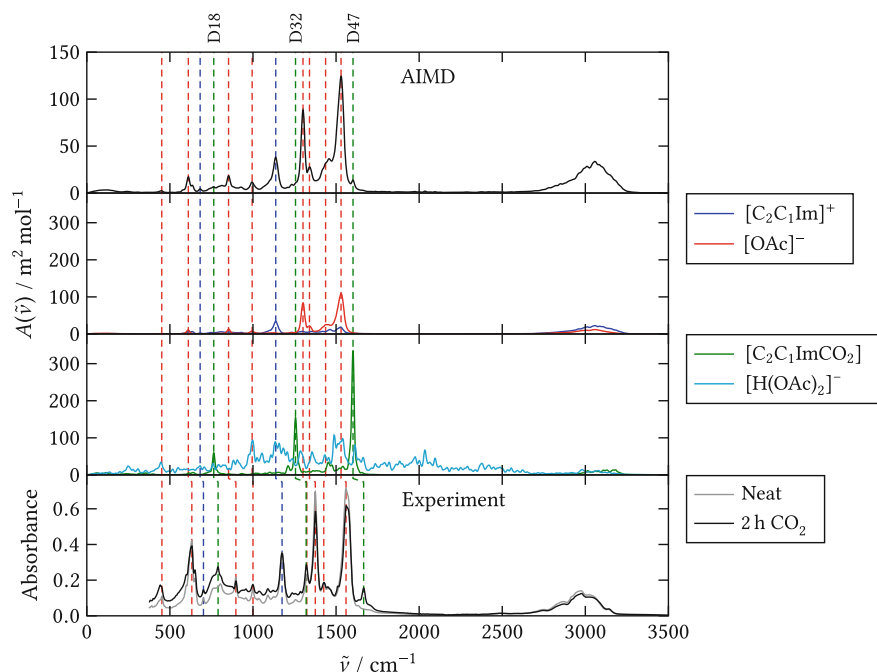


Fig. 4.25 IR spectra of $[\text{C}_2\text{C}_1\text{ImCO}_2]$ in $[\text{C}_2\text{C}_1\text{Im}][\text{OAc}]$: disentanglement of cation, anion, carboxylate, and $[\text{H}(\text{OAc})_2]^-$ contributions in an AIMD simulation of 35 $[\text{C}_2\text{C}_1\text{Im}][\text{OAc}]$ ion pairs with one $[\text{C}_2\text{C}_1\text{ImCO}_2]$ molecule and one acetic acid molecule. The experimental IR spectrum has been provided by Prof. Dr. Tibor Pasinszki. The *dashed lines* indicate the peak assignment to cation, anion, and carboxylate. The experimental spectrum of the neat ionic liquid (see Fig. 4.17) is drawn in gray for comparison

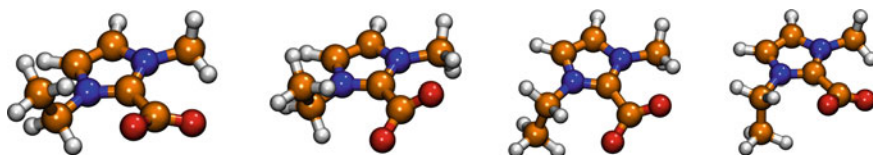
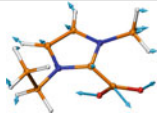


Fig. 4.26 Reference structures for the normal coordinate analysis of $[\text{C}_2\text{C}_1\text{ImCO}_2]$ in $[\text{C}_2\text{C}_1\text{Im}][\text{OAc}]$. Adapted from reference [16], reprinted with the permission of AIP Publishing

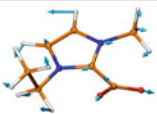
permutations of the hydrogen atoms were distinguished by the root-mean-square deviation of all six dihedral angles across the $\text{C}_{\text{Me}}-\text{N}$ bond and all nine dihedral angles across the $\text{C}_{\text{Et}}-\text{C}_{\text{Et}}$ bond with a width parameter of $\sigma = 20^\circ$. To discriminate the four structurally different minima, the root-mean-square deviation of all four dihedral angles across the $\text{C}-\text{C}$ bond connecting the carboxylate group to the ring and the two $\text{C}_{\text{Im}}-\text{N}-\text{C}_{\text{Et}}-\text{C}_{\text{Et}}$ dihedral angles was employed with a width parameter of $\sigma = 5^\circ$. The permutations of the oxygen atoms were not considered because the carboxyl group does not completely turn around during the simulation. The result

Table 4.10 Normal coordinate assignment for $[\text{C}_2\text{C}_1\text{ImCO}_2]$ in $[\text{C}_2\text{C}_1\text{Im}][\text{OAc}]$

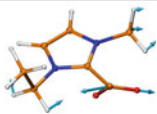
No.	$\tilde{\nu}_{\text{AIMD}}/\text{cm}^{-1}$	$\tilde{\nu}_{\text{exp}}/\text{cm}^{-1}$	Description
D18	764	790	In-plane OCO bending
D32	1256	1320	Symmetric CO stretching + in-plane $\text{C}_{\text{Im}}\text{H}$ bending
D47	1602	1666	Antisymmetric CO stretching



D18



D32



D47

of the normal coordinate analysis shows that all three intense IR bands are related to the carboxyl group: the antisymmetric CO stretching mode, the symmetric CO stretching mode mixed with ring CH bending vibrations, and the OCO bending mode (see Table 4.10).

As the disentangled contributions (see Fig. 4.25) are normalized to one molecule, the bands of the carboxylate appear much weaker in the total spectrum of the simulation cell due to the concentration ratios. Nevertheless, the antisymmetric CO stretching mode at 1602 cm^{-1} should act as a good indicator for the formation of the carboxylate in the ionic liquid. This agrees very well with the experimental observation³: after treatment of $[\text{C}_2\text{C}_1\text{Im}][\text{OAc}]$ with carbon dioxide for two hours, the peak at 1666 cm^{-1} is easily identified, showing that the carboxylate is readily formed.

The increasing background in the fingerprint region found experimentally is likely related to the acetic acid in the $[\text{H}(\text{OAc})_2]^-$ complex. Due to the dynamics of the proton [49, 50] and the large conformational flexibility, its spectral contribution is obtained with limited quality from the simulation, but it is still possible to identify some bands at similar positions as in the bare $[\text{OAc}]^-$. The spectrum clearly indicates that the complex should show up as a very broad background in the IR spectrum.

The simulation of the physical absorption shows the carbon dioxide with the antisymmetric CO stretching mode at 2291 cm^{-1} and the OCO bending modes around 600 cm^{-1} (see Fig. 4.27 and Table 4.11). The latter are degenerate in the gas phase, but they appear as a split peak with maxima at 598 and 626 cm^{-1} in the liquid. The extent of this splitting has been suggested to provide insight into the strength of the anion–carbon dioxide interactions [51], which are very strong in the case of $[\text{OAc}]^-$ [52, 53]. The symmetric CO stretching vibration, which is forbidden by symmetry in the gas phase, possesses a very low IR intensity in the liquid, and its wavenumber is found to be 1282 cm^{-1} in the power spectrum. Due to its separation from all other components of the system, the antisymmetric CO stretching vibration

³I would like to thank Prof. Dr. Tibor Pasinszki for providing the corresponding data, where carbon dioxide was passed above stirred $[\text{C}_2\text{C}_1\text{Im}][\text{OAc}]$ and IR spectra were measured after different time ranges.

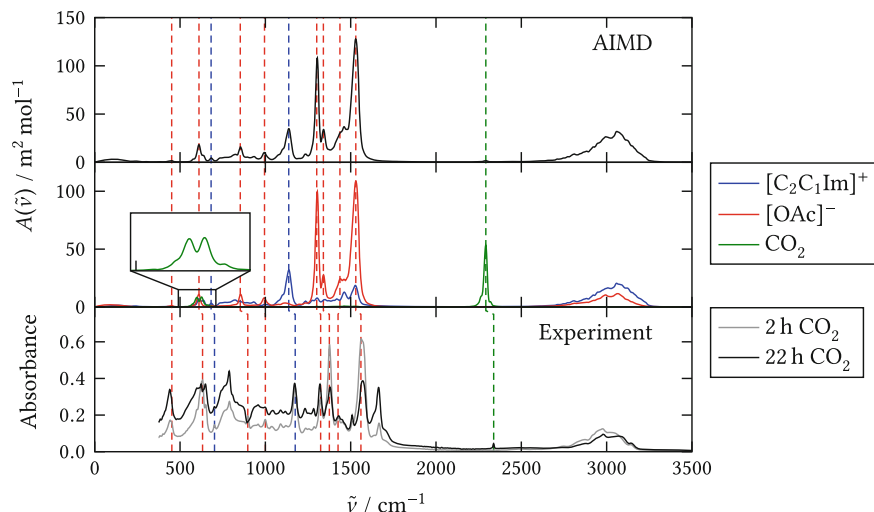


Fig. 4.27 IR spectra of carbon dioxide in $[\text{C}_2\text{C}_1\text{Im}][\text{OAc}]$: disentanglement of cation, anion, and carbon dioxide contributions in an AIMD simulation of 36 $[\text{C}_2\text{C}_1\text{Im}][\text{OAc}]$ ion pairs with one carbon dioxide molecule. The experimental IR spectrum has been provided by Prof. Dr. Tibor Pasinszki. The *dashed lines* indicate the peak assignment to cation, anion, and carbon dioxide. The experimental spectrum of the ionic liquid after two hours of treatment with carbon dioxide (see Fig. 4.25) is drawn in *gray* for comparison. The *inset* magnifies the spectrum of the carbon dioxide molecule around 600 cm^{-1}

Table 4.11 Vibrational wavenumbers of carbon dioxide in $[\text{C}_2\text{C}_1\text{Im}][\text{OAc}]$ and in the gas phase obtained from AIMD simulations of one carbon dioxide molecule in 36 $[\text{C}_2\text{C}_1\text{Im}][\text{OAc}]$ ion pairs and of a single carbon dioxide molecule. The experimental wavenumbers are taken from Ref. [45]

No.	$\tilde{\nu}_{\text{AIMD}}/\text{cm}^{-1}$		$\tilde{\nu}_{\text{exp}}/\text{cm}^{-1}$		Description
	In $[\text{C}_2\text{C}_1\text{Im}][\text{OAc}]$	Gas phase	Gas phase	Gas phase	
1	598/626	627	667	667	OCO bending
2	1282	1289	1337	1337	Symmetric CO stretching
3	2291	2313	2349	2349	Antisymmetric CO stretching

allows to identify physically absorbed carbon dioxide very easily. Thus, the experimental spectra reveal that chemical absorption is the primary way of carbon dioxide incorporation in $[\text{C}_2\text{C}_1\text{Im}][\text{OAc}]$, since there is no peak around 2300 cm^{-1} after treatment with carbon dioxide for two hours. Only at higher concentrations (after 22 h of treatment with carbon dioxide), a small band indicating physical absorption is observed. The increased bands of the carboxylate and the stronger background in the experimental spectrum show that the ionic liquid contains significant amounts of the carboxylate and acetic acid at this point. Therefore, the AIMD simulation of one carbon dioxide molecule in the pure ionic liquid might not be fully adequate

anymore to reflect the experiment. Nevertheless, it is still possible to qualitatively study the wavenumber shifts of the carbon dioxide compared to the gas phase (see Table 4.11). A slight redshift of all bands is found, which is caused by the interaction of the carbon dioxide with the anions as well as the cations [22, 53]. This agrees with the experimental result, where the antisymmetric CO stretching occurs at 2337 cm^{-1} in the ionic liquid, which is slightly below the wavenumber of 2349 cm^{-1} in the gas phase [45]. Similar shifts have been observed in other ionic liquids that do not show the chemical absorption process [51, 54]. Another effect of the interaction between carbon dioxide and the surrounding ions is the distortion of the molecular symmetry, which lifts the degeneracy of the OCO bending modes and allows for the small intensity gain of the symmetric CO stretching vibration. Due to the coincidence with an intense band of the acetate ion, the peak splitting cannot be verified in the experiment here, but it has been observed in IR measurements of 1-butyl-3-methylimidazolium tetrafluoroborate and hexafluorophosphate [51].

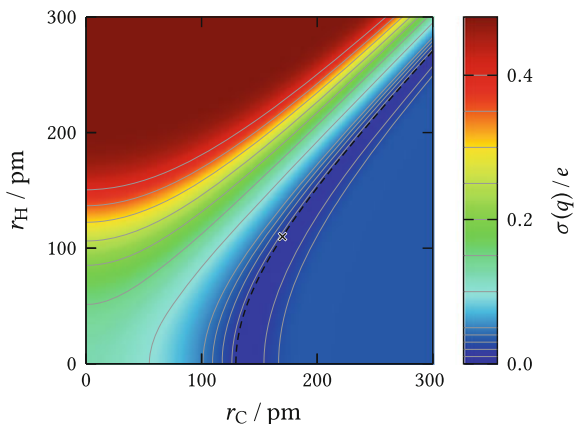
4.5 Voronoi Tessellation of the Electron Density

4.5.1 Selection of the Radii

In Sect. 3.4.2, the idea of the radical Voronoi tessellation as an alternative to the maximally localized Wannier functions was introduced. An important parameter in this approach are the radii that are assigned to the Voronoi sites, which are the atoms of the AIMD simulations here. In principle, the electron density should be separated in a chemically reasonable sense between the molecules, so hydrogen atoms should, e.g., have smaller radii than carbon atoms and oxygen atoms. A readily accessible quantity to assess the distribution of the electron density are the resulting partial charges of the atoms and the molecules. In the simulation of a molecular liquid, e.g., the molecules are expected to be neutral on average. This suggests to take a snapshot of the simulation cell and to calculate the charge distribution function, which is just a histogram of all molecular charges. As long as the whole simulation cell does not carry a charge, the mean value of the molecular charge distribution is automatically zero. The standard deviation, however, shows the difference of the individual charges from zero. Thus, it appears to be a reasonable criterion to demand that the standard deviation of the charge distribution should be as small as possible for a proper tessellation of the electron density.

As the first example, one snapshot of an AIMD simulation of 16 benzene molecules (see Appendix A for computational details) is analyzed. Since benzene only consists of carbon atoms and hydrogen atoms, there are just two radii that can be varied. This allows to visualize the standard deviation as a function of the radii in a two-dimensional contour plot (see Fig. 4.28). Apparently, the contour lines are simple hyperbolas. This is a direct consequence of the tessellation procedure: although the radii constitute two parameters, only the position of the cell face between a car-

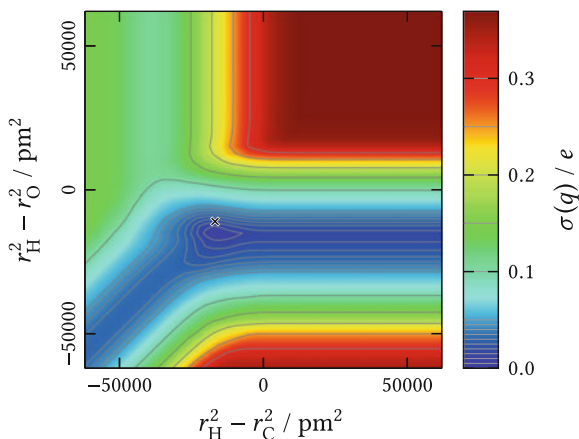
Fig. 4.28 Standard deviation of the molecular charge distribution in a calculation of 16 benzene molecules as a function of the Voronoi radii. The values are given as multiples of the elementary charge. The *black cross* marks the van der Waals radii, and the *dashed line* connects all combinations leading to the same tessellation as the van der Waals radii



bon atom and a hydrogen atom determines the dissection of the electron density. It follows from the definition of the radical Voronoi tessellation (see Eq. (3.74)) that this position is directly related to the difference of the squared radii $r_H^2 - r_C^2$, since adding the same arbitrary number to both squared radii does not change the inequality in (3.74). As the difference of the squared radii is not bound to a particular range, this also shows that the cell face of two neighboring atoms is not necessarily located between them, so that atoms can be situated outside of their respective cell. This happens in the upper left corner and the lower right corner of the contour plot for benzene. On the plateaus, the radius of one atom kind is so large that the other atom kind does not have a cell at all. Since the cell faces are always located halfway between equivalent atoms even in the radical Voronoi tessellation, the same result could be obtained by using the original Voronoi tessellation just with the atoms of one kind as Voronoi sites. While the standard deviation of the charge distribution becomes very large if only the hydrogen atoms have a cell, it is interesting to note that it is quite low if only the carbon atoms remain. Its value is significantly lower than the one obtained with the original Voronoi tessellation employing all atoms, which can be found on the diagonal from the lower left corner to the upper right corner. This indicates that the hydrogen atoms play a minor role for an appropriate dissection of the benzene molecules. The global minimum of the standard deviation is found in the valley between the carbon atom plateau and the diagonal. Most importantly, applying van der Waals radii or any combination with the same difference of the squared radii yields a result very close to this minimum. This shows that a radical Voronoi tessellation using van der Waals radii as Voronoi radii provides a very reasonable distribution of the electron density to the benzene molecules, as it should generally be expected due to the purpose these radii have been developed for.

The next example is one snapshot from an AIMD simulation of 16 methanol molecules (see Appendix A for computational details). Methanol contains hydrogen atoms, carbon atoms, and oxygen atoms, so there are three radii to be varied. It might be argued that different radii should be assigned to the hydrogen atoms in the hydroxyl

Fig. 4.29 Standard deviation of the molecular charge distribution in a calculation of 16 methanol molecules as a function of the Voronoi radii. The values are given as multiples of the elementary charge. The black cross marks the van der Waals radii



group and the methyl group, but the same radius is assigned to all atoms of one kind for simplicity here, as also, e.g., the van der Waals radii do not distinguish such cases. Although there are three radii, only two parameters determine the tessellation because just the differences of the squared radii are important (see above). This allows to show the standard deviation in a two-dimensional contour plot again, but this time as a function of two differences of squared radii (see Fig. 4.29). Any combination of differences could be used on the axes without losing or gaining information, and $r_{\text{H}}^2 - r_{\text{C}}^2$ and $r_{\text{H}}^2 - r_{\text{O}}^2$ were selected for the presentation here. With this choice, horizontal lines and vertical lines correspond to the same location of the cell faces between hydrogen atoms and oxygen or carbon atoms, respectively. On diagonal lines from the lower left corner to the upper right corner, the difference $r_{\text{C}}^2 - r_{\text{O}}^2$ is constant, so these lines correspond to the same location of the cell faces between carbon atoms and oxygen atoms. The surface of the standard deviation consists of three plateaus in the corners that are separated by three valleys along the horizontal, the vertical, and the diagonal. In the upper right corner, only the hydrogen atoms have a Voronoi cell, while only the carbon atoms remain in the upper left corner, and the tessellation just contains the oxygen atoms in the lower right corner. Consequently, the carbon atoms disappear in the valley to the right side, the oxygen atoms vanish in the valley to the top, and the hydrogen atoms do not have a cell in the valley to the lower left corner. The deepest valley is the one leading to the right side, indicating that it is most important to correctly place the cell faces between hydrogen and oxygen atoms for a reasonable distribution of the electron density to the methanol molecules. This can be explained by the structure of methanol, which implicates that intermolecular contacts are primarily formed between hydrogen atoms as well as hydrogen and oxygen atoms while the size of the carbon atoms only influences the intramolecular dissection. The global minimum of the standard deviation is found where the three valleys meet. Most importantly, the van der Waals radii are very close to this minimum again. This shows that they provide a reasonable tessellation also for a molecular liquid with significant intermolecular interactions.

It is interesting to study also the partial charges of carbon atoms and oxygen atoms resulting from the radical Voronoi tessellation in the methanol simulation (see Fig. 4.30). In contrast to the mean value of the molecular charge, which is determined by the total charge of the simulation cell, the mean values of the atomic charges are not necessarily zero. Instead, they lie in a certain range that depends on the kind of the atom and the total number of electrons. If the radii are chosen in such a way that an atom has no cell at all, it just remains the effective nuclear charge defined by the pseudopotential. For the carbon atom, this is $+4e$ on the right side of the plot, and for the oxygen atom, this is $+6e$ in the upper part of the plot. As this value is fixed, also the corresponding standard deviations vanish in these regions. In the opposite case, the radius of one atom kind is so large that it is the only one remaining in the tessellation. On average, all 14 electrons of the methanol molecule are assigned to this atom kind then, resulting in average net charges of $-10e$ and $-8e$ for carbon and oxygen, respectively. Since the cell faces are not generally equal to the molecular boundaries in this case, the standard deviations have finite values in these regions. As before, it is possible to find a minimum in the standard deviation between these two extrema. This time however, the van der Waals radii are not as close to the minimum as for the molecular charges. In particular for the carbon atom, a lower standard deviation is obtained if covalent radii are employed, and the partial charge of $+0.2e$ with covalent radii is chemically more intuitive than the partial charge of $-2.5e$ with van der Waals radii. This is not surprising, since covalent radii have been fitted to resemble intramolecular bond lengths and, therefore, should yield a more reasonable intramolecular distribution of the electron density. For the oxygen atom, both sets of radii do not reach the minimum of the standard deviation, and they provide more similar charges of $-0.1e$ (covalent) and $-0.5e$ (van der Waals). This result is an indication of the dilemma that occurs for a proper choice of the radii to obtain reasonable atomic partial charges. While the covalent radii yield an appropriate distribution of the electron density within the molecule, the van der Waals radii are needed at the same time to separate the electron density between the molecules. It is not possible to simultaneously use two sets of radii in the tessellation, but the following two-step procedure to calculate atomic partial charges in bulk phase simulations can be suggested: At first, molecular cells should be created by a radical Voronoi tessellation with van der Waals radii and a subsequent unification of the atomic cells that belong to the same molecule. Afterwards, another radical Voronoi tessellation with covalent radii should be applied to each molecular cell to obtain new atomic cells with a better intramolecular separation. Future work could focus on an implementation of this method in TRAVIS.

In ionic liquids, the charges assigned to the ions by the Voronoi tessellation are of particular interest. Thus, one snapshot from an AIMD simulation of 36 $[\text{C}_2\text{C}_1\text{Im}][\text{OAc}]$ ion pairs (see Appendix A for computational details) is considered now. This ionic liquid contains four different kinds of atoms: hydrogen, carbon, oxygen, and nitrogen, so three differences of squared radii can be chosen independently. For that reason, it is hard to completely visualize the mean charge and the standard deviation as a function of the radii. Instead, a plot of the standard deviation as a function of the mean charge is presented (see Fig. 4.31). Each combination

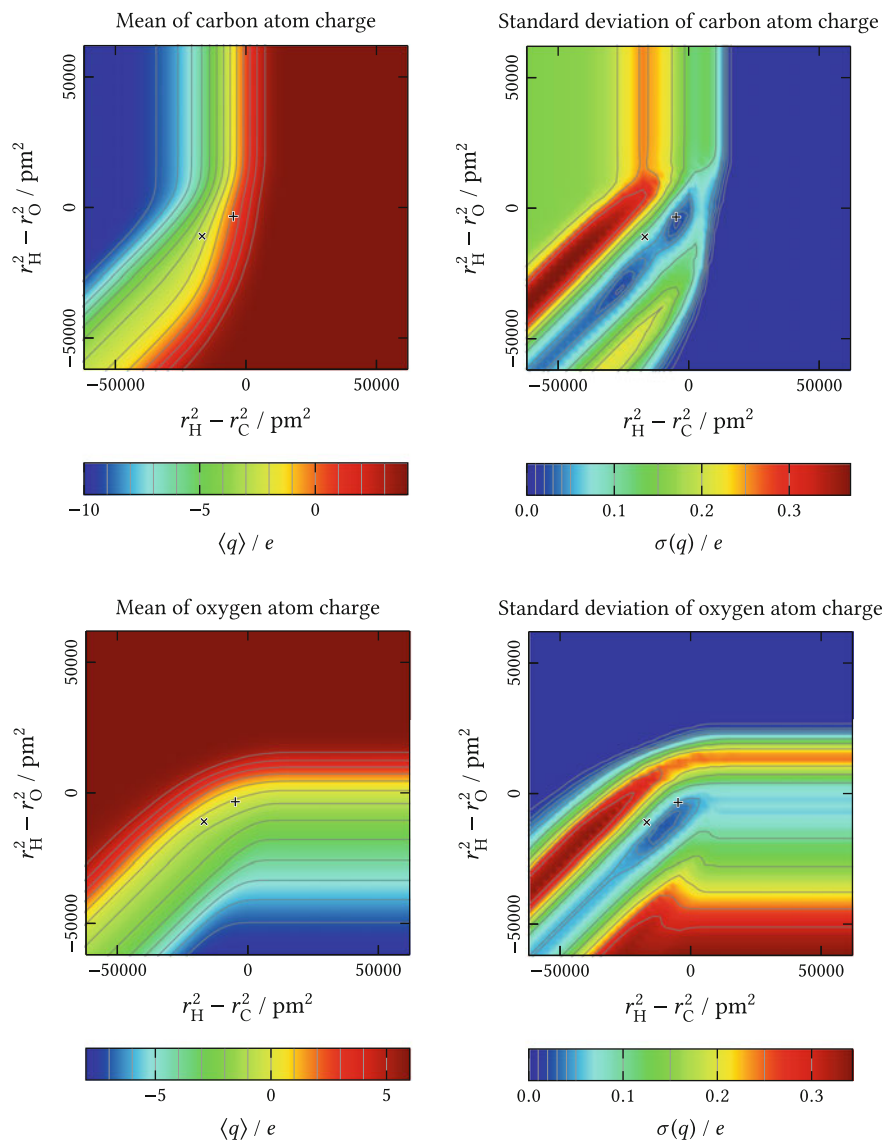


Fig. 4.30 Mean values and standard deviations of the atomic partial charges in a calculation of 16 methanol molecules as a function of the Voronoi radii. The values are given as multiples of the elementary charge. The *cross signs* and the *plus signs* mark van der Waals radii and covalent radii, respectively

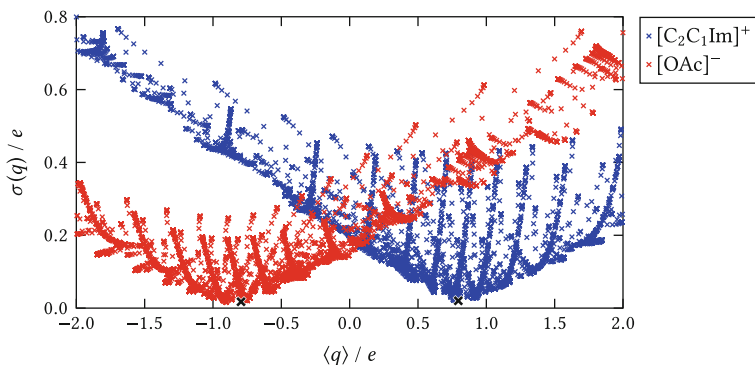


Fig. 4.31 Standard deviation of the anion's and the cation's charge distribution in a calculation of 36 $[\text{C}_2\text{C}_1\text{Im}][\text{OAc}]$ ion pairs as a function of the corresponding mean charge. The axes are scaled in multiples of the elementary charge. The *black* crosses mark the result with van der Waals radii

of radii adds one point for the cation and one point for the anion to this diagram. Apparently, the points form a V-shaped pattern for both the cation and the anion, allowing to identify the minimum of the standard deviation easily. Two results are very important to note. As indicated by the black crosses, the radical Voronoi tessellation with van der Waals radii yields a result that is very close to the minimal standard deviation, so these radii provide also a reasonable separation of the ions in the ionic liquid. Furthermore, the van der Waals radii result in ionic charges of $\pm 0.8e$ instead of the $\pm 1.0e$ for the isolated ions. Charge transfer effects that lead to such reduced ion charges in ionic liquids have already been discussed in the literature (see article [55] and references therein). In classical molecular dynamics simulations with fixed atomic partial charges, the total ion charges are usually chosen between $\pm 0.6e$ and $\pm 0.9e$ to model such effects [56–64]. These charges are often selected on the basis of static calculations of single ions or ion pairs in the gas phase, but Mulliken population analysis [57], Blöchl charges [59], and density-derived electrostatic and chemical charges [64] employed in *ab initio* calculations of the bulk phase have also been used to confirm these values. Here, another justification of the reduced ionic charges in an ionic liquid is found by a radical Voronoi tessellation of the electron density in bulk phase simulations, where van der Waals radii are applied, which deliver an almost minimal standard deviation of the charge distribution.

The examples presented in this section show that it is a chemically reasonable criterion to demand that the radii in the radical Voronoi tessellation should be selected in such a way that the standard deviation in the charge distribution is minimal. This suggests to find the best radii for each particular system by an optimization algorithm that minimizes this standard deviation. This should be of particular interest for the *ab initio* calculation of atomic partial charges that are needed for classical molecular dynamics simulations, as it constitutes a rigorous procedure without adjustable parameters. Future work could focus on this aspect. The examples also show that van der Waals radii are often close to optimal for the separation of molecules or ions in the

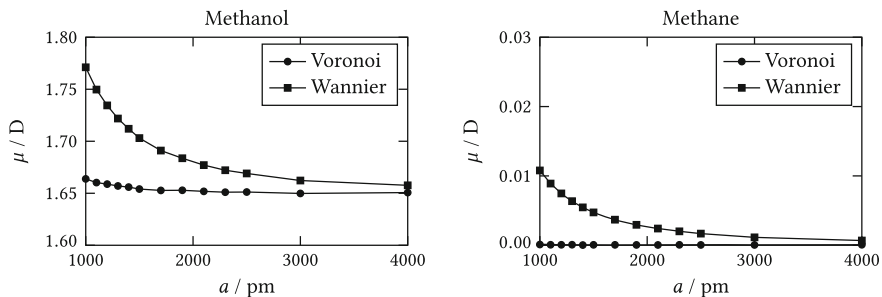


Fig. 4.32 Dipole moments of a single methanol molecule and a single methane molecule by integration of the electron density and maximally localized Wannier function centers as a function of the cell size

bulk phase. Thus, it can safely be recommended to employ van der Waals radii for the calculation of vibrational spectra.

4.5.2 Dipole Moments

For the calculation of vibrational spectra, the molecular dipole moment is the most important quantity to be obtained from a Voronoi tessellation of the electron density. This approach is intended to be used as a replacement for the technique of maximally localized Wannier functions (see Sect. 3.4). Before IR and Raman spectra obtained by these two methods are analyzed in Sect. 4.5.3, the dipole moments are directly compared here. At first, single point calculations of several small test molecules were performed for their respective equilibrium geometries in the gas phase⁴ to avoid the influence of the molecular separation. In this case, the Voronoi approach effectively corresponds to an integration over the whole electron density, it just simplifies the treatment of the boundaries if the molecule is located near a face of the simulation cell. As the maximally localized Wannier functions stem from a unitary transformation of the Kohn–Sham orbitals, they provide the same total electron density and should, in principle, yield the same dipole moment as the Voronoi method.

Since the electronic structure method used for the bulk phase simulations in this thesis relies on periodic boundary conditions, these were also employed for the gas phase calculations. In doing so, the cubic simulation cell should be sufficiently large to avoid the interaction of the molecule with its periodic images, and for that reason, the dependence of the dipole moments on the cell size is studied first. For a methanol molecule (see Fig. 4.32), a significant difference of the two techniques is found in small cells. The Voronoi dipole moment can be regarded as converged within the numerical accuracy of the method at a cell size of $a = 1500$ pm, and also the

⁴I would like to thank Roman Elfgen for carrying out some of the calculations presented in this section.

relative difference between $a = 1000$ pm and $a = 4000$ pm is less than one percent. In contrast, the Wannier dipole moment shows a much stronger dependence on the cell size and it converges very slowly. Nevertheless, both methods yield the same dipole moment of 1.65 D in the limit of a large cell. This value is slightly lower than the experimental result of 1.68 D [65], and the deviation has to be attributed to the electronic structure method. However, the Wannier method clearly seems to suffer from intrinsic problems in small cells. A completely analogous behavior is observed with other polar molecules such as water, ammonia, and formaldehyde.

The issue of the Wannier approach becomes even more severe in the case of certain nonpolar molecules. For methane (see Fig. 4.32), which cannot have a dipole moment due to its symmetry, the Voronoi method yields a vanishing dipole moment within the numerical accuracy for any cell size. The Wannier localization results in a dipole moment of more than 0.01 D with $a = 1000$ pm instead. Only in very large cells, the Wannier dipole moment reaches zero, so this is a deficiency of the Wannier method. The same behavior is found in calculations of acetylene, where the Wannier dipole moment is even 0.07 D with $a = 1000$ pm. For other nonpolar molecules, however, the Wannier method agrees with the Voronoi approach about the vanishing dipole moment, e.g., for ethane and ethylene. A systematic rule for which nonpolar systems the Wannier approach shows an artificial dipole moment has not been found yet.

Another issue of the Wannier technique occurs in the special case of benzene. This nonpolar molecule belongs to the class for which the Wannier localization introduces an artificial dipole moment, and this becomes even larger than 0.2 D in small simulation cells (see Fig. 4.33). The Wannier function centers in benzene are arranged in a pattern of alternating single bonds and double bonds, just as in the well-known Kekulé formula [66] (see Sect. 4.5.3 for further details). There are two such patterns, and the solution to which the localization converges depends only on the internal numerics of the implementation. It is important to note that this also influences the orientation of the artificial dipole moment, as it is apparent in the components of the dipole vector (see Fig. 4.33 for the z component, the other components show the same behavior). Between $a = 3000$ pm and $a = 4000$ pm, the

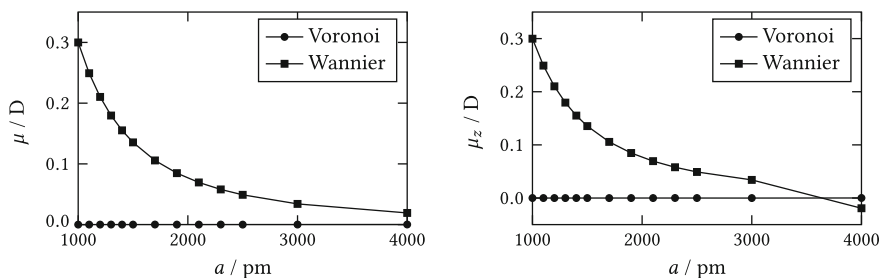


Fig. 4.33 Magnitude μ and z component μ_z of the dipole moment of a single benzene molecule by integration of the electron density and maximally localized Wannier function centers as a function of the cell size

dipole vector is inverted because the Wannier localization switches between the two patterns of single bonds and double bonds.

The application of a cubic simulation cell with periodic boundary conditions always disturbs the rotational invariance of the system to a certain degree. To investigate if the result of the Wannier localization strongly depends on this, the orientation of the molecules in the simulation cell was varied starting from the structures used above. In a systematic manner, arbitrary rotations in the three-dimensional space can be represented by the Euler angles ϕ , θ , and ψ [67], which describe three consecutive rotations about specific coordinate axes. There exist different conventions to which axis each angle refers, and the one that constructs the final rotation matrix according to

$$\mathbf{R} = \begin{pmatrix} 1 & 0 & 0 \\ 0 & \cos \phi & \sin \phi \\ 0 & -\sin \phi & \cos \phi \end{pmatrix} \begin{pmatrix} \cos \theta & 0 & -\sin \theta \\ 0 & 1 & 0 \\ \sin \theta & 0 & \cos \theta \end{pmatrix} \begin{pmatrix} \cos \psi & \sin \psi & 0 \\ -\sin \psi & \cos \psi & 0 \\ 0 & 0 & 1 \end{pmatrix} \quad (4.1)$$

was applied here. Due to the cubic symmetry of the simulation cell, a sufficiently large number of orientations can be sampled if each angle takes values of 0.0° , 22.5° , and 45.0° . This results in 27 combinations, which are systematically ordered for the visualization in such a way that ϕ varies slowliest and ψ varies fastest. For each of the rotated structures, single point calculations were performed with a cell size of $a = 1200$ pm to recalculate the dipole moments. At first, the magnitude of the dipole moments is studied for the molecules methanol and benzene (see Fig. 4.34). As it should be expected, the molecular orientation in the simulation cell has a negligible influence on the Voronoi dipole moment in both cases. The Wannier dipole moment is almost constant for methanol too, but it is important to note that it shows strong fluctuations for benzene. To visualize also the direction of the dipole vector with respect to the molecule, the following procedure is used: For each molecular orientation, the normalized difference vector of the Voronoi dipole moment and the Wannier dipole moment is calculated. Furthermore, each rotation matrix is applied to the normalized difference vector of the first orientation with $(\phi, \theta, \psi) = (0^\circ, 0^\circ, 0^\circ)$. For each orientation, these two vectors are compared (see Fig. 4.34 for the x components, the other components show the same behavior). In the case of methanol, the vectors agree very well, showing that it does not matter for the result whether the molecule or the dipole vector is rotated. This means that the dipole moment is independent of the molecular orientation in the simulation cell, and the Wannier localization always adds a constant offset. The picture is, however, very different for benzene, where the two vectors do not coincide for most orientations. This means that not only the magnitude but also the direction of the dipole vector in the molecular coordinate system strongly depends on the orientation of the benzene molecule in the simulation cell. While the constant offset in methanol can be tolerated and possibly fixed afterwards, the situation in benzene is a clear deficiency of the Wannier method. For IR spectra, e.g., the time derivative of the dipole moment is used, so the constant in methanol

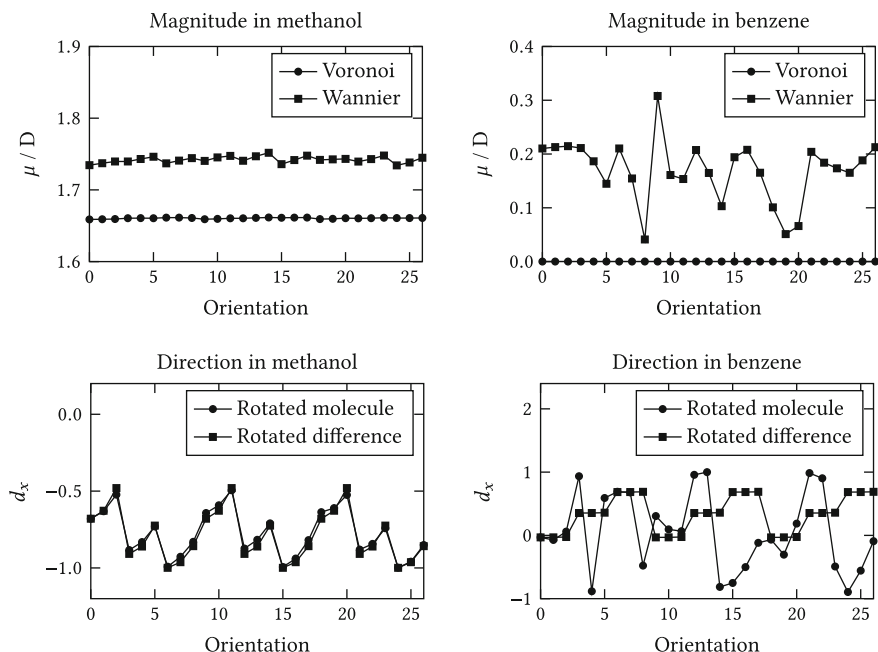


Fig. 4.34 Dipole moment μ of methanol and benzene by integration of the electron density and maximally localized Wannier function centers for different molecular orientations in the simulation cell, and x component d_x of the normalized difference vector between these two methods for different molecular orientations in the simulation cell

vanishes, but the situation in benzene is likely to introduce artifacts in the spectrum (this is confirmed in Sect. 4.5.3).

To compare Voronoi dipole moments and Wannier dipole moments in the bulk phase, a sequence of 20 steps was taken from an AIMD simulation of 16 methanol molecules under periodic boundary conditions (see Appendix A for computational details). The dipole moment curves of one particular molecule (see Fig. 4.35) show that the magnitude of the Wannier dipole moment is larger, and that its fluctuations are stronger. The difference in the magnitude is also apparent in the average over all 16 molecules (see Fig. 4.35), where the standard deviation additionally indicates that the Wannier dipole moments have a broader distribution. Beside the general issues of the Wannier localization that were discussed for the gas phase, another explanation has to be considered for the liquid additionally. In the Wannier approach, each Wannier function center is assigned to exactly one molecule, so the total electron density is dissected in such a way that all molecules are neutral. In the Voronoi method instead, the electron density can flow between the cells and the molecules carry temporarily fluctuating charges. Considering a certain piece of electron density moving from one molecule toward its neighbor, this fully contributes to an increase of the Wannier dipole moment, but it only increases the Voronoi dipole moment until the cell face

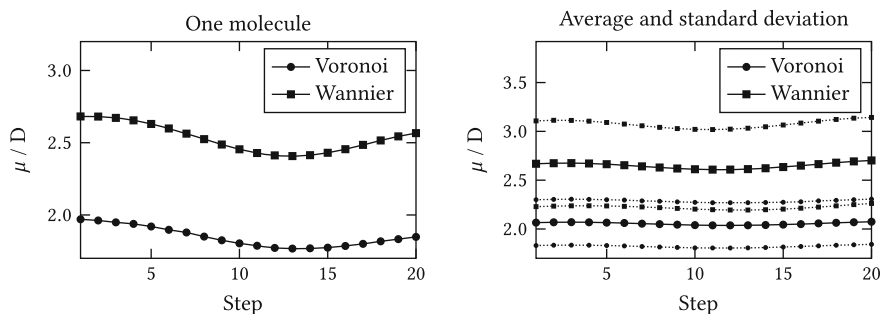


Fig. 4.35 Dipole moment of one selected molecule and average dipole moment of all molecules in a bulk phase simulation of 16 methanol molecules over 20 steps. The *dotted lines* indicate the standard deviation

is reached while it transfers to a change in the charge from then on. Therefore, the Voronoi dipole moments are smaller, have a narrower distribution, and show less fluctuations than the Wannier dipole moments.

The experimental dipole moment of methanol in the liquid phase is 2.87 D [68], which is in better agreement with the Wannier technique. However, it has to be taken into consideration that such experimental values are usually based on models like the Debye theory [69], which relate molecular dipole moments to the macroscopically measurable susceptibility due to orientational polarization. Since these models presume neutral molecules, it cannot be expected that the Voronoi approach with temporarily fluctuating charges accurately reproduces them.

4.5.3 Vibrational Spectra

In the last section, it was shown that the Wannier approach and the Voronoi method do not necessarily yield the same dipole moments. In the gas phase, this appears to be a general deficiency of the Wannier localization, while in the liquid phase, differences in the molecular separation have to be considered too. To investigate how these effects transfer to IR and Raman spectra, the two techniques are compared in this regard for several bulk phase simulations (see Appendix A for computational details). Except for neat $[\text{C}_2\text{C}_1\text{Im}][\text{OAc}]$, all spectra presented in this section have been published in Ref. [70].

The assessment starts with methanol (see Fig. 4.36). Both approaches agree very well concerning relative intensities and peak shapes, but the Voronoi method yields significantly lower absolute intensities. This is a direct consequence of the decreased dipole fluctuations mentioned before (see Sect. 4.5.2). In linear approximation, the IR intensity is proportional to the square of the dipole moment change (see Sect. 2.4.2), so the absolute intensities are closely related to the amplitude of the dipole fluctuations in the MD approach. To assess whether the Voronoi method or the Wannier

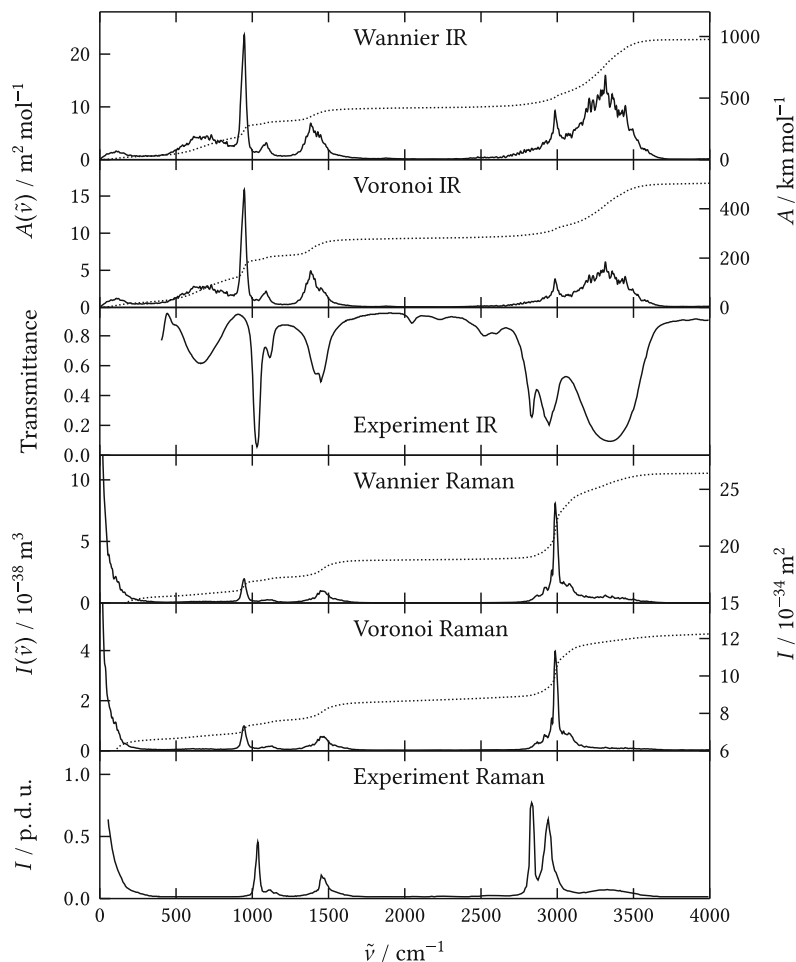


Fig. 4.36 Spectra of methanol in the liquid phase: comparison of IR and Raman spectra by Wannier approach and Voronoi approach from an AIMD simulation of 16 methanol molecules. The *dotted lines* show the integrals with the scales on the *right* side. The experimental spectra are taken from Ref. [7]

method performs better in this respect, accurate experimental data would be needed and the influence of the approximations in the electronic structure calculation had to be considered in greater detail. For the interpretation of the experiment, however, the relative peak intensities and the band positions are often more important, and these are reproduced in a very similar manner by both methods [7].

Also for benzene, the IR spectra show a good general agreement (see Fig. 4.37). The only important difference is the additional broad band feature predicted by the

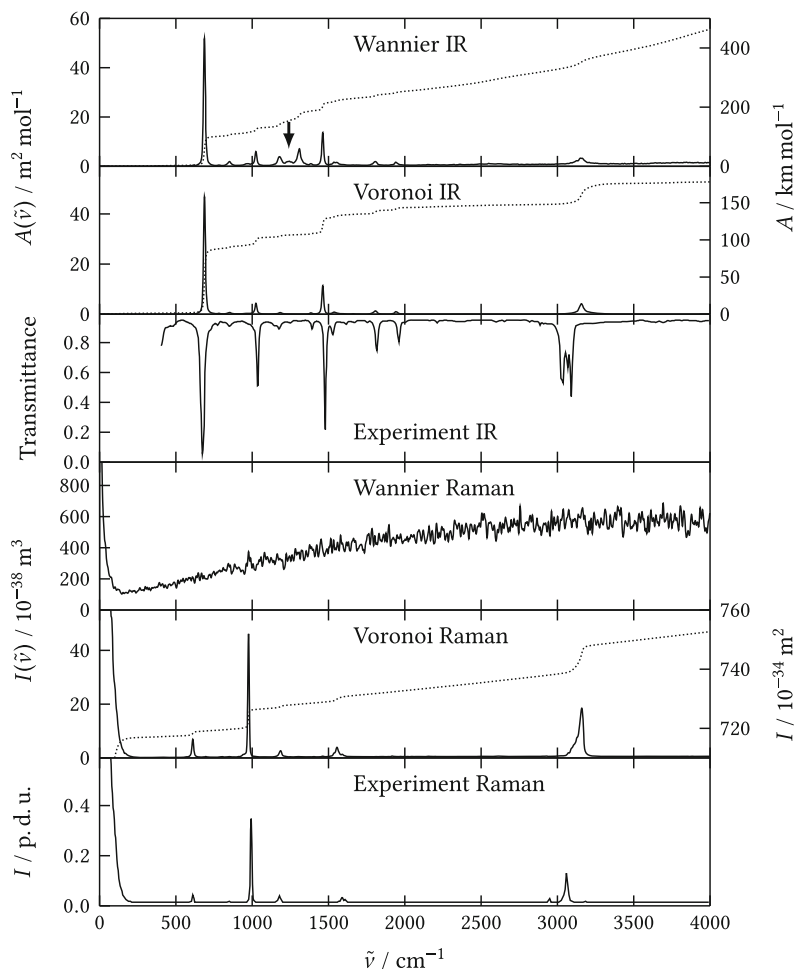


Fig. 4.37 Spectra of benzene in the liquid phase: comparison of IR and Raman spectra by Wannier approach and Voronoi approach from an AIMD simulation of 16 benzene molecules. The *dotted lines* show the integrals with the scales on the *right* side. The experimental spectra are taken from Ref. [7]. The *arrow* marks the artificial band introduced by the Wannier localization

Wannier method between 1200 and 1350 cm^{-1} as marked by the arrow. This is neither found with Voronoi dipole moments, nor is there a corresponding peak in the experimental data [7, 71]. The reason for that is the combination of the artificial dipole moment and the two possible solutions of the Wannier localization in benzene. The maximally localized Wannier function centers are arranged in a pattern of alternating single bonds and double bonds (see Fig. 4.38), which can be placed in two different ways. As shown in Sect. 4.5.2, this also influences the direction of the artificial dipole vector, so switching the bond pattern directly transfers to a change of the dipole moment that should appear in the IR spectrum. In the equilibrium structure

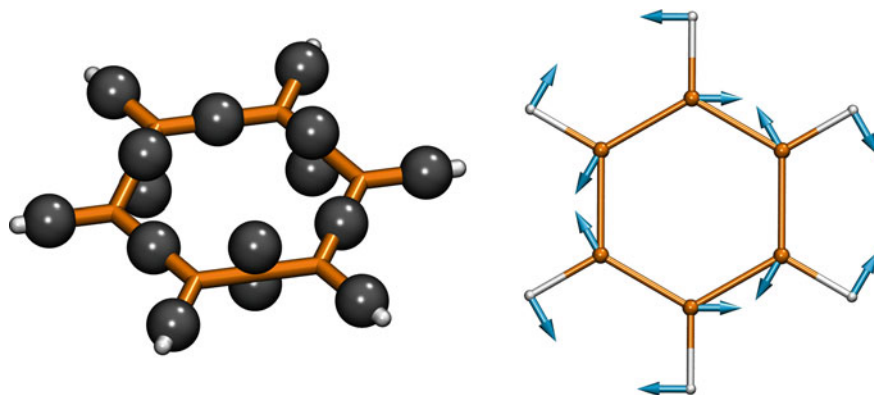


Fig. 4.38 *Left:* Wannier function centers in benzene. *Right:* Normal mode deforming benzene toward cyclohexatriene. Adapted from reference [70] with permission from the PCCP Owner Societies

with equal C–C bond lengths, it is arbitrary which solution is reached, but during the AIMD, the bond lengths fluctuate and it is reasonable to assume that shorter distances are preferred for the placement of the double bonds. This suggests that the bond pattern should primarily follow a vibrational mode that changes the C–C bond lengths alternatingly. In the normal coordinate analysis, one such mode is found, which deforms the benzene toward cyclohexatriene (see Fig. 4.38), and the power spectrum of this mode exactly matches the shape of the additional band feature in the Wannier IR spectrum.

Due to the artificial IR band when Wannier function centers are employed, the Voronoi spectrum agrees better with the experiment. A deficiency is again the blueshift and the underestimated intensity of the CH stretching modes. However, it is important to point out that the two bands between 1750 and 2000 cm^{-1} are reproduced very well, as this is the wavenumber region where overtones and combination bands of aromatic compounds typically appear.

The artificial dipole moment in the Wannier method constitutes an even more severe problem for the estimation of polarizabilities. If the Wannier localization does not converge to the same bonding pattern in the two calculations with external electric field and without external electric field, the flipping dipole vector strongly interferes with the change in the dipole moment induced by the electric field. This artificially increases the resulting polarizability by orders of magnitude, leading to strong spikes in its time development, and making the Fourier transform unsuitable as a Raman spectrum (see Fig. 4.37). The Voronoi method does not suffer from this problem and it provides a Raman spectrum that is in very good agreement with experimental data [7, 72], so it clearly outperforms the Wannier approach in the case of benzene.

Since it contains an aromatic ring, phenol is expected to show the same effects in the Wannier spectra as benzene. However, it intrinsically absorbs IR radiation in the wavenumber region of the cyclohexatriene mode around 1310 cm^{-1} , so the potentially present artificial band in the IR spectrum is not discernible (see Fig. 4.39). Instead, both approaches agree very well with each other and also with the experimental data [7, 73, 74] below 2000 cm^{-1} . The only differences in the Voronoi spectrum are the significantly reduced absolute intensity similar to methanol, and the reduced

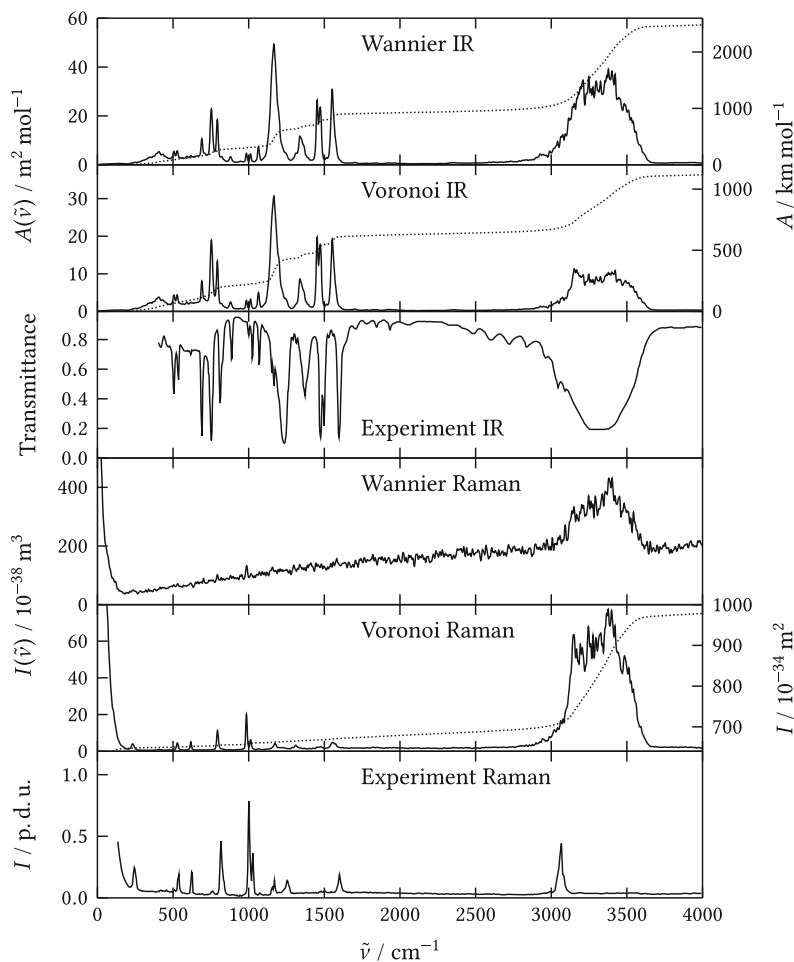


Fig. 4.39 Spectra of phenol in the liquid phase: comparison of IR and Raman spectra by Wannier approach and Voronoi approach from an AIMD simulation of 32 phenol molecules. The *dotted lines* show the integrals with the scales on the *right* side. The experimental spectra are taken from Ref. [7]

relative intensity of the broad OH stretching band. In contrast, the Raman spectra clearly reveal the deficiency of the Wannier localization for phenol (see Fig. 4.39). Although the broad OH stretching band can be identified and the absolute noise level is reduced in comparison to benzene, the Wannier spectrum is still unsuitable for a detailed analysis. The Voronoi approach, instead, provides a reasonable spectrum that agrees very well with the experiment [7, 74, 75] below 2000 cm^{-1} . A clear deficiency is only the overestimation of the OH and CH stretching vibrations above 3000 cm^{-1} , but also the literature data [7, 74, 75] is not fully consistent at this point. Since this intense band is even discernible in the noise of the Wannier spectrum and it is rather insensitive to changes of the Voronoi radii, it is unlikely to be a specific issue of the Voronoi method. To check if it is a particular problem of the BLYP exchange-correlation functional selected for the AIMD, static calculations of a single phenol molecule were carried out comparing BLYP with the meta-GGA functional TPSS and the hybrid functional B3LYP (see Fig. 4.40). The gas phase calculations cannot reproduce the broad OH stretching band caused by the intermolecular hydrogen bonding in the bulk. The three functionals yield slightly different band positions, but they agree very well on the intensities. This indicates that also the choice of the exchange-correlation functional is not responsible, and the intensity mismatch between simulation and experiment seems to be a more general issue of DFT.

In Sect. 4.5.1, the charge transfer between the ions in $[\text{C}_2\text{C}_1\text{Im}][\text{OAc}]$ was discussed. Due to the discrete nature of the Wannier function centers, the charges are quantized to integer numbers in the Wannier approach, and in particular, they are fixed at $\pm 1.0e$ for the ions in $[\text{C}_2\text{C}_1\text{Im}][\text{OAc}]$. In contrast, the electron density is con-

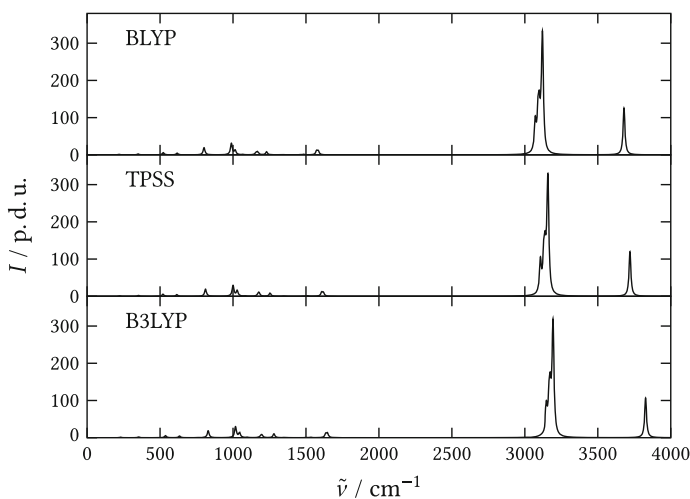


Fig. 4.40 Raman spectra of phenol in the gas phase by static calculations employing three different exchange-correlation functionals. The lines are broadened by Lorentzian functions with a FWHM of 15 cm^{-1}

tinuously divided by the radical Voronoi tessellation, and the ions in $[\text{C}_2\text{C}_1\text{Im}][\text{OAc}]$ carry average charges of $\pm 0.8e$ if van der Waals radii are applied. Consequently, deviations in the vibrational spectra might be expected too. The most important difference in the IR spectra (see Fig. 4.41) concerns the broad CH stretching band around 3000 cm^{-1} . While the Wannier approach assigns a significant part of the intensity to the anion, there is almost no anion contribution to this band in the Voronoi spectrum. In linear approximation, the IR spectrum can only possess peaks at the wavenumbers of the normal modes. Reconsidering the normal coordinate analysis of $[\text{C}_2\text{C}_1\text{Im}][\text{OAc}]$ (cf. Figs. 4.20 and 4.21) reveals that the cation has three broad modes that match the IR band while the anion has only three sharp modes in the corresponding wavenumber range and no mode that matches the IR band. This

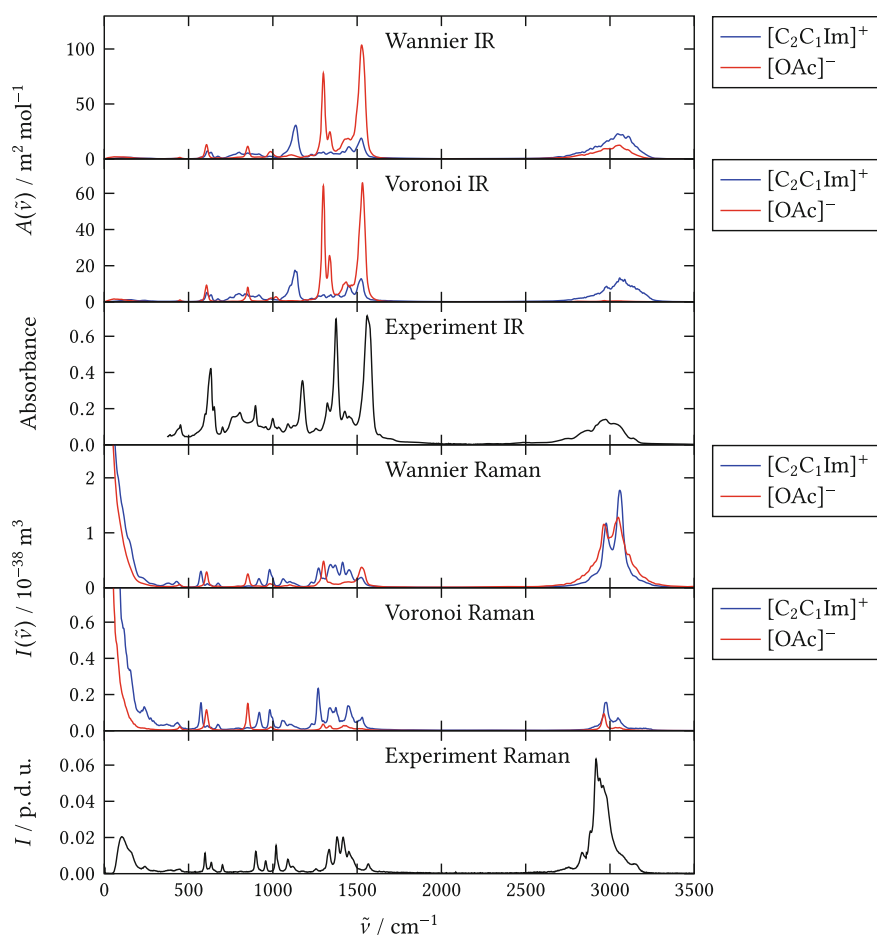


Fig. 4.41 Spectra of neat $[\text{C}_2\text{C}_1\text{Im}][\text{OAc}]$: comparison of IR and Raman spectra by Wannier approach and Voronoi approach from an AIMD simulation of 36 $[\text{C}_2\text{C}_1\text{Im}][\text{OAc}]$ ion pairs. The experimental spectra have been provided by Prof. Dr. Tibor Pasinszki

means that the broad band around 3000 cm^{-1} should preferably be assigned only to the cation and not to the anion. In this regard, the Voronoi method performs much better than the Wannier method, and it makes the IR spectrum consistent with the normal coordinate analysis. In the Raman spectra (see Fig. 4.41), the Voronoi approach predicts a much lower intensity and a significantly different shape for the CH stretching band around 3000 cm^{-1} . While the Wannier spectrum is superior regarding the intensity of this band relative to the other peaks in the spectrum, the Voronoi spectrum reproduces the experimental shape of this band much better. Furthermore, significant differences are apparent between 1200 and 1600 cm^{-1} . In particular, the two anion peaks in this wavenumber range are significantly reduced in the Voronoi spectrum. This suggests an alternative assignment in comparison to Sect. 4.4.1 and Ref. [16]. The experimental Raman peaks at 1334 and 1567 cm^{-1} that were assigned to modes A8 and A12 of the anion could also be matched to modes C27 and C40 of the cation. The latter describe a mixture of $\text{C}_{\text{Et}}\text{N}$ stretching and $\text{C}_{\text{Me}}\text{N}$ stretching, and a $\text{C}_{\text{Im}}\text{C}_{\text{Im}}$ stretching vibration, respectively. However, both the Voronoi approach and the Wannier approach are not fully consistent with the experimental result in this part of the Raman spectrum.

Similar effects as in the neat ionic liquid are also found in the IR spectra of the mixture with water (see Fig. 4.42). Again, the main difference between Wannier and Voronoi method concerns the intensity assigned to the anion in the wavenumber region above 3000 cm^{-1} . Although the anion does not possess any broad normal modes, it has a very broad IR band in the Wannier spectrum. In this system, the IR intensity is transferred not only from the cation but in particular from the water

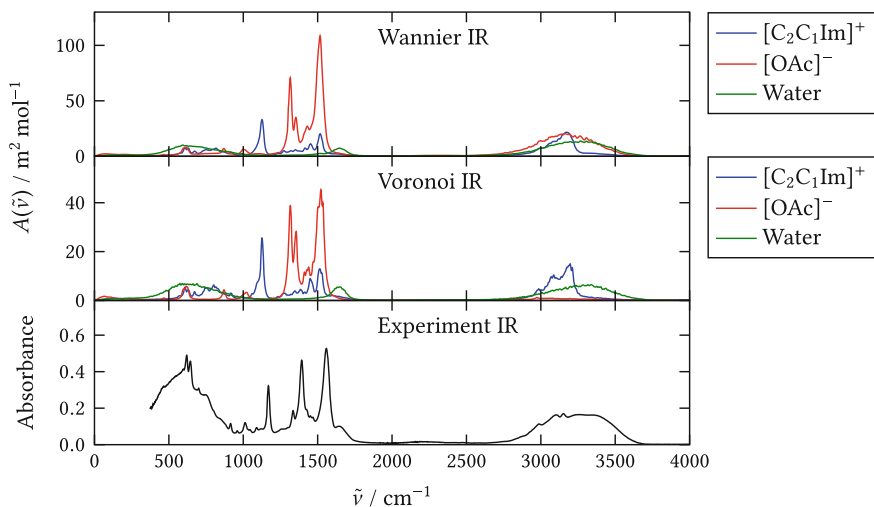


Fig. 4.42 IR spectra of a $[\text{C}_2\text{C}_1\text{Im}][\text{OAc}]$ -water mixture: comparison of IR spectra by Wannier approach and Voronoi approach from an AIMD simulation of 27 $[\text{C}_2\text{C}_1\text{Im}][\text{OAc}]$ ion pairs with 81 water molecules. The experimental spectrum has been provided by Prof. Dr. Tibor Pasinszki

molecules, which possess two very broad OH stretching modes in this wavenumber range. The Voronoi approach provides a more reasonable separation of the molecules and the ions in this respect, and it assigns almost no IR intensity to the anion above 3000 cm^{-1} . This makes the result more consistent with the picture of the normal coordinates.

4.6 Vibrational Circular Dichroism

4.6.1 Assessment of the Magnetic Moments

The general methodology to predict VCD spectra in the MD approach was described in Sect. 3.5. Of particular importance is the calculation of magnetic moments, for which a new approach is proposed in this thesis. Before the VCD spectra are analyzed for several examples, the accuracy of the magnetic moments with respect to the parameters entering their calculation is assessed. These parameters are the timestep at which the electron density needs to be sampled, the convergence threshold in the BiCGstab(*l*) algorithm, and the background electron density to stabilize the solution. The model system for this purpose should preferably be a chiral molecule, and 2-butanol was selected here as it is the smallest chiral alkanol.

For the simulation of IR and Raman spectra, it is sufficient to sample the dipole moments and the polarizabilities with a step size of 4 fs. With the simulation timestep of 0.5 fs used for all AIMD simulations in this thesis, this means that the dipole moments and the polarizabilities need to be calculated in every eighth step. According to the Nyquist–Shannon theorem, this provides the spectrum up to a wavenumber of 4170 cm^{-1} . In principle, this would be sufficient for VCD spectra too, but it has to be taken into consideration that the time derivative of the electron density enters the calculation of the magnetic moments. To find the timestep that is needed to obtain this time derivative with reasonable accuracy, the 2-butanol molecule was simulated with a timestep of 0.1 fs and the electron density was saved in all steps. At first, the magnetic moment was calculated in each step by taking the whole trajectory, and using a background electron density of $6.7 \cdot 10^{-3}\text{ e/nm}^3$ and a relative convergence criterion of $1 \cdot 10^{-3}$ (cf. Sect. 3.5). Afterwards, only every fifth step and every tenth step of the trajectory were processed, so the time derivative is computed with step sizes of 0.5 and 1.0 fs. A comparison of the resulting magnetic moments (see Fig. 4.43) within a time range of 20 fs shows that the difference between 0.1 and 0.5 fs is in the order of $10^{-5}\mu_{\text{B}}$, which usually corresponds to a relative error of about 1%. For a step size of 1.0 fs, the deviation to a step size of 0.1 fs reaches values in the order of $10^{-4}\mu_{\text{B}}$, yielding a relative error around 5%. This indicates that the even larger step size of 4 fs recommended for dipole moments is surely insufficient for magnetic moments. On the other hand, the result suggests that the usual simulation timestep of 0.5 fs does not need to be reduced if the electron density is processed in every step. Considering that this timestep introduces further deviations regarding,

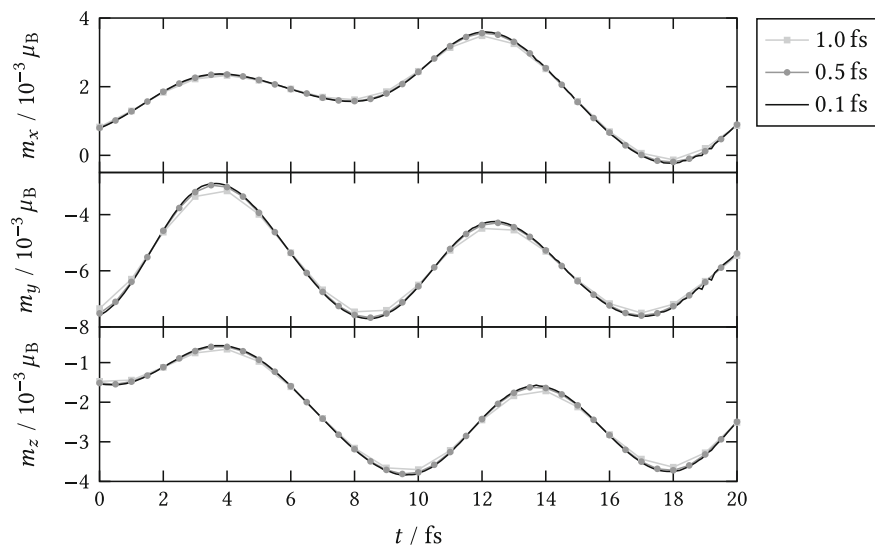


Fig. 4.43 Vector components of the magnetic moment of a single 2-butanol molecule for three different timesteps

e.g., the vibrational wavenumbers (see Sect. 3.2.3), the relative difference in the order of 1% in the magnetic moments due to the cruder approximation of the time derivative is absolutely tolerable.

The next parameter to be studied is the relative convergence threshold in the BiCGstab(l) algorithm that is applied as described in Sect. 3.5. Three different values are compared for a timestep of 0.5 fs and a background electron density of $6.7 \cdot 10^{-3} e/\text{nm}^3$ (see Fig. 4.44). The value of $1 \cdot 10^{-3}$ chosen in the comparison of different timesteps above is very tight, since in some snapshots, the solution algorithm is even not able to reach this threshold. However, it is obvious that less tight criteria are sufficient to obtain a reasonably converged magnetic moment. Even with a value $5 \cdot 10^{-2}$, the relative deviations are in the order of a few percent. The threshold of $1 \cdot 10^{-2}$ appears to be a proper choice, and thus, a threshold of $5 \cdot 10^{-3}$ should be a safe recommendation.

An important issue for the calculation of magnetic moments are large empty regions in the simulation cell. At these points, the scalar field $\alpha(\mathbf{r})$ in the partial differential equation (3.92) can take, in principle, arbitrary values without influencing the resulting current density. This strongly hampers the convergence of the solution algorithm, and for the 2-butanol simulation here, it is not possible to obtain a reasonable result in any snapshot of the trajectory. To avoid this problem, a constant background electron density is added to the system. To a small extent, this allows a current to flow everywhere in the simulation cell, and it makes the solution of the differential equation much more stable. For 2-butanol, it is found that a minimal background electron density in the order of $6.7 \cdot 10^{-3} e/\text{nm}^3$ (equal to 10^{-6} a. u.)

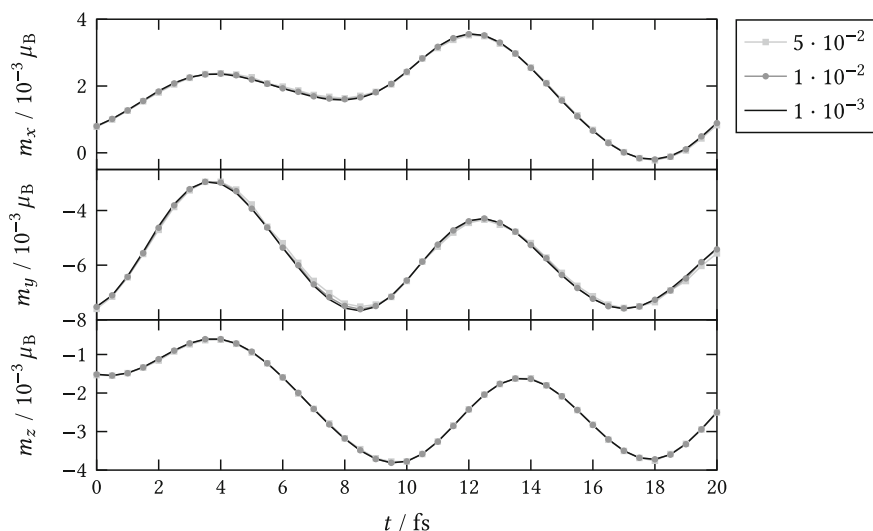


Fig. 4.44 Vector components of the magnetic moment of a single 2-butanol molecule for three different convergence criteria in the BiCGstab(l) algorithm

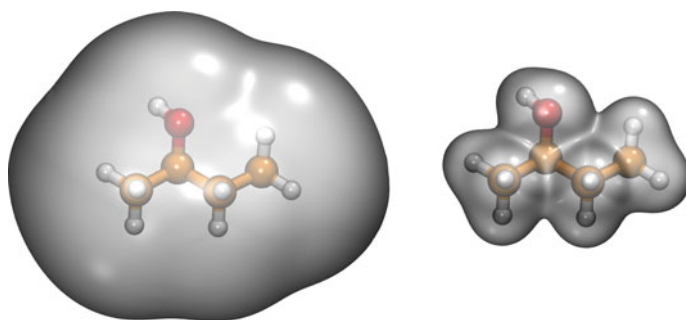


Fig. 4.45 Isosurfaces of the electron density in 2-butanol. *Left:* $\rho = 1.3 \cdot 10^{-2} e/\text{nm}^3$, *right:* $\rho = 50 e/\text{nm}^3$

is needed. Significantly smaller choices do not sufficiently stabilize the algorithm. Still, this value is by several orders of magnitude lower than the electron density in the molecule near the nuclei (see Fig. 4.45) and the influence on the magnetic moment should be negligible. This can be confirmed by comparing the result with two larger values of the background electron density (see Fig. 4.46). This shows that clear effects on the magnetic moment start to be visible with a background electron density of $6.7 \cdot 10^{-1} e/\text{nm}^3$. Since the result with $6.7 \cdot 10^{-2} e/\text{nm}^3$ is almost equal to $6.7 \cdot 10^{-3} e/\text{nm}^3$, it is safe to assume that the latter does not influence the magnetic moment in an unacceptable manner. Finally, it should be noted that the background electron density is not needed at all for bulk phase simulations. In this case, calcula-

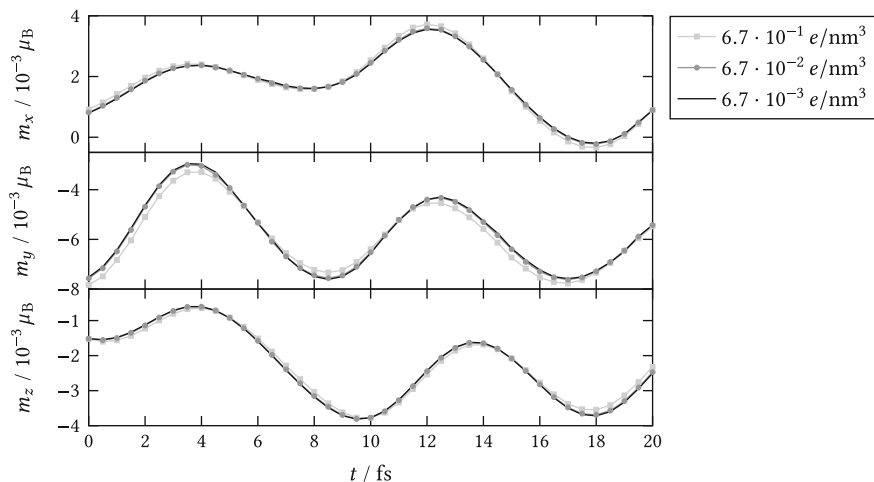


Fig. 4.46 Vector components of the magnetic moment of a single 2-butanol molecule for three different values of the background electron density

tions with the unmodified electron density from the AIMD simulation proved to be stable in all systems investigated here.

4.6.2 Analysis of the Spectra

As shown in the last section, the magnetic moments are reasonably converged with the parameters selected for the solution of Eq. (3.92). The resulting VCD spectra are investigated for several different systems in this section. As the first example, a single 2-butanol molecule in the (*R*)-configuration is chosen (see Appendix A for computational details). Beside the magnetic moments, also the dipole moments are needed for the VCD spectrum (see Sect. 3.5), so the IR spectrum is immediately available for analysis too. Both spectra are compared to experimental data of a dilute (0.029 mol/L) solution of (*R*)-2-butanol in carbon disulfide [76], which should provide a reasonable approximation to the gas phase [77] (see Fig. 4.47). Due to the restrictions imposed by the experimental setup and the IR bands of carbon disulfide, the measured spectra are only available between 900 and 1400 cm^{-1} , but this is the most important wavenumber region in the case of 2-butanol.

The IR spectra are in good agreement, but the simulation shows the significant redshift that has been observed in other systems before. This concerns in particular the two intense bands at 910 and 989 cm^{-1} in the experiment, for which the AIMD predicts wavenumbers of 857 and 932 cm^{-1} , respectively. The OH stretching mode appears with an intense peak at 3671 cm^{-1} in the simulated spectrum. Due to the coupling with the torsion of the C–O bond showing up at 227 cm^{-1} , the OH

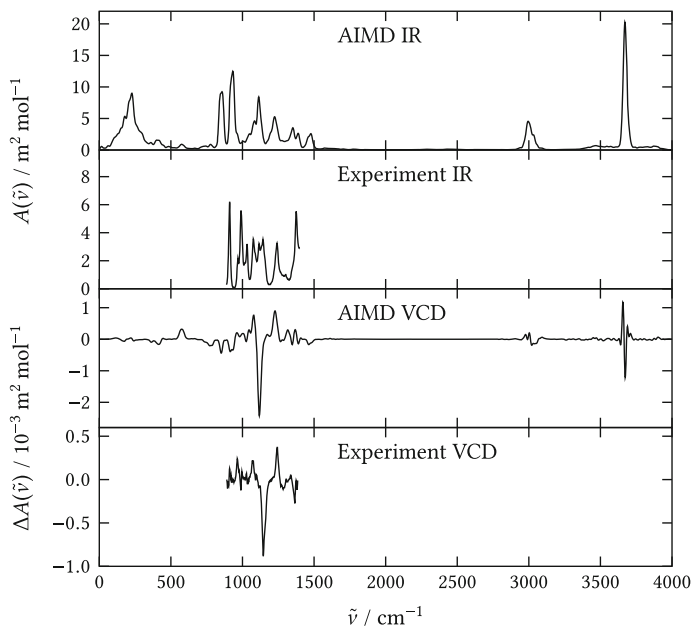


Fig. 4.47 IR spectrum and VCD spectrum from an AIMD simulation of (*R*)-2-butanol in the gas phase. The experimental spectra of a (*R*)-2-butanol solution in carbon disulfide (0.029 mol/L) are taken from Ref. [76]

stretching band possesses broad satellite peaks analogous to the effect observed in methanol (see Sect. 4.1.1). The most important result for the investigation in this section is that the simulation reproduces the shape of the VCD spectrum very well. The experimental pattern with a positive peak at 1076 cm^{-1} followed by a strong negative peak at 1143 cm^{-1} and another positive peak at 1241 cm^{-1} appears in the same manner also in the simulated spectrum. The wavenumbers are slightly shifted, so the bands are found at 1078 , 1118 , and 1227 cm^{-1} in the AIMD, but the intensity ratios are in very good agreement. The coincidence is of particular interest regarding the conformational flexibility of 2-butanol. Both the C–O bond and the central C–C bond have three distinct torsional minima on the potential energy surface, resulting in nine conformations for the molecule. Static calculations reveal that they significantly differ in the VCD spectra [76, 77], but apparently, the AIMD simulation properly averages over all important conformers. It should be noted that simulated VCD spectra are more sensitive to noise than simulated IR spectra. The experiment does not include the wavenumber region of the OH stretching band, but since there is only one vibrational mode, it is unlikely that it would show a strong positive peak next to a strong negative peak as predicted by the AIMD, and this should be considered as noise. Finally, it should also be recognized that the absolute intensities in simulation and experiment agree very well for both the IR and the VCD spectrum.

Due to the ability to form intermolecular hydrogen bonds, significant differences in the spectra of the gas phase and the liquid phase of 2-butanol are expected. For that

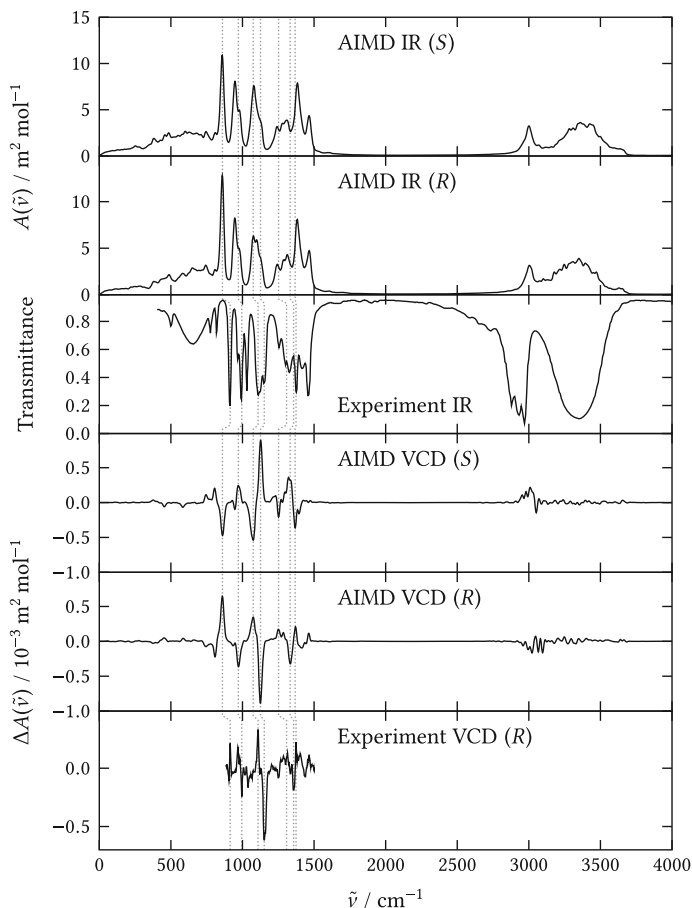


Fig. 4.48 IR spectra and VCD spectra of 2-butanol in the (*R*)-configuration and the (*S*)-configuration from AIMD simulations of 16 2-butanol molecules. The *dotted lines* facilitate the comparison of the VCD spectra of the enantiomers and show the assignment between simulation and experiment. The experimental IR spectrum is taken from Ref. [78]. The experimental VCD spectrum of the (*R*)-configuration is taken from Ref. [76]

reason, two bulk phase AIMD simulations of 16 2-butanol molecules under periodic boundary conditions were carried out, one for each enantiomer (see Appendix A for computational details). Simulating both configurations allows for an important basic test of the VCD model proposed in this thesis, since the VCD spectra of enantiomers generally differ only in the sign of the intensity while the band shapes are equal. The AIMD simulation, of course, should reproduce this effect. The obtained IR and VCD spectra are compared to experimental data [76, 78] (see Fig. 4.48) where the VCD spectrum has been recorded for the (*R*)-enantiomer. It has to be noted that the simulated IR spectra of the enantiomers show minor differences, indicating that the spectra are not strictly converged with respect to the system size and the simulation

time. Nevertheless, the experimental IR spectrum is reproduced very well, though the already known redshift in the fingerprint region as well as the blueshift and the reduced intensity of the CH stretching modes are found. Comparing to the gas phase, the most distinct changes concern the broad OH stretching band above 3000 cm^{-1} and the broad band of the librations around 600 cm^{-1} . This is very similar to methanol (see Sect. 4.2.1), but 2-butanol also shows significant differences in the fingerprint region between 800 and 1600 cm^{-1} . The only important deficiency in this wavenumber range regards the two separate experimental peaks at 992 and 1031 cm^{-1} , for which the simulation predicts only one band at 947 cm^{-1} with a shoulder at 975 cm^{-1} .

Comparing the VCD spectra of the two enantiomers shows that the AIMD simulations meet the expected result: each band with a positive sign in the (*S*)-configuration has a negative sign in the (*R*)-configuration and vice versa, so the proposed VCD model is valid regarding this basic property of VCD spectroscopy. Minor differences in the intensity ratios occur for the same reason as in the IR spectra. Furthermore, the simulated spectrum of the (*R*)-enantiomer is in very good agreement with the experiment, as the pattern of positive and negative bands is reproduced very well. The only exception is the positive peak found at 968 cm^{-1} in the experiment, which is missing in the simulation. However, this is the wavenumber region, where also the IR spectrum deviates from the experiment, so this is unlikely to be a particular issue of the VCD model. Comparing gas phase and liquid phase, the most important change is the vanishing positive band at 1241 cm^{-1} . According to the normal coordinate analysis, this band belongs to the COH bending mode. In the liquid, this vibration is shifted to the region of the CH bending modes around 1400 cm^{-1} . The behavior of this vibration due to the hydrogen bonding in the liquid is reproduced very well by the simulation, showing again that AIMD is suited to model bulk phase effects in vibrational spectra.

The next example system is a bulk phase simulation of 16 propylene oxide molecules in the (*R*)-configuration (see Appendix A for computational details). The IR and VCD spectra are compared to experimental data of the liquid [79–81] (see Fig. 4.49). The general agreement of simulation and experiment is very good, only the relative intensity of the band at 782 cm^{-1} is overestimated in the simulation and a redshift of most fingerprint bands is observed again. This concerns in particular the peaks found at 747 and 829 cm^{-1} in the IR experiment, for which the simulation predicts wavenumbers of 683 and 782 cm^{-1} , respectively. Furthermore, several bands are merged in the IR spectrum, so the AIMD shows only two peaks instead of four between 1300 and 1550 cm^{-1} , and the splitting of the two signals around 1100 cm^{-1} is less pronounced. These effects directly transfer to the VCD spectrum, where the simulated intensities in the negative–positive–negative peak feature around 1100 cm^{-1} are decreased in comparison to the experiment. In the IR spectrum, the bands of shifted modes are just merged, while in the VCD spectrum, the intensities of peaks with opposite sign can cancel each other. This makes the shape of VCD spectra more sensitive to a shift of the wavenumbers by the underlying AIMD. The same applies to the weak bands observed at 1458 and 1499 cm^{-1} in the VCD experiment. Moreover, the simulation predicts a positive peak at 782 cm^{-1} , for which no counterpart is found in the experimental spectrum. Nevertheless, it is important to

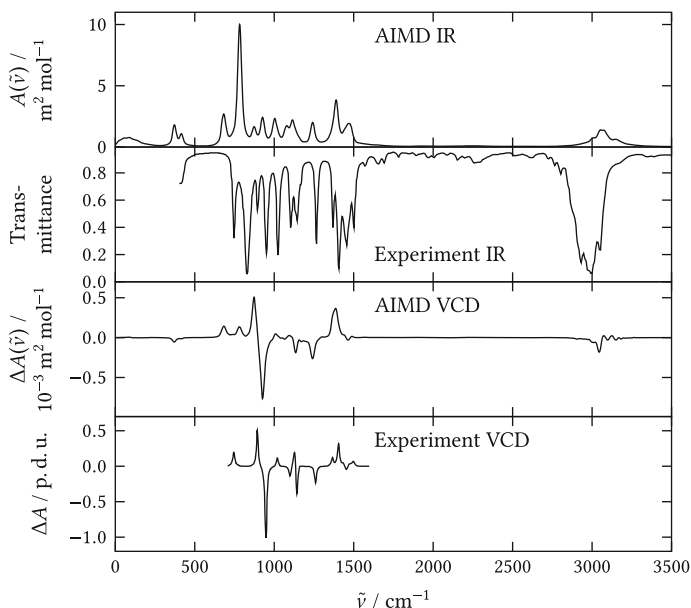


Fig. 4.49 IR spectrum and VCD spectrum from an AIMD simulation of 16 (*R*)-propylene oxide molecules. The experimental IR spectrum is taken from Ref. [79]. The experimental VCD spectrum is the inverted spectrum of the (*S*)-enantiomer from Ref. [80]

note that the intense experimental bands at 895, 950, and 1407 cm^{-1} are reproduced very well by the simulation.

The last example is a bulk phase simulation of 16 (1*R*, 5*R*)-(+)- α -pinene molecules (see Appendix A for computational details). The IR and VCD spectra are compared to experimental data of the liquid [78, 82] (see Fig. 4.50). The IR spectrum of α -pinene possesses a lot of bands in the fingerprint region, and due to the shifts of wavenumbers and intensities, it is hard to find a fully unambiguous assignment between simulation and experiment. A combined comparison of simulated and measured IR and VCD spectra, however, allows to match the bands as indicated by the dotted lines. This shows that many of the distinct features in the VCD spectrum are reproduced very well by the simulation. Considerable differences concern the negative peak at 1265 cm^{-1} in the experiment, which is partially merged with another negative band at 1197 cm^{-1} in the simulation, the negative peak at 1063 cm^{-1} in the experiment, which is missing in the simulation, and the predicted negative band at 1143 cm^{-1} in the AIMD, for which no counterpart is observed in the experiment. It should be noted that some of the fingerprint bands are blue-shifted in the simulation opposed to the trend found for other molecules. Since the deviations of the AIMD from the experiment are not limited to the VCD spectrum but occur in the IR spectrum to the same extent, they should not primarily be attributed to the model for the magnetic moments, but to the electronic structure method in the underlying AIMD.

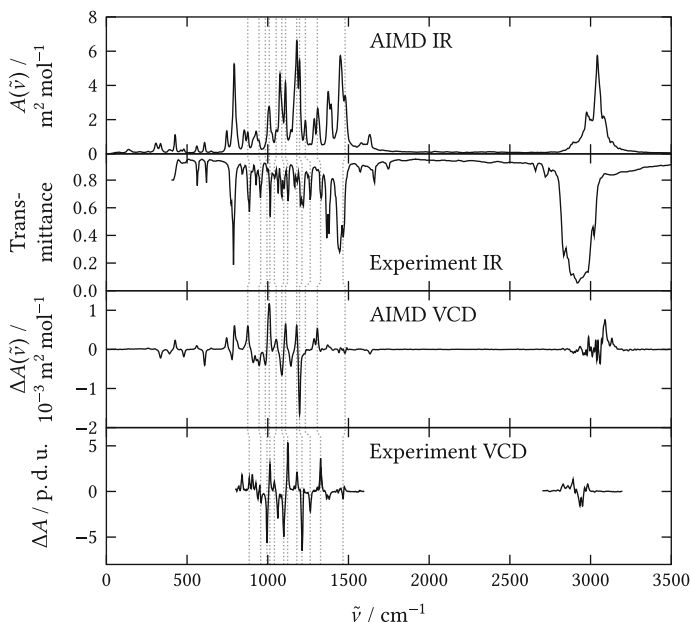


Fig. 4.50 IR spectrum and VCD spectrum from an AIMD simulation of 16 (1*R*, 5*R*)-(+)- α -pinene molecules. The experimental IR spectrum is taken from Ref. [78]. The experimental VCD spectrum is taken from Ref. [82]. The dotted lines indicate the assignment of simulation and experiment

The most important result of the comparison is that the simulated VCD spectrum is clearly sufficient to identify the correct enantiomer of α -pinene, so the combination of experiment and calculation could readily be used to determine the absolute configuration of the molecule.

References

1. M. Thomas, M. Brehm, R. Fligg, P. Vöhringer, B. Kirchner, *Phys. Chem. Chem. Phys.* **15**, 6608–6622 (2013)
2. E. Plyler, *J. Res. Bur. Stand.* **48**, 281 (1952)
3. A.V. Stuart, G.B.B.M. Sutherland, *J. Chem. Phys.* **24**, 559–570 (1956)
4. M. Falk, E. Whalley, *J. Chem. Phys.* **34**, 1554–1568 (1961)
5. Y. Yu, Y. Wang, K. Lin, N. Hu, X. Zhou, S. Liu, *J. Phys. Chem. A* **117**, 4377–4384 (2013)
6. T. Pasinszki, G. Vass, D. Klapstein, N.P.C. Westwood, *J. Phys. Chem. A* **116**, 3396–3403 (2012)
7. SDBSWeb: <http://sdb.s.riodb.aist.go.jp> (National Institute of Advanced Industrial Science and Technology). Accessed 26 Aug 2014
8. F. Kollipost, J. Andersen, D.W. Mahler, J. Heimdal, M. Heger, M.A. Suhm, R. Wugt Larsen, *J. Chem. Phys.* **141**, 174314 (2014)
9. J.E. Bertie, K.H. Michaelian, *J. Chem. Phys.* **109**, 6764–6771 (1998)
10. SDBSWeb: <http://sdb.s.riodb.aist.go.jp> (National Institute of Advanced Industrial Science and Technology). Accessed 2 July 2015

11. T. Chakraborty, A. Verma, *Spectrochim. Acta Part A* **58**, 1013–1023 (2002)
12. M. Olschewski, J. Lindner, P. Vöhringer, *Angew. Chem. Int. Ed.* **52**, 2602–2605 (2013)
13. M. Olschewski, S. Knop, J. Lindner, P. Vöhringer, *Angew. Chem. Int. Ed.* **52**, 9634–9654 (2013)
14. M. Dahlqvist, M. Hotokka, M. Räsänen, *Chem. Phys.* **229**, 137–147 (1998)
15. M. Dahlqvist, R. Sillanpää, *J. Mol. Struct.* **524**, 141–149 (2000)
16. M. Thomas, M. Brehm, O. Hollóczki, Z. Kelemen, L. Nyulási, T. Pasinszki, B. Kirchner, *J. Chem. Phys.* **141**, 024510 (2014)
17. O. Hollóczki, D. Gerhard, K. Massone, L. Szarvas, B. Németh, T. Veszprémi, L. Nyulási, *New J. Chem.* **34**, 3004–3009 (2010)
18. J.P. Hallett, C.L. Liotta, G. Ranieri, T. Welton, *J. Org. Chem.* **74**, 1864–1868 (2009)
19. M.Y. Lui, L. Crowhurst, J.P. Hallett, P.A. Hunt, H. Niedermeyer, T. Welton, *Chem. Sci.* **2**, 1491–1496 (2011)
20. M. Brehm, H. Weber, A.S. Pensado, A. Stark, B. Kirchner, *Phys. Chem. Chem. Phys.* **14**, 5030–5044 (2012)
21. M. Brehm, H. Weber, A.S. Pensado, A. Stark, B. Kirchner, *Z. Phys. Chem.* **227**, 177–204 (2013)
22. O. Hollóczki, D.S. Firaha, J. Friedrich, M. Brehm, R. Cybik, M. Wild, A. Stark, B. Kirchner, *J. Phys. Chem. B* **117**, 5898–5907 (2013)
23. H. Rodríguez, G. Gurau, J.D. Holbrey, R.D. Rogers, *Chem. Commun.* **47**, 3222–3224 (2011)
24. G. Gurau, H. Rodríguez, S.P. Kelley, P. Janiczek, R.S. Kalb, R.D. Rogers, *Angew. Chem. Int. Ed.* **50**, 12024–12026 (2011)
25. N.R. Dhumal, H.J. Kim, J. Kiefer, *J. Phys. Chem. A* **113**, 10397–10404 (2009)
26. S. Katsyuba, P. Dyson, E. Vandyukova, A. Chernova, A. Vidiš, *Helv. Chim. Acta* **87**, 2556–2565 (2004)
27. E.R. Talaty, S. Raja, V.J. Storhaug, A. Dölle, W.R. Carper, *J. Phys. Chem. B* **108**, 13177–13184 (2004)
28. N.E. Heimer, R.E.D. Sesto, Z. Meng, J.S. Wilkes, W.R. Carper, *J. Mol. Liq.* **124**, 84–95 (2006)
29. S.A. Katsyuba, E.E. Zvereva, A. Vidiš, P.J. Dyson, *J. Phys. Chem. A* **111**, 352–370 (2007)
30. J. Kiefer, J. Fries, A. Leipertz, *Appl. Spectrosc.* **61**, 1306–1311 (2007)
31. Q.-G. Zhang, N.-N. Wang, Z.-W. Yu, *J. Phys. Chem. B* **114**, 4747–4754 (2010)
32. S.-W. Hu, Z.-X. Wang, F. Qu, T.-W. Chu, X.-Y. Wang, *J. Phys. Chem. A* **115**, 13452–13466 (2011)
33. J.X. Mao, A.S. Lee, J.R. Kitchin, H.B. Nulwala, D.R. Luebke, K. Damodaran, *J. Mol. Struct.* **1038**, 12–18 (2013)
34. T. Köddermann, C. Wertz, A. Heintz, R. Ludwig, *ChemPhysChem* **7**, 1944–1949 (2006)
35. A. Yokozeki, D.J. Kasprzak, M.B. Shiflett, *Phys. Chem. Chem. Phys.* **9**, 5018–5026 (2007)
36. K. Fumino, A. Wulf, R. Ludwig, *Angew. Chem. Int. Ed.* **47**, 8731–8734 (2008)
37. J.-C. Lassègues, J. Grondin, D. Cavagnat, P. Johansson, *J. Phys. Chem. A* **113**, 6419–6421 (2009)
38. A. Wulf, K. Fumino, R. Ludwig, *J. Phys. Chem. A* **114**, 685–686 (2010)
39. J.-C. Lassègues, J. Grondin, D. Cavagnat, P. Johansson, *J. Phys. Chem. A* **114**, 687–688 (2010)
40. L.A. Blanchard, D. Hancu, E.J. Beckman, J.F. Brennecke, *Nature* **399**, 28–29 (1999)
41. J.L. Anderson, J.K. Dixon, J.F. Brennecke, *Acc. Chem. Res.* **40**, 1208–1216 (2007)
42. J.F. Brennecke, B.E. Gurkan, *J. Phys. Chem. Lett.* **1**, 3459–3464 (2010)
43. F. Jutz, J.-M. Andanson, A. Baiker, *Chem. Rev.* **111**, 322–353 (2011)
44. M.B. Shiflett, A. Yokozeki, *J. Chem. Eng. Data* **54**, 108–114 (2009)
45. M. Besnard, M.I. Cabaço, F. Vaca Chávez, N. Pinaud, P.J. Sebastião, J.A.P. Coutinho, Y. Danten, *Chem. Commun.* **48**, 1245–1247 (2012)
46. M.I. Cabaço, M. Besnard, Y. Danten, J.A.P. Coutinho, *J. Phys. Chem. A* **116**, 1605–1620 (2012)
47. M. Besnard, M.I. Cabaço, F. Vaca Chávez, N. Pinaud, P.J. Sebastião, J.A.P. Coutinho, J. Mascetti, Y. Danten, *J. Phys. Chem. A* **116**, 4890–4901 (2012)
48. S. Stevanovic, A. Podgoršek, A.A.H. Pádua, M.F. Costa Gomes, *J. Phys. Chem. B* **116**, 14416–14425 (2012)

49. M. Thomas, M. Brehm, O. Hollóczki, B. Kirchner, *Chem. Eur. J.* **20**, 1622–1629 (2014)
50. O. Hollóczki, *Inorg. Chem.* **53**, 835–846 (2014)
51. S.G. Kazarian, B.J. Briscoe, T. Welton, *Chem. Commun.*, 2047–2048 (2000)
52. B. Bhargava, S. Balasubramanian, *Chem. Phys. Lett.* **444**, 242–246 (2007)
53. O. Hollóczki, Z. Kelemen, L. Könczöl, D. Szieberth, L. Nyulászi, A. Stark, B. Kirchner, *ChemPhysChem* **14**, 315–320 (2013)
54. T. Seki, J.-D. Grunwaldt, A. Baiker, *J. Phys. Chem. B* **113**, 114–122 (2009)
55. O. Hollóczki, F. Malberg, T. Welton, B. Kirchner, *Phys. Chem. Chem. Phys.* **16**, 16880–16890 (2014)
56. T.I. Morrow, E.J. Maginn, *J. Phys. Chem. B* **106**, 12807–12813 (2002)
57. M. Bühl, A. Chaumont, R. Schurhammer, G. Wipff, *J. Phys. Chem. B* **109**, 18591–18599 (2005)
58. T.G.A. Youngs, C. Hardacre, *ChemPhysChem* **9**, 1548–1558 (2008)
59. J. Schmidt, C. Krekeler, F. Dommert, Y. Zhao, R. Berger, L. Delle Site, C. Holm, *J. Phys. Chem. B* **114**, 6150–6155 (2010)
60. M. Kohagen, M. Brehm, J. Thar, W. Zhao, F. Müller-Plathe, B. Kirchner, *J. Phys. Chem. B* **115**, 693–702 (2011)
61. M. Kohagen, M. Brehm, Y. Lingscheid, R. Giernoth, J. Sangoro, F. Kremer, S. Naumov, C. Jacob, J. Kärger, R. Valiullin, B. Kirchner, *J. Phys. Chem. B* **115**, 15280–15288 (2011)
62. V. Chaban, *Phys. Chem. Chem. Phys.* **13**, 16055–16062 (2011)
63. C. Schröder, *Phys. Chem. Chem. Phys.* **14**, 3089–3102 (2012)
64. A. Mondal, S. Balasubramanian, *J. Phys. Chem. B* **118**, 3409–3422 (2014)
65. I. Mukhopadhyay, K. Sastry, *J. Mol. Spectrosc.* **312**, 51–53 (2015)
66. A. Kekulé, *Justus Liebig's Ann. Chem.* **162**, 77–124 (1872)
67. H. Goldstein, C. Poole, J. Safko, *Klassische Mechanik* (Wiley-VCH, Weinheim, 2012)
68. N. Sieffert, M. Bühl, M.-P. Gaigeot, C.A. Morrison, *J. Chem. Theory Comput.* **9**, 106–118 (2013)
69. G. Wedler, H. Freund, *Lehrbuch der Physikalischen Chemie* (Wiley-VCH, Weinheim, 2012)
70. M. Thomas, M. Brehm, B. Kirchner, *Phys. Chem. Chem. Phys.* **17**, 3207–3213 (2015)
71. C.R. Bailey, J.B. Hale, C.K. Ingold, J.W. Thompson, *J. Chem. Soc.*, 931–941 (1936)
72. W.R. Angus, C.K. Ingold, A.H. Leckie, *J. Chem. Soc.*, 925–931 (1936)
73. R.A. Friedel, *J. Am. Chem. Soc.* **73**, 2881–2884 (1951)
74. J. Evans, *Spectrochim. Acta* **16**, 1382–1392 (1960)
75. H.W. Wilson, R.W. Macnamee, J.R. Durig, *J. Raman Spectrosc.* **11**, 252–255 (1981)
76. F. Wang, P.L. Polavarapu, *J. Phys. Chem. A* **104**, 10683–10687 (2000)
77. S. Shin, M. Nakata, Y. Hamada, *J. Phys. Chem. A* **110**, 2122–2129 (2006)
78. SDBSWeb: <http://sdb.sriodb.aist.go.jp> (National Institute of Advanced Industrial Science and Technology). Accessed 28 July 2015
79. SDBSWeb: <http://sdb.sriodb.aist.go.jp> (National Institute of Advanced Industrial Science and Technology). Accessed 10 Aug 2015
80. R. Kawiecki, F. Devlin, P. Stephens, R. Amos, N. Handy, *Chem. Phys. Lett.* **145**, 411–417 (1988)
81. M. Losada, P. Nguyen, Y. Xu, *J. Phys. Chem. A* **112**, 5621–5627 (2008)
82. C. Guo, R.D. Shah, R.K. Dukor, T.B. Freedman, X. Cao, L.A. Nafie, *Vib. Spectrosc.* **42**, 254–272 (2006)

Chapter 5

Conclusion and Outlook

In the framework of this thesis, the application of AIMD simulations to model the vibrational spectra of liquids was discussed. The techniques known in the literature were extended by several new ideas, and all algorithms presented here were implemented in the open-source trajectory analysis software package TRAVIS, making everything publicly available to the scientific community for immediate utilization.

The basic equations that define the spectra in terms of Fourier transforms of correlation functions were derived in an alternative manner with the harmonic oscillator as the reference system. While this is usually started from the Heisenberg picture of quantum mechanics [1, 2], approximating the quantum correlation functions by classical correlation functions and introducing quantum correction factors, the approach chosen here highlights the close relation of AIMD simulations and static calculations with respect to vibrational properties. Using several selected example potentials, it was analyzed in detail how the methodology transfers to anharmonic systems. This revealed that MD simulations generally include anharmonicity effects, but the approximation of the nuclei as classical particles imposes certain restrictions on the effects that can be observed. Accordingly, MD based spectra always show overtones at integer multiples and combination bands at exact sums and differences of the corresponding fundamental frequencies. Furthermore, the band positions depend on the energy or the temperature of the simulation. At low energies, the MD samples the potential energy surface only in the close vicinity of a minimum, which can be approximated by a quadratic function very well, so the peaks appear at the harmonic frequencies of the system. At higher energies, the MD also reaches the more anharmonic parts of the potential energy surface, so the band positions and the intensities are shifted. Due to this energy dependence, it is usually impossible to quantitatively determine the amount of anharmonicity, but the examples of cyanofornyl chloride, cyanofornyl bromide, and carbon tetrachloride showed that a very good qualitative picture can be obtained in many cases if the simulations are performed at ambient temperature or slightly above. Even the intensity shifts due to Fermi resonances can in principle be seen in MD based spectra, but this requires that the frequency of an

overtone closely matches another fundamental frequency, and the frequency shifts induced by the assumption of classical nuclei often prevent that this effect is observed in investigations of real systems.

For the evaluation of molecular dipole moments and polarizabilities in a bulk phase AIMD simulation, the scheme of maximally localized Wannier functions was employed first. This is common practice to simulate IR spectra in the literature [2]. The polarizabilities can be obtained by relocalizing the Wannier functions under the influence of an external electric field and calculating the differences of the dipole moments. A simplification compared to the method reported in the literature [3, 4] that applies the field only in one direction and uses only a part of the polarizability tensor proved to work well for reasonable Raman spectra in the liquid phase. This is due to the fact that the molecules usually adopt all possible orientations with respect to the cell coordinate axes in a typical bulk phase AIMD simulation, so averaging the orientation of the simulation cell with respect to the laboratory coordinate system provides only a minor improvement.

The applications of the method to several organic molecules demonstrated the suitability of AIMD simulations to model bulk phase effects on vibrational spectra, as, e.g., the influence of the hydrogen bonding in liquid methanol was correctly reproduced. This is of particular importance for ionic liquids due to their strong and dynamic network of diverse intermolecular interactions. In the case of $[\text{C}_2\text{C}_1\text{Im}][\text{OAc}]$, the gas phase and the liquid phase show significant differences regarding the formation of a carbene, so static calculations of a single ion pair are insufficient to accurately model the vibrational spectra of the liquid. In contrast, the predictions of the AIMD simulation are in very good agreement with the experiment. This is also true for the effects observed in a mixture of $[\text{C}_2\text{C}_1\text{Im}][\text{OAc}]$ and water, as well as the physical and chemical absorption of carbon dioxide. The influence of the ionic liquid as a solvent on the physically absorbed carbon dioxide could be reproduced very well. The implementation of a normal coordinate analysis [5, 6] allows to assign the experimentally observed bands to specific molecular vibrations. Moreover, it provides a detailed insight into the CH stretching modes, indicating that the ring hydrogen atoms of the cation are heavily involved in the hydrogen bonding network, as it was also concluded in the structural analyses of this system [7, 8].

Due to the computational effort needed for the calculation of the Wannier functions, an alternative approach to obtain molecular dipole moments and polarizabilities was developed in the course of this thesis. It is based on a radical Voronoi tessellation and integration of the electron density. Thus, it avoids the costly localization procedure, as it just relies on the electron density data inherently available in an AIMD simulation. An important parameter of the radical Voronoi tessellation are the radii that are assigned to the Voronoi sites. As a reasonable criterion for the adequacy of a certain set of radii, the standard deviation of the charge distribution was required to be minimal. If the molecular charge is considered, this minimum is usually close to the result that is obtained by simply applying van der Waals radii to the atoms. This is not surprising, since van der Waals radii have been fitted to reproduce intermolecular distances. Furthermore, this condition yields average charges of $\pm 0.8 e$ for the ions in $[\text{C}_2\text{C}_1\text{Im}][\text{OAc}]$, which is another support for the generally accepted fact that the

ionic charges are reduced by charge transfer effects in ionic liquids [9]. In the same way, it should also be possible to obtain reasonable atomic partial charges by minimizing the standard deviations in the corresponding distribution functions. It was found that the result is often close to the minimum if covalent radii are employed. However, this leads to the conflict that one set of radii is needed to optimally separate the electron density between the molecules while another set of radii provides the best distribution of the electron density within the molecules. Future work could focus on an implementation that allows a two-step procedure, where molecular cells are created with one set of radii and these molecular cells are further tessellated using another set of radii.

Regarding the dipole moments, it could be shown that there exist many molecules for which the Wannier function scheme introduces artifacts in small periodic simulation cells. In particular, it assigns a finite dipole moment to certain molecules that are actually nonpolar due to their symmetry. In most cases, only a constant offset is added to the dipole moment, and this does not affect neither the IR spectra, where the time derivative of the dipole moment enters, nor the polarizabilities, where the difference of two dipole moments is taken. In the special situation of a benzene ring, however, there are two solutions the localization can converge to, and they differ in the orientation of the artificial dipole moment. Regular switches between these solutions appear as an artificial band in the IR spectrum, and they totally prevent the calculation of polarizabilities and Raman spectra. The Voronoi approach does not suffer from this issue, and it allowed to simulate the spectra of benzene and phenol in very good agreement with the experiment.

In general, the Voronoi method yields vibrational spectra of similar quality as the Wannier function scheme, but it saves a lot of computation time. For the phenol simulation with the Wannier centers calculated in every eighth step, e.g., the localization took approximately one third of the total time needed to perform the whole AIMD, corresponding to ten days with parallelization on 32 processor cores of the employed computer cluster. In contrast, the electron density data could be processed within 30 min using TRAVIS without parallelization on a workstation computer. This allows to recommend the Voronoi approach as a favorable alternative to the Wannier function scheme for the calculation of vibrational spectra in the liquid phase by AIMD. It should be noted that the Voronoi tessellation is totally independent of the underlying electronic structure method in the AIMD. Thus, it can easily be combined with any technique that is able to provide the total electron density.

To extend the AIMD approach toward a simulation of VCD spectra in the liquid phase, a novel method to calculate magnetic moments was developed in the course of this thesis. The electron density from an AIMD simulation is processed and a partial differential equation is solved to compute the electric current density on the basis of the continuity equation and the request that there should not be any eddy currents. According to the classical definition, the current density allows to calculate the magnetic moment of the simulation cell. In combination with the Voronoi tessellation technique, this also provides individual molecular magnetic moments. These can be used to obtain the VCD spectrum as the Fourier transform of the dipole moment–magnetic moment cross-correlation function. It was shown that the

magnetic moments are reasonably converged with respect to the timestep of the simulation, the background electron density needed in gas phase systems, and the threshold of the BiCGstab(l) algorithm. All the example systems chosen here could be treated without major issues, but future work could still try to improve the convergence behavior and the stability of the solution of the partial differential equation by testing other algorithms known in the literature [10]. Using the examples of 2-butanol, propylene oxide, and α -pinene, it could be shown that the approach provides VCD spectra in very good agreement with experimental data. All the essential features of the spectra were reproduced by the simulations, in particular also the bulk phase effects in 2-butanol could be modeled. In contrast to previous work in a QM/MM framework [11, 12], the new approach does not rely on atomic partial charges obtained by population analyses, but it uses the complete information contained in the electron density. Furthermore, it does not need special implementations of perturbation theory [13, 14], but it can straightforwardly be coupled with any electronic structure method that is able to provide the electron density. Although the authors of reference [13] are aiming for a direct application in AIMD, a study that shows a complete VCD spectrum had not appeared in the literature—to the best of the author’s knowledge—prior to the submission of this thesis in October 2015. In any case, the approach presented here can be considered as the one of the first employments of AIMD for VCD spectra that treats the whole system on the same level of theory.

The proposal of a model for VCD spectra immediately raises the question about Raman optical activity (ROA). In principle, the necessary ingredients should be available now. The intensities in ROA spectra depend on the electric dipole–electric dipole polarizability tensor, the electric dipole–magnetic dipole polarizability tensor, and the electric dipole–electric quadrupole polarizability tensor in static calculations (see, e.g., Ref. [15]). The former tensor was simply called polarizability throughout this thesis, and it is already known from Raman spectra. The latter two tensors should similarly be obtainable by the method of a finite electric field. One just needs to calculate the differences in the magnetic dipole moment and the electric quadrupole moment. However, it has to be checked carefully if the magnetic moment induced by an external electric field can be computed with the density derivative in the differential equation (3.92) approximated by the finite difference of two densities under the influence of an external electric field. If this works correctly, the tensor derivatives along the normal coordinates in the expressions for static calculations (see, e.g., Ref. [15]) have to be replaced by certain cross-correlation functions, and this should yield formulas for the simulation of ROA spectra by AIMD.

Another interesting extension are resonance Raman spectra, where the frequency of the incident laser matches an electronic transition of the system. This enhances the Raman signal by several orders of magnitude, and it also shifts the relative intensities in the spectrum. One of the different techniques to model these effects by static calculations relies on the equations for nonresonant Raman spectra shown in Sect. 2.4.3, but inserts the dynamic polarizability at the laser frequency [16]. This is easily transferred to the MD approach, as one just needs to apply the dynamic polarizability in the expressions shown in Sect. 3.3. The dynamic polarizability for this purpose can

be evaluated by linear response theory [17], or by real-time time-dependent density functional theory as shown by static calculations in earlier works of the author [18, 19]. In the latter method, the Kohn–Sham orbitals are propagated according to the time-dependent form of the Kohn–Sham equations (2.17) after excitation with a finite electric field pulse. The time development of the dipole moment is recorded during the propagation, and its Fourier transform directly yields the dynamic polarizability as a function of the frequency afterwards. This can readily be combined with the Voronoi tessellation to get the molecular quantities in a bulk phase simulation if the full electron density is saved during the propagation. In contrast to the single point calculation with an external electric field needed to get the static polarizability (see Sect. 3.4), this requires, however, a complete real-time propagation at regular intervals of the AIMD simulation, so it tremendously increases the computational demands. Nevertheless, it would also provide the electronic spectrum of the system and it would pave the way for an investigation of surface-enhanced Raman scattering [18, 20] by AIMD.

References

1. D. McQuarrie, *Statistical Mechanics* (University Science Books, Sausalito, 2000)
2. D. Marx, J. Hutter, *Ab Initio Molecular Dynamics: Basic Theory and Advanced Methods* (Cambridge University Press, Cambridge, 2009)
3. R.J. Heaton, P.A. Madden, S.J. Clark, S. Jahn, *J. Chem. Phys.* **125**, 144104 (2006)
4. M. Salanne, R. Vuilleumier, P.A. Madden, C. Simon, P. Turq, B. Guillot, *J. Phys. Condens. Matter* **20**, 494207 (2008)
5. G. Mathias, M.D. Baer, *J. Chem. Theory Comput.* **7**, 2028–2039 (2011)
6. G. Mathias, S.D. Ivanov, A. Witt, M.D. Baer, D. Marx, *J. Chem. Theory Comput.* **8**, 224–234 (2012)
7. M. Brehm, H. Weber, A.S. Pensado, A. Stark, B. Kirchner, *Phys. Chem. Chem. Phys.* **14**, 5030–5044 (2012)
8. M. Brehm, H. Weber, A.S. Pensado, A. Stark, B. Kirchner, *Z. Phys. Chem.* **227**, 177–204 (2013)
9. O. Hollóczki, F. Malberg, T. Welton, B. Kirchner, *Phys. Chem. Chem. Phys.* **16**, 16880–16890 (2014)
10. R. Barrett, M. Berry, T. Chan, J. Demmel, J. Donato, J. Dongarra, V. Eijkhout, R. Pozo, C. Romine, H. van der Vorst, *Templates for the Solution of Linear Systems: Building Blocks for Iterative Methods*, Society for Industrial and Applied Mathematics, 1994, Electronic version: <http://www.netlib.org/templates/templates.pdf>. Accessed 12 Sep 2014
11. S. Yang, M. Cho, *J. Chem. Phys.* **131**, 135102 (2009)
12. J.-H. Choi, M. Cho, *J. Chem. Theory Comput.* **7**, 4097–4103 (2011)
13. A. Scherrer, R. Vuilleumier, D. Sebastiani, *J. Chem. Theory Comput.* **9**, 5305–5312 (2013)
14. A. Scherrer, F. Agostini, D. Sebastiani, E.K.U. Gross, R. Vuilleumier, *J. Chem. Phys.* **143**, 074106 (2015)
15. S. Luber, C. Herrmann, M. Reiher, *J. Phys. Chem. B* **112**, 2218–2232 (2008)
16. L. Jensen, L.L. Zhao, J. Autschbach, G.C. Schatz, *J. Chem. Phys.* **123**, 174110 (2005)
17. L. Jensen, J. Autschbach, G.C. Schatz, *J. Chem. Phys.* **122**, 224115 (2005)
18. M. Thomas, *Diplomarbeit*, Friedrich-Schiller-Universität Jena (2012)
19. M. Thomas, F. Latorre, P. Marquetand, *J. Chem. Phys.* **138**, 044101 (2013)
20. M. Thomas, S. Mühlig, T. Deckert-Gaudig, C. Rockstuhl, V. Deckert, P. Marquetand, *J. Raman Spectrosc.* **44**, 1497–1505 (2013)

Appendix A

Computational Details

A.1 Ab Initio Molecular Dynamics Simulations

All AIMD simulations discussed in this thesis were performed using the CP2K software package [6]. For solving the electronic structure problem, the QUICKSTEP module [7] of CP2K provides an efficient implementation of DFT in terms of the Gaussian and plane waves method [8] in combination with the OT approach [9] (see Sect. 2.2.4). In all simulations, the molecularly optimized double-zeta basis set MOLOPT-DZVP-SR-GTH [10] was applied to all atoms together with the corresponding GTH pseudopotentials [11–13] and a plane wave cutoff of 280 Ry. Smoothing algorithms (NN10 for the density and NN10_SMOOTH for its derivative) were employed to reduce grid effects on the exchange-correlation potential, and the convergence criterion for the OT iterations (EPS_SCF) was set to 10^{-5} . The nuclei were propagated with a timestep of 0.5 fs, and the temperature was adjusted by a Nosé–Hoover thermostat chain [14–17]. Further parameters such as the exchange-correlation functional, the size of the cubic simulation cell with periodic boundaries, the target temperature, and the thermostat coupling time constant are individually given for each simulation in Table A.1.

The simulations of neat $[\text{C}_2\text{C}_1\text{Im}][\text{OAc}]$ (I1) and the $[\text{C}_2\text{C}_1\text{Im}][\text{OAc}]$ –water mixture (I2) were prepared and started by Dr. Martin Brehm. Detailed structural analyses of these trajectories can be found in Refs. [18, 19]. The trajectories were extended in the course of this thesis to obtain the vibrational spectra. The simulations of physically (I3) and chemically (I4) absorbed carbon dioxide in $[\text{C}_2\text{C}_1\text{Im}][\text{OAc}]$ were prepared and started by Dr. Oldamur Hollóczy. A detailed structural discussion of the physical absorption can be found in Refs. [20, 21]. Also these trajectories were extended in the course of this thesis to obtain the vibrational spectra. For all other bulk phase simulations, initial configurations were obtained with classical force fields using the LAMMPS software package [22]. Force constants for bonds, angles, dihedral angles, and improper torsions, as well as Lennard-Jones parameters were taken from the

Table A.1 AIMD simulation parameters: exchange-correlation functional with dispersion correction, cubic cell size a , density ρ , thermostat target temperature T , equilibration time t_{eq} , production time t_{sim} , and thermostat coupling time constant τ_{sim} during production run

System	Functional	a/pm	$\rho/\text{g cm}^{-3}$	T/K	t_{eq}/ps	t_{sim}/ps	$\tau_{\text{sim}}/\text{fs}$
G1	1 methanol						
	a BLYP-D3 [1–3]	1000.0	–	400	3.1	31.2	100.0
	b			10	5.6	32.9	
	c			100	4.1	30.8	
	d			1000	3.5	31.7	
G2	1 acetone						
	BLYP-D3 [1–3]	1000.0	–	400	3.2	31.0	100.0
G3	1 nitromethane						
	BLYP-D3 [1–3]	1000.0	–	400	4.8	31.8	100.0
G4	1 cyanofornyl chloride						
	PBE-D3 [3, 4]	1200.0	–	400	10.0	120.0	50.0
G5	1 cyanofornyl bromide						
	PBE-D3 [3, 4]	1200.0	–	400	10.0	76.3	50.0
L1	16 methanol						
	BLYP-D3 [1–3]	1025.0	0.79	400	1.1	60.7	100.0
L2	32 carbon tetrachloride						
	PBE-D3 [3, 4]	1725.9	1.59	400	5.0	27.9	50.0
S1	32 carbon tetrachloride + 1 methanol						
	BLYP-D3 [1–3]	1733.2	1.58	400	9.7	36.7	100.0
S2	32 carbon tetrachloride + 1 pinacol						
	BLYP-D3 [1–3]	1743.2	1.58	400	7.6	33.6	100.0
I1	36 [C ₂ C ₁ Im][OAc]						
	BLYP-D2 [1, 2, 5]	2121.2	1.07	350	18.9	91.8	16.7
I2	27 [C ₂ C ₁ Im][OAc] + 81 water						
	BLYP-D2 [1, 2, 5]	2158.2	1.00	350	15.0	113.1	16.7
I3	36 [C ₂ C ₁ Im][OAc] + 1 carbon dioxide						
	BLYP-D3 [1–3]	2121.2	1.07	350	5.5	103.3	50.0
I4	35 [C ₂ C ₁ Im][OAc] + 1 [C ₂ C ₁ ImCO ₂] + 1 acetic acid						
	BLYP-D3 [1–3]	2121.2	1.07	350	10.0	106.3	50.0
V1	16 benzene						
	BLYP-D3 [1–3]	1331.1	0.88	400	12.2	30.0	50.0
V2	32 phenol						
	BLYP-D3 [1–3]	1751.9	0.93	400	8.0	30.2	50.0
C1	1 (<i>R</i>)-2-butanol						
	BLYP-D3 [1–3]	1200.0	–	400	5.0	30.0	50.0
C2	16 (<i>R</i>)-2-butanol						
	BLYP-D3 [1–3]	1345.0	0.81	400	10.0	30.0	50.0

(continued)

Table A.1 (continued)

System	Functional	a/pm	$\rho/\text{g cm}^{-3}$	T/K	t_{eq}/ps	t_{sim}/ps	$\tau_{\text{sim}}/\text{fs}$
C3	16 (<i>S</i>)-2-butanol						
	BLYP-D3 [1–3]	1345.0	0.81	400	10.0	30.0	50.0
C4	16 (<i>R</i>)-propylene oxide						
	BLYP-D3 [1–3]	1230.0	0.83	400	10.0	30.0	50.0
C5	16 (1 <i>R</i> , 5 <i>R</i>)-(+)– α -pinene						
	BLYP-D3 [1–3]	1615.0	0.86	400	5.0	30.0	50.0

general AMBER force field [23]. Electrostatic interactions were modeled by atomic partial charges derived from a restrained electrostatic potential fit [24] in the isolated molecule. To equilibrate the AIMD simulations, massive thermostating was applied with a coupling time constant of 10 fs.

Dipole moments in the AIMD can be obtained by a Wannier localization or a Voronoi tessellation of the electron density (see Sect. 3.4). Which method was used for which simulation is shown in Table A.2. The maximally localized Wannier function centers resulting from the Wannier localization were saved as atoms in the trajectories. The electron density needed for the Voronoi tessellation performed by TRAVIS was written to files in Gaussian cube format, which provide the density values on a regular grid. Such a representation of the electron density is directly available in the Gaussian and plane waves method, and due to the large amount of data, the internal grid of CP2K can be written with a certain stride to the hard disk. A stride of 2 proved to work well for the calculation of IR and Raman spectra in the molecular liquids (L1, V1, V2), but a stride of 1 significantly reduced the noise in the Raman spectrum of $[\text{C}_2\text{C}_1\text{Im}][\text{OAc}]$ (I1) and is generally recommended for the simulation of VCD spectra to improve the stability of the magnetic moments. An important limitation in this regard is the required disk space. Saving the electron density with a stride of 2 in every eighth timestep yielded, e. g., 68 GB of data for the simulation of phenol (V2). This amount can readily be handled on contemporary computer systems, but writing the electron density with a stride of 1 in all simulation steps would increase the size by a factor of 64, and this is still a challenge for today’s hardware. For that reason, a streaming scheme was implemented where TRAVIS runs in parallel to the AIMD simulation and directly processes the Gaussian cube files written by CP2K, eliminating the need for large amounts of disk space.

For the gas phase simulations of methanol (G1a), acetone (G2), and nitromethane (G3), histograms of the dipole moments obtained by Wannier localization are shown in Fig. A.1. Each of the distributions possesses a single maximum and reveals the oscillations of the dipole moment due to the molecular vibrations. The average values are 1.81 D for methanol, 3.12 D for acetone, and 3.68 D for nitromethane with standard deviations of 0.10 D, 0.15 D, and 0.17 D, respectively. The corresponding

Table A.2 Methods used to obtain dipole moments and polarizabilities for the AIMD simulations. The start time t_{start} and the end time t_{end} are given relative to the beginning of the production run of the whole simulation (see Table A.1). Their difference t is the time over which the spectra are sampled. The Wannier localization was performed or the electron density was saved, respectively, with a stride of Δt_{dip} . The dipole moments were evaluated with an external field to obtain polarizabilities with a stride of Δt_{pol} . The internal grid representation of the electron density in CP2K was written to Gaussian cube files with the stride given in the last column

System	Method	$t_{\text{start}}/\text{ps}$	t_{end}/ps	t/ps	$\Delta t_{\text{dip}}/\text{fs}$	$\Delta t_{\text{pol}}/\text{fs}$	Cube stride
G1a	Wannier	0.0	31.2	31.2	0.5	2.5	–
G2	Wannier	0.0	31.0	31.0	0.5	2.5	–
G3	Wannier	0.0	31.8	31.8	0.5	2.5	–
G4	Wannier	20.0	120.0	100.0	2.5	–	–
G5	Wannier	0.0	76.3	76.3	2.5	–	–
L1	Wannier	0.0	30.7	30.7	0.5	2.5	–
	Wannier	30.7	60.7	30.0	4.0	4.0	–
	Voronoi	30.7	60.7	30.0	4.0	4.0	2
L2	Wannier	0.0	27.9	27.9	2.5	2.5	–
S1	Wannier	0.0	36.7	36.7	2.5	–	–
S2	Wannier	0.0	33.6	33.6	2.5	–	–
I1	Wannier	49.6	70.0	20.4	2.5	2.5	–
	Voronoi	71.8	91.8	20.0	4.0	4.0	1
I2	Wannier	61.6	93.1	31.5	2.5	–	–
	Voronoi	93.1	113.1	20.0	4.0	–	2
I3	Wannier	83.1	103.3	20.2	2.5	–	–
I4	Wannier	80.6	106.3	25.7	2.5	–	–
V1	Wannier	0.0	30.0	30.0	4.0	4.0	–
	Voronoi	0.0	30.0	30.0	4.0	4.0	2
V2	Wannier	0.0	30.2	30.2	4.0	4.0	–
	Voronoi	0.0	30.0	30.0	4.0	4.0	2
C1	Voronoi	0.0	30.0	30.0	0.5	–	1
C2	Voronoi	0.0	30.0	30.0	0.5	–	1
C3	Voronoi	0.0	30.0	30.0	0.5	–	1
C4	Voronoi	0.0	30.0	30.0	0.5	–	1
C5	Voronoi	0.0	30.0	30.0	0.5	–	1

experimental dipole moments determined in the gas phase are 1.68 D for methanol [25], 2.90 D for acetone [26], and 3.46 D for nitromethane [27], which are all slightly overestimated by the simulations. The main reason is the issue of the Wannier functions in small simulation cells that is discussed in Sect. 4.5.2. Further deviations can be caused by the electronic structure method, but in general, DFT with the employed exchange-correlation functional describes the dipole moment of the molecules in a reasonable manner.

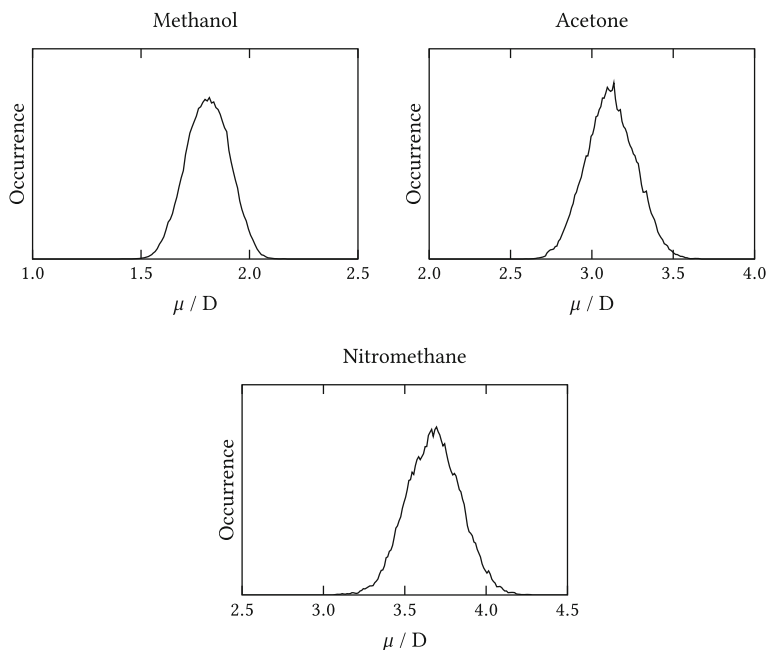


Fig. A.1 Dipole distribution functions of methanol from simulation G1a, acetone from simulation G2, and nitromethane from simulation G3 obtained by the method of maximally localized Wannier functions

A.2 Static Calculations

Static calculations of vibrational spectra were always performed in the following way: Starting from a reasonable guess of the structure, a full geometry optimization was carried out first. Afterwards, the Hessian of the potential energy was calculated numerically by finite differences of analytic first derivatives. The detailed setups employed in the course of this thesis are, however, slightly different.

The calculations of methanol, acetone, and nitromethane in Sect. 4.1.1 were performed using TURBOMOLE 6.0 [28, 29]. DFT was applied within the RI approximation [30–34] employing the BLYP exchange-correlation functional [1, 2] and Grimme’s dispersion correction D2 [5]. The polarized triple-zeta basis set def2-TZVP [35] was applied to all atoms, and the polarizability derivatives were calculated analytically [36]. The resulting dipole moments are 1.68 D for methanol, 2.90 D for

acetone, and 3.45 D for nitromethane. These values are in very good agreement with the experimental data (see Sect. A.1).

The calculations of carbon tetrachloride in Sect. 4.2.2 were carried out using TURBOMOLE 6.5 [29, 37]. DFT was applied combining Grimme's dispersion correction D3 [3] with eight different exchange-correlation functionals: BLYP [1, 2], BP86 [1, 38], PBE [4], B97D [5], TPSS [39], B3LYP [40], PBE0 [41], and TPSSh [42]. The RI approximation [30–34] was employed for the GGA functionals, and the polarized triple-zeta basis set def2-TZVP [35] was applied to all atoms.

The calculations of $[\text{C}_2\text{C}_1\text{Im}][\text{OAc}]$ in Sect. 4.4.1 were performed using CP2K with the same parameters in the electronic structure calculation as for the AIMD simulations (see Sect. A.1). The BLYP exchange-correlation functional [1, 2] was employed with Grimme's dispersion correction D3 [3]. The cubic cell sizes were 2000.0 and 2500.0 pm for the single ion pair and the cluster of five ion pairs, respectively. The same methodology was also used to optimize the reference structures for all the normal coordinate analyses and to calculate the dipole moments in Sect. 4.5.2.

The calculations of phenol in Sect. 4.5.3 were performed using ORCA 3.0.2 [43]. DFT was applied within the RI approximation [44, 45] employing the exchange-correlation functionals BLYP [1, 2], TPSS [39], and B3LYP [40] in combination with Grimme's dispersion correction D3 [3]. The polarized triple-zeta basis set def2-TZVPP [34, 35] was applied to all atoms.

References

1. A.D. Becke, *Phys. Rev. A* **38**, 3098–3100 (1988)
2. C. Lee, W. Yang, R.G. Parr, *Phys. Rev. B* **37**, 785–789 (1988)
3. S. Grimme, J. Antony, S. Ehrlich, H. Krieg, *J. Chem. Phys.* **132**, 154104 (2010)
4. J.P. Perdew, K. Burke, M. Ernzerhof, *Phys. Rev. Lett.* **77**, 3865–3868 (1996)
5. S. Grimme, *J. Comput. Chem.* **27**, 1787–1799 (2006)
6. J. Hutter, M. Iannuzzi, F. Schiffmann, J. VandeVondele, *WIREs Comput. Mol. Sci.* **4**, 15–25 (2014)
7. J. VandeVondele, M. Krack, F. Mohamed, M. Parrinello, T. Chassaing, J. Hutter, *Comput. Phys. Commun.* **167**, 103–128 (2005)
8. G. Lippert, M. Parrinello, J. Hutter, *Mol. Phys.* **92**, 477–488 (1997)
9. J. VandeVondele, J. Hutter, *J. Chem. Phys.* **118**, 4365–4369 (2003)
10. J. VandeVondele, J. Hutter, *J. Chem. Phys.* **127**, 114105 (2007)
11. S. Goedecker, M. Teter, J. Hutter, *Phys. Rev. B* **54**, 1703–1710 (1996)
12. C. Hartwigsen, S. Goedecker, J. Hutter, *Phys. Rev. B* **58**, 3641–3662 (1998)
13. M. Krack, *Theor. Chem. Acc.* **114**, 145–152 (2005)
14. S. Nosé, *J. Chem. Phys.* **81**, 511–519 (1984)
15. S. Nosé, *Mol. Phys.* **52**, 255–268 (1984)
16. W.G. Hoover, *Phys. Rev. A* **31**, 1695–1697 (1985)
17. G.J. Martyna, M.L. Klein, M. Tuckerman, *J. Chem. Phys.* **97**, 2635–2643 (1992)

18. M. Brehm, H. Weber, A.S. Pensado, A. Stark, B. Kirchner, *Phys. Chem. Chem. Phys.* **14**, 5030–5044 (2012)
19. M. Brehm, H. Weber, A.S. Pensado, A. Stark, B. Kirchner, *Z. Phys. Chem.* **227**, 177–204 (2013)
20. O. Hollóczki, D.S. Firaha, J. Friedrich, M. Brehm, R. Cybik, M. Wild, A. Stark, B. Kirchner, *J. Phys. Chem. B* **117**, 5898–5907 (2013)
21. O. Hollóczki, Z. Kelemen, L. Könczöl, D. Szieberth, L. Nyulászi, A. Stark, B. Kirchner, *ChemPhysChem* **14**, 315–320 (2013)
22. S. Plimpton, *J. Comput. Phys.* **117**, 1–19 (1995)
23. J. Wang, R.M. Wolf, J.W. Caldwell, P.A. Kollman, D.A. Case, *J. Comput. Chem.* **25**, 1157–1174 (2004)
24. U.C. Singh, P.A. Kollman, *J. Comput. Chem.* **5**, 129–145 (1984)
25. I. Mukhopadhyay, K. Sastry, *J. Mol. Spectrosc.* **312**, 51–53 (2015)
26. J.D. Swalen, C.C. Costain, *J. Chem. Phys.* **31**, 1562–1574 (1959)
27. E. Tannenbaum, R.J. Myers, W.D. Gwinn, *J. Chem. Phys.* **25**, 42–47 (1956)
28. TURBOMOLE V6.0 2009, a development of University of Karlsruhe and Forschungszentrum Karlsruhe GmbH, 1989–2007, TURBOMOLE GmbH, since 2007, <http://www.turbomole.com>
29. R. Ahlrichs, M. Bär, M. Häser, H. Horn, C. Kölmel, *Chem. Phys. Lett.* **162**, 165–169 (1989)
30. O. Treutler, R. Ahlrichs, *J. Chem. Phys.* **102**, 346–354 (1995)
31. K. Eichkorn, O. Treutler, H. Öhm, M. Häser, R. Ahlrichs, *Chem. Phys. Lett.* **242**, 652–660 (1995)
32. K. Eichkorn, F. Weigend, O. Treutler, R. Ahlrichs, *Theor. Chem. Acc.* **97**, 119–124 (1997)
33. M. Sierka, A. Hogekamp, R. Ahlrichs, *J. Chem. Phys.* **118**, 9136–9148 (2003)
34. F. Weigend, *Phys. Chem. Chem. Phys.* **8**, 1057–1065 (2006)
35. F. Weigend, R. Ahlrichs, *Phys. Chem. Chem. Phys.* **7**, 3297–3305 (2005)
36. D. Rappoport, F. Furche, *J. Chem. Phys.* **126**, 201104 (2007)
37. TURBOMOLE V6.5 2013, a development of University of Karlsruhe and Forschungszentrum Karlsruhe GmbH, 1989–2007, TURBOMOLE GmbH, since 2007, <http://www.turbomole.com>
38. J.P. Perdew, *Phys. Rev. B* **33**, 8822–8824 (1986)
39. J. Tao, J.P. Perdew, V.N. Staroverov, G.E. Scuseria, *Phys. Rev. Lett.* **91**, 146401 (2003)
40. P.J. Stephens, F.J. Devlin, C.F. Chabalowski, M.J. Frisch, *J. Phys. Chem.* **98**, 11623–11627 (1994)
41. C. Adamo, V. Barone, *J. Chem. Phys.* **110**, 6158–6170 (1999)
42. V.N. Staroverov, G.E. Scuseria, J. Tao, J.P. Perdew, *J. Chem. Phys.* **119**, 12129–12137 (2003)
43. F. Neese, *WIREs Comput. Mol. Sci.* **2**, 73–78 (2012)
44. F. Neese, *J. Comput. Chem.* **24**, 1740–1747 (2003)
45. F. Neese, F. Wennmohs, A. Hansen, U. Becker, *Chem. Phys.* **356**, 98–109 (2009)

Appendix B

Mathematical Derivations

B.1 Correlation of Periodic Functions

Autocorrelation

The autocorrelation of a time-dependent function $A(\tau)$ is the expected value over τ of the product $A^*(\tau)A(\tau + t)$ as a function of the time difference t , which is given by

$$R_A(t) = \langle A^*(\tau)A(\tau + t) \rangle_\tau = \lim_{T \rightarrow \infty} \frac{1}{2T} \int_{-T}^T A^*(\tau)A(\tau + t) d\tau. \quad (\text{B.1})$$

Applying this to the harmonic oscillator trajectory $x(t) = x_0 \cos(\omega_0 t + \varphi)$ leads to

$$\begin{aligned} R_x(t) &= \lim_{T \rightarrow \infty} \frac{1}{2T} \int_{-T}^T x_0^2 \cos(\omega_0 \tau + \varphi) \cos(\omega_0(\tau + t) + \varphi) d\tau \\ &= \lim_{T \rightarrow \infty} \frac{1}{2T} \int_{-T}^T x_0^2 \left[\cos^2(\omega_0 \tau) \left(\cos(\omega_0 t) \cos^2 \varphi - \sin(\omega_0 t) \sin \varphi \cos \varphi \right) \right. \\ &\quad \left. - \sin(\omega_0 \tau) \cos(\omega_0 \tau) \left(\sin(\omega_0 t) \cos^2 \varphi + 2 \cos(\omega_0 t) \sin \varphi \cos \varphi - \sin(\omega_0 t) \sin^2 \varphi \right) \right. \\ &\quad \left. + \sin^2(\omega_0 \tau) \left(\sin(\omega_0 t) \sin \varphi \cos \varphi + \cos(\omega_0 t) \sin^2 \varphi \right) \right] d\tau \\ &= x_0^2 \left(\cos(\omega_0 t) \cos^2 \varphi - \sin(\omega_0 t) \sin \varphi \cos \varphi \right) \\ &\quad \lim_{T \rightarrow \infty} \frac{1}{2T} \int_{-T}^T \cos^2(\omega_0 \tau) d\tau - x_0^2 \left(\sin(\omega_0 t) \cos^2 \varphi \right. \\ &\quad \left. + 2 \cos(\omega_0 t) \sin \varphi \cos \varphi - \sin(\omega_0 t) \sin^2 \varphi \right) \lim_{T \rightarrow \infty} \frac{1}{2T} \int_{-T}^T \sin(\omega_0 \tau) \cos(\omega_0 \tau) d\tau \\ &\quad \left. + x_0^2 \left(\sin(\omega_0 t) \sin \varphi \cos \varphi + \cos(\omega_0 t) \sin^2 \varphi \right) \lim_{T \rightarrow \infty} \frac{1}{2T} \int_{-T}^T \sin^2(\omega_0 \tau) d\tau, \quad (\text{B.2}) \end{aligned}$$

where the trigonometric sum and difference formulas are applied, the integral is split, and constant factors are placed outside the integrals and the limits. The three new integrals are given by

$$\begin{aligned} \lim_{T \rightarrow \infty} \frac{1}{2T} \int_{-T}^T \cos^2(\omega_0 \tau) d\tau &= \lim_{T \rightarrow \infty} \frac{1}{2T} \left[\frac{\omega_0 \tau + \sin(\omega_0 \tau) \cos(\omega_0 \tau)}{2\omega_0} \right]_{\tau=-T}^T \\ &= \lim_{T \rightarrow \infty} \frac{1}{2T} \left(\frac{\sin(\omega_0 T) \cos(\omega_0 T) + \omega_0 T}{\omega_0} \right) = \frac{1}{2}, \end{aligned} \quad (\text{B.3})$$

$$\lim_{T \rightarrow \infty} \frac{1}{2T} \int_{-T}^T \sin(\omega_0 \tau) \cos(\omega_0 \tau) d\tau = \lim_{T \rightarrow \infty} \frac{1}{2T} \left[-\frac{\cos^2(\omega_0 \tau)}{2\omega_0} \right]_{\tau=-T}^T = 0, \quad (\text{B.4})$$

$$\begin{aligned} \lim_{T \rightarrow \infty} \frac{1}{2T} \int_{-T}^T \sin^2(\omega_0 \tau) d\tau &= \lim_{T \rightarrow \infty} \frac{1}{2T} \left[\frac{\omega_0 \tau - \sin(\omega_0 \tau) \cos(\omega_0 \tau)}{2\omega_0} \right]_{\tau=-T}^T \\ &= \lim_{T \rightarrow \infty} \frac{1}{2T} \left(\frac{\omega_0 T - \sin(\omega_0 T) \cos(\omega_0 T)}{\omega_0} \right) = \frac{1}{2}. \end{aligned} \quad (\text{B.5})$$

Inserting these expressions into (B.2) yields

$$\begin{aligned} R_x(t) &= \frac{1}{2} x_0^2 (\cos(\omega_0 t) \cos^2 \varphi - \sin(\omega_0 t) \sin \varphi \cos \varphi) \\ &\quad + \frac{1}{2} x_0^2 (\sin(\omega_0 t) \sin \varphi \cos \varphi + \cos(\omega_0 t) \sin^2 \varphi) \\ &= \frac{1}{2} x_0^2 \cos(\omega_0 t) (\cos^2 \varphi + \sin^2 \varphi) = \frac{1}{2} x_0^2 \cos(\omega_0 t). \end{aligned} \quad (\text{B.6})$$

Autocorrelation of the Derivative

The autocorrelation of the time derivative $\dot{A}(\tau) = dA(\tau)/d\tau$ is given by

$$R_{\dot{A}}(t) = \langle \dot{A}^*(\tau) \dot{A}(\tau + t) \rangle_{\tau} = -\frac{d^2}{dt^2} R_A(t). \quad (\text{B.7})$$

This can be shown by inserting the definition of the derivative:

$$\begin{aligned} R_{\dot{A}}(t) &= \lim_{T \rightarrow \infty} \frac{1}{2T} \int_{-T}^T \dot{A}^*(\tau) \dot{A}(\tau + t) d\tau \\ &= \lim_{T \rightarrow \infty} \frac{1}{2T} \int_{-T}^T \lim_{g \rightarrow 0} \frac{A^*(\tau + g) - A^*(\tau)}{g} \lim_{h \rightarrow 0} \frac{A(\tau + t + h) - A(\tau + t)}{h} d\tau \\ &= \lim_{g \rightarrow 0} \lim_{h \rightarrow 0} \left[\frac{1}{gh} \lim_{T \rightarrow \infty} \frac{1}{2T} \int_{-T}^T (A^*(\tau + g) - A^*(\tau)) (A(\tau + t + h) - A(\tau + t)) d\tau \right] \\ &= \lim_{g \rightarrow 0} \lim_{h \rightarrow 0} \left[\frac{1}{gh} \left(\lim_{T \rightarrow \infty} \frac{1}{2T} \int_{-T}^T A^*(\tau + g) A(\tau + t + h) d\tau \right. \right. \\ &\quad \left. \left. - \lim_{T \rightarrow \infty} \frac{1}{2T} \int_{-T}^T A^*(\tau + g) A(\tau + t) d\tau \right. \right. \\ &\quad \left. \left. - \lim_{T \rightarrow \infty} \frac{1}{2T} \int_{-T}^T A^*(\tau) A(\tau + t + h) d\tau + \lim_{T \rightarrow \infty} \frac{1}{2T} \int_{-T}^T A^*(\tau) A(\tau + t) d\tau \right) \right] \end{aligned}$$

$$\begin{aligned}
&= \lim_{g \rightarrow 0} \lim_{h \rightarrow 0} \left[\frac{1}{gh} (R_A(t-g+h) - R_A(t-g) - R_A(t+h) + R_A(t)) \right] \\
&= \lim_{g \rightarrow 0} \left[\frac{1}{g} \left(\frac{d}{dt} R_A(t-g) - \frac{d}{dt} R_A(t) \right) \right] = -\frac{d^2}{dt^2} R_A(t), \tag{B.8}
\end{aligned}$$

where uniform convergence is presumed to ensure the permutability of the limits and the integral.

Vector Autocorrelation

The autocorrelation of an n -dimensional vectorial quantity $\mathbf{A}(\tau)$ is the expected value over τ of the scalar product $\mathbf{A}^*(\tau) \cdot \mathbf{A}(\tau + t)$ as a function of the time difference t . It is given by

$$\begin{aligned}
R_{\mathbf{A}}(t) &= \langle \mathbf{A}^*(\tau) \cdot \mathbf{A}(\tau + t) \rangle_{\tau} = \lim_{T \rightarrow \infty} \frac{1}{2T} \int_{-T}^T \mathbf{A}^*(\tau) \cdot \mathbf{A}(\tau + t) d\tau \\
&= \lim_{T \rightarrow \infty} \frac{1}{2T} \int_{-T}^T \sum_{i=1}^n A_i^*(\tau) A_i(\tau + t) d\tau = \sum_{i=1}^n \lim_{T \rightarrow \infty} \frac{1}{2T} \int_{-T}^T A_i^*(\tau) A_i(\tau + t) d\tau \\
&= \sum_{i=1}^n R_{A_i}(t), \tag{B.9}
\end{aligned}$$

so it is the sum of the autocorrelations of the vector components in an orthonormal basis.

Cross-Correlation

The cross-correlation of two time-dependent functions $A(\tau)$ and $B(\tau)$ is the expected value over τ of the product $A^*(\tau)B(\tau + t)$ as a function of the time difference t , which is given by

$$R_{AB}(t) = \langle A^*(\tau)B(\tau + t) \rangle_{\tau} = \lim_{T \rightarrow \infty} \frac{1}{2T} \int_{-T}^T A^*(\tau)B(\tau + t) d\tau. \tag{B.10}$$

The autocorrelation is the special case of the cross-correlation of a function $A(\tau)$ with itself:

$$R_{\mathbf{A}}(t) = R_{AA}(t). \tag{B.11}$$

Calculating the cross-correlation of two harmonic oscillator trajectories $x_i(t) = x_i \cos(\omega_i t + \varphi_i)$ and $x_j(t) = x_j \cos(\omega_j t + \varphi_j)$ leads to

$$\begin{aligned}
R_{x_i x_j}(t) &= \lim_{T \rightarrow \infty} \frac{1}{2T} \int_{-T}^T x_i x_j \cos(\omega_i \tau + \varphi_i) \cos(\omega_j(\tau + t) + \varphi_j) d\tau \\
&= \lim_{T \rightarrow \infty} \frac{1}{2T} \int_{-T}^T x_i x_j \left[\cos(\omega_i \tau) \cos(\omega_j \tau) (\cos(\omega_j t) \cos \varphi_i \cos \varphi_j \right. \\
&\quad \left. - \sin(\omega_j t) \cos \varphi_i \sin \varphi_j) + \sin(\omega_i \tau) \cos(\omega_j \tau) \right] d\tau
\end{aligned}$$

$$\begin{aligned}
& \left(\sin(\omega_j t) \sin \varphi_i \sin \varphi_j - \cos(\omega_j t) \sin \varphi_i \cos \varphi_j \right) \\
& - \cos(\omega_i \tau) \sin(\omega_j \tau) \left(\sin(\omega_j t) \cos \varphi_i \cos \varphi_j + \cos(\omega_j t) \cos \varphi_i \sin \varphi_j \right) \\
& + \sin(\omega_i \tau) \sin(\omega_j \tau) \left(\sin(\omega_j t) \sin \varphi_i \cos \varphi_j + \cos(\omega_j t) \sin \varphi_i \sin \varphi_j \right) \Big] d\tau \\
= & x_i x_j \left(\cos(\omega_j t) \cos \varphi_i \cos \varphi_j - \sin(\omega_j t) \cos \varphi_i \sin \varphi_j \right) \\
& \lim_{T \rightarrow \infty} \frac{1}{2T} \int_{-T}^T \cos(\omega_i \tau) \cos(\omega_j \tau) d\tau \\
& + x_i x_j \left(\sin(\omega_j t) \sin \varphi_i \sin \varphi_j - \cos(\omega_j t) \sin \varphi_i \cos \varphi_j \right) \\
& \lim_{T \rightarrow \infty} \frac{1}{2T} \int_{-T}^T \sin(\omega_i \tau) \cos(\omega_j \tau) d\tau \\
& - x_i x_j \left(\sin(\omega_j t) \cos \varphi_i \cos \varphi_j + \cos(\omega_j t) \cos \varphi_i \sin \varphi_j \right) \\
& \lim_{T \rightarrow \infty} \frac{1}{2T} \int_{-T}^T \cos(\omega_i \tau) \sin(\omega_j \tau) d\tau \\
& + x_i x_j \left(\sin(\omega_j t) \sin \varphi_i \cos \varphi_j + \cos(\omega_j t) \sin \varphi_i \sin \varphi_j \right) \\
& \lim_{T \rightarrow \infty} \frac{1}{2T} \int_{-T}^T \sin(\omega_i \tau) \sin(\omega_j \tau) d\tau, \tag{B.12}
\end{aligned}$$

where the trigonometric sum and difference formulas are applied, the integral is split, and constant factors are placed outside the integrals and the limits. For $\omega_i \neq \omega_j$, the four new integrals are given in the following way:

$$\begin{aligned}
\lim_{T \rightarrow \infty} \frac{1}{2T} \int_{-T}^T \cos(\omega_i \tau) \cos(\omega_j \tau) d\tau &= \lim_{T \rightarrow \infty} \frac{1}{2T} \int_{-T}^T \frac{\cos((\omega_i + \omega_j)\tau)}{2} + \frac{\cos((\omega_i - \omega_j)\tau)}{2} d\tau \\
&= \lim_{T \rightarrow \infty} \frac{1}{2T} \left[\frac{\sin((\omega_i + \omega_j)\tau)}{2(\omega_i + \omega_j)} + \frac{\sin((\omega_i - \omega_j)\tau)}{2(\omega_i - \omega_j)} \right]_{\tau=-T}^T \\
&= \lim_{T \rightarrow \infty} \frac{1}{2T} \left(\frac{\sin((\omega_i + \omega_j)T)}{\omega_i + \omega_j} + \frac{\sin((\omega_i - \omega_j)T)}{\omega_i - \omega_j} \right) = 0, \tag{B.13}
\end{aligned}$$

$$\begin{aligned}
\lim_{T \rightarrow \infty} \frac{1}{2T} \int_{-T}^T \sin(\omega_i \tau) \cos(\omega_j \tau) d\tau &= \lim_{T \rightarrow \infty} \frac{1}{2T} \int_{-T}^T \frac{\sin((\omega_i + \omega_j)\tau)}{2} + \frac{\sin((\omega_i - \omega_j)\tau)}{2} d\tau \\
&= \lim_{T \rightarrow \infty} \frac{1}{2T} \left[-\frac{\cos((\omega_i + \omega_j)\tau)}{2(\omega_i + \omega_j)} - \frac{\cos((\omega_i - \omega_j)\tau)}{2(\omega_i - \omega_j)} \right]_{\tau=-T}^T \\
&= \lim_{T \rightarrow \infty} \frac{1}{2T} \left(-\frac{\cos((\omega_i + \omega_j)T)}{\omega_i + \omega_j} - \frac{\cos((\omega_i - \omega_j)T)}{\omega_i - \omega_j} \right) = 0, \tag{B.14}
\end{aligned}$$

$$\lim_{T \rightarrow \infty} \frac{1}{2T} \int_{-T}^T \cos(\omega_i \tau) \sin(\omega_j \tau) d\tau = \lim_{T \rightarrow \infty} \frac{1}{2T} \int_{-T}^T \sin(\omega_i \tau) \cos(\omega_j \tau) d\tau = 0, \tag{B.15}$$

$$\lim_{T \rightarrow \infty} \frac{1}{2T} \int_{-T}^T \sin(\omega_i \tau) \sin(\omega_j \tau) d\tau = \lim_{T \rightarrow \infty} \frac{1}{2T} \int_{-T}^T -\frac{\cos((\omega_i + \omega_j)\tau)}{2} + \frac{\cos((\omega_i - \omega_j)\tau)}{2} d\tau$$

$$\begin{aligned}
&= \lim_{T \rightarrow \infty} \frac{1}{2T} \left[-\frac{\sin((\omega_i + \omega_j)\tau)}{2(\omega_i + \omega_j)} + \frac{\sin((\omega_i - \omega_j)\tau)}{2(\omega_i - \omega_j)} \right]_{\tau=-T}^T \\
&= \lim_{T \rightarrow \infty} \frac{1}{2T} \left(-\frac{\sin((\omega_i + \omega_j)T)}{\omega_i + \omega_j} + \frac{\sin((\omega_i - \omega_j)T)}{\omega_i - \omega_j} \right) = 0.
\end{aligned} \tag{B.16}$$

Therefore, the cross-correlation vanishes if the frequencies are different:

$$R_{x_i x_j}(t) = 0, \quad \omega_i \neq \omega_j. \tag{B.17}$$

For $\omega_i = \omega_j$, the integrals are given in Eqs. (B.3)–(B.5). It remains

$$\begin{aligned}
R_{x_i x_j}(t) &= \frac{1}{2} x_i x_j (\cos(\omega_i t) \cos \varphi_i \cos \varphi_j - \sin(\omega_i t) \cos \varphi_i \sin \varphi_j) \\
&\quad + \frac{1}{2} x_i x_j (\sin(\omega_i t) \sin \varphi_i \cos \varphi_j + \cos(\omega_i t) \sin \varphi_i \sin \varphi_j) \\
&= \frac{1}{2} x_i x_j (\cos(\omega_i t) \cos(\varphi_i - \varphi_j) + \sin(\omega_i t) \sin(\varphi_i - \varphi_j)), \quad \omega_i = \omega_j.
\end{aligned} \tag{B.18}$$

It should be noted that the sum in Eq. (3.16) also contains $R_{x_j x_i}(t)$, which is given by

$$R_{x_j x_i}(t) = \frac{1}{2} x_i x_j (\cos(\omega_i t) \cos(\varphi_i - \varphi_j) - \sin(\omega_i t) \sin(\varphi_i - \varphi_j)), \quad \omega_i = \omega_j. \tag{B.19}$$

Thus, only the cosine function without a phase remains also if the autocorrelation of a linear combination of two harmonic vibrations with the same frequency is calculated.

B.2 Correlation of Discrete Data Sets

Autocorrelation

The autocorrelation of a quantity A in a finite MD trajectory with a discrete timestep Δt is given by

$$R_A(n\Delta t) = \frac{1}{N-n} \sum_{i=0}^{N-n-1} A_i^* A_{i+n}, \quad \text{with } n = 0, \dots, N-1, \tag{B.20}$$

where $(A_i)_{i=0}^{N-1}$ are the values of A in the N snapshots of the simulation, and i numbers the steps of the trajectory.

Applying this to the harmonic oscillator trajectory $A_i = x_0 \cos(i\omega_0\Delta t + \varphi)$ yields

$$\begin{aligned}
R_A(n\Delta t) &= \frac{1}{N-n} \sum_{i=0}^{N-n-1} x_0^2 \cos(i\omega_0\Delta t + \varphi) \cos((i+n)\omega_0\Delta t + \varphi) \\
&= \frac{1}{N-n} \sum_{i=0}^{N-n-1} x_0^2 \left[\cos^2(i\omega_0\Delta t) \left(\cos(n\omega_0\Delta t) \cos^2\varphi - \sin(n\omega_0\Delta t) \sin\varphi \cos\varphi \right) \right. \\
&\quad - \sin(i\omega_0\Delta t) \cos(i\omega_0\Delta t) \left(\sin(n\omega_0\Delta t) \cos^2\varphi + 2 \cos(n\omega_0\Delta t) \sin\varphi \cos\varphi \right. \\
&\quad \left. \left. - \sin(n\omega_0\Delta t) \sin^2\varphi \right) \right. \\
&\quad \left. + \sin^2(i\omega_0\Delta t) \left(\sin(n\omega_0\Delta t) \sin\varphi \cos\varphi + \cos(n\omega_0\Delta t) \sin^2\varphi \right) \right] \\
&= \frac{x_0^2}{N-n} \left(\cos(n\omega_0\Delta t) \cos^2\varphi - \sin(n\omega_0\Delta t) \sin\varphi \cos\varphi \right) \sum_{i=0}^{N-n-1} \cos^2(i\omega_0\Delta t) \\
&\quad - \frac{x_0^2}{N-n} \left(\sin(n\omega_0\Delta t) \cos^2\varphi + 2 \cos(n\omega_0\Delta t) \sin\varphi \cos\varphi \right. \\
&\quad \left. - \sin(n\omega_0\Delta t) \sin^2\varphi \right) \sum_{i=0}^{N-n-1} \sin(i\omega_0\Delta t) \cos(i\omega_0\Delta t) \\
&\quad + \frac{x_0^2}{N-n} \left(\sin(n\omega_0\Delta t) \sin\varphi \cos\varphi + \cos(n\omega_0\Delta t) \sin^2\varphi \right) \sum_{i=0}^{N-n-1} \sin^2(i\omega_0\Delta t),
\end{aligned} \tag{B.21}$$

where the trigonometric sum and difference formulas are applied, the sum is split, and constant factors are placed outside the sums. The three new sums are calculated in the following way:

$$\begin{aligned}
\sum_{j=0}^{N-n-1} \cos^2(j\omega_0\Delta t) &= \sum_{j=0}^{N-n-1} \left(\frac{\exp(ij\omega_0\Delta t) + \exp(-ij\omega_0\Delta t)}{2} \right)^2 \\
&= \frac{1}{4} \sum_{j=0}^{N-n-1} (\exp(2ij\omega_0\Delta t) + \exp(-2ij\omega_0\Delta t) + 2) \\
&= \frac{1}{4} \sum_{j=0}^{N-n-1} \exp(2ij\omega_0\Delta t) + \frac{1}{4} \sum_{j=0}^{N-n-1} \exp(-2ij\omega_0\Delta t) + \frac{1}{2}(N-n),
\end{aligned} \tag{B.22}$$

where the definition of the cosine in terms of exponential functions is used and the sum is split. The two individual sums are partial sums of geometric series, so the first one is given by

$$\begin{aligned}
\sum_{j=0}^{N-n-1} \exp(2ij\omega_0\Delta t) &= \sum_{j=0}^{N-n-1} (\exp(2i\omega_0\Delta t))^j \\
&= \frac{1 - (\exp(2i\omega_0\Delta t))^{N-n}}{1 - \exp(2i\omega_0\Delta t)} = \frac{1 - \exp(2i(N-n)\omega_0\Delta t)}{1 - \exp(2i\omega_0\Delta t)}
\end{aligned} \tag{B.23}$$

for $\omega_0 \Delta t \neq z \pi$, $z \in \mathbb{Z}$. Since the Nyquist–Shannon theorem limits the sampling by $\omega_{\max} \Delta t = \pi$, the case $\omega_0 \Delta t = z \pi$ is not considered further. The timestep in a simulation should always be chosen small enough to sample all vibrational frequencies of the system. Applying this also to the second geometric series, using Euler’s formula for the exponential, and employing the trigonometric sum and difference formulas leads to

$$\begin{aligned}
 \sum_{j=0}^{N-n-1} \cos^2(j\omega_0 \Delta t) &= \frac{1}{4} \left(\frac{1 - \exp(2i(N-n)\omega_0 \Delta t)}{1 - \exp(2i\omega_0 \Delta t)} \right. \\
 &\quad \left. + \frac{1 - \exp(-2i(N-n)\omega_0 \Delta t)}{1 - \exp(-2i\omega_0 \Delta t)} + 2(N-n) \right) \\
 &= \frac{1}{4} \left(2(N-n) + 1 - \cos(2N\omega_0 \Delta t) \cos(2n\omega_0 \Delta t) \right. \\
 &\quad \left. - \sin(2N\omega_0 \Delta t) \sin(2n\omega_0 \Delta t) \right. \\
 &\quad \left. + \frac{\cos(\omega_0 \Delta t)}{\sin(\omega_0 \Delta t)} (\sin(2N\omega_0 \Delta t) \cos(2n\omega_0 \Delta t) \right. \\
 &\quad \left. - \cos(2N\omega_0 \Delta t) \sin(2n\omega_0 \Delta t)) \right) \quad (\text{B.24})
 \end{aligned}$$

In the same way, the other sums in (B.21) are obtained:

$$\begin{aligned}
 &\sum_{j=0}^{N-n-1} \sin(j\omega_0 \Delta t) \cos(j\omega_0 \Delta t) \\
 &= \sum_{j=0}^{N-n-1} \frac{\exp(ij\omega_0 \Delta t) - \exp(-ij\omega_0 \Delta t)}{2i} \frac{\exp(ij\omega_0 \Delta t) + \exp(-ij\omega_0 \Delta t)}{2} \\
 &= \frac{1}{4i} \sum_{j=0}^{N-n-1} (\exp(2ij\omega_0 \Delta t) - \exp(-2ij\omega_0 \Delta t)) \\
 &= \frac{1}{4i} \left(\frac{1 - \exp(2i(N-n)\omega_0 \Delta t)}{1 - \exp(2i\omega_0 \Delta t)} - \frac{1 - \exp(-2i(N-n)\omega_0 \Delta t)}{1 - \exp(-2i\omega_0 \Delta t)} \right) \\
 &= \frac{1}{4} \left(\cos(2N\omega_0 \Delta t) \sin(2n\omega_0 \Delta t) - \sin(2N\omega_0 \Delta t) \cos(2n\omega_0 \Delta t) \right. \\
 &\quad \left. + \frac{\cos(\omega_0 \Delta t)}{\sin(\omega_0 \Delta t)} (1 - \cos(2N\omega_0 \Delta t) \cos(2n\omega_0 \Delta t) - \sin(2N\omega_0 \Delta t) \sin(2n\omega_0 \Delta t)) \right) \quad (\text{B.25})
 \end{aligned}$$

$$\begin{aligned}
 &\sum_{j=0}^{N-n-1} \sin^2(j\omega_0 \Delta t) \\
 &= \sum_{j=0}^{N-n-1} \left(\frac{\exp(ij\omega_0 \Delta t) - \exp(-ij\omega_0 \Delta t)}{2i} \right)^2
 \end{aligned}$$

$$\begin{aligned}
&= -\frac{1}{4} \sum_{j=0}^{N-n-1} (\exp(2ij\omega_0\Delta t) + \exp(-2ij\omega_0\Delta t) - 2) \\
&= -\frac{1}{4} \left(\frac{1 - \exp(2i(N-n)\omega_0\Delta t)}{1 - \exp(2i\omega_0\Delta t)} + \frac{1 - \exp(-2i(N-n)\omega_0\Delta t)}{1 - \exp(-2i\omega_0\Delta t)} - 2(N-n) \right) \\
&= \frac{1}{4} \left(2(N-n) - 1 + \cos(2N\omega_0\Delta t) \cos(2n\omega_0\Delta t) + \sin(2N\omega_0\Delta t) \sin(2n\omega_0\Delta t) \right. \\
&\quad \left. - \frac{\cos(\omega_0\Delta t)}{\sin(\omega_0\Delta t)} (\sin(2N\omega_0\Delta t) \cos(2n\omega_0\Delta t) - \cos(2N\omega_0\Delta t) \sin(2n\omega_0\Delta t)) \right) \quad (\text{B.26})
\end{aligned}$$

Inserting these terms into (B.21), and applying the trigonometric sum and difference formulas yields

$$R_A(n\Delta t) = \frac{1}{2} x_0^2 \cos(n\omega_0\Delta t) + \frac{x_0^2 \cos((N-1)\omega_0\Delta t + 2\varphi)}{2(N-n) \sin(\omega_0\Delta t)} \sin((N-n)\omega_0\Delta t). \quad (\text{B.27})$$

Cross-Correlation

The cross-correlation of two quantities A and B in a finite MD trajectory with a discrete timestep Δt is given by

$$R_{AB}(n\Delta t) = \frac{1}{N-n} \sum_{i=0}^{N-n-1} A_i^* B_{i+n}, \quad \text{with } n = 0, \dots, N-1, \quad (\text{B.28})$$

where $(A_i)_{i=0}^{N-1}$ and $(B_i)_{i=0}^{N-1}$ are the respective values of A and B in the N snapshots of the simulation, and i numbers the steps of the trajectory.

Applying this to two harmonic oscillator trajectories

$$A_i = x_A \cos(i\omega_A\Delta t + \varphi_A), \quad B_i = x_B \cos(i\omega_B\Delta t + \varphi_B) \quad (\text{B.29})$$

with $\omega_A \neq \omega_B$ yields very long expressions that are not shown here. With the aid of a computer algebra system (e. g., MAXIMA [1]), however, it is possible to find out that the discrete cross-correlation does not vanish as in the continuous case, but is proportional to $1/(N-n)$ and $1/((\cos((\omega_B - \omega_A)\Delta t) - 1)(\cos((\omega_B + \omega_A)\Delta t) - 1))$, so it becomes large if a long correlation depth is chosen, as well as if both frequencies are similar and very high or very low.

Correlation by Fourier Transform

The discrete Fourier transform is defined as

$$\tilde{A}_k = \mathcal{F}(A)_k = \sum_{j=0}^{N-1} A_j \exp\left(-\frac{2\pi ijk}{N}\right), \quad (\text{B.30})$$

and its inverse is

$$A_k = \mathcal{F}^{-1}(\tilde{A})_k = \frac{1}{N} \sum_{j=0}^{N-1} \tilde{A}_j \exp\left(\frac{2\pi i j k}{N}\right). \quad (\text{B.31})$$

It should be noted that the factor $1/N$ in the inverse transform is usually omitted in publicly available computer codes for fast Fourier transforms such as, e. g., the FFTW library [2] and has to be inserted by hand.

According to Wiener–Khintchine theory [3, 4], the autocorrelation of a function can be calculated by taking the square of the absolute value of its Fourier transform and applying the inverse Fourier transform. This approach bears the advantage that fast Fourier transform algorithms feature a better scaling behavior [2] than the direct computation according to (B.20). If the method is applied to a discrete data set, an auxiliary data set $(B_i)_{i=0}^{2N-1}$ defined by

$$B_i = \begin{cases} A_i & \text{if } 0 \leq i \leq N-1 \\ 0 & \text{if } N \leq i \leq 2N-1 \end{cases} \quad (\text{B.32})$$

has to be introduced. The autocorrelation of the original data set $(A_i)_{i=0}^{N-1}$ is given by

$$R_A(n\Delta t) = \frac{1}{N-n} \mathcal{F}^{-1}(|\mathcal{F}(B)|^2)_n, \quad \text{with } n = 0, \dots, N-1. \quad (\text{B.33})$$

This can be shown by inserting the definition of the discrete Fourier transform of $(B_i)_{i=0}^{2N-1}$,

$$\tilde{B}_j = \sum_{k=0}^{2N-1} B_k \exp\left(-\frac{2\pi i j k}{2N}\right), \quad (\text{B.34})$$

into the inverse discrete Fourier transform of the squared absolute value:

$$\begin{aligned} \mathcal{F}^{-1}(|\mathcal{F}(B)|^2)_n &= \frac{1}{2N} \sum_{j=0}^{2N-1} |\tilde{B}_j|^2 \exp\left(\frac{2\pi i j n}{2N}\right) = \frac{1}{2N} \sum_{j=0}^{2N-1} \tilde{B}_j^* \tilde{B}_j \exp\left(\frac{2\pi i j n}{2N}\right) \\ &= \frac{1}{2N} \sum_{j=0}^{2N-1} \left[\left(\sum_{k=0}^{2N-1} B_k^* \exp\left(\frac{2\pi i j k}{2N}\right) \right) \right. \\ &\quad \left. \left(\sum_{l=0}^{2N-1} B_l \exp\left(-\frac{2\pi i j l}{2N}\right) \right) \exp\left(\frac{2\pi i j n}{2N}\right) \right] \\ &= \frac{1}{2N} \sum_{k=0}^{2N-1} \sum_{l=0}^{2N-1} \left[B_k^* B_l \sum_{j=0}^{2N-1} \exp\left(\frac{2\pi i j (k-l+n)}{2N}\right) \right]. \end{aligned}$$

As the B_i vanish for $i > N - 1$, the limits of the sums over k and l can be rewritten:

$$\begin{aligned}
&= \frac{1}{2N} \sum_{k=0}^{N-1} \sum_{l=0}^{N-1} \left[B_k^* B_l \sum_{j=0}^{2N-1} \exp\left(\frac{2\pi i j(k-l+n)}{2N}\right) \right] \\
&= \frac{1}{2N} \sum_{k=0}^{N-1} \sum_{m=-n}^{N-n-1} \left[B_k^* B_{m+n} \sum_{j=0}^{2N-1} \exp\left(\frac{2\pi i j(k-m)}{2N}\right) \right] \\
&= \frac{1}{2N} \sum_{k=0}^{N-1} \sum_{m=0}^{N-n-1} \left[B_k^* B_{m+n} \sum_{j=0}^{2N-1} \exp\left(\frac{2\pi i j(k-m)}{2N}\right) \right] \\
&\quad + \frac{1}{2N} \sum_{k=0}^{N-1} \sum_{m=-n}^{-1} \left[B_k^* B_{m+n} \sum_{j=0}^{2N-1} \exp\left(\frac{2\pi i j(k-m)}{2N}\right) \right].
\end{aligned}$$

The sum over j is the partial sum of a geometric series that vanishes if $k - m$ is not an integer multiple of $2N$. In the first term, this is the case except for $k = m$, where the sum over j takes the value $2N$,

$$\begin{aligned}
&= \frac{1}{2N} \sum_{k=0}^{N-1} \sum_{m=0}^{N-n-1} [B_k^* B_{m+n} \cdot 2N \delta_{km}] \\
&\quad + \frac{1}{2N} \sum_{k=0}^{N-1} \sum_{m=-n}^{-1} \left[B_k^* B_{m+n} \sum_{j=0}^{2N-1} \exp\left(\frac{2\pi i j(k-m)}{2N}\right) \right] \\
&= \sum_{k=0}^{N-n-1} B_k^* B_{k+n} + \frac{1}{2N} \sum_{k=0}^{N-1} \sum_{m=-n}^{-1} \left[B_k^* B_{m+n} \sum_{j=0}^{2N-1} \exp\left(\frac{2\pi i j(k-m)}{2N}\right) \right].
\end{aligned}$$

For the second term, another index shift is required to apply this fact:

$$\begin{aligned}
&= \sum_{k=0}^{N-n-1} B_k^* B_{k+n} + \frac{1}{2N} \sum_{k=0}^{N-1} \sum_{p=2N-n}^{2N-1} \left[B_k^* B_{p+n-2N} \sum_{j=0}^{2N-1} \exp\left(\frac{2\pi i j(2N+k-p)}{2N}\right) \right] \\
&= \sum_{k=0}^{N-n-1} B_k^* B_{k+n} + \frac{1}{2N} \sum_{k=0}^{N-1} \sum_{p=2N-n}^{2N-1} \left[B_k^* B_{p+n-2N} \sum_{j=0}^{2N-1} \exp\left(\frac{2\pi i j(k-p)}{2N}\right) \right] \\
&= \sum_{k=0}^{N-n-1} B_k^* B_{k+n} + \frac{1}{2N} \sum_{k=0}^{N-1} \sum_{p=2N-n}^{2N-1} [B_k^* B_{p+n-2N} \cdot 2N \delta_{kp}] \\
&= \sum_{k=0}^{N-n-1} B_k^* B_{k+n} + \sum_{k=2N-n}^{N-1} B_k^* B_{k+n-2N}. \tag{B.35}
\end{aligned}$$

For $n < N$, the second sum is empty and only the first sum remains. Except for the prefactor $1/(N-n)$, the latter is equal to the definition of the autocorrelation (B.20).

The second sum is the reason for the introduction of the auxiliary data set. If the method is applied to the original data set with N points, the terms of the second sum mix into the first sum.

In a similar manner, for the cross-correlation of two data sets $(A_i)_{i=0}^{N-1}$ and $(C_i)_{i=0}^{N-1}$, the auxiliary data sets $(B_i)_{i=0}^{2N-1}$ and $(D_i)_{i=0}^{2N-1}$ are introduced according to

$$B_i = \begin{cases} A_i & \text{if } 0 \leq i \leq N-1 \\ 0 & \text{if } N \leq i \leq 2N-1 \end{cases}, \quad D_i = \begin{cases} C_i & \text{if } 0 \leq i \leq N-1 \\ 0 & \text{if } N \leq i \leq 2N-1 \end{cases}. \quad (\text{B.36})$$

The cross-correlation is given by

$$R_{AB}(n\Delta t) = \frac{1}{N-n} \mathcal{F}^{-1}((\mathcal{F}(B))^* \mathcal{F}(D))_n, \quad \text{with } n = 0, \dots, N-1. \quad (\text{B.37})$$

The proof is completely analogous to the one for the autocorrelation above, just instead of $|\tilde{B}_j|^2$, the product $\tilde{B}_j^* \tilde{D}_j$ has to be inserted.

Integral of the Fourier Transform

For any data set $(A_i)_{i=0}^{N-1}$ that is collected with a discrete timestep Δt , the integral over its discrete Fourier transform is given by

$$\sum_{k=0}^{N-1} \tilde{A}_k \Delta \omega = N A_0 \Delta \omega = A_0 \frac{2\pi}{\Delta t}. \quad (\text{B.38})$$

This can be shown by inserting the definition (B.30) of the discrete Fourier transform:

$$\begin{aligned} \sum_{k=0}^{N-1} \tilde{A}_k \Delta \omega &= \sum_{k=0}^{N-1} \left[\left(\sum_{j=0}^{N-1} A_j \exp\left(-\frac{2\pi i j k}{N}\right) \right) \Delta \omega \right] \\ &= \sum_{j=0}^{N-1} \left[A_j \Delta \omega \sum_{k=0}^{N-1} \exp\left(-\frac{2\pi i j k}{N}\right) \right] \end{aligned}$$

The sum over k is the partial sum of a geometric series that vanishes if j is not an integer multiple of N . This is the case except for $j = 0$, where the sum over k takes the value N ,

$$= \sum_{j=0}^{N-1} [A_j \Delta \omega N \delta_{0j}] = N A_0 \Delta \omega. \quad (\text{B.39})$$

B.3 Transition Moments of the Quantum Harmonic Oscillator

The transition moment of a harmonic oscillator with the eigenfrequency ω_0 between the states m and n is given by

$$\langle \chi_m | x | \chi_n \rangle = \begin{cases} \sqrt{n+1} \sqrt{\frac{\hbar}{2m\omega_0}} & \text{if } m = n + 1 \\ \sqrt{n} \sqrt{\frac{\hbar}{2m\omega_0}} & \text{if } m = n - 1 \\ 0 & \text{otherwise} \end{cases} \quad (\text{B.40})$$

This can be shown by inserting the wave functions of the harmonic oscillator given in Sect. 2.4.1:

$$\begin{aligned} \langle \chi_m | x | \chi_n \rangle &= \int_{-\infty}^{\infty} x \chi_m(x) \chi_n(x) dx \\ &= \int_{-\infty}^{\infty} \frac{1}{\sqrt{2^m m!}} \frac{1}{\sqrt{2^n n!}} \sqrt{\frac{m\omega_0}{\pi \hbar}} x H_m \left(\sqrt{\frac{m\omega_0}{\hbar}} x \right) H_n \left(\sqrt{\frac{m\omega_0}{\hbar}} x \right) \exp \left(-\frac{m\omega_0}{\hbar} x^2 \right) dx. \end{aligned} \quad (\text{B.41})$$

Using the recursive definition

$$H_{n+1}(x) = 2x H_n(x) - 2n H_{n-1}(x) \quad (\text{B.42})$$

of the Hermite polynomials, the integral can be rewritten as

$$\begin{aligned} \langle \chi_m | x | \chi_n \rangle &= \int_{-\infty}^{\infty} \frac{1}{\sqrt{2^m m!}} \frac{1}{\sqrt{2^n n!}} \frac{1}{\sqrt{\pi}} H_m \left(\sqrt{\frac{m\omega_0}{\hbar}} x \right) \left[\frac{1}{2} H_{n+1} \left(\sqrt{\frac{m\omega_0}{\hbar}} x \right) \right. \\ &\quad \left. + n H_{n-1} \left(\sqrt{\frac{m\omega_0}{\hbar}} x \right) \right] \exp \left(-\frac{m\omega_0}{\hbar} x^2 \right) dx \\ &= \int_{-\infty}^{\infty} \frac{1}{\sqrt{2^m m!}} \frac{1}{\sqrt{2^n n!}} \frac{1}{\sqrt{\pi}} \frac{1}{2} H_m \left(\sqrt{\frac{m\omega_0}{\hbar}} x \right) H_{n+1} \left(\sqrt{\frac{m\omega_0}{\hbar}} x \right) \exp \left(-\frac{m\omega_0}{\hbar} x^2 \right) dx \\ &\quad + \int_{-\infty}^{\infty} \frac{1}{\sqrt{2^m m!}} \frac{1}{\sqrt{2^n n!}} \frac{1}{\sqrt{\pi}} n H_m \left(\sqrt{\frac{m\omega_0}{\hbar}} x \right) H_{n-1} \left(\sqrt{\frac{m\omega_0}{\hbar}} x \right) \exp \left(-\frac{m\omega_0}{\hbar} x^2 \right) dx. \end{aligned} \quad (\text{B.43})$$

Applying the orthogonality relation

$$\int_{-\infty}^{\infty} \exp(-x^2) H_m(x) H_n(x) dx = 2^n \cdot n! \cdot \sqrt{\pi} \cdot \delta_{mn} \quad (\text{B.44})$$

of the Hermite polynomials, the first integral evaluates to

$$\begin{aligned}
& \int_{-\infty}^{\infty} \frac{1}{\sqrt{2^m m!}} \frac{1}{\sqrt{2^n n!}} \frac{1}{\sqrt{\pi}} \frac{1}{2} H_m \left(\sqrt{\frac{m\omega_0}{\hbar}} x \right) H_{n+1} \left(\sqrt{\frac{m\omega_0}{\hbar}} x \right) \exp \left(-\frac{m\omega_0}{\hbar} x^2 \right) dx \\
&= \frac{1}{\sqrt{2^m m!}} \frac{1}{\sqrt{2^n n!}} \frac{1}{\sqrt{\pi}} \frac{1}{2} \sqrt{\frac{\hbar}{m\omega_0}} \cdot 2^m \cdot m! \cdot \sqrt{\pi} \cdot \delta_{m,n+1} = \frac{1}{2} \delta_{m,n+1} \sqrt{\frac{2^m m!}{2^n n!}} \sqrt{\frac{\hbar}{m\omega_0}},
\end{aligned} \tag{B.45}$$

and the second integral is given by

$$\begin{aligned}
& \int_{-\infty}^{\infty} \frac{1}{\sqrt{2^m m!}} \frac{1}{\sqrt{2^n n!}} \frac{1}{\sqrt{\pi}} n H_m \left(\sqrt{\frac{m\omega_0}{\hbar}} x \right) H_{n-1} \left(\sqrt{\frac{m\omega_0}{\hbar}} x \right) \exp \left(-\frac{m\omega_0}{\hbar} x^2 \right) dx \\
&= \frac{1}{\sqrt{2^m m!}} \frac{1}{\sqrt{2^n n!}} \frac{1}{\sqrt{\pi}} n \sqrt{\frac{\hbar}{m\omega_0}} \cdot 2^m \cdot m! \cdot \sqrt{\pi} \cdot \delta_{m,n-1} = n \delta_{m,n-1} \sqrt{\frac{2^m m!}{2^n n!}} \sqrt{\frac{\hbar}{m\omega_0}}.
\end{aligned} \tag{B.46}$$

For $m = n + 1$, only the first integral remains and takes the value $\sqrt{(n+1)\hbar/(2m\omega_0)}$. For $m = n - 1$, only the second integral remains and takes the value $\sqrt{n\hbar/(2m\omega_0)}$. In all other cases, both integrals vanish and the transition moment is zero.

B.4 Verlet Integration of the Classical Harmonic Oscillator

For a particle of mass m in the one-dimensional harmonic potential $V(x) = kx^2/2$, the Verlet algorithm with the timestep Δt yields the trajectory

$$x(n\Delta t) = x_n = A \cos(\omega_V n \Delta t + \varphi), \tag{B.47}$$

where the amplitude A and the phase φ are determined by the initial conditions, and the frequency ω_V is related to the frequency $\omega_0 = \sqrt{k/m}$ of the exact solution (2.50) by

$$\omega_V = \frac{1}{\Delta t} \arccos \left(1 - \frac{1}{2} \omega_0^2 \Delta t^2 \right). \tag{B.48}$$

This is valid as long as the timestep fulfills the condition $\omega_0 \Delta t < 2$.

This can be shown by transforming the recurrence relation of the Verlet algorithm to an explicit form. According to Eq. (2.39), the position in the n th step is given by

$$x_n = 2x_{n-1} - x_{n-2} + \frac{F_{n-1}}{m} \Delta t^2. \tag{B.49}$$

In the harmonic potential, the force is $F_{n-1} = -kx_{n-1} = -m\omega_0^2 x_{n-1}$, so this can be written as

$$x_n - (2 - \omega_0^2 \Delta t^2) x_{n-1} + x_{n-2} = 0. \tag{B.50}$$

This is a linear homogeneous recurrence relation with constant coefficients, which can be solved by the ansatz $x_n = \lambda^n$:

$$\begin{aligned}\lambda^n - (2 - \omega_0^2 \Delta t^2) \lambda^{n-1} + \lambda^{n-2} &= 0 \\ \lambda^{n-2} (\lambda^2 - (2 - \omega_0^2 \Delta t^2) \lambda + 1) &= 0.\end{aligned}\quad (\text{B.51})$$

The root $\lambda = 0$ is not considered further as it would provide the trivial trajectory $x_n = 0$. For $\omega_0 \Delta t < 2$, the second factor (the characteristic polynomial of the recurrence relation) possesses the roots

$$\lambda_{1,2} = 1 - \frac{1}{2} \omega_0^2 \Delta t^2 \pm \frac{1}{2} i \omega_0 \Delta t \sqrt{4 - \omega_0^2 \Delta t^2}.\quad (\text{B.52})$$

The exponential form of this complex expression reads as

$$\lambda_{1,2} = \exp(\pm i\alpha) \quad \text{with} \quad \alpha = \arccos\left(1 - \frac{1}{2} \omega_0^2 \Delta t^2\right),\quad (\text{B.53})$$

so the general solution of the recurrence relation is

$$x_n = C_1 \lambda_1^n + C_2 \lambda_2^n = C_1 \exp(in\alpha) + C_2 \exp(-in\alpha)\quad (\text{B.54})$$

with the constants C_1 and C_2 that are determined by the initial conditions. It is convenient to write this as

$$x_n = A \cos(n\alpha + \varphi) \quad \text{with} \quad A = 2\sqrt{C_1 C_2} \quad \text{and} \quad \varphi = \arccos\left(\frac{C_1 + C_2}{2\sqrt{C_1 C_2}}\right),\quad (\text{B.55})$$

since this form shows that the trajectory is a harmonic vibration

$$x_n = A \cos(\omega_V n \Delta t + \varphi)\quad (\text{B.56})$$

with the frequency

$$\omega_V = \frac{\alpha}{\Delta t} = \frac{1}{\Delta t} \arccos\left(1 - \frac{1}{2} \omega_0^2 \Delta t^2\right).\quad (\text{B.57})$$

If the initial position x_0 and the initial velocity v_0 are chosen, the amplitude A and phase φ are determined by the equation system

$$A \cos \varphi = x_0\quad (\text{B.58})$$

$$A \cos(\omega_V \Delta t + \varphi) = x_1 = x_0 \left(1 - \frac{1}{2} \omega_0^2 \Delta t^2\right) + v_0 \Delta t,\quad (\text{B.59})$$

where the velocity form of the Verlet algorithm (2.40) is used to obtain x_1 . The solution is given by

$$A = \sqrt{x_0^2 + \frac{v_0^2}{\omega_0^2 \left(1 - \frac{1}{4}\omega_0^2 \Delta t^2\right)}}, \quad \varphi = \begin{cases} -\arccos\left(\frac{x_0}{A}\right) & \text{if } v_0 \geq 0 \\ \arccos\left(\frac{x_0}{A}\right) & \text{if } v_0 < 0 \end{cases}. \quad (\text{B.60})$$

For the exact solution $x(t) = A \cos(\omega_0 t + \varphi)$ (see Eq.(2.50)), the same initial conditions yield the equation system

$$A \cos \varphi = x_0 \quad (\text{B.61})$$

$$-A\omega_0 \sin \varphi = v_0 \quad (\text{B.62})$$

with the solution

$$A = \sqrt{x_0^2 + \frac{v_0^2}{\omega_0^2}}, \quad \varphi = \begin{cases} -\arccos\left(\frac{x_0}{A}\right) & \text{if } v_0 \geq 0 \\ \arccos\left(\frac{x_0}{A}\right) & \text{if } v_0 < 0 \end{cases}. \quad (\text{B.63})$$

This means that not only the frequency, but also the amplitude and the phase are influenced if the Verlet algorithm is employed to integrate the equations of motion for the harmonic oscillator.

B.5 Finite Difference Derivatives

The second-order central finite difference derivative of a cosine function $\cos(\omega t + \varphi)$ is given by

$$D \cos(\omega t + \varphi) = \frac{\cos(\omega(t + \Delta t) + \varphi) - \cos(\omega(t - \Delta t) + \varphi)}{2\Delta t} = -\omega \sin(\omega t + \varphi) \frac{\sin(\omega \Delta t)}{\omega \Delta t}. \quad (\text{B.64})$$

This means that the exact derivative $d(\cos(\omega t + \varphi))/dt = -\omega \sin(\omega t + \varphi)$ is multiplied by the sinc function $\sin(\omega \Delta t)/(\omega \Delta t)$.

This can be shown by applying the trigonometric sum and difference formulas:

$$\begin{aligned} D \cos(\omega t + \varphi) &= \frac{\cos(\omega(t + \Delta t) + \varphi) - \cos(\omega(t - \Delta t) + \varphi)}{2\Delta t} \\ &= \frac{1}{2\Delta t} \left(\cos(\omega t + \varphi) \cos(\omega \Delta t) - \sin(\omega t + \varphi) \sin(\omega \Delta t) \right. \\ &\quad \left. - \cos(\omega t + \varphi) \cos(\omega \Delta t) - \sin(\omega t + \varphi) \sin(\omega \Delta t) \right) \\ &= -\frac{\sin(\omega t + \varphi) \sin(\omega \Delta t)}{\Delta t} \\ &= -\omega \sin(\omega t + \varphi) \frac{\sin(\omega \Delta t)}{\omega \Delta t}. \end{aligned} \quad (\text{B.65})$$

B.6 Reference Point for Molecular Moments

Infrared Spectrum of a Translating Oscillator

If an oscillator is charged, its translational motion shows up in the IR spectrum depending on the choice of the origin for the dipole moment.

This can be shown in the following way: According to Eq. (3.84), the dipole moment of an oscillator with the translating center of mass $\mathbf{s}(t)$ is given by

$$\boldsymbol{\mu}(t) = \boldsymbol{\mu}^s(t) + q\mathbf{s}(t), \quad (\text{B.66})$$

where $\boldsymbol{\mu}(t)$ is the dipole moment with the coordinate origin as reference point, $\boldsymbol{\mu}^s(t)$ is the dipole moment with the center of mass as reference point, and q is the charge. The time derivative of the dipole moment reads as

$$\dot{\boldsymbol{\mu}}(t) = \dot{\boldsymbol{\mu}}^s(t) + q\dot{\mathbf{s}}(t). \quad (\text{B.67})$$

Thus, the autocorrelation is

$$\begin{aligned} \langle \dot{\boldsymbol{\mu}}(\tau) \cdot \dot{\boldsymbol{\mu}}(\tau + t) \rangle_{\tau} &= \langle (\dot{\boldsymbol{\mu}}^s(\tau) + q\dot{\mathbf{s}}(\tau)) \cdot (\dot{\boldsymbol{\mu}}^s(\tau + t) + q\dot{\mathbf{s}}(\tau + t)) \rangle_{\tau} \\ &= \langle \dot{\boldsymbol{\mu}}^s(\tau) \cdot \dot{\boldsymbol{\mu}}^s(\tau + t) \rangle_{\tau} + q \langle \dot{\boldsymbol{\mu}}^s(\tau) \cdot \dot{\mathbf{s}}(\tau + t) \rangle_{\tau} \\ &\quad + q \langle \dot{\mathbf{s}}(\tau) \cdot \dot{\boldsymbol{\mu}}^s(\tau + t) \rangle_{\tau} + q^2 \langle \dot{\mathbf{s}}(\tau) \cdot \dot{\mathbf{s}}(\tau + t) \rangle_{\tau}, \end{aligned} \quad (\text{B.68})$$

so it contains additional charge-dependent terms involving the center of mass velocity in contrast to the autocorrelation $\langle \dot{\boldsymbol{\mu}}^s(\tau) \cdot \dot{\boldsymbol{\mu}}^s(\tau + t) \rangle_{\tau}$ that is obtained in a coordinate system fixed at the oscillator.

Magnetic Moment of a Translating Electron Density

The magnetic moment of a translating electron density distribution $\rho(\mathbf{r}, t)$ with the centroid $\mathbf{s}(t)$ is given by

$$\mathbf{m}(t) = \mathbf{m}^s(t) + \frac{1}{2}\mathbf{s}(t) \times \mathbf{J}^s(t) + \frac{1}{2}\boldsymbol{\mu}^s(t) \times \frac{\partial \mathbf{s}(t)}{\partial t} + \frac{1}{2}q(t)\mathbf{s}(t) \times \frac{\partial \mathbf{s}(t)}{\partial t}, \quad (\text{B.69})$$

where $\mathbf{m}^s(t)$ and $\mathbf{J}^s(t)$ are the magnetic moment and the total current density in the centroid coordinate system, respectively. This can be, e. g., a molecule with center of mass $\mathbf{s}(t)$ that is translating and vibrating. The analogous expression for the total current density reads as

$$\mathbf{J}(t) = \mathbf{J}^s(t) + q(t)\frac{\partial \mathbf{s}(t)}{\partial t}, \quad (\text{B.70})$$

where $q(t)$ is the total charge of the electron density distribution.

This can be shown in the following way: It is assumed that the electron density can be separated by

$$\rho(\mathbf{r}, t) = \rho_0(\mathbf{r} - \mathbf{s}(t)) + \rho_1(\mathbf{r} - \mathbf{s}(t), t), \quad (\text{B.71})$$

where $\rho_0(\mathbf{r})$ is the equilibrium electron density that depends on the time only implicitly due to the translation of the centroid, and $\rho_1(\mathbf{r}, t)$ collects all changes in the electron density due to vibrations, which keep the centroid fixed. The time derivative of the electron density reads as

$$\frac{\partial \rho(\mathbf{r}, t)}{\partial t} = -\nabla \rho_0(\mathbf{r} - \mathbf{s}(t)) \cdot \frac{\partial \mathbf{s}(t)}{\partial t} + \frac{\partial \rho_1(\mathbf{r} - \mathbf{s}(t), t)}{\partial t} - \nabla \rho_1(\mathbf{r} - \mathbf{s}(t), t) \cdot \frac{\partial \mathbf{s}(t)}{\partial t}, \quad (\text{B.72})$$

and the gradient is given by

$$\nabla \rho(\mathbf{r}, t) = \nabla \rho_0(\mathbf{r} - \mathbf{s}(t)) + \nabla \rho_1(\mathbf{r} - \mathbf{s}(t), t). \quad (\text{B.73})$$

Inserting this into the differential equation (3.92) yields

$$\frac{\partial \rho_1(\mathbf{r} - \mathbf{s}(t), t)}{\partial t} - \nabla \rho(\mathbf{r}, t) \cdot \frac{\partial \mathbf{s}(t)}{\partial t} = \nabla \rho(\mathbf{r}, t) \cdot \nabla \alpha(\mathbf{r}, t) + \rho(\mathbf{r}, t) \Delta \alpha(\mathbf{r}, t). \quad (\text{B.74})$$

A similar ansatz is made for $\alpha(\mathbf{r}, t)$:

$$\alpha(\mathbf{r}, t) = \alpha_0(\mathbf{r} - \mathbf{s}(t)) + \alpha_1(\mathbf{r} - \mathbf{s}(t), t), \quad (\text{B.75})$$

where $\alpha_0(\mathbf{r})$ is the solution without vibrations of the electron density distribution. In this case, the current density should be proportional to the velocity, so it is required that $\nabla \alpha_0(\mathbf{r}) = -\partial \mathbf{s}(t)/\partial t$. This leads to

$$\nabla \alpha(\mathbf{r}, t) = -\frac{\partial \mathbf{s}(t)}{\partial t} + \nabla \alpha_1(\mathbf{r} - \mathbf{s}(t), t) \quad (\text{B.76})$$

$$\Delta \alpha(\mathbf{r}, t) = \Delta \alpha_1(\mathbf{r} - \mathbf{s}(t), t). \quad (\text{B.77})$$

Inserting this into (B.74) yields

$$\begin{aligned} \frac{\partial \rho_1(\mathbf{r} - \mathbf{s}(t), t)}{\partial t} - \nabla \rho(\mathbf{r}, t) \cdot \frac{\partial \mathbf{s}(t)}{\partial t} &= -\nabla \rho(\mathbf{r}, t) \cdot \frac{\partial \mathbf{s}(t)}{\partial t} \\ &\quad + \nabla \rho(\mathbf{r}, t) \cdot \nabla \alpha_1(\mathbf{r} - \mathbf{s}(t), t) + \rho(\mathbf{r}, t) \Delta \alpha_1(\mathbf{r} - \mathbf{s}(t), t) \\ \frac{\partial \rho_1(\mathbf{r} - \mathbf{s}(t), t)}{\partial t} &= \nabla \rho(\mathbf{r}, t) \cdot \nabla \alpha_1(\mathbf{r} - \mathbf{s}(t), t) + \rho(\mathbf{r}, t) \Delta \alpha_1(\mathbf{r} - \mathbf{s}(t), t). \end{aligned} \quad (\text{B.78})$$

Replacing $\mathbf{r} - \mathbf{s}(t)$ by \mathbf{r}' , this is exactly the differential equation (3.92) in a coordinate system with fixed centroid. This means that $\alpha_1(\mathbf{r}, t)$ can be used to calculate the current density in the centroid coordinate system.

Using the current density $\mathbf{j}(\mathbf{r}) = -\rho(\mathbf{r}, t) \nabla \alpha(\mathbf{r}, t)$, the magnetic moment is given by

$$\begin{aligned}
\mathbf{m}(t) &= \frac{1}{2} \int_{C_i^+(\mathbf{r})} \mathbf{r} \times \mathbf{j}(\mathbf{r}) \, d\mathbf{r} \\
&= \frac{1}{2} \int_{C_i^+(\mathbf{r})} \mathbf{r} \times \frac{\partial \mathbf{s}(t)}{\partial t} \rho(\mathbf{r}, t) \, d\mathbf{r} - \frac{1}{2} \int_{C_i^+(\mathbf{r})} \mathbf{r} \times \nabla \alpha_1(\mathbf{r} - \mathbf{s}(t), t) \rho(\mathbf{r}, t) \, d\mathbf{r} \\
&= \frac{1}{2} \left(\int_{C_i^+(\mathbf{r})} \mathbf{r} \rho(\mathbf{r}, t) \, d\mathbf{r} \right) \times \frac{\partial \mathbf{s}(t)}{\partial t} \\
&\quad - \frac{1}{2} \int_{C_i^+(\mathbf{r}')} (\mathbf{r}' + \mathbf{s}(t)) \times \nabla \alpha_1(\mathbf{r}', t) (\rho_0(\mathbf{r}') + \rho_1(\mathbf{r}', t)) \, d\mathbf{r}' \\
&= \frac{1}{2} \boldsymbol{\mu}(t) \times \frac{\partial \mathbf{s}(t)}{\partial t} - \frac{1}{2} \mathbf{s}(t) \times \left(\int_{C_i^+(\mathbf{r}')} \nabla \alpha_1(\mathbf{r}', t) (\rho_0(\mathbf{r}') + \rho_1(\mathbf{r}', t)) \, d\mathbf{r}' \right) \\
&\quad - \frac{1}{2} \int_{C_i^+(\mathbf{r}')} \mathbf{r}' \times \nabla \alpha_1(\mathbf{r}', t) (\rho_0(\mathbf{r}') + \rho_1(\mathbf{r}', t)) \, d\mathbf{r}' \\
&= \frac{1}{2} (\boldsymbol{\mu}^s(t) + q(t) \mathbf{s}(t)) \times \frac{\partial \mathbf{s}(t)}{\partial t} + \frac{1}{2} \mathbf{s}(t) \times \mathbf{J}^s(t) + \mathbf{m}^s(t) \\
&= \frac{1}{2} \boldsymbol{\mu}^s(t) \times \frac{\partial \mathbf{s}(t)}{\partial t} + \frac{1}{2} q(t) \mathbf{s}(t) \times \frac{\partial \mathbf{s}(t)}{\partial t} + \frac{1}{2} \mathbf{s}(t) \times \mathbf{J}^s(t) + \mathbf{m}^s(t), \quad (\text{B.79})
\end{aligned}$$

and the total current density is given by

$$\begin{aligned}
\mathbf{J}(t) &= \int_{C_i^+(\mathbf{r})} \mathbf{j}(\mathbf{r}) \, d\mathbf{r} \\
&= \int_{C_i^+(\mathbf{r})} \frac{\partial \mathbf{s}(t)}{\partial t} \rho(\mathbf{r}, t) \, d\mathbf{r} - \int_{C_i^+(\mathbf{r})} \nabla \alpha_1(\mathbf{r} - \mathbf{s}(t), t) \rho(\mathbf{r}, t) \, d\mathbf{r} \\
&= \frac{\partial \mathbf{s}(t)}{\partial t} \int_{C_i^+(\mathbf{r})} \rho(\mathbf{r}, t) \, d\mathbf{r} - \int_{C_i^+(\mathbf{r}')} \nabla \alpha_1(\mathbf{r}', t) (\rho_0(\mathbf{r}') + \rho_1(\mathbf{r}', t)) \, d\mathbf{r}' \\
&= q(t) \frac{\partial \mathbf{s}(t)}{\partial t} + \mathbf{J}^s(t). \quad (\text{B.80})
\end{aligned}$$

References

1. Maxima, a computer algebra system. Version 5.27.0 (2010), <http://maxima.sourceforge.net>
2. M. Frigo, S. Johnson, Proc. IEEE **93**, 216–231 (2005)
3. N. Wiener, Acta Math. **55**, 117–258 (1930)
4. A. Khintchine, Math. Ann. **109**, 604–615 (1934)

Appendix C

The Method of Imaginary Time Propagation

The time-independent nuclear Schrödinger equation (2.9) can be solved by the method of imaginary time propagation (see, e. g., Refs. [1–4]). The explanation starts with the time-dependent Schrödinger equation (2.1), which can be rewritten in the integral form

$$|\Phi(t)\rangle = \exp\left(-\frac{i}{\hbar}\mathcal{H}t\right)|\Phi(0)\rangle \quad (\text{C.1})$$

for a Hamiltonian \mathcal{H} that does not explicitly depend on time. The exponential is the time-evolution operator or propagator of the system. The eigenfunctions $|\Psi_i\rangle$ of the Hamiltonian, which satisfy the time-independent Schrödinger equation (2.3), form a complete basis, so they can be used to express the initial state $|\Phi(0)\rangle$ as a linear combination of eigenstates:

$$\begin{aligned} |\Phi(t)\rangle &= \exp\left(-\frac{i}{\hbar}\mathcal{H}t\right) \sum_{i=0}^{\infty} c_i |\Psi_i\rangle \\ &= \sum_{i=0}^{\infty} c_i \exp\left(-\frac{i}{\hbar}E_i t\right) |\Psi_i\rangle, \end{aligned} \quad (\text{C.2})$$

where E_i is the energy eigenvalue corresponding to $|\Psi_i\rangle$. If the time t is replaced by the imaginary time $-i\tau$ in this expression, it results

$$|\Phi(\tau)\rangle = \sum_{i=0}^{\infty} c_i \exp\left(-\frac{1}{\hbar}E_i \tau\right) |\Psi_i\rangle. \quad (\text{C.3})$$

This means that the coefficients in the basis expansion of $|\Phi(\tau)\rangle$ are exponentially damped with increasing τ . In the limit $\tau \rightarrow \infty$, only the state with the lowest energy eigenvalue E_0 remains, so $|\Phi(\tau)\rangle$ becomes the ground state $|\Psi_0\rangle$. Thus, starting from an arbitrary initial state $|\Phi(0)\rangle$, a sufficiently long propagation in imaginary

time yields the ground state of the system. Higher eigenstates can be obtained by starting with an initial state that is orthogonal to all lower eigenstates.

Since the Hamiltonian in the nuclear Schrödinger equation (2.9) consists of a kinetic part and a potential part, $\mathcal{H} = \mathcal{T} + \mathcal{V}$, the propagation can be performed with the split operator technique in practice. This means that a finite timestep $\Delta\tau$ is employed and the propagator is split according to

$$\exp\left(-\frac{\Delta\tau}{\hbar}\mathcal{H}\right) = \exp\left(-\frac{1}{2}\frac{\Delta\tau}{\hbar}\mathcal{V}\right)\exp\left(-\frac{\Delta\tau}{\hbar}\mathcal{T}\right)\exp\left(-\frac{1}{2}\frac{\Delta\tau}{\hbar}\mathcal{V}\right) + \mathcal{O}(\Delta\tau^3). \quad (\text{C.4})$$

The splitting is not exact because \mathcal{T} and \mathcal{V} do not commute. The wave function is represented on a discrete grid in real space, and the potential propagator with $\mathcal{V} = V(x)$ is easily applied by multiplication. The kinetic propagator with $\mathcal{T} = p^2/(2m)$, however, can only be applied by a simple multiplication in momentum space, but a change between real space and momentum space is readily possible by Fourier transform. This leads to the following computation scheme for one propagation step: At first, a half step in real space is performed by multiplication with the potential propagator. Then, the wave function is transformed to momentum space by a Fourier transform and the kinetic propagator is applied by multiplication. Afterwards, an inverse Fourier transform is applied and another half step is carried out in real space by multiplying with the potential propagator. Finally, the wave function has to be normalized, since the imaginary time propagator is not unitary. For excited states, also all lower states have to be removed from the wave function by Gram–Schmidt orthogonalization after each propagation step.

For the systems studied in Sect. 3.2.3, the propagation timestep was always chosen as $\Delta\tau = 12.1$ as (equal to 0.5 a. u.). For the one-dimensional examples, the real space grid consisted of 2048 points with a spacing of $\Delta x = 0.529$ pm (equal to 0.01 a. u.). It ranged from -529 to 554 pm for the harmonic potential, and from -265 to 819 pm for the Morse potential. For all the two-dimensional cases, the real space grid consisted of 256×256 points with a spacing of $\Delta x = \Delta y = 1.06$ pm (equal to 0.02 a. u.), ranging from -135 to 135 pm along both axes.

References

1. M.D. Feit, J.A. Fleck, J. Chem. Phys. **78**, 301–308 (1983)
2. J. Auer, E. Krotscheck, S.A. Chin, J. Chem. Phys. **115**, 6841–6846 (2001)
3. L. Lehtovaara, J. Toivanen, J. Eloranta, J. Comput. Phys. **221**, 148–157 (2007)
4. P. Bader, S. Blanes, F. Casas, J. Chem. Phys. **139**, 124117 (2013)